THE USE OF RADIUM ISOTOPES TO INVESTIGATE BOUNDARY EXCHANGES IN COASTAL OCEAN SYSTEMS

by

William J. Burt

Submitted in partial fulfillment of the requirements
for the degree of Doctor of Philosophy

at

Dalhousie University
Halifax, Nova Scotia
March 2015

for everyone who has helped get me here, both in present and in past

(R.G.I)

TABLE OF CONTENTS

List of Tables . . . . . **vii**

List of Figures . . . . . **viii**

Abstract . . . . . **x**

List of Abbreviations and Symbols Used . . . . . **xi**

Acknowledgements . . . . . **xii**

Chapter 1 Introduction **1**

1.1 Carbonate System Parameters 2

1.2 Boundary Fluxes 3

1.3 Radium Isotope Tracers 5

1.4 Study Regions 6
1.4.1 Bedford Basin 7
1.4.2 The Scotian Shelf 8
1.4.3 The North Sea 10

1.5 Objectives 12

1.6 Outline 13

Chapter 2 Methodology **15**

2.1 Sampling for Radium Isotopes 15
2.1.1 Large-Volume Water Sampling 15
2.1.2 Radium Extraction 16

2.2 The RaDeCC Counter 18

2.3 $^{223/224}$Ra Data Processing I - cpm to dpm 20
2.3.1 Calculating RaDeCC Efficiency 22

2.4 $^{223/224}$Ra Data Processing II - Activity Corrections 24

2.5 Calculation of Uncertainties 26
2.5.1 Relative Counting Uncertainty 27
2.5.2 Error Propagation Technique 28
2.5.3 Comparison of Techniques 29

2.6 $^{223/224}$Ra Counting Procedures 30

2.7 ^{228}Ra Analysis 31

2.8 Consideration of Measurement Accuracy and the Signal to Noise Ratio . 32
2.8.1 Background and Noise 32
2.8.2 Replicates and Intercalibrations 34

2.9 Future Improvements to Radium Methodology 35

2.10 Collection and Analysis of Carbonate System Parameters 36
2.10.1 Dissolved Inorganic Carbon 36
2.10.2 Total Alkalinity 37

Chapter 3 Sediment-Water Column Fluxes in Bedford Basin 38

3.1 Abstract 38

3.2 Introduction 39

3.3 Methods 41
3.3.1 Study Site 41
3.3.2 Analytical Methods 43
3.3.3 Vertical Mixing Coefficients Derived from Radium Tracers . . . 46
3.3.4 Calculating Benthic Radium, Carbon, Oxygen, and Nutrient Fluxes 47
3.3.5 Numerical Simulations of the 1-D Model 49

3.4 Results 50
3.4.1 Radium Distribution 50
3.4.2 ^{224}Ra, DIC, O_2 and Nutrient Fluxes 52

3.5 Discussion 57
3.5.1 K_Z measurements 57
3.5.2 Deep-water Intrusion 58
3.5.3 Remineralization of Organic Material 59
3.5.4 Numerical Model Results 62
3.5.5 Carbon Budgets 64

3.6 Conclusions 65

3.7 Acknowledgements 66

Chapter 4 Radium Isotope Distributions and Cross-Shelf Transport on the Scotian Shelf 67

4.1 Abstract 67

4.2 Introduction 68

4.3 Oceanographic Setting 70

4.4 Methods . . . 72
4.4.1 Sample Collection and Analysis . . . 72
4.4.2 Determining Diffusive Mixing Coefficients using Ra isotopes . . 73
4.4.3 2-D Numerical Radium Simulations . . . 74

4.5 Results . . . 75
4.5.1 Ra Distribution . . . 75

4.6 Discussion . . . 78
4.6.1 Evaluation of Background Ra Signals . . . 78
4.6.2 Vertical Radium Distributions: Seafloor Ra Additions . . . 79
4.6.3 Horizontal Dispersion of the Outer-Shelf Ra Signal . . . 80
4.6.4 Horizontal Mixing Coefficients: 1-D Diffusion Model . . . 81
4.6.5 Optimized Coefficients using a 2-D Diffusion Model . . . 82
4.6.6 Estimates of Carbon and Nutrient Transport . . . 83

4.7 Conclusions . . . 88

4.8 Acknowledgements . . . 89

Chapter 5 Sediment-Water Column Exchange in the North Sea . . . 90

5.1 Abstract . . . 90

5.2 Introduction . . . 91

5.3 Study Area . . . 93

5.4 Methods . . . 96
5.4.1 Sample Collection and Analysis . . . 96
5.4.2 Flux Calculations from Incubations . . . 98
5.4.3 Radium Inventories . . . 98
5.4.4 Ra Mass Balance . . . 99
5.4.5 Passive Tracer Modeling . . . 101

5.5 Results and Discussion . . . 103
5.5.1 North Sea Ra Distributions and Sources . . . 103
5.5.2 Independent Estimates of Benthic Ra Flux . . . 107
5.5.3 Sediment-water Ra exchange: important mechanisms and dominant controls . . . 111
5.5.4 Pore water fluxes and implications for carbon biogeochemistry . 116
5.5.5 Passive Tracer Study . . . 118

5.6 Conclusions . . . 120

5.7 Acknowledgements . . . 121

Chapter 6 Evaluating North Sea Carbon Sources using Radiogenic and Stable Carbon Isotope Tracers . . . 122

6.1 Abstract . . . 122

6.2 Introduction . . . 123

6.3 Oceanographic Setting . . . 125

6.4 Methods . . . 127
6.4.1 Sample Collection and Analysis . . . 127
6.4.2 Formulation of the 1-D Diffusion Model . . . 128
6.4.3 Determination of the Biological Component of DIC (DIC_{bio}) . . . 128
6.4.4 Calculating Biological Fractionation using DIC_{bio} and $\delta^{13}C_{DIC}$ . . . 130

6.5 Results and Discussion . . . 131
6.5.1 North Sea Surface Distributions . . . 131
6.5.2 Biological Fractionation and Freshwater $\delta^{13}C_{DIC}$ Signals . . . 134
6.5.3 Coastal Carbon Fluxes . . . 137
6.5.4 ^{228}Ra as a Tracer of AT . . . 141

6.6 Summary and Conclusions . . . 145

6.7 Acknowledgements . . . 146

Chapter 7 Conclusions . . . 147

7.1 Methodological Improvements and Novel Approaches . . . 147

7.2 Major Findings . . . 148

7.3 Outlook and Perspectives . . . 150

Appendix A North Sea Ra Data Table . . . 154

Appendix B Copyright Permissions . . . 157

Bibliography . . . 158

LIST OF TABLES

2.1 Summary of RaDeCC system counting efficiencies during the study 23

2.2 Summary of background counts 33

2.3 RaDeCC intercalibration results 35

3.1 Daily results of K_Z, A_0, as well as benthic fluxes of ^{224}Ra, DIC and oxygen 52

3.2 Comparison of methods for benthic carbon and oxygen fluxes . . . 54

3.3 Chemical fluxes in Bedford Basin 56

4.1 Onshore chemical fluxes at the 80 m depth horizon 87

5.1 Values used in mass-balance model 102

5.2 Radium incubation and pore water results 109

5.3 Comparison of radium benthic flux estimates 115

A.1 Summary of North Sea radium samples 154

LIST OF FIGURES

1.1 Citation record for topic search 'radium' and 'ocean' 6
1.2 Bathymetric maps of the Bedford Basin and Scotian Shelf 8
1.3 Schematic cross-sections of the Scotian Shelf and North Sea . . . 9
1.4 Bathymetric map of the North Sea 11

2.1 Radium extraction apparatus 17
2.2 The RaDeCC counting system 19
2.3 ^{232}Th and ^{235}U decay chains 20
2.4 RaDeCC voltage curve 25

3.1 Schematic cross-section and bathymetric map of Bedford Basin . . 42
3.2 Weekly temperature and salinity profiles from August 2010 to January 2011 44
3.3 Deep water oxygen saturation in Bedford Basin 45
3.4 Time series of Chl a, POC, deep-water oxygen and nutrients, and temperature depth profiles in Bedford Basin 48
3.5 Vertical profiles and ln transformations of ^{224}Ra activity 51
3.6 Vertical profiles of AT, DIC, and oxygen 53
3.7 Deep-water nutrient time-series 55
3.8 Finite difference model results 63

4.1 Oceanographic setting on the Scotian Shelf 71
4.2 Nearshore station map and associated ^{224}Ra activities 76
4.3 Cross-sections of ^{224}Ra and potential density along Scotian Shelf transects 77
4.4 Offshore ^{224}Ra transects with best-fit curves 81
4.5 2-D radium diffusion model output 83
4.6 Chemical gradients at 80 m depth horizon, and cross-sections of carbon and nutrients 86

5.1 Bathymetric map of North Sea with station locations 94
5.2 Mass-balance setup in the Southeastern Bight 100
5.3 Surface distributions of radium, salinity and stratification 104
5.4 Vertical profiles of radium and potential density anomaly 105
5.5 Offshore transects of radium inventories 107
5.6 Relationships between radium efflux, mean grain size, porosity, and stir rate 112
5.7 Comparison between radium-based and direct incubation-based alkalinity fluxes 117
5.8 ECOSMO model output 119

6.1 Oceanographic setting in the North Sea 126
6.2 North Sea surface distribution maps 131
6.3 Vertical profiles of $\delta^{13}C_{DIC}$ 132
6.4 Offshore transects of modeled and observed ^{224}Ra and ^{228}Ra . . . 133
6.5 Covariations of DIC, $\delta^{13}C_{DIC}$, and DIC_{bio} 135
6.6 Salinity relationship with $\delta^{13}C_{DIC}$ 137
6.7 Correlation of radium with $\delta^{13}C_{DIC}$ and metabolic DIC 139
6.8 Metabolic DIC inventories in the southern North Sea 141
6.9 Salinity and ^{228}Ra as tracers of North Sea alkalinity 142
6.10 Changes in proton concentration induced by removing coastal alkalinity inputs 144

7.1 Further insight into ventilation events in Bedford Basin 151
7.2 Potential future Ra related studies on the Scotian Shelf 152

ABSTRACT

Coastal seas are of major economic and social importance for the majority of the human population, and are amongst the most biologically and geochemically active areas of the biosphere. Coastal systems are also highly dynamic and complex areas of the global oceans, due in part to the extensive interactions that occur at the system boundaries. Carbon and nutrient fluxes across these boundaries at the seafloor, the atmosphere, the land, and the shelf-break, fuel intense biological activity and high spatial and temporal variability characteristic of coastal seas. Despite their importance, the magnitudes of dissolved material exchanges across these boundaries represent a significant area of uncertainty in coastal ocean biogeochemistry. This research utilizes naturally-occurring radium isotope tracers (^{224}Ra, ^{223}Ra, ^{228}Ra), which have well defined land and seafloor sources, to quantify cross-boundary fluxes in various coastal regions of the North Atlantic ocean.

This thesis presents flux measurements in a series of coastal regimes, throughout which a clear progression can be seen in the overall scope of the research. The initial study utilizes vertical radium profiles and a 1-D diffusion model to quantify benthic fluxes of carbon, nutrients and oxygen at a time-series station in a small enclosed basin (Bedford Basin, Nova Scotia). This work is then extended to transects of radium measurements across an open continental shelf (Scotian Shelf, northwestern Atlantic) which are combined with 2-D numerical simulations to yield estimates of cross-shelf carbon and nutrient transport from the adjacent deep ocean. Finally, a comprehensive basin-wide radium survey in a semi-enclosed shelf sea of the northeastern Atlantic (the North Sea) is used to provide detailed assessment of sediment-water column exchanges across the region and land-ocean interaction at the European continental coastline. Despite differences in the geometry and spatial scale of each region, significant boundary exchange in all the regimes provides the opportunity to quantify important carbon inputs using radium-based techniques. Overall, this research provides a greater understanding of both the magnitude and biogeochemical impact of boundary exchanges in coastal waters, while also encouraging and guiding future radium studies through novel methodology and detailed results.

LIST OF ABBREVIATIONS AND SYMBOLS USED

Roman symbol	Description	Units
A_0	Activity at source location or at time zero	dpm 100 L^{-1}
Ac	Actinium isotope	dpm 100 L^{-1}
AT	Total Alkalinity	μmol kg^{-1}
$\delta^{13}C_{DIC}$	Stable carbon isotope signature of DIC	‰ VPDB
DIC	Dissolved Inorganic Carbon	μmol kg^{-1}
DIC_{bio}	Biological component of DIC	μmol kg^{-1}
H^+	Hydrogen Ion	mol L^{-1}
K_X	Coefficient of horizontal turbulent diffusion	m^2 s^{-1}
K_Z	Coefficient of vertical turbulent diffusion	m^2 s^{-1}
pCO_2	Partial pressure of CO_2	μatm
POC	Particulate Organic Carbon	mg C m^{-3}
POM	Particulate Organic Matter	no units listed
Po	Polonium isotope	no units listed
Ra	Radium isotope	dpm 100 L^{-1}
Rn	Radon isotope	no units listed
Th	Thorium isotope	dpm 100 L^{-1}
S	Salinity	no units
T	Temperature	°C
$t_{1/2}$	Isotope half-life	days
VPDB	Vienna Pee Dee Belemite	no units

Greek symbol	Description	Units
ϵ	biological isotope fractionation factor	no units
λ	radioactive decay constant	day^{-1}
ρ	density of water	kg m^{-3}
σ_θ	potential density anomaly	kg m^{-3}

ACKNOWLEDGEMENTS

A massive thank you to Helmuth, who has always given me incredible guidance, fantastic opportunities, and a lasting friendship. I have always considered myself extremely lucky to have you as a supervisor. Also, many thanks to Katja, John, and Markus, who have helped shape this thesis and have kept me on track along the way. Thank you Katja (again), Jean-Pierre, Corinna, and Ute for improving all of the manuscripts by walking me through numerical simulations.

I am grateful for all the friends and colleagues I have made both at Dalhousie, and abroad. Thank you to all my fellow Dalhousie grad students, you are what kept me sane while I sat in room 5638 day after day. Also, thank you to all of my colleagues across the Atlantic: Heiko, Mathilde, Johannes, Abdir, and Hein, and Michiel. A special thank you to Steven Colbert, who helped guide me through the early years of radium isotope analyses, and who gave me a jump-start when my research really needed it. So many thanks are necessary to the crews of the Hudson, Sigma T, and Pelagia. These working relationships are what make fieldwork in oceanography really special. Thank you for the countless amounts of help fixing broken instruments, carrying jugs of water, and making me laugh when I really needed it.

Thank you Ma, and thank you Pa. I could not have come this far without your support. Thanks to Jenn, for being the best damn sister a guy could ask for, and for publishing enough papers to ignite my new-found research competitiveness. Lastly, thanks to JMC, to whom I am utterly dependent on for love and support, and who has enough of both to get me through anything...even a PhD.

CHAPTER 1

INTRODUCTION

The persistent and rapid rise of atmospheric carbon dioxide (CO_2) concentrations since the beginning of the industrial revolution has two major global environmental consequences. The first is the enhancement of the greenhouse effect, wherein outgoing radiation is increasingly radiated back towards the Earth's surface, resulting in an increase in global temperatures (i.e. global warming) (*IPCC*, 2007). The second is ocean acidification, as higher atmospheric CO_2 concentrations increase the uptake of CO_2–a weak acid–by the global surface ocean. This process poses an immediate threat, not only to individual organisms, but also to the fundamental structure of marine ecosystems as a whole. Throughout the majority of the open ocean, net CO_2 uptake is observed, and the extent and spatial distribution of this uptake has been well documented (*Sabine et al.*, 2004; *Takahashi et al.*, 2009). However, CO_2 exchange, and acidification in general, is much more complex in coastal waters.

While coastal seas represent only 8 % of the total ocean surface area, they host as much as one third of global marine primary production, and thus house disproportionately large fluxes of carbon and nutrients (*Gattuso et al.*, 1998). As a result, biogeochemical cycling in coastal waters is more complex and intense, undergoes higher seasonal variabilities, and has a greater overall uncertainty relative to open ocean systems. Carbon cycling in coastal oceans is also complicated by land-derived inputs. This includes high atmospheric nitrogen and sulphur inputs, which induce additional acidification (*Doney et al.*, 2009), and high nutrient loads from rivers and groundwater, which lead to coastal eutrophication (*Borges and Gypens*, 2010). Observational case-studies in the North Sea, located in the coastal northeast Atlantic, estimate CO_2 uptake rates which are an order of magnitude

larger than the global mean (*Kempe and Pegler*, 1991; *Frankignoulle and Borges*, 2001; *Thomas et al.*, 2004), while on the Scotian Shelf, in the northwest Atlantic, annual net CO_2 outgassing is observed (*Shadwick et al.*, 2010). In order to explain these variations in air-sea CO_2 fluxes, and gain insight into coastal ocean acidification, a better understanding of the sources, sinks, and underlying mechanisms of the coastal carbon cycle is required. One step towards a complete understanding can be achieved by investigating fluxes across the other three boundaries in coastal seas: the seafloor, the land, and the open ocean.

1.1 Carbonate System Parameters

Once dissolved into seawater, CO_2 exists in four species: aqueous carbon dioxide (CO_2(aq)), carbonic acid (H_2CO_3), bicarbonate ion (HCO_3^-), and carbonate ion (CO_3^{2-}). The first two species are difficult to distinguish analytically, and H_2CO_3 is highly unstable in seawater, thus these terms are often reported together simply as CO_2:

$$[CO_2(aq)] + [H_2CO_3] = [CO_2]. \tag{1.1}$$

The sum of these three species is termed as the total dissolved inorganic carbon (DIC):

$$DIC = [CO_2] + [HCO_3^-] + [CO_3^{2-}]. \tag{1.2}$$

This total value can be measured because lowering the pH of a seawater sample causes the DIC to be converted entirely into CO_2, which can then be quantitatively determined. Another key parameter which can be measured with good precision is the total alkalinity (AT) of seawater. AT is a near-conservative parameter that can be defined as the charge balance in seawater, or, as it is described here, the buffering capacity of seawater (for example, see *Dickson* (1981)). Seawater alkalinity is created by an excess of bases formed from weak acids (pKa>4.5 at 25°C) relative to strong acids (pKa<4.5 at 25°C). When introducing an acid to seawater, as is the case during CO_2 uptake, these bases of weak acids act as 'proton acceptors', buffering pH changes. The excess in proton (H^+ ion) acceptors can be quantified in units of moles of H^+ ion equivalents per kilogram of seawater, written as:

$$AT \simeq [HCO_3^-] + 2 * [CO_3^{2-}] + [B(OH)_4^-] + [OH^-] - [H^+]. \tag{1.3}$$

This equation neglects species which have an insignificant contribution. Using this definition, AT is measured by incrementally adding protons to a seawater sample (i.e. an acid-base titration). The AT and, to a much greater extent, the DIC of seawater can be altered by a number of biologically-mediated processes, such as carbonate precipitation or dissolution, photosynthesis and respiration. The addition of freshwaters, which contain varying ionic concentrations, also affect DIC and AT.

DIC and AT data, which are presented in chapters 3 through 6, are directly measured from seawater samples. The analytical procedures for these measurements are outlined in chapter 2. In addition to the equations describing DIC (Eq. 1.2) and AT (Eq. 1.3), equilibrium equations exist which relate CO_2, HCO_3^- and CO_3^{2-} species. Utilizing all of these equations, DIC and AT are used to calculate other carbonate system parameters, such as the partial pressure of carbon dioxide (pCO_2) or pH. These calculations have been automated into the *CO_2sys* program developed by *Lewis and Wallace* (1998).

1.2 Boundary Fluxes

Continental shelf systems are, by definition, shallower than 200 m depth, and are characterized by high rates of primary productivity. These features lead to significant organic matter deposition on the seafloor. Within sediments, organic material is broken down via oxidation by a variety of bacterially-mediated reactions, which occur in a step-wise fashion depending on the availability of particular electron acceptors. The efflux of the reaction byproducts back into the overlying water column – termed here as sediment-water column exchange – constitutes an important contribution to the biogeochemical cycles of carbon, nutrients and various metal species.

When organic matter deposition rates are high, only a fraction of deposited material can be oxidized using oxygen, leaving anaerobic oxidation processes to play a more central role. The extent to which these different oxidation reactions contribute to organic matter remineralization regulates how benthic fluxes affect the carbon cycle. For example, the use of allochthonous nitrate or sulphate as electron acceptors during denitrification or sulphate reduction, respectively, results in net AT production in sediments. Denitrification irreversibly generates alkalinity whereas sulphate reduction is often reversible unless coupled with pyrite burial. Benthic AT release plays a major role in buffering the effects of ocean acidification in coastal regions, but the extent to which it occurs remains largely

unknown for many coastal systems. Organic matter remineralization can produce both DIC and AT, or can produce DIC while consuming AT. As a result, each remineralization reaction produces a characteristic DIC:AT ratio. Aerobic respiration produces DIC while reducing AT slightly due to nitrate release (DIC:AT $\sim$ -6.6), denitrification releases DIC and AT in nearly equal amounts (DIC:AT $\sim$ 1.25), and sulphate reduction releases 0.99 moles of AT per mole of DIC (DIC:AT $\sim$ 1) (*Chen and Wang*, 1999). Therefore, measuring the DIC:AT ratio of a given flux provides information regarding the dominant remineralization processes which have occurred within the sediments. Similarly, DIC to nitrate (DIC:NO_3^-) ratios can help assess the relative contributions of aerobic respiration, which produces both DIC and nitrate (when assuming organic material is produced in near-Redfield ratios, this produces DIC:NO_3^- in a ratio of $\sim$ 106/16 or $\sim$ 6.6), and anaerobic denitrification, which yields higher DIC:NO_3^- ratios, as DIC is produced but nitrate is consumed.

Important material exchanges also occur at the coastal-open ocean boundary (i.e. the shelf-edge). Offshore subsurface waters are relatively enriched in DIC and nutrients compared to shelf waters, due to the gradual buildup of respiratory products over time. Onshore transport of these waters has been shown to fuel primary production in many coastal regions, including continental shelves of the northwest Atlantic (e.g. *Riley* (1967)). As a result, previous major scientific programs like the Shelf-Edge Exchange Programs (SEEP I and II) in the northwest Atlantic, and the Ocean Margin Exchange programs (OMEX I and II) in the northeast Atlantic, have been devoted to quantifying cross-shelf transport (*Rowe et al.*, 1986; *Biscaye et al.*, 1994; *Wollast and Chou*, 2001). Nevertheless, this particular input remains relatively poorly constrained in most coastal systems.

Finally, inputs at the land-ocean boundary (e.g. from rivers, estuaries, and groundwater) can represent a very large source of carbon and nutrients to coastal waters, particularly in heavily-populated regions. Consequently, coastal seas are often labeled as effective filters for anthropogenic nutrient inputs to the open ocean (*Meybeck et al.*, 2007; *Fennel*, 2010). Nearshore environments, such as estuaries or lagoons, are often highly eutrophied due to the combined inputs from land-ocean and sediment-water column boundaries. Also, these areas are often poorly ventilated, making them ideal sites for anaerobic remineralization, and thus their flushing into the open waters can be especially important in coastal biogeochemical cycles. Land-ocean interaction has been shown to play an important role in the cycling

of nutrients, trace metals, and AT in the North Sea (*Thomas et al.*, 2009; *Moore et al.*, 2011; *Winde et al.*, 2014), and is known to affect air-sea CO_2 exchange (*Omar et al.*, 2010). Nevertheless, prior studies of land-sea interactions have focused primarily on near-shore areas, and thus much is still unknown regarding the effects of land-ocean interaction on the open North Sea, and other shelf seas.

1.3 Radium Isotope Tracers

The key to utilizing radionuclides as oceanographic tools is to measure isotopes that decay on timescales that match the timescales of the particular process of interest. In general, the 'detection window' of an isotope, or the time it exists in measurable quantities, is equal to 4-6 times its half-life ($t_{1/2}$). Any isotopic measurement is also considered to be an integrated observation over that time period. Therefore, observed activities of the short-lived radium (Ra) isotope pair, ^{224}Ra ($t_{1/2}$ = 3.6 days) and ^{223}Ra ($t_{1/2}$ = 11.4 days), correspond to an integrated view of processes occurring on approximately two-week and two-month timescales, respectively. These time scales correspond to many shorter term coastal processes, such as organic matter remineralization, benthic DIC, AT, and nutrient fluxes, and smaller scale water-mass mixing. Meanwhile, the longer-lived ^{228}Ra isotope ($t_{1/2}$ = 5.7 years), can be used to trace larger scale water mass mixing processes.

Radium is not a bioactive or particle reactive element, and thus exhibits a conservative behavior in the water column. Furthermore, radium has no atmospheric source and is formed exclusively by the decay of sediment-bound thorium and actinium isotopes. Thorium and actinium are rapidly scavenged out of the water column, leading to their enrichment in the underlying sediments, as well as a very low radium background in the water column. The return to secular equilibrium involves the release of radium into the water column, which occurs almost entirely at the sediment-water and land-ocean interfaces, and is often readily detectable above the low water column background. Considering its well constrained sources, as well as its conservative behavior, radium can be considered a model tracer for physical mixing away from coastal boundaries. With the development of the RaDeCC counting apparatus in the mid-1990's (see *Moore and Arnold* (1996)), the use of radium in oceanographic studies has increased steadily over the past two decades (Figure 1.1) (*Charette and Scholten*, 2008). Using radium, much has been learned regarding the importance of submarine groundwater discharge in coastal

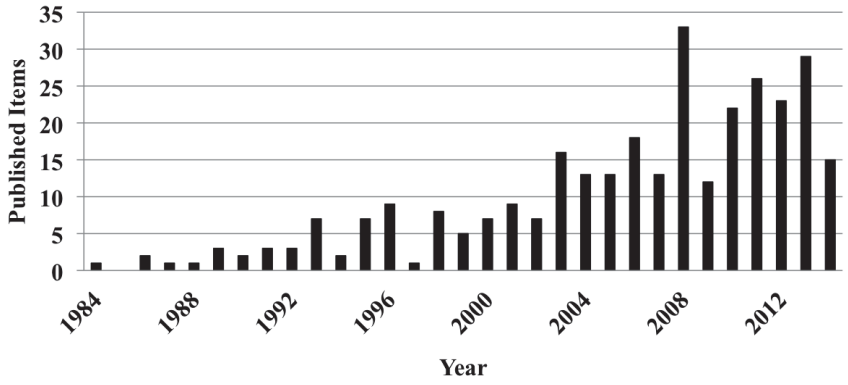

Figure 1.1: Citation record from Web of Science topic search for 'radium' and 'ocean'. This shows the steady increase in radium-based oceanographic studies over the past three decades.

biogeochemistry (*Kelly and Moran*, 2002; *Moore*, 2003; *Kwon et al.*, 2014), residence times and flushing of lagoons and estuaries into coastal waters (*Dulaiova and Burnett*, 2008; *Moore and de Oliveira*, 2008), and general rates of water-mass mixing (*Moore*, 2000; *Hancock et al.*, 2006; *Colbert and Hammond*, 2008).

Throughout this study, radium is utilized in a number of ways. Gradients in radium activity are used to quantify coefficients of physical mixing (described as K_X and K_Z). Previously, these types of coefficients have been estimated using seasonal salinity changes (*Ketchum and Keen*, 1955) or spatial salinity gradients (*Coachman and Walsh*, 1981). Here, mixing coefficients are then applied to parallel measurements of DIC, AT, nitrate and phosphate to estimate boundary fluxes, and flux ratios of these species. Similarities in conservative behaviors over large scales lead to the introduction of long-lived ^{228}Ra as an ideal tracer of AT. This study also presents a variety of numerical modeling applications for radium. Specifically, radium models are used to: 1) reproduce observations to test the steady-state assumptions of commonly-used analytical models, 2) quantitatively compare observational and modeled distributions to inversely calculate mixing rates in multiple dimensions, and 3) validate independently calculated, observation-based radium flux terms.

1.4 Study Regions

This research presents a series of independent studies conducted in three different coastal regions of the North Atlantic. These study sites span three distinct types of coastal region:

an enclosed basin, an extended platform, and an open regional sea (*Meybeck et al.*, 2007). Little or no prior radium sampling has been conducted at any of the study sites, thus the data presented here represent a further expansion of the global radium database at a time when radium-based studies are beginning to reach global scales (see, for example, *Kwon et al.* (2014)). Throughout this research, the study regions also increase in spatial scale, which reflects the improvements made in the sampling methodology, as well as an increase in the scope of the radium isotopic techniques. Chapter 3 presents work conducted at a single Bedford Basin time-series station. Chapters 4 through 6 focus on two well-studied continental shelf systems of the North Atlantic: the Scotian Shelf, located in the Canadian northwest Atlantic, and the North Sea, located in the European northeast Atlantic. Whereas both regions play important roles in the biogeochemical cycling of the North Atlantic Ocean, the characteristics of their carbon and nutrient cycles are distinctly different. Here, a brief background for each region is presented.

1.4.1 Bedford Basin

Bedford Basin, located within Halifax Harbour (Figure 1.2), is of substantial economic and environmental importance on a regional scale, housing a large international seaport and a recently developed ship building facility for the Canadian Navy. The basin has been collecting anthropogenic runoff from the surrounding Halifax Regional Municipality for over a century. Direct discharge of untreated sewage, industrial waste from shipyard activities, and leaching of solid waste on land into the basin have left the fine-grained clay sediments highly contaminated with copper, lead and zinc, which has been an environmental concern for many decades (*Buckley and Winters*, 1992).

Studies focusing on the Bedford Basin carbon cycle began over four decades ago. Early estimates of primary productivity and vertical export were made by *Platt and Conover* (1971), while further details on spatial and temporal variability in primary production were given by *Platt* (1975). Organic carbon sedimentation rates have been studied extensively using sediment traps (*Hargrave et al.*, 1976; *Hargrave and Taguchi*, 1978; *Taguchi and Hargrave*, 1978). Since the establishment of the weekly Bedford Basin Monitoring Program in 1991, an overall understanding of biogeochemical cycling in Bedford Basin has increased steadily, including studies related to plankton speciation and abundances (*Li and Dickie*, 2001), bloom dynamics (*Azetsu-Scott and Johnson*, 1994), and impacts of sewage effluent (*Pan and Rao*, 1997). Nonetheless, studies focused specifically on Bedford

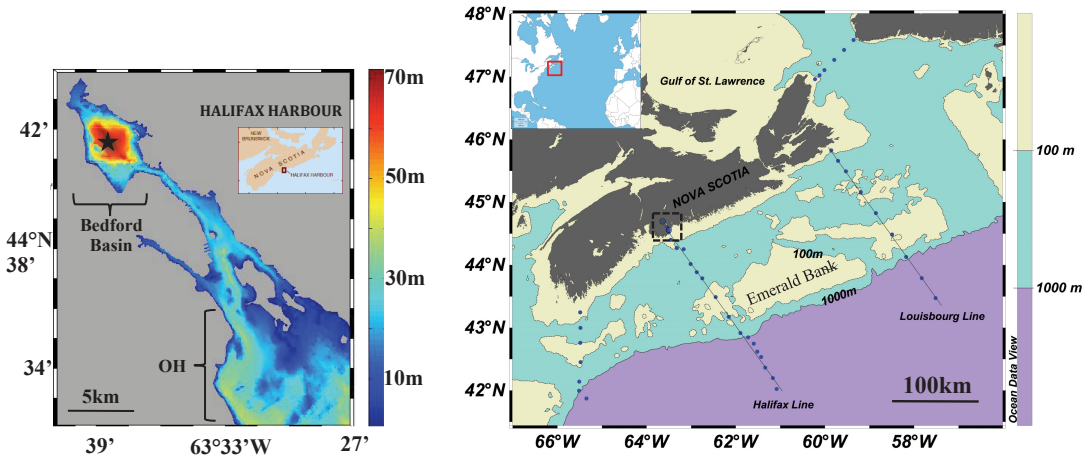

Figure 1.2: **Left:** Bathymetric map of Halifax Harbour and Bedford Basin. Black star indicates location of Bedford Basin sampling site. OH = Outer Harbour. **Right:** Bathymetric map of the Scotian Shelf. Black dashed box indicates location of Halifax Harbour. Cross-shelf sampling transects are shown. Offshore banks (including Emerald Bank) are shallow regions (<100 m depth) near the shelf-break. Inset map shows location of the Scotian Shelf in the northwest Atlantic. Note the different scale bars in the left and right panels.

Basin sediments have almost entirely related to their high toxicity (*Tay et al.*, 1992; *Buckley et al.*, 1995), and it appears that no study to date has directly measured benthic carbon and nutrient fluxes. Despite an in depth understanding of productivity and sedimentation, knowledge of the carbon cycle is incomplete without estimates of the benthic return flux.

1.4.2 The Scotian Shelf

Waters exiting Bedford Basin flow through Halifax Harbour and onto the open Scotian Shelf (Figure 1.2). The Scotian Shelf is a broad, highly productive continental margin which hosts an active fishery as well as oil and gas exploration. The irregular shelf topography includes a series of offshore banks and channels (Figure 1.2), which influences the regional circulation and brings the seafloor in close contact with surface waters far offshore. The Scotian Shelf contains predominantly Arctic waters which flow, as part of the Nova Scotian and Labrador currents, parallel to the coastline in a southwest direction (see Figure 1.3 for a schematic cross-section). The region exhibits net CO_2 outgassing on an annual scale, the extent and variability of which have been well documented (*Shadwick et al.*, 2010, 2011; *Shadwick and Thomas*, 2011). The high surface water pCO_2 required for net outgassing is thought to be sourced from upwelling or vertical entrainment of

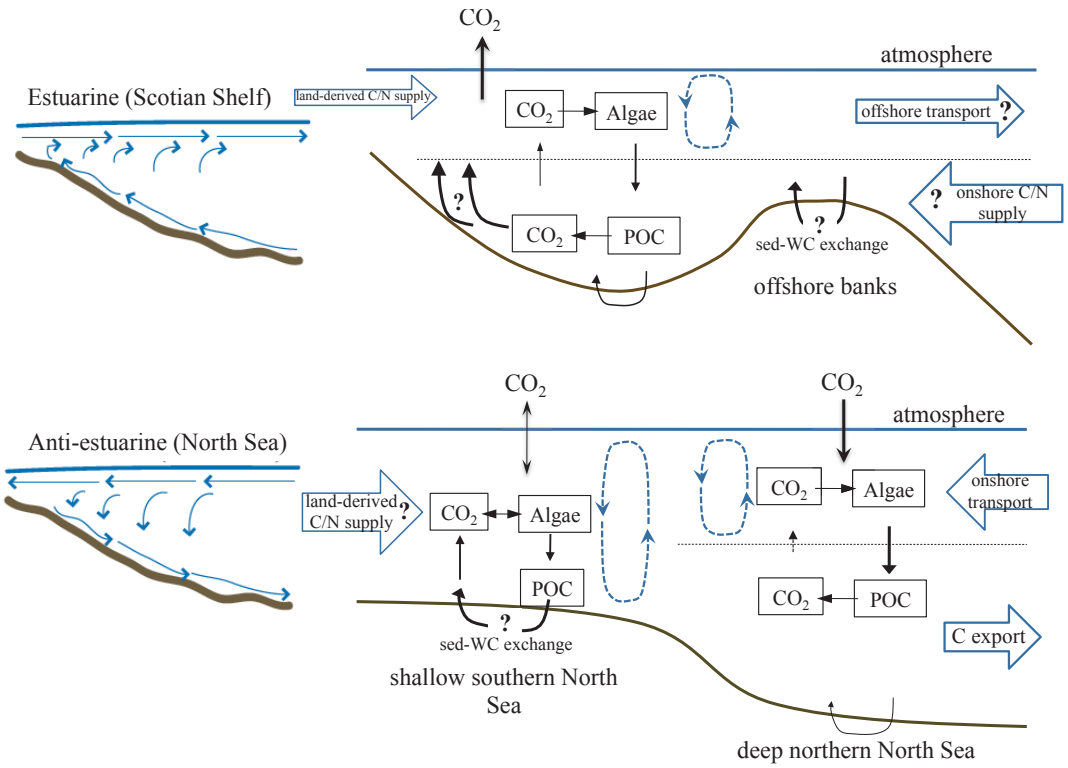

Figure 1.3: A schematic representation of the Scotian Shelf (**top**), and North Sea (**bottom**). Question marks (?) label the key areas of uncertainty in these regions which are addressed in this research. Circulation diagrams on the left are taken from *Shadwick et al.* (2010), and some aspects of the North Sea cycling are taken from *Thomas et al.* (2004). POC = Particulate Organic Carbon.

carbon and nutrient-rich deep waters. The region is characterized as an upwelling system, due in part to predominantly westerly winds creating Ekman transport in a southerly (i.e. offshore) direction. However, no quantitative evidence exists that links observed CO_2 fluxes to this upwelling. Furthermore, the ultimate carbon and nutrient sources of these subsurface waters are thought to be the onshore flow (i.e. the return flow) from the open ocean (*Shadwick et al.*, 2011), yet the extent of this process is also undefined.

The current understanding of cross-shelf carbon and nutrient cycling on the Scotian Shelf is illustrated in Figure 1.3. Offshore transport in surface waters has been briefly discussed in studies focused on understanding the flushing rates of Halifax Harbour onto the Scotian Shelf, either using box models (*Petrie and Yeats*, 1990), or sophisticated 3D hydrodynamical models (*Shan et al.*, 2011). Onshore transport of subsurface waters onto the shelf was identified by *Smith* (1978) using a moored current profiler at the shelf break.

Houghton et al. (1978) used these findings to quantify an advective onshore nutrient flux sufficient to support observed high levels of primary productivity. However, these prior studies describe the onshore flow of waters through distinct topographic channels rather than the more general onshore material fluxes illustrated in Figure 1.3. Recent numerical models of the northwestern Atlantic shelf report uncertainty regarding onshore flux terms (*Fennel*, 2010). Finally, studies of sediment-water column interaction on the Scotian Shelf have focused almost entirely on the central basins, where sediments accumulate at higher rates, are finer-grained, and are more organic-rich than in regions closer to shore, or atop shallow banks (*Buckley*, 1991; *Boudreau et al.*, 1998; *Mucci et al.*, 2000). *Grant et al.* (1991) found that oxygen demand and community metabolism is much greater within sediment depocenters (i.e. deep basins) compared to adjacent areas on the shelf. In contrast, studies atop shallow banks have focused on their small-scale circulation features and their effects on general shelf circulation (*Han and Loder*, 2003). The highest abundances of cod and haddock eggs have been observed above shallow banks, thus they are considered to be vital spawning areas for these economically important species (*Brander and Hurley*, 1992). On the Scotian Shelf as a whole, uncertainties still exist regarding exchanges across the land-ocean, shelf-open ocean, and sediment-water column boundaries (see Figure 1.3).

1.4.3 The North Sea

The North Sea is of substantial international economic importance. In addition to fisheries activity, the North Sea is a site of extensive resource extraction, including numerous offshore oil and gas platforms, and large wind-farms (*Emeis et al.*, 2015). The North Sea is dominated by Gulf Stream water that enters and exits predominantly through the northern boundary (Figure 1.4) (*Huthnance*, 1995). Freshwater inputs are provided by European continental rivers, while low salinity waters also enter from the Baltic Sea (Figure 1.4). Like the Scotian Shelf, the North Sea lies in a temperate climate, and the westerly winds generate a southward Ekman transport of surface water, which in this case is onshore, and establishes a downwelling circulation (Figure 1.3). Downwelling of productive surface waters, and subsequent offshore transport in the subsurface, results in a net export of organic material to the open North Atlantic, which has led to the characterization of the North Sea as an effective carbon shelf pump (*Thomas et al.*, 2004; *Bozec et al.*, 2005). As a consequence of the shelf pump, the North Sea exhibits a strong net uptake of CO_2 (*Thomas et al.*, 2004). The North Sea is also characterized by an extensive shallow southern region,

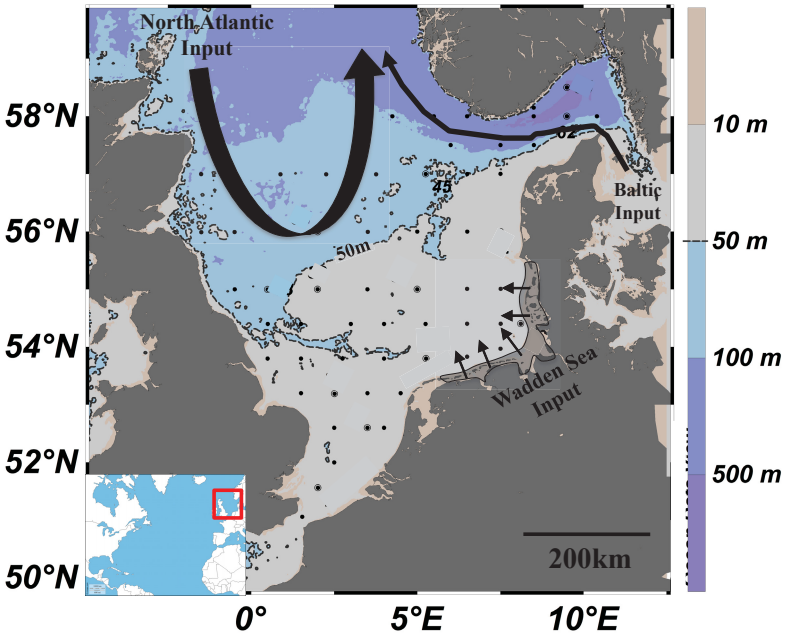

Figure 1.4: Bathymetric Map of the North Sea. Black arrows show major water inputs and general circulation patterns. Area of the Wadden Sea is outlined. Inset map shows location of the North Sea in the northeast Atlantic.

where predominantly tidal forcing creates a fully-mixed water column throughout the year. In this region, sediment-water interaction is substantial (*Slomp et al.*, 1997), yet the impact of this exchange on the overall biogeochemistry of the system is not fully understood. The North Sea is also one of the most heavily populated coastal regions in the world, and as a result, continental runoff, rich in nutrients and organic material, has a major impact on North Sea carbon and nutrient cycling. Much of this runoff first enters the Wadden Sea, an extensive tidal estuary extending from the northern Netherlands to northern Denmark, covering approximately 5000 km^2 (Figure 1.4). Extensive organic matter respiration occurs within these regions, and as a result, many recent studies are devoted to understanding the impact of these coastal inputs on the biogeochemistry of the North Sea (e.g. *Pätsch and Kühn* (2008); *Schwichtenberg* (2013)).

The North Sea is one of most studied coastal regions in the world. More recently, this has included the development of numerous sophisticated biogeochemical models, the results of which have called attention to areas of uncertainty in our understanding of the system. For example, the need for more sophisticated three-dimensional modeling of

sediment-water column interactions was demonstrated by *Luff and Moll* (2004). Similarly, *Daewel and Schrum* (2013) concluded that uncertainties in model output are likely related to the missing representation of land-ocean interaction from the European continental coast. The impact of Wadden Sea output on the carbonate system of the North Sea was modeled in detail by *Schwichtenberg* (2013). Nevertheless, due to the complex spatial and temporal nature of both sediment-water column and land-ocean interactions, large-scale models of the North Sea still struggle to adequately describe these processes.

1.5 Objectives

One goal of this thesis research is to develop methodologies for radium isotope sampling at Dalhousie University, and as a result, introduce novel applications for radium isotopes in future studies. Method development during this study includes building a sampling apparatus for large-volume radium sampling aboard different vessels, and creating detailed instructions regarding processing techniques and error estimation. Using these methods, the principal objective of this research is to address a variety of uncertainties that exist regarding transport across the boundaries of the three study sites, and to investigate the impact of these boundary exchanges on the biogeochemical cycling of the systems. The gaps in our current understanding are what motivate this study:

- Primary productivity, sediment deposition rates, and sediment characteristics are relatively well-constrained in the Bedford Basin (e.g. *Hargrave and Taguchi* (1978)), yet direct benthic flux estimates are lacking. As a result, the contributions of benthic return fluxes to the carbon budget of the basin are unknown. Furthermore, the basin undergoes large episodic ventilation events which likely have large biogeochemical impacts, yet previously, these events have only been described in a physical sense, and with little detail.

- On the Scotian Shelf, onshore transport of deep-ocean waters is thought to fuel observed CO_2 outgassing at the surface, yet to date, no quantitative evidence exists for this mechanism. Similarly, no estimates are available regarding offshore mixing in surface waters, which can transport land-derived materials onto the shelf or shelf-waters into the deep-ocean (see Figure 1.3).

- Extensive mixing above the shallow offshore banks of the Scotian Shelf has been well documented (e.g. *Hannah et al.* (2001)), but relatively little is known regarding the extensive sediment-water column exchange that may occur as a result of this turbulent mixing, or the potential biogeochemical impact of exchange products being mixed rapidly into surface waters.

- In the North Sea, the extent and biogeochemical impact of sediment-water column exchange are relatively poorly understood. Specific areas of uncertainty include the rates of in-situ physical exchange, the physical mechanisms responsible for exchange, as well as the spatial and temporal variability of exchange. Improved understanding in these areas could help parameterization of sediment modules into biogeochemical models.

- Whereas the processes affecting the stable carbon isotope signature of DIC ($\delta^{13}C_{DIC}$) are relatively well understood for the open ocean, this study aims to reveal the processes which may be important in coastal regions by analyzing North Sea surface distributions of both stable and radioisotopes.

- Studies pointing to metabolic processes in the Wadden Sea as an important contributor to North Sea DIC and AT budgets are often confined to observations within small areas of the Wadden Sea (*Moore et al.*, 2011; *Winde et al.*, 2014). Whereas numerical simulations of the North Sea by *Schwichtenberg* (2013) predict a strong impact of these land-derived inputs, observational verification of these impacts in the North Sea are still needed.

1.6 Outline

This thesis uses a manuscript-based approach. Chapter 2 provides a detailed description of the methods used throughout the study, with focus on the radium methodologies. Chapters 3 to 5 are consistent with the individual manuscripts published in peer-reviewed journals, while chapter 6 is to be submitted in the spring/summer of 2015. Each of these chapters includes a brief introduction, methodology, and site description, relevant to each individual study. Chapter 3 describes vertical mixing rates and benthic fluxes in Bedford Basin. Chapter 4 expands on this by quantifying mixing rates and flux terms on a larger scale (i.e.

across the Scotian Shelf), and in both horizontal and vertical directions. The second part of this research takes place in the North Sea, with chapter 5 focusing on sediment-water column exchange, and chapter 6 describing land-ocean interactions by combining radium with stable carbon isotope analyses.

CHAPTER 2

METHODOLOGY

The following chapter provides a detailed description of the sampling and analytical methods used throughout the research. Aside from a small subset of ^{228}Ra data collected on the Scotian Shelf in the 1980s, this study represents the first attempt at collecting radium (Ra) isotopes for all three study regions. As a result, a substantial amount of the experimental effort for this project has been centered around developing techniques for sampling, analyzing and processing data for these isotopes. This chapter provides detailed descriptions of the developed techniques. Chapters 3 through 6 include sections describing the specific methods used in the individual studies.

2.1 Sampling for Radium Isotopes

2.1.1 Large-Volume Water Sampling

In coastal ocean environments, Ra isotopes often exhibit very low activities in the water column. As a result, sample volumes greater than 100 L are required for most samples to obtain the high count rates necessary for reliable activity estimates (*Moore*, 2008). More details on count rates and uncertainties are provided in subsequent sections. Prior to Ra extraction, all water samples were prefiltered to remove particles and thus avoid significant contamination from the decay of particle-bound Th and Ac parent isotopes. This was achieved by pumping samples through 10 μm and 1 μm filter cartridges.

Given the common space and time constraints aboard ships, collection and prefiltering of such large volumes presented a logistical challenge. Thus, sampling approaches evolved throughout the study to try and maximize efficiency and accuracy during sample collection (Figure 2.1). The first samples in 2010 were collected by filling numerous 20 L carboys

from Niskin bottles attached to a rosette. Each carboy was then weighed three times on a regular bathroom scale before pumping the water through filter cartridges and into a large barrel. A 10 L volume uncertainty was applied to all such samples (on total volumes ranging from 101-212 L), which was chosen as a cautious upper estimate based on the inaccuracies of the weighing procedure. For subsequent field campaigns, samples were pumped through a TM Series Electronic Digital Water Meter (TM050-N), which provided a digitized volume estimate with a 0.1 L precision and an accuracy within 3 % of the sample volume. Carboys were avoided by draining samples directly from Niskin bottles into large barrels, and subsequently pumping water through the filters and water meter into a separate barrel. During the 2011 North Sea cruise, water was pumped from multiple Niskin bottles into a single line, which then passed through the filters and water meter, thus entirely automating the process. As a result of this improvement in efficiency, 99 water-column samples with an average volume of 136 L were collected during the 3-week North Sea cruise, while only 34 samples with comparable volumes were collected during the 3-week AZMP cruise in 2010.

2.1.2 Radium Extraction

Once prefiltered, radium was quantitatively extracted from the water sample onto an acrylic fiber. The fiber is coated with manganese dioxide (MnO_2), which effectively scavenges dissolved metals, including radium, from seawater (*Moore and Reid*, 1973). Acrylic fibers are used because of their low Ra blank, while MnO_2 has a large bonding surface area on the fibers and does not wash off easily (*Moore*, 1976). For all samples, 20 g of fiber was loosely packed into a plastic cartridge. Initially, approximately 1 L of deionized (DI) water was pumped through the fiber-filled cartridge to remove any loosely bound MnO_2. Then, using a peristaltic pump, the entire sample volume was pumped through the cartridge at a slow ($\leq$ 1 L min^{-1}) and constant flow rate. To test the efficiency of Ra extraction, two columns were placed in series, and extraction efficiency (E_{ext}) was calculated as follows:

$$E_{ext} = \frac{A}{A+B} * 100 \tag{2.1}$$

where A is the activity of the first sample in the series, and B is the activity of the second. During the study, a total of 9 samples were collected in a series, with an average extraction efficiency of 93 $\pm$ 3 %. *Moore* (2008) ran a series of tests and found a similar average

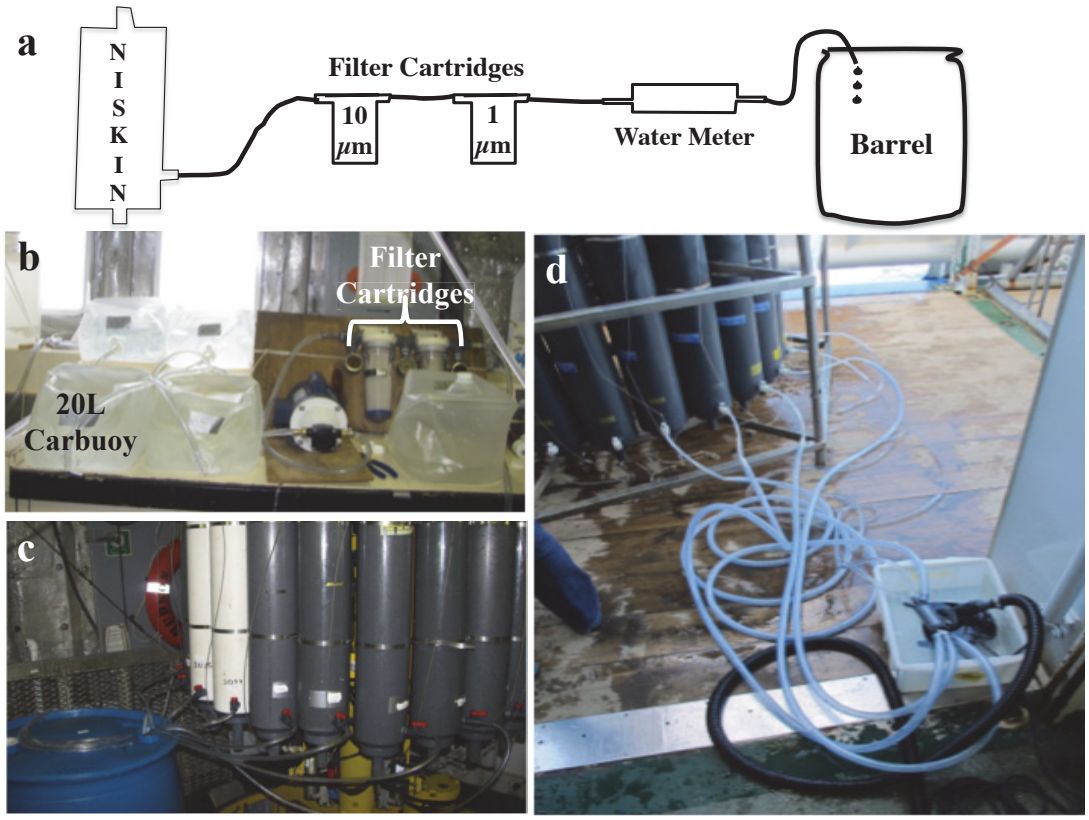

Figure 2.1: **(a)** Schematic showing the extraction process. Pictures show the differing sampling methods used. **(b)** Prefiltering of pre-weighed carboys aboard the CCGS Hudson in April 2010. **(c)** Draining Niskins directly aboard the Hudson in April 2011. **(d)** Active pumping of multiple Niskins into a single line aboard the Pelagia in September 2011.

efficiency (97 %).

Following Ra extraction, DI water was pumped through the cartridges to remove salt from the fiber. Salt crystals have been shown to decrease instrument efficiency by inhibiting radon emanation from the fibers (see section 2.3.1) (*Sun and Torgersen*, 1998a). Using a compressed air source, the samples were then dried to a specific water/fiber ratio between 0.3 and 1.1. This ratio ensures the maximum emanation of radon isotopes from the fiber during the counting procedure (*Sun and Torgersen*, 1998a). Therefore, each individual cartridge and the dry fiber was pre-weighed before the extraction procedure, then during drying, the cartridge was often removed and weighed until the appropriate moisture content is reached. Due to the difficulties of weighing samples in rough seas, attempts to calibrate the drying procedure were made onboard before each cruise by wetting and drying a 20 g sample multiple times and recording the time needed to reach the proper dryness. Nevertheless, keeping samples equally saturated before drying and maintaining a constant flow-rate of compressed air proved difficult. As a result, the exact moisture content of some samples counted at sea was unknown. Once dried, the sample cartridges were sealed using air-tight stopper caps until they are counted.

2.2 The RaDeCC Counter

Radioactivity is defined as the number of decays that occur per unit time. Therefore, radium isotope activities are determined by 'counting' the decays of a sample using the Radium Delayed Coincidence Counting (RaDeCC) system (Figure 2.2). The Dalhousie RaDeCC system consists of two separate counters (specified as c1 and c2), which run independently. The RaDeCC system utilizes two key characteristics of ^{223}Ra and ^{224}Ra (written together as $^{223/224}$Ra): the gaseous form of their respective radon (Rn) daughter isotopes ($^{219/220}$Rn, $t_{1/2}$ = 4 s and 56 s), and the rapid and precise decays of both the Rn isotope pair and their Polonium daughters ($^{215/216}$Po, $t_{1/2}$ = 2 ms and 150 ms). Once a sample cartridge is mounted onto the RaDeCC system, the Ra that decays and emanates off the fiber as gaseous Rn is carried through the system by a helium carrier gas. Helium is used because of its low density, which allows an alpha particle to travel a longer distance within the Scintillation cell (i.e. the counting cell). This maximizes the effectiveness of the counter in registering all decays, and thus, increases the efficiency of the instrument (*Moore*, 2008). Also, its differing density to the ambient air allows for the easy detection

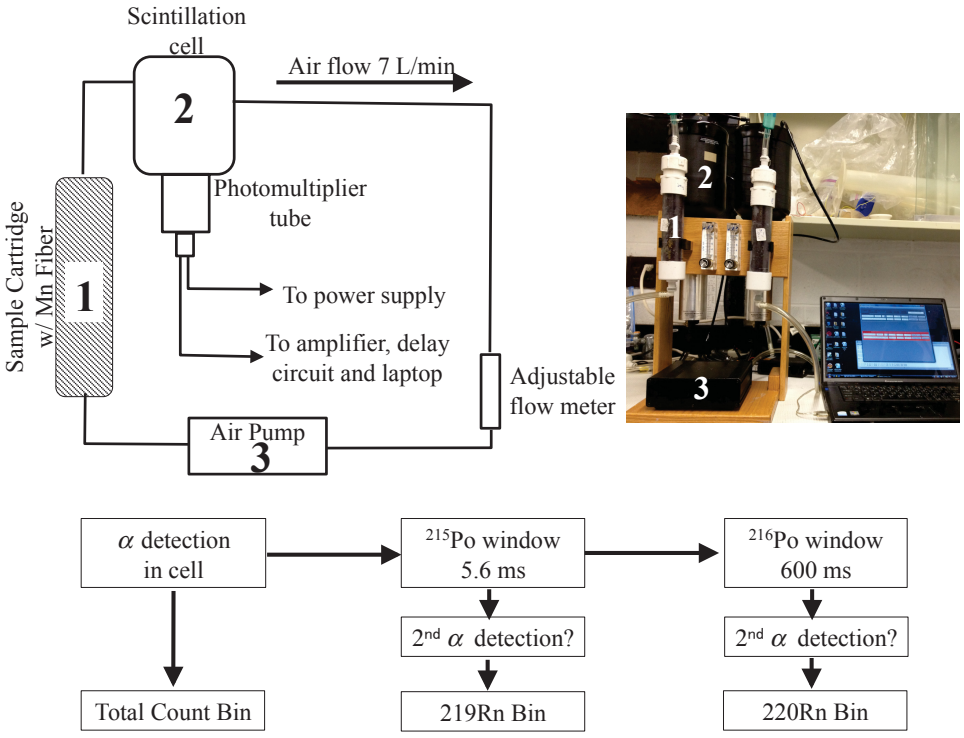

Figure 2.2: Illustrations of the RaDeCC system. Top left: Schematic of closed-loop system layout. Arrow indicates direction of air flow. Numbers in the schematic correspond to the items labeled in the photo (top right). Bottom: Schematic flow chart of the delayed coincidence circuit following an initial alpha (α) decay. Both schematics modified from *Moore and Arnold* (1996).

of leaks in the system by monitoring the flow meter. Helium is also used to initially flush the system ($\sim$1 minute) before closing the loop by reconnecting the air-pump outlet to the sample cartridge (Figure 2.2). The pump is turned on, and the sample is run for 5 minutes before the counting is recorded. During this time, any built-up $^{219/220}$Rn in the cartridge will decay completely, and the ^{224}Ra-^{220}Rn isotope pair will reach secular equilibrium. Unlike ^{224}Ra-^{220}Rn, the ^{223}Ra-^{219}Rn isotope pair is not well mixed throughout the system, as the vast majority of ^{219}Rn ($t_{1/2}$ = 4 s) will be counted on its first pass through the counting cell.

The counting process occurs in the scintillation cell. The scintillation cell contains a crystal that fluoresces when struck by an alpha particle. The resulting photons of light are then converted into an electrical signal by a photomultiplier tube, and that signal is

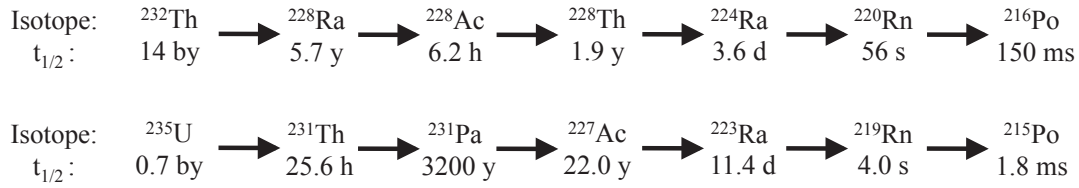

Figure 2.3: Isotopes of the ^{232}Th and ^{235}U decay chains which are relevant for this study. The decay of ^{227}Ac involves a short-lived intermediate ^{227}Th isotope, which is not shown. by = billion years.

amplified, recorded and stored (Figure 2.2). Within the cell, the detection of an initial electrical signal sets off a series of electronic circuits, or count windows. Using these circuits, the RaDeCC specifies whether the alpha particle was formed by decay of ^{219}Rn, ^{220}Rn, or another isotope all together, and the decay is binned accordingly. A flowchart describing this process is given in Figure 2.2. Following the initial alpha detection, the first count window opens for 5.6 ms ($\sim$ 3 half-lives of ^{215}Po). If another alpha particle is detected during this time, it is likely a result of ^{215}Po decay, in which case the initial decay was from ^{219}Rn. This 'coincidence' decay is recorded as a 'count' in the ^{219}Rn bin. Shortly after the first circuit closes, another window opens for 600 ms ($\sim$ 4 half-lives of ^{216}Po), and any coincidental decay within this count window is recorded in the ^{220}Rn bin. If no coincidental decay occurs, the initial count is recorded in the 'total' count bin. The raw data is displayed in real time, and provides the count time (in minutes), the number of counts recorded in each bin at 1-minute intervals, as well as the calculated count rates (in counts per minute, or cpm). The processing steps for these raw data along with the uncertainties associated with the method are described in the subsequent sections.

2.3 $^{223/224}$Ra Data Processing I - cpm to dpm

Data processing involves a number of step-wise calculations which convert raw count rates of ^{220}Rn (cpm_{220}) and ^{219}Rn (cpm_{219}), into activities of ^{224}Ra and ^{223}Ra respectively. These calculations, described below, are also summarized by *Garcia-Solsona et al.* (2008).

First, the data file is checked for any irregularities. Electronic issues and power surges can cause orders-of-magnitude higher counts to be recorded during a 1-minute interval. In these cases, the particular interval can be eliminated from the data file, or if caught during counting, as was the case for all spikes in this study, the sample is simply stopped

and recounted. The first data correction is for spurious counts not associated with ^{220}Rn or ^{219}Rn decay which can occur during the circuit openings for either bin. The equation describing the extent of these 'chance' counts (CC) was derived by *Giffin et al.* (1963) as:

$$CC = \frac{(cpm_{tot} - cpm_{220} - cpm_{219})^2 * t_{window}}{1 - (cpm_{tot} - cpm_{220} - cpm_{219}) * t_{window}}. \tag{2.2}$$

The count rates (cpm) registered in all three bins (the total, 220 and 219 bins) come directly from the raw data, and t_{window} represents the time the count window is open. Using the appropriate t_{window}, this correction is applied to both the ^{220}Rn and ^{219}Rn data. A second chance count correction is necessary for any cross-talk which occurs during circuit openings. For example, the initial 5.6 ms count window, which captures the majority of ^{215}Po decays, is long enough to also capture 2.55 % of the ^{216}Po decays. Therefore, the corrected count rate for the ^{219}Rn bin ($cpm_{219final}$) is written as follows:

$$cpm_{219final} = cpm_{219} - CC_{219} - [(cpm_{220} - CC_{220}) * 0.0255], \tag{2.3}$$

where the final term on the right hand side is the cross-talk correction. The cross-talk correction in the ^{219}Rn bin can be substantial for samples with very high ^{224}Ra activity. In these cases, samples can be recounted for ^{219}Rn at a time when ^{224}Ra has mostly decayed, but significant ^{223}Ra still remains on the fiber (between 7-16 days after collection). Despite the fact that sample activities throughout this study were not large enough to require these recounts, they were done unless a sample backlog was encountered. The corresponding correction for the ^{220}Rn bin is often negligible, and thus is not shown here. In order to move from units of counts to actual activities (rates of isotope disintegrations), a ratio of the counts recorded by the RaDeCC to the actual number of disintegrations in the sample cartridge must be estimated for each counter and each bin. This ratio is known as the total instrument efficiency (E_{220} or E_{219}), and is included in the following efficiency correction:

$$dpm_{220} = \frac{cpm_{220final}}{E_{220}} \quad \text{or} \quad dpm_{219} = \frac{cpm_{219final}}{E_{219}}. \tag{2.4}$$

Instrument efficiencies are calculated by repeatedly counting 'standard' fibers with a known activity of $^{223/224}$Ra. Once calculated, these single unitless E_{220} and E_{219} values are applied throughout the dataset to the appropriate isotope. The product of this equation (dpm_{220} or dpm_{219}) now describes the activity of ^{220}Rn or ^{219}Rn present on the fiber, which,

due to the secular equilibrium between Rn and Ra, is equivalent to the respective activities of ^{224}Ra and ^{223}Ra. Therefore, the left side of this equation can be rewritten as dpm_{223} or dpm_{224}.

2.3.1 Calculating RaDeCC Efficiency

According to *Sun and Torgersen* (1998a), the total instrument efficiency can be broken down into three categories: the system efficiency, the emanation efficiency, and the cell efficiency. The system efficiency is the ratio of decays that occur in the counting cell relative to the decays that occur in the whole system and is largely dependent on the gas flow rate and the volumes of the various parts of the closed loop (Figure 2.2). The emanation efficiency is the ratio of the number of Rn atoms that are picked up by the carrier gas, to the total number of Rn atoms produced, and is maximized by regulating the moisture content on the fibers (described above). Finally, the cell efficiency is the ratio of counts recorded by the counting cell to the total decays that occur in the cell. This is largely dependent on the voltage set on the photomultiplier tube (PMT), which receives signals from the cell and relays them to the laptop. At low voltage, no counts are recorded, while at high voltages, large background counts can occur. A range of moderate voltages, however, will produce a plateau in cell efficiency with reasonable backgrounds. If these efficiencies can be estimated, the total efficiency is evaluated as the product of the three. Total instrument efficiency is usually measured directly using standard fibers with known radium activities.

The commonly used standards for ^{224}Ra and ^{223}Ra are solutions of ^{232}Th and ^{227}Ac respectively. Through the concept of secular equilibrium, the activity of these long-lived parent isotopes will be equivalent to the activity of the shorter-lived radium daughters. These standards were prepared by a former colleague in 2009, prior to the start of this study. First, the two standards for measuring efficiency of ^{224}Ra counting (labeled Th1 and Th2) were made by diluting a ^{232}Th solution with an activity of 50 dpm, to activities of 10.42 and 9.88 dpm respectively. This dilution was done to bring values closer to the anticipated sample values. The original ^{227}Ac solution with an activity of 10 dpm was used to make a single standard for measuring the efficiency of ^{223}Ra counting (labeled Ac3). These three solutions were then filtered through three separate Mn-fibers several times to ensure complete adsorption of Th and Ac. Once made, these standard cartridges were counted regularly throughout the study (see Table 2.1) to monitor any changes in

Table 2.1: Summary of standard runs and calculated counter efficiencies for all sampling periods. Data for each individual chapter use the mean (Avg) efficiency, and its standard deviation (SD), from the corresponding sampling period(s).

Sampling Region		**Counter 1**			**Counter 2**		
(Date)		**Th1**	**Th2**	**Ac3**	**Th1**	**Th2**	**Ac3**
Scotian Shelf	Avg	-	-	-	-	0.489	0.433
(04/2010)	SD	-	-	-	-	0.031	0.024
	n	-	-	-	-	9	11
Bedford Basin	Avg	0.345	0.335	0.282	0.508	0.488	0.424
(09/2010 - 01/2011)	SD	0.001	0.027	0.025	0.025	0.024	0.016
	n	3	9	7	5	7	5
Scotian Shelf	Avg	0.288	0.241	0.196	0.486	0.501	0.420
(04/2011 - 07/2011)	SD	0.003	0.025	-	0.036	0.013	0.050
	n	2	3	1	3	3	2
North Sea	Avg	0.256	0.230	0.168	0.528	0.491	0.399
(09/2011)	SD	0.015	0.024	0.016	0.032	0.068	0.018
	n	6	3	5	4	3	4
	Avg	0.286	0.295	0.231	0.509	0.490	0.423
All	SD	0.041	0.056	0.061	0.032	0.032	0.026
	n	11	15	13	12	22	22

efficiency and to detect any potential malfunction in the system due to electronic issues or physical damage while at sea.

The efficiency for a given count is calculated by taking the corrected count rate (e.g. $cpm_{219final}$) for a standard run, and dividing by the known activity of the standard. For example, if the Th2 standard produced a count rate of 5.00 cpm, the corresponding system efficiency at counting ^{224}Ra would be 0.51 (5.00/9.88). For ^{227}Ac ($t_{1/2}$ =21.7 y), decay of the standard must be taken into account, while decay of ^{232}Th ($t_{1/2}$ =14 billion years) is negligible. For each dataset used in the study, a single efficiency is calculated for each isotope by taking the mean of all standard runs made throughout the dataset. As mentioned earlier, two independent counters are used in this study, thus each counter has its own efficiencies for ^{224}Ra and ^{223}Ra. The average efficiencies for each counter, as determined by the three standards, are shown in Table 2.1. For both counters, the Th1 and Th2 standards produce nearly identical average ^{220}Rn efficiencies. For all three standards, the slightly lower efficiency in the ^{219}Rn bin is due to a slightly lower system efficiency, as some ^{219}Rn ($t_{1/2}$ = 4 s) will decay before reaching the counter (*Moore and Arnold*, 1996).

Table 2.1 clearly shows lower efficiencies for counter 1 compared to counter 2. Initially, this discrepancy was more drastic, and the counter was sent back to the manufacturer prior to the Scotian Shelf cruise (04/2010). A slight error on the original voltage curves was detected and the counter was returned just before the Bedford Basin sampling program. Despite minor improvements to efficiency, consistent weekly sampling during this time required the use of both counters. Counter 1 continued to be used throughout the remainder of the study because efficiencies remained stable during each sampling period, and samples placed on both counters in succession gave similar activities. However, decreases in counter 1 efficiency were observed with each subsequent sampling period (see Table 2.1). These intra-cruise variabilities on counter 1 are not encompassed in the reported uncertainties. To further examine counter 1 efficiencies, a series of laboratory tests were conducted in January 2012. These tests included creating a voltage curve, whereby standards were counted multiple times over a range of instrument voltages, which can be altered manually. The shape of the voltage curve on counter 1 differed from that sent from the manufacturer, showing a plateau at a much higher voltage (see Figure 2.4). Consequently, the voltage for counter 1 was changed in February 2012. Standards run after this calibration yielded average counter 1 efficiencies of 0.45 $\pm$ 0.03 and 0.38 $\pm$ 0.02 for the Th2 and Ac3 standards respectively, which are comparable to those found on counter 2, and nearly double the pre-calibration values on counter 1 (see Table 2.1). These data are not reported in Table 2.1, as they were acquired after the $^{223/224}$Ra analyses were completed. It is now clear that the consideration of an independent voltage curve should have been conducted upon receiving the RaDeCC in early 2009. The alteration to the system was performed rather late for use in this study, but it will ensure better results for future Ra sampling.

2.4 $^{223/224}$Ra Data Processing II - Activity Corrections

In order to produce accurate Ra activities with the correct units, further corrections for volume, decay, and supported activity are made. The volume correction is done by dividing the dpm value by the sample volume and multiplying by 100, yielding a value with units commonly used in short-lived Ra studies (dpm 100 L^{-1}). This value describes the total $^{223/224}$Ra activity during the count. Although pre-filtering of samples will remove the majority of the parent Ac and Th isotopes, some residual activity of these parents are still adsorbed onto the Mn-fiber. Therefore the Ra activity produced by its parent isotopes,

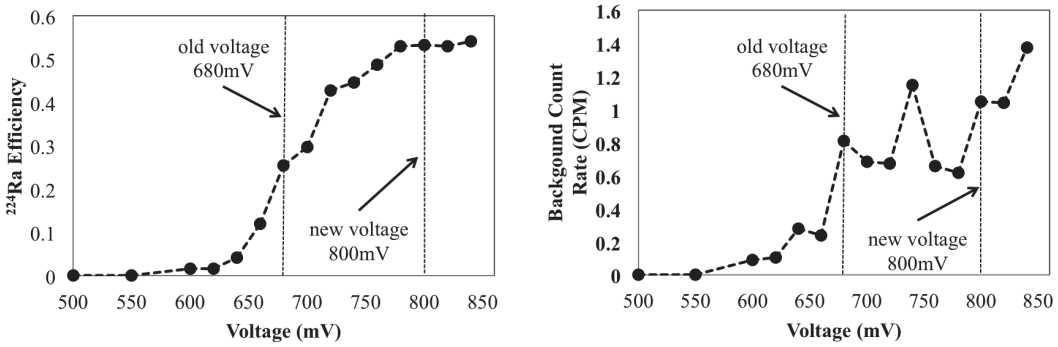

Figure 2.4: Results of the voltage curve conducted in January 2012. Increasing instrument voltage also results in more electronic noise, and thus an increase in average background counts. At 800 mV, a near-doubling in efficiency was coupled with a 20-30 % increase in background, which remained well below the recommended maximum value (*Moore and Arnold*, 1996).

termed as the 'supported' $^{223/224}$Ra (dpm$_{227Ac/228Th}$), must be subtracted from the total activity.

According to *Garcia-Solsona et al.* (2008), supported $^{223/224}$Ra is measured by recounting the Mn-fiber once each isotope has decayed to < 2 % of its original activity (3 weeks and 2 months after collection, for ^{224}Ra and ^{223}Ra respectively). At this time, $^{223/224}$Ra are in secular equilibrium with their parent isotopes, thus the activities measured using these counts are a direct measurement of the ^{228}Th and ^{227}Ac activities. However, the parent isotopes have very low natural abundances and thus these 'supported' counts require many hours of counting time. With only two (or sometimes only 1) counter(s) available for use, it can be difficult to find time to make supported counts during busy sampling periods. As a result, activities of the parent isotopes are often calculated using only the first two counts ($<$ 2 days, and 7-16 days after collection). This method, which is described below, was suggested through personal communication with Dr. Michiel Rutgers van-der Loeff at the AWI institute in Bremerhaven, Germany.

The total activity of ^{224}Ra on the fiber during the second count ($dpm_{224Ra@t2}$) can be written as follows:

$$dpm_{224Ra@t2} = dpm_{228Th} + dpm_{224Ra@t1}e^{-\lambda dt}, \tag{2.5}$$

where the dpm_{228Th} term is the activity of the parent Th on the fiber, the decay of which is

negligible over a few weeks. The second term is the ^{224}Ra activity during the first count, taking into account the decay of the unsupported Ra that occurred between the first count (t1) and the second count (t2) (dt = t2-t1). With data from the two counts providing the two unknowns in this equation, it can be rearranged and solved for dpm_{228Th}. The equivalent calculation is made using dpm_{223} to determine dpm_{227Ac}.

Once the 'supported' $^{223/224}$Ra is removed, the initial Ra decay which occurred between sample collection and the first count is accounted for. Corrections for supported Ra and initial decay are performed together in the following formula:

$$ex^{223/224}Ra = \frac{dpm_{223/224} - dpm_{227Ac/228Th}}{e^{(\lambda t_{dec})}}, \tag{2.6}$$

where the left side of the equation is now the final unsupported, or excess (ex) $^{223/224}$Ra activity at the initial time of sample collection. Considering that the numerator on the right hand side is the unsupported $^{223/224}$Ra activity at the time of counting, this equation is simply a rearrangement of the general model for exponential decay ($A = A_0 e^{-kt}$) with λ as the isotope decay constant (ln2/$t_{1/2}$), and t_{dec} is the decay time between sample collection, and the mid-point of the sample count.

Garcia-Solsona et al. (2008) and others correct for decay before subtracting the supported activity, but the supported component of the $^{223/224}$Ra activity is constantly producing $^{223/224}$Ra, and thus does not decay with the unsupported component. Therefore, we corrected for decay only once the supported activity was removed. Regardless of the correct application of the formula, altering these steps has only a very minor effect on the final result.

Throughout the following chapters, all 223 or 224 radium activities refer to these 'excess' activities (ex$^{223/224}$Ra), with units of dpm 100 L^{-1}. The corresponding uncertainties for these values are calculated throughout the various processing steps, and are detailed below.

2.5 Calculation of Uncertainties

$^{223/224}$Ra activities are often reported with relative errors, but different methods are used to estimate this uncertainty. Here, we will approach the overall uncertainty using two different techniques, both of which have been used in the literature, and discuss the advantages and limitations of each. First, relative counting uncertainty is based entirely on the counts

recorded by the instrument, and assumes that all other sources of error are insignificant. In contrast, the propagation of errors takes into account the relative counting error, and propagates the value through each of the processing steps described above.

2.5.1 Relative Counting Uncertainty

The alpha decays recorded by the RaDeCC can be considered random events which occur over a specific time interval (i.e. during the counting time). Therefore, this random event counting process will follow a Poisson Distribution. In that case, if x is the number of counts recorded during the count time, the probability distribution of x counts occurring ($P(x)$) can be written as,

$$P(x) = \frac{\mu^x}{x!}e^{-\mu}, \tag{2.7}$$

where μ is the average number of counts (#counts) that are registered during the time interval. According to a Poisson distribution, both the expected value (or mean) of x, and its variance, are equal to μ. Therefore, the mean and standard deviation of each counting measurement can be written as $\mu \pm \sqrt{\mu}$, and the percent relative uncertainty (Δ_{rel}) for the raw count rate in the ^{220}Rn bin (cpm_{220}) is written as:

$$\Delta_{rel} cpm_{220} = \frac{\sqrt{\mu}}{\mu} * 100 = \frac{\sqrt{\text{\#counts}_{corr}}}{\text{\#counts}_{corr}} * 100, \tag{2.8a}$$

$$\text{where } \text{\#counts}_{corr} = cpm_{220final} * \text{count time} \tag{2.8b}$$

As the equation indicates, the ability to estimate the mean improves (i.e. the relative error decreases) as the number of counts increases. For example, counting all samples to a minimum threshold of 400 counts in the ^{220}Rn bin results in a relative uncertainty of $\leq$5 % for ^{224}Ra. Recording 100 counts in the ^{220}Rn bin would produce a 10 % uncertainty. Studies which use this method multiply their final activities by this relative error and report Ra uncertainties as one standard deviation (one sigma) based on counting statistics (e.g. *Colbert and Hammond* (2007)).

It is also important to note that these relative counting errors are only a measurement of the instruments precision, because they give no indication of the closeness to the "true" activity, or the accuracy, of the measurement. Therefore, using this method assumes that the distance from the actual activity is relatively small, and the direction of the inaccuracy is the same for all samples. Some $^{223/224}$Ra studies, including the Bedford Basin work

presented here (chapter 3), focused only on the relative difference in activity between samples, which requires that samples be precise relative to each other, rather than be accurate to their true activities. In this case, relative uncertainty may be practical. On the other hand, for studies focused on the particular amount of $^{223/224}$Ra present (e.g. chapter 5), the accuracy of the measurement is crucial. Furthermore, in order for the distance from the"true" activity to be relatively small, the errors associated with chance counts, volume, efficiency, and supported Ra, which pertain more to the accuracy of the measurement, must be insignificant. In the following section, the relative counting error is propagated through all the remaining processing steps to test the validity of the assumption, investigate the largest sources of error, and present a more thorough approach to $^{223/224}$Ra uncertainty calculations.

2.5.2 Error Propagation Technique

This approach utilizes the law of uncertainty propagation for uncorrelated variables, which for a function (f) with variables x and y, can be written as:

$$\Delta f(x,y) = \sqrt{\left|\frac{\partial f}{\partial x}\right| \Delta x^2 + \left|\frac{\partial f}{\partial y}\right| \Delta y^2}, \tag{2.9}$$

where Δ represents the absolute error. This formula is applied to most processing steps to determine the error associated with that particular calculation. The first step is to calculate the absolute counting errors in all three bins ($\Delta cpm_{total/220/219}$), which, following Eq. 2.8, is performed as follows:

$$\Delta cpm_{total/220/219} = cpm_{total/220/219} * \Delta_{rel} cpm_{total/220/219}. \tag{2.10a}$$

$$= \frac{\text{\#counts}}{\text{count time}} * \frac{\sqrt{\text{\#counts}}}{\text{\#counts}} \tag{2.10b}$$

$$= \frac{\sqrt{\text{\#counts}}}{\text{count time}} \tag{2.10c}$$

The '#counts' term here refers to the uncorrected raw counts as independant chance-count and cross-talk corrections are made in the subsequent steps. Using $\Delta cpm_{total/220/219}$, the uncertainty associated with the chance count correction ($\Delta CC_{220/219}$) is found by applying Eq. 2.9 to Eq. 2.2 using the appropriate t_{window}. Following this concept for the cross-talk correction as well, the corrected count rate for the ^{219}Rn bin will have an uncertainty equal

to:

$$\Delta cpm_{219final} = \sqrt{(\Delta cpm_{219})^2 + (\Delta CC_{219})^2 + (0.0255 * \sqrt{(\Delta cpm_{220})^2 + (\Delta CC_{220})^2})^2}. \tag{2.11}$$

Propagating the error through the efficiency calculation requires an individual uncertainty on the total system efficiency. For this, we take the standard deviation of all measurements made using the standard fibers for a given dataset (see Table 2.1). As is shown in Table 2.1, this error can vary by as much as a factor of 5 between cruises, between counters, or between standards. Despite its varying magnitude, the efficiency uncertainty is consistently the dominant source of error throughout the processing procedure used here. For this reason, much care should be taken when running standards, and they should be ran as often as possible. In contrast, the volume correction plays a relatively minor role in the error propagation, especially when using a water meter during sample collection.

The final step in error propagation involves the corrections for decay and supported $^{223/224}$Ra (see Eq. 2.6). The decay correction induces no additional error, as λ is a constant and t_{dec} is known to within a few minutes. Looking at Eq. 2.6, if we treat the $e^{\lambda t_{dec}}$ term as a constant, the propagation becomes:

$$\Delta ex^{223/224}Ra = \frac{1}{e^{(\lambda t_{dec})}} \sqrt{(\Delta dpm_{223/224})^2 + (\Delta dpm_{227Ac/228Th})^2}. \tag{2.12}$$

For some datasets, an assumption was made that the $dpm_{227Ac/228Th}$ term has the same relative error as the $dpm_{223/224}$ term, whereas for other datasets, the $\Delta dpm_{227Ac/228Th}$ term was ignored because the parent activities were so small that their associated error terms were deemed negligible. This is a reasonable assumption for ^{227}Ac, but likely results in a slight underestimation of the total uncertainty for ^{224}Ra. The $\Delta ex^{223/224}$Ra term is the final absolute uncertainty for the radium measurements. In chapters 3-6, $\Delta ex^{223/224}$Ra are reported with all activities, and in some cases, they are shown as relative uncertainties.

2.5.3 Comparison of Techniques

The propagation of errors method includes, among others, the relative counting uncertainty, thus propagation of error will always provide a larger uncertainty. To investigate the magnitude of this discrepancy, uncertainties on $^{223/224}$Ra samples collected in the largest dataset (the North Sea) are recalculated using both methods. For all 128 measured activities, the relative counting uncertainty method yields an average ^{224}Ra uncertainty of 7.9 %,

whereas propagation of errors provides an average error of 13.2 %. Using propagation of errors increases the uncertainty measurement by 68 %, which is a considerable amount.

In some cases, the uncertainty on a given Ra measurement can influence not only the uncertainty of the discussed results, but the actual results themselves. For example, in the Bedford Basin study (see chapter 3), coefficients of vertical mixing (K_Z) are estimated using a weighted least squares regression through vertical gradients of ^{224}Ra. The weights assigned by the regression function take into account the uncertainties of the ^{224}Ra measurements. Therefore, both the slope, and its associated error, are affected by changing the uncertainty on the original ^{224}Ra activity. Using the ^{224}Ra profile for November 3^{rd} as an example (see Table 3.1), a K_Z of 3.29 $\pm$ 0.97 m^2 s^{-1} is reported using the propagation of error technique. Using relative counting uncertainty, this value would be 2.88 $\pm$ 0.38 m^2 s^{-1}. This change in the ^{224}Ra uncertainties result in a 60 % decrease in the K_Z uncertainty, but also a 12 % decrease in the K_Z value itself. These discrepancies also carry over into estimates of carbon, oxygen and nutrient fluxes, which are calculated using the mixing coefficients.

As mentioned above, the largest source of error encountered during uncertainty propagation is the correction for efficiency. The efficiency uncertainty is directly related to the variability encountered during repeated counts of standard fibers. Therefore, to not include this correction in the overall uncertainty calculation is fundamentally flawed, as it is the only step which involves the use of a reference material. Using relative counting uncertainty alone results in a considerable underestimation of the final measurement uncertainty, which in some cases can affect results, and it excludes the use of a reference material. For these reasons, complete error propagation, as described above, is recommended for $^{223/224}$Ra analysis.

2.6 $^{223/224}$Ra Counting Procedures

The majority of $^{223/224}$Ra samples were run until a threshold of 400 counts were registered in the ^{220}Rn bin, which required anywhere between 1-20 hours of counting. This count threshold provided a relatively low and constant counting uncertainty, while also simplifying the counting procedure.

Throughout this study, samples were counted between two and four times. All samples underwent an initial count as quickly as possible ($<$ 2 days) after collection to minimize

decay of ^{224}Ra. For most samples, a second count was conducted between 7 and 16 days after collection. Data from the second count were used to calculate ^{223}Ra activities with minimal cross-talk interference (see section 2.3), or to calculate 'supported' activities (see section 2.4). When time permitted, a third and/or fourth count was conducted between 3 and 12 weeks after collection to obtain direct estimates of 'supported' $^{223/224}$Ra.

2.7 ^{228}Ra Analysis

Originally designed to provide precise measurements of $^{223/224}$Ra, the RaDeCC can also be used to quantify the ^{228}Ra activity on an appropriately aged Mn-fiber. The concepts and methods involved in this calculation, which are summarized here, are taken from an unpublished document provided by a colleague at the University of Southern California.

The RaDeCC provides a measurement of the ^{220}Rn activity on the Mn-fiber at a given time. The Mn-fibers, which contain the $^{223/224}$Ra, will contain other species of radium, as well as dissolved species of thorium, actinium, and other metals. The longer-lived 228-radium isotope (^{228}Ra) is located four decay steps above ^{220}Rn in the ^{232}Th chain.

$$\begin{array}{ccccccccc} {}^{228}Ra & \rightarrow & {}^{228}Ac & \rightarrow & {}^{228}Th & \rightarrow & {}^{224}Ra & \rightarrow & {}^{220}Rn \\ 5.75yrs & & 6.15hrs & & 1.91yrs & & 3.66days & & 56.4sec \end{array}$$

The activity of ^{220}Rn at a given count time is dependent on the activities of all the parent isotopes shown above, at that time. Despite its relatively low activity, the ^{228}Th initially extracted onto the Mn-fiber contributes to ^{220}Rn activity for a long time because of its long half life. During this time, secular equilibrium cannot be reached between ^{228}Ra and ^{220}Rn, thus the activity of ^{228}Ra cannot be directly measured using the RaDeCC.

As mentioned earlier, equilibrium between ^{228}Th and ^{220}Rn is reached after about 3 weeks (i.e. following ^{224}Ra decay), which allowed for direct measurement of ^{228}Th during the 'supported counts' (Eq. 2.5). Similarly, ^{228}Ac is very short lived, so ^{228}Ra rapidly reaches equilibrium with ^{228}Th. ^{228}Ac has extremely low natural abundances, so although its activity cannot be measured, it's original contribution to ^{228}Th activity is deemed negligible. In essence, after about 3 weeks, the ^{228}Ac and ^{224}Ra terms are removed from the decay chain, and the activity of ^{228}Th becomes the key to calculating the activity of ^{228}Ra using the RaDeCC.

Counts made for $^{223/224}$Ra provided the ^{228}Th activity at the initial time of sampling. After more substantial aging of the fiber ($>$ 2 years), significant ^{228}Ra decay will create an ingrowth of ^{228}Th on the fiber. With ^{228}Th and ^{220}Rn having long reached secular equilibrium, recounting the aged fiber yields the ^{228}Th activity at the current time of counting. Taking into account the various decay constants, the difference between the original and ingrown ^{228}Th activities are used to calculate the original ^{228}Ra activity.

The ^{228}Ra measurements require all of the same corrections made for $^{223/224}$Ra, with the exception that the final combined correction for decay and supported counts (Eq. 2.6) is replaced by an equation involving Th ingrowth and decay constants of all 5 species shown in the decay chain above. With this slight change taken into account, ^{228}Ra uncertainties are calculated using the same propagation of uncertainties approach described above.

2.8 Consideration of Measurement Accuracy and the Signal to Noise Ratio

The previous sections outline in detail the methods used to quantify both the Ra activity of a seawater sample, and the uncertainties associated with that quantification. Independent of individual error propagation, it is important to assess how close the reported activities are to the true activities of the water samples, especially given that no globally recognized standard material exists for this method. To accomplish this, the various measures taken to ensure the accuracy of the methods described above are outlined here. This includes assessing how much of the signal received from the RaDeCC can be attributed to the actual Ra activity of the sample, and how much is background noise. Also, replicate measurements and calibrations of the standard fibers are discussed.

2.8.1 Background and Noise

One of the major advantages to counting $^{223/224}$Ra on the RaDeCC system is the very low backgrounds of the detectors. Background counts are caused by buildup of other decay products (namely ^{222}Rn and ^{226}Ra) in the scintillation cell. Therefore, backgrounds tend to increase during times of consistent sample counting. To avoid this contamination, the counter was purged after every sample by pumping ambient air through the system. The majority of samples were also preceded by a background count, wherein an empty cartridge was counted for a minimum of 30 minutes. If these counts were below acceptable

Table 2.2: Summary of background counts measured during Bedford Basin and Scotian Shelf sampling periods.

Count Bin	Average background (cpm)
On Land (n = 53)	
^{220}Rn	0.007
^{219}Rn	0
At Sea (n = 97)	
^{220}Rn	0.020
^{219}Rn	0.001

background values as suggested in the literature (2.0 cpm, 0.05 cpm and 0.005 cpm for the total, ^{220}Rn and ^{219}Rn bins respectively, *Garcia-Solsona et al.* (2008)), the sample count was conducted (as described in section 2.6). Otherwise, the purge and background count were repeated.

Table 2.2 shows typical backgrounds on the counters during the study. In general, higher backgrounds were measured while at sea, likely due to the constant use of the counters. Poor air circulation in the ship laboratory or higher electronic noise may have also contributed. Nevertheless, when considering the lowest non-zero ^{224}Ra activity observed in this study (0.01 dpm 100 L^{-1}, outer-Scotian Shelf), the average 'at sea' background count rate in the 220 bin (Table 2.2) represents only 5 % of the measured count rate in that bin. For the vast majority of samples, these background counts would represent < 2 % of a sample count rate. In the laboratory, zero background counts were often observed. It is also important to note an inherent correction is already made for any background counts caused by decay of other materials in the detector (see chance counts correction, Eq. 2.2). Given all of this, background signals are considered to have no influence on the measured Ra activities.

This study involves, for the most part, radium sampling in open coastal waters, where activities are generally very low. When conducting chemical analyses at low concentrations or activities, it is imperative to have very low sample contamination. This issue was most relevant on the Scotian Shelf, where activities were consistently very low, and where many samples were collected using the ship's intake system, a method which has been shown to introduce contamination during prior studies (*Charette et al.*, 2007). As a result, background signals are addressed in detail during that study (see chapter 4, section 4.6.1).

2.8.2 Replicates and Intercalibrations

Due to water and time constraints during the various cruises, no replicate samples were taken during this study. Nonetheless, at seven North Sea stations with a fully-mixed water column, three separate Ra samples were collected in a ten-meter vertical span (e.g. at 23, 26 and 29 meters depth). The chemical characteristics of these samples (i.e. temperature, salinity, DIC etc.) were identical, thus they are considered to be pseudo-replicates. At each of these seven stations, the relative standard deviation (standard deviation / mean) for the three ^{224}Ra measurements ranged from 3-9 %, which is within the error margins of the samples themselves (6-12 %). In other words, the ^{224}Ra activities in pseudo-replicate samples were indistinguishable from one another.

Recently, a global intercalibration study was conducted in an attempt to reevaluate the techniques for Ra isotope analysis and to ensure the accuracy of Ra data collected aboard a variety of GEOTRACES cruises. This included a global RaDeCC system laboratory performance test, wherein numerous Mn-fiber standards prepared by the International Atomic Energy Agency (IAEA) laboratory were sent to various laboratories across the globe for analysis. The methods for IAEA standard preparation, which match those used here, as well as the results of the experiments, are described by *Charette et al.* (2012). In March 2011, after the formal intercalibration experiment was completed, four IAEA standards were received and counted on the RaDeCC system at Dalhousie. Each standard was counted between 2-4 times, using both counters, and corrected activities were calculated using the instrument efficiencies from the Bedford Basin sampling campaign (see Table 2.1). Counts of Th1 and Th2 standards done during IAEA standard counts yielded similar efficiencies to the Bedford Basin campaign values. By comparing the results of these IAEA standard counts with those from the 12 participating laboratories reported by *Charette et al.* (2012), the performance of the RaDeCC system used in this research can be assessed. The results of this comparison are summarized in Table 2.3.

A number of discussion points can be drawn from the results in Table 2.3. First, the analysis of ^{224}Ra on all three IAEA standards yielded values within 10 % of the reference values. Repeat counts on each standard yielded standard deviations which encompass the reported IAEA reference values listed by *Charette et al.* (2012). Furthermore, the Dalhousie RaDeCC performed better than a number of other laboratories, as indicated by the relatively large interlaboratory standard deviations. These results provide confidence

Table 2.3: Dalhousie University RaDeCC performance results for ^{224}Ra and ^{223}Ra analysis. All activities are reported in units of dpm 100 L^{-1}.

Standard	Reported Activity	Dal Activity ± StDev$^{(1)}$	Interlab Mean ± StDev$^{(2)}$
^{224}Ra			
IAEA - I	9.64	10.13 ± 0.70 (n=3)	9.71 ± 0.86
IAEA - C	14.64	15.02 ± 0.55 (n=4)	14.69 ± 2.24
IAEA - G	11.10	11.51 ± 0.41 (n=4)	10.45 ± 1.06
^{223}Ra			
IAEA - E	10.180	7.60 ± 0.70 (n=2)	7.33 ± 1.56
IAEA - I	1.050	0.907 ± 0.14 (n=3)	1.56 ± 0.18
IAEA - C	2.310	1.772 ± 0.44 (n=4)	1.98 ± 0.43

(1) Standard deviation of repeated counts (number of repeated counts shown).
(2) Standard deviation of reported values from the 12 participating laboratories.

that the Dalhousie RaDeCC provided accurate ^{224}Ra activities throughout this research.

For ^{223}Ra analysis, the Dalhousie RaDeCC significantly underestimates the activities of all three IAEA standards, but around half of the participating labs reported similar underestimations. A very high spread between labs was also observed. Given these results, *Charette et al.* (2012) conclude that a fundamental problem exists in the ^{227}Ac standard method. This issue was addressed in detail by *Moore and Cai* (2013), wherein the authors show that the efficiency in the ^{219}Rn bin can be calculated by subtracting a constant factor from the efficiency in the ^{220}Rn bin. Whereas this study does not incorporate these changes, it is suggested that future studies utilize this new method during ^{223}Ra processing. Uncertainties in ^{223}Ra efficiencies are compounded further by very low natural activities in the samples (see section 5.5.2.1). For these reasons, ^{223}Ra data are used scarcely in this research, with the vast majority of the analyses and interpretations done using ^{224}Ra data.

2.9 Future Improvements to Radium Methodology

Further insight into extraction efficiency and background activities could be obtained by separating a very large seawater sample ($\sim$ 500 L) into three subsamples, and extracting the Ra in each subsample through three or more cartridges in series. These tests would be best conducted in the laboratory directly before a cruise, as the RaDeCC often experiences a counting backlog both during, and in the weeks following, sample collection. This would also partially fulfill the need for more replicate sampling. Future sampling strategies should budget for one station with triplicate sampling, or multiple stations sampled in

duplicate. For background measurements, a cartridge filled with Mn-fiber and wetted with DI water may be more appropriate than using an empty cartridge.

2.10 Collection and Analysis of Carbonate System Parameters

Throughout this research, radium measurements were made in parallel to a number of chemical species. Whereas analyses for nutrient species (NO_3^-, PO_4^{3-}) and stable carbon isotopes ($\delta^{13}C_{DIC}$) were done elsewhere, all dissolved inorganic carbon (DIC) and total alkalinity (AT) measurements made in the Bedford Basin and the Scotian Shelf were measured by the lab group at Dalhousie University. Seawater for DIC and AT samples was collected in 250 mL borosilicate glass bottles with stoppers, and were either analyzed immediately following collection, or spiked with Mercuric Chloride ($HgCl_2$) to halt biological activity before storing in the dark for later analysis. Concentrations of DIC and AT are determined using a VINDTA 3C (Versatile Instrument for the Determination of Total Alkalinity, by Marianda). Both DIC and AT are calibrated using certified reference materials (CRMs) provided by the Scripps Institute of Oceanography. CRMs are seawater samples with precise DIC and AT concentrations, which are analyzed on the VINDTA before and after every small batch of samples. Measured deviations from certified values are used to calibrate the samples. This calibration effort results in DIC and AT uncertainties typically less than 3 μmol kg^{-1} (relative uncertainty $\leq$0.2 %). Details regarding each individual measurement, following *Dickson et al.* (2007), are provided below.

2.10.1 Dissolved Inorganic Carbon

DIC is determined by coulometric titration. Initially, a small volume of phosphoric acid (8.5 % H_3PO_4) along with a precise volume of sample water are combined in a glass stripper cell. The addition of the strong acid transforms all of the DIC into CO_2, which is then stripped from the solution by a CO_2-free carrier gas (N_2) into the coulometer cell. In the coulometer cell, CO_2 gas combines with ethanolamine to form a weak hydroxyethylcarbamic acid:

$$CO_2 + HO(CH_2)_2NH_2 \rightarrow HO(CH_2)_2NHCOO^- + H^+. \tag{2.13}$$

This acidification of the solution results in a color change, due to the presence of a thymolphthalein indicator. The quantification of DIC is based on the titration of this

solution with hydroxide ions:

$$H^+ + OH^- \rightarrow H_2O, \tag{2.14}$$

which are formed by electrolyzing water:

$$H_2O + e^- \rightarrow \frac{1}{2}H_2(g) + OH^- \tag{2.15}$$

and dissolving a silver anode

$$Ag(s) \rightarrow Ag^+ + e^-. \tag{2.16}$$

The color change of the solution during titration is monitored by light transmittance. The number of hydroxide ions required to titrate the solution back to its original color is directly related to the number of electrons formed, which is measured by the coulometer as the total charge. This charge then relates to a molar quantity of DIC using Faraday's law.

2.10.2 Total Alkalinity

Total alkalinity is determined by potentiometric titration. Here, a precise volume of sample water is transferred into a cell and titrated with a hydrochloric acid (HCl) solution. Acid is added automatically in 0.15 mL doses by a piston burette, and the titration is monitored by measuring the pH of the mixed solution after every acid addition. The pH is measured as the electromotive force (e.m.f., measured in millivolts) between a pH electode/reference electrode pair. By the end of the titration, the burette has added 4.20 mL of acid, dropping the pH of the solution to around 3. Using the resulting dataset, the VINDTA software uses a type of iterative least-squares linear regression (defined as a modified Gran approach, *Dickson et al.* (2007)) to automatically compute total alkalinity.

CHAPTER 3

SEDIMENT-WATER COLUMN FLUXES IN BEDFORD BASIN

3.1 Abstract

Exchanges between sediment pore waters and the overlying water column play a significant role in the chemical budgets of many important chemical constituents. Direct quantification of such benthic fluxes requires explicit knowledge of the sediment properties and biogeochemistry. Alternatively, changes in water column properties near the sediment-water interface can be exploited to gain insight into the sediment biogeochemistry and benthic fluxes. Here, a 1-D diffusive mixing model is applied to near-bottom water column profiles of ^{224}Ra activity in order to yield vertical eddy diffusivities (K_Z), based upon which the diffusive exchange of dissolved inorganic carbon (DIC), nutrients and oxygen (O_2), across the sediment-water interface is assessed in a coastal inlet, Bedford Basin, Nova Scotia, Canada. Numerical model results are consistent with the assumptions regarding a constant, single benthic source of ^{224}Ra, the lack of advective mixing, and a predominantly benthic source and sink of DIC and O_2, respectively, with minimal water column respiration in the deep waters of Bedford Basin. Near-bottom observations of DIC, O_2 and nutrients provide flux ratios similar to Redfield values, suggesting that benthic respiration of primarily marine organic matter is the dominant driver. Furthermore, a relative deficit of nitrate in the observed flux ratios indicates that denitrification also plays a role in the oxidation of organic matter, although its occurrence was not strong enough to allow us to detect the corresponding AT fluxes out of the sediment. Finally, comparison with other carbon sources reveal the observed benthic DIC release as a significant contributor to the Bedford

Basin carbon system.[1]

3.2 Introduction

A fraction of the particulate organic matter (POM) generated photosynthetically in the euphotic zone settles to the sediment where microbes utilize a variety of electron acceptors to respire this organic material producing dissolved inorganic carbon (DIC) and nutrients. As a result, sediment pore waters become highly concentrated in many chemical constituents relative to the overlying water column (*Moore et al.*, 2011; *Charette et al.*, 2007) so that small volumes of released fluid can have disproportionately large affects on biogeochemical cycles and budgets (*Berelson et al.*, 1987). Furthermore, if considering the area over which these processes can occur, from smaller basins to entire continental margins, fluxes from sediments can be a major source or sink in various coastal chemical budgets (*Fennel et al.*, 2006). For example, in the shallow mud flats of the North Sea, anaerobic alkalinity generation within the sediments, and its subsequent release, may facilitate up to 25 % of the North Sea CO_2 uptake (*Thomas et al.*, 2009). Pore water fluxes in the shallow Wadden Sea have been shown to largely control the budgets of numerous important chemical constituents, including alkalinity, silica, manganese and uranium (*Moore et al.*, 2011). Consequently, many studies have focused on quantifying the release of pore waters and/or solutes in coastal environments (*Colbert and Hammond*, 2008; *Jahnke and Jahnke*, 2000; *Hancock et al.*, 2006; *Simmons*, 1992), and modeling the biogeochemistry of chemical fluxes across the sediment-water interface (*Fennel et al.*, 2009).

Pore waters enter the water column via a number of different physical processes, many of which occur at slow rates, making their detection and quantification difficult (*Burnett et al.*, 2003). However, if it is assumed that fluxes across the sediment-water interface are controlled by diffusive processes, such fluxes out of the pore waters into the overlying water column can be inferred using the short-lived radioactive tracer, radium-224 (^{224}Ra), a powerful tool commonly used for estimating various types of fluxes from sediment pore waters. Due to its high affinity for sediment surfaces, thorium-228 (^{228}Th), the longer-lived

[1] Aside from minor alterations to the wording, this chapter consists of a manuscript by *Burt et al.* (2013) entitled *Sediment-Water Column Fluxes of Carbon, Oxygen and Nutrients in Bedford Basin, Nova Scotia, Inferred from ^{224}Ra Measurements* published in Biogeosciences.

parent isotope of ^{224}Ra, is ever present within bottom sediments. Consequently, ^{224}Ra, which has a much lower affinity for sediment surfaces, is constantly produced and becomes highly concentrated in the interstitial pore water. As this ^{224}Ra diffuses into the overlying water column, ^{224}Ra is mixed away from its source, and its activity decreases. Utilizing the decay timescales of ^{224}Ra ($t_{1/2}$ = 3.66 d), diffusion rates near the seafloor can be estimated and subsequently applied to chemical gradients of other dissolved constituents.

Sediment-water column exchange of carbon and nutrients is often quantified using in-situ benthic flux chambers (*Berelson et al.*, 1987; *Jahnke et al.*, 2000; *Jahnke and Jahnke*, 2000). Alternatively, benthic fluxes can be estimated by measuring pore water profiles of nutrients or metals (*Emerson et al.*, 1984; *Jahnke et al.*, 2005; *Lettmann et al.*, 2012) or more recently, radium isotopes (*Hancock et al.*, 2006; *Colbert and Hammond*, 2008; *Moore et al.*, 2011) and applying models to the resulting gradients. Modeling pore water data, however, requires a thorough understanding of various sediment characteristics (i.e. composition, porosity, density), which often involve intricate lab experiments using sediment cores and can result in highly uncertain estimates, especially when dealing with permeable sediments (*Huettel and Webster*, 2001).

Previous studies in Bedford Basin have indirectly measured rates of organic carbon sedimentation and sediment oxygen uptake using sediment trap data (*Hargrave et al.*, 1976; *Hargrave and Taguchi*, 1978). However, it appears that no prior research has described direct benthic flux observations in Bedford Basin, making this study the first to do so. Here, a more direct observational approach is applied to measure the fluxes of ^{224}Ra, DIC and dissolved oxygen (O_2) between the sediments and water column that relies on water column observations. Specifically, the vertical diffusive flux of the short-lived ^{224}Ra from the seafloor into the bottom water in Bedford Basin (Halifax Harbour, NS) is estimated. Then, a 1-D diffusion model is applied to near-bottom vertical profiles of ^{224}Ra to asses both the vertical eddy diffusivity in the water column (K_Z), and the ^{224}Ra activity at the sediment surface (A_0). These calculated values, along with estimates of the benthic flux of ^{224}Ra per unit area of seafloor, are compared to other published values from similar studies. Near-bottom gradients of DIC and O_2 are then used in conjunction with the estimates of K_Z to quantify the diffusive release of carbon into the water column and corresponding uptake of O_2 by the sediments. Further, estimates of nutrient (nitrate and phosphate) fluxes are also made using time-series observations of oxygen and nutrients at the bottom of

the basin. Calculated flux ratios provide insight about the dominant pathways of organic matter remineralization, and a time-dependent finite difference diffusion model is used to test the assumptions regarding steady-state and the contributions of secondary sources and sinks. By relating the inferred carbon flux with estimates of both riverine DIC input and uptake by primary production, the relative contribution of the benthic DIC flux to the carbon budget in Bedford Basin is established.

3.3 Methods

3.3.1 Study Site

Observations were made between October and December of 2010 at the Compass Buoy station in Bedford Basin, Nova Scotia, Canada (44°41'30" N, 60°38'30" W). Bedford Basin is a small enclosed bay (6 km long by 4 km wide) at the northwestern end of Halifax Harbour (Figure 3.1). The Basin reaches water depths of over 70 m, while the rest of Halifax Harbour is relatively shallow (Figure 3.1). The only major fresh water source in the region, the Sackville River, drains into the northwestern side of Bedford Basin with an approximate annual discharge of 1.5 x 10^8 m^3 yr^{-1} (*Kepkay et al.*, 1997). At the southeastern edge, water exits into the Narrows, eventually leading to the Halifax Outer Harbour and the Scotian Shelf.

The general circulation pattern of Halifax Harbour is described as a two-layer estuarine type circulation with a relatively fresh upper layer moving seaward driven by inputs from the Sackville River and a saltier deep-water return flow (*Fader and Miller*, 2008). However, this circulation is at its weakest in Bedford Basin, with a mean surface outflow of 0.2 cm s^{-1}. Also, the entrance to the Narrows is marked by a shallow sill with a depth of about 20 m. While significant tidal currents can be observed within the Narrows, the presence of the sill largely prevents mixing below 20-30 m depth in the Basin (*Shan et al.*, 2011). As a result, and as seen in the homogenous temperature and salinity distributions (Figure 3.2), the subsurface layers of Bedford Basin are a relatively stable environment, which, for the purpose of this study, allows us to apply the 1-D diffusive model described below. However, periodic storms in the spring and fall can result in deep water ventilation events, one of which occurred in October 2010 and terminated toward the start of the sampling period (Figures 3.1-3.3). These events can result from wind-induced deep vertical mixing during periods of minimum stratification (*Punshon and Moore*, 2004).

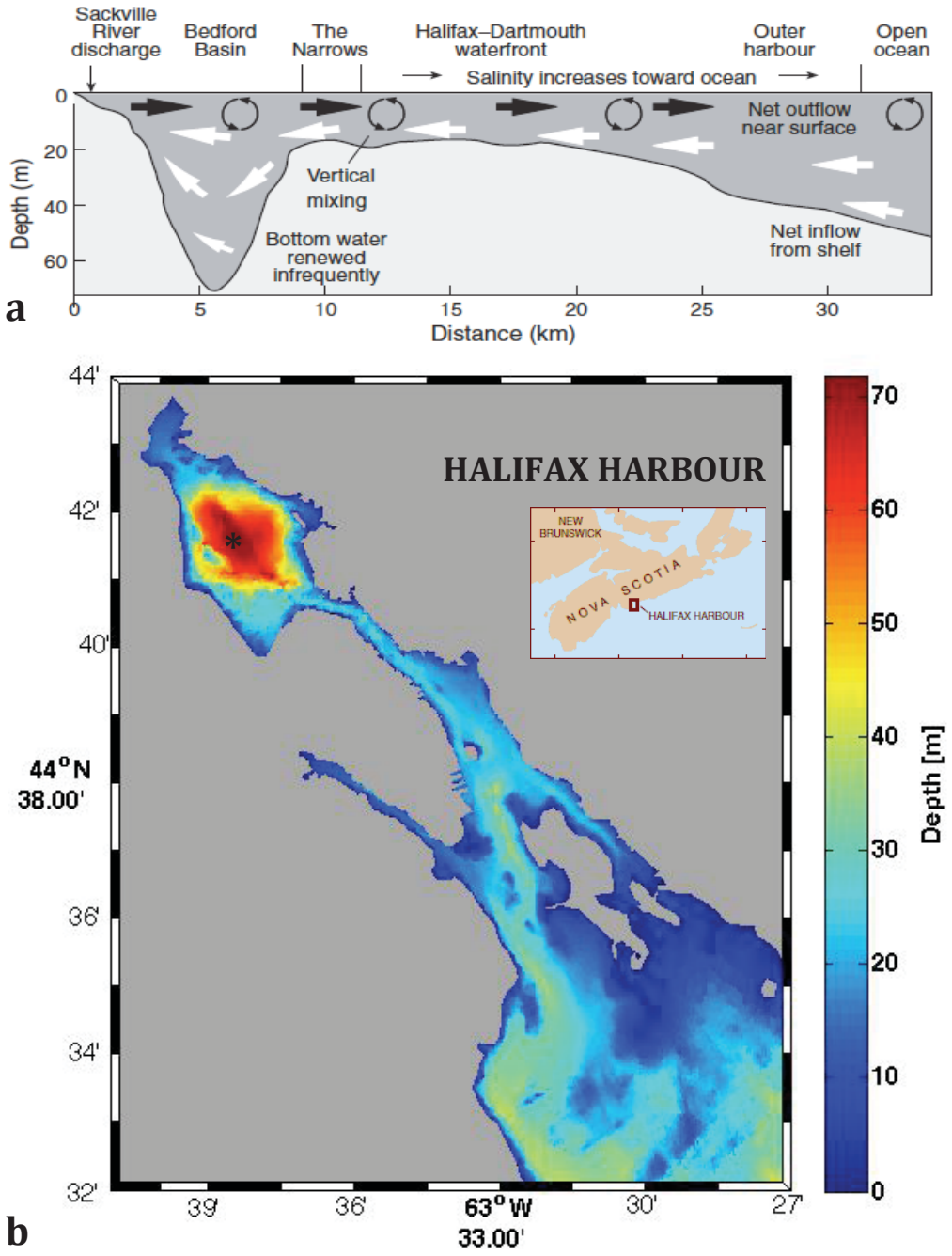

Figure 3.1: **(a)** Schematic cross-section of Halifax Harbour (with permission from *Fader and Miller* (2008)). **(b)** Bathymetric map of Halifax Harbour, showing the Compass Buoy Site (*) in Bedford Basin. Figure redrawn from Burt et al. (2013a) with permission from Copernicus Publications.

However, the October 2010 event is more likely to have resulted via lateral intrusion, the mechanism of which is described as a combination of strong along-shore winds and large tides, causing a build-up of coastal sea level and bringing dense water from the outer harbour over the sill and into the deep basin (*Platt et al.*, 1972). Regardless of the specific mechanism for their occurrence, these events result in abrupt changes in the physical and chemical characteristics of the deep water column (Figure 3.2), bringing surface waters saturated with O_2 into the deep basin and preventing the deep waters from reaching anoxic conditions (Figure 3.3) (*Hargrave et al.*, 1976). Concurrently, deep waters, rich in DIC and nutrients, are brought to the surface, occasionally marking the onset of the spring or autumn phytoplankton bloom (Figure 3.3).

The close proximity of Bedford Basin to both the Bedford Institute of Oceanography (BIO) and Dalhousie University permits convenient access for weekly measurements. The Bedford Basin Plankton Monitoring Program conducted at BIO has been carrying out weekly measurements of various water properties, including nutrients, plankton records, and CTD profiles at the Compass Buoy Site for nearly 30 years (Li and Dickie, 2001). Also, the lack of significant horizontal or vertical advective flows in the deep waters of Bedford Basin allows for a reliable application of the assumptions necessary for the 1-D diffusion model utilized in this study. These assumptions follow those made by Moore (2000), and are described in more detail below.

3.3.2 Analytical Methods

Samples of ^{224}Ra were taken aboard the vessel CCGS Sigma T, operated out of the Bedford Institute of Oceanography. In total, five vertical profiles of ^{224}Ra were sampled regularly over a six week period between October and December of 2010. Each sample requires a large volume of water (150-200 L) which was obtained at the surface ($\sim$2 m) using a small bilge pump that was lowered over the side of the vessel, and at depth using repeated casts of 30 L Niskin bottles lowered to the appropriate depths. Sampling depths varied for each daily profile due to varying weather conditions, with bottom sampling depths ranging from 66-70 m and a vertical spacing of 6-8 m between samples (see Figure 3.5). Once collected, sample volumes were pumped through 10 μm and 1 μm cartridge filters to remove any particles, effectively removing all sources of the parent ^{228}Th isotopes. The water was then passed slowly ($<$1 L min^{-1}) through plastic cartridges packed with 20 g of pre-weighed MnO_2-impregnated fiber, which quantitatively extracts the Ra isotopes

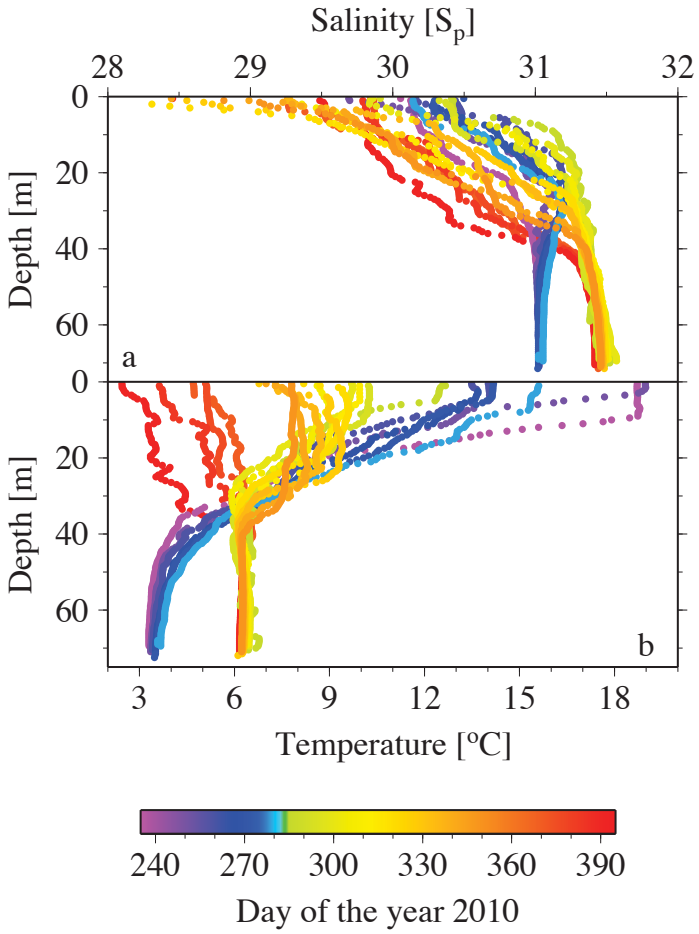

Figure 3.2: Weekly vertical profiles of salinity (Sp) **(a)** and temperature **(b)** from August 2010 (day 237) – January 2011 (day 391). The colorbar has been adjusted at day 282 (09-Oct) in order to better illustrate the abrupt changes in the deep waters around that day. Figure redrawn from Burt et al. (2013a) with permission from Copernicus Publications.

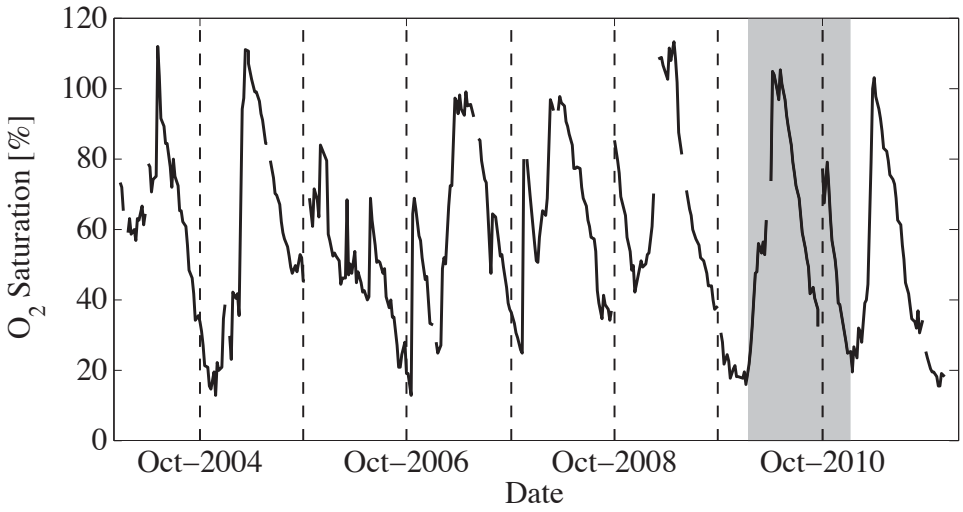

Figure 3.3: Deep-water (60 m) oxygen saturation time-series at the Compass Buoy Site in Bedford Basin. Vertical dotted lines are drawn at mid-October of each year. An abrupt increase indicates a deep-water mixing event. Two distinct events are shown to occur in 2010 (shaded box). Figure redrawn from Burt et al. (2013a) with permission from Copernicus Publications.

(*Moore*, 1987). The fibers were then rinsed with de-ionized water and dried to a water/fiber ratio between 0.3-1 using compressed air to maximize the emanation of radon (Rn) from the fibers during counting (*Sun and Torgersen*, 1998b).

In order to analyze ^{224}Ra activities of samples, the cartridges were placed onto the RaDeCC coincidence counting system described by *Moore and Arnold* (1996). Using the electronic time windows within a photomultiplier tube (PMT), the instrument is able to identify and distinguish between the alpha particles created by the decay of ^{224}Ra as well as its respective daughter, ^{220}Rn. To minimize initial decay, all samples were counted within 2 days of collection. The samples were then aged for approximately 3 weeks, allowing all excess ^{224}Ra to equilibrate with parent ^{228}Th before recounting to calculate the initial supported Ra. The uncertainty in the ^{224}Ra measurements ranges between 7-10 %. The majority of the Ra samples were also accompanied by bottle samples of dissolved inorganic carbon (DIC) and alkalinity (AT). These samples were collected and poisoned with a $HgCl_2$ solution to halt biological activity, before being stored for later analysis. Both DIC and AT were analyzed on the VINDTA 3C (Versatile Instrument for the Determination of Titration Alkalinity by Marianda) by coulometric and potentiometric titrations respectively (see *Johnson et al.* (1993) for a full description of instrumental

methods). Vertical profiles of temperature, conductivity, and pressure were collected using a seabird SBE25 CTD profiler, equipped with a Beckman/YSI type dissolved oxygen sensor. Additionally, discrete bottle samples (at 1, 5, 10, 60 m depth) were taken by Niskin bottle and analyzed for various biological and chemical species as part of the Bedford Basin Monitoring Program, providing time-series data of O_2, nitrate (NO_3^-), phosphate (PO_4^{3-}), chlorophyll (chla) and particulate organic carbon (POC) during the sampling period. This additional sampling always took place within 1 day of radium sampling. Nitrate and phosphate were measured using a Technicon II autoanalyzer, chla analysis was done using a fluorescence technique (Turner Design Model 10 Fluorometer) (*Li and Dickie*, 2001), and POC was measured on a Perkin Elmer Series II CHNS/O Analyzer 2400 (for more information, please refer to *Li and Harrison* (2008)).

3.3.3 Vertical Mixing Coefficients Derived from Radium Tracers

The method for quantifying turbulent diffusion near the sediment surface is based on the 1-D model used in conjunction with short-lived Ra isotopes by *Moore* (2000), and subsequently applied in various settings (*Moore*, 2003; *Charette et al.*, 2007; *Men et al.*, 2011; *Moore and de Oliveira*, 2008). The original model quantified the diffusive flux of short-lived Ra isotopes in the horizontal direction from a point source (i.e. the coast) towards the open ocean. The model used here takes the same basic concepts used in the *Moore* (2000) model, and applies them in the vertical direction, similar to the approach taken in the deep Southern Ocean by *Charette et al.* (2007), describing the vertical transport of ^{224}Ra, via turbulent diffusion, from its source on the sediment surface.

Assuming that the activity distribution of the radioactive tracer Ra (A) in the water column is controlled by inputs, transport and radioactive decay (with decay constant λ), the change in Ra activity over time (∂A/∂t) is described using a general diffusion equation with an additional decay term,

$$\frac{\partial A}{\partial t} = K_Z \frac{\partial^2 A}{\partial z^2} - \lambda A. \tag{3.1}$$

Here, z represents the vertical distance from the sediment surface. The 1-D diffusion model is applied in the vertical direction and assumed to have a single constant source of Ra, with activity A_0, at the lower boundary representing the sediment surface (z = 0). Radium is mixed away from the surface by turbulent diffusion at a constant rate K_Z. The

activity will drop to 0 at some distance from the source ($A \rightarrow 0$ as $z \rightarrow \infty$). Assuming steady-state, the vertical distribution of A is described by:

$$A(z) = A_0 e^{-z\sqrt{\lambda/K_Z}}, \tag{3.2}$$

where $A(z)$ is the ^{224}Ra activity at depth z. Taking the natural log of Eq. 3.2 yields a linear equation of the ln of activity over depth, i.e.,

$$\ln(A(z)) = \ln(A_0) - z\sqrt{\lambda/K_Z}, \tag{3.3}$$

from which the slope ($\sqrt{\lambda/K_Z}$) and intercept ($\ln(A_0)$) can be obtained by linear least-squares regression. The vertical eddy diffusion coefficient (K_Z) can then be determined from the slope using knowledge of the ^{224}Ra decay constant (λ = 0.19 d^{-1}).

3.3.4 Calculating Benthic Radium, Carbon, Oxygen, and Nutrient Fluxes

By obtaining estimates of eddy diffusivity and interface activity, one can calculate the flux of Ra from a unit area of seafloor into the overlying water column. Integrating Eq. 3.2 over z from 0 to ∞ yields:

$$Q_{Ra} = A_0\sqrt{\frac{K_Z}{\lambda}}, \tag{3.4}$$

where Q_{Ra} is the benthic radium flux (atoms Ra m^{-2} s^{-1}).

Next, according to Ficks first law, combining the vertical concentration gradients ([mmol m^{-3}] m^{-1}) in carbon (dDIC/dz) and oxygen (dO_2/dz), with the Ra-derived eddy diffusivities (K_Z), the vertical fluxes of carbon and oxygen per square meter of sediment surface (mmol m^{-2} d^{-1}), can be computed for each sampling day:

$$Q_{DIC} = -K_Z\left[\frac{dDIC}{dz}\right] \tag{3.5}$$

$$Q_{O2} = -K_Z\left[\frac{dO_2}{dz}\right]. \tag{3.6}$$

Assuming negligible respiration within the deep water column, a type II regression routine, which accounts for errors in both input variables, was used to determine the slopes of O_2 vs. NO_3^- ($m_{O2vs.NO_3^-}$), PO_4^{3-} ($m_{O2vs.PO_4^{3-}}$) and DIC ($m_{O2vs.DIC}$). These slopes were

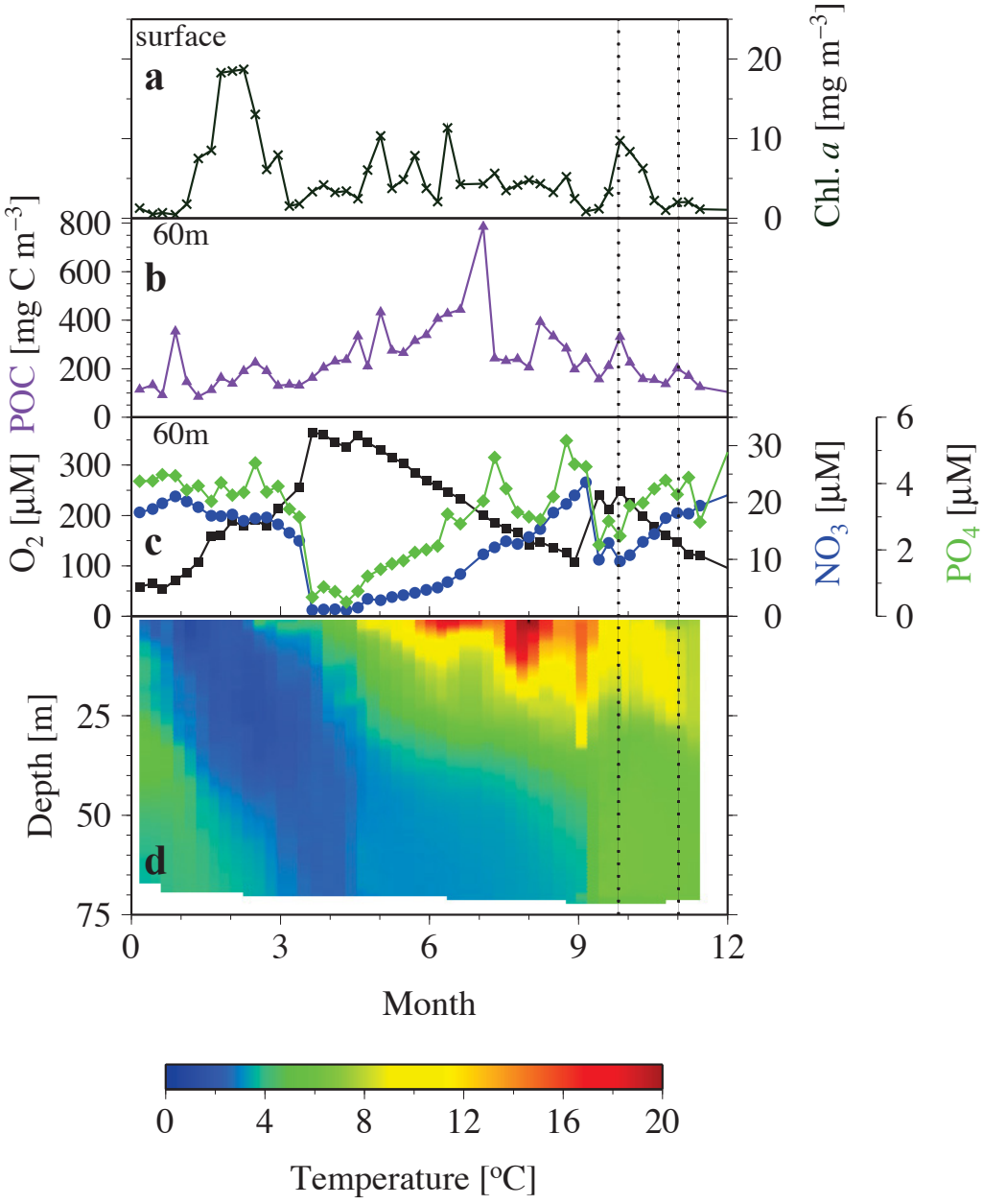

Figure 3.4: Time series of surface Chl a **(a)**, deep-water particulate organic carbon (POC) **(b)**, deep-water oxygen and nutrients **(c)**, and temperature depth profiles **(d)** in Bedford Basin during 2010. Black dashed lines indicate the sampling period of the study. Figure redrawn from Burt et al. (2013a) with permission from Copernicus Publications.

applied to the oxygen flux (Q_{O2}) in order to calculate the benthic nutrient fluxes, $Q_{NO_3^-}$ and $Q_{PO_4^{3-}}$ (mmol m^{-2} d^{-1}), respectively:

$$Q_{NO_3^-} = \frac{Q_{O2}}{m_{O2vs.NO_3^-}} \tag{3.7}$$

$$Q_{PO_4^{3-}} = \frac{Q_{O2}}{m_{O2vs.PO_4^{3-}}}. \tag{3.8}$$

The uncertainties are reported for the majority of the values calculated in this analysis using the standard error propagation formula for uncorrelated variables. First, the uncertainty for each individual parameter (i.e. ^{224}Ra, DIC) is determined. These values are then applied to the linear fits using a weighted least-squares regression routine in MATLAB, which fits the data while taking into account the uncertainties and provides a separate uncertainty in the resulting slope and intercept coefficients.

3.3.5 Numerical Simulations of the 1-D Model

The above application of the 1-D diffusion model to the ^{224}Ra data requires a steady-state assumption in order to analytically solve Eq. 3.1. However, by creating a time-dependent 1-D finite difference model, this equation can be solved numerically, and in doing so, can test the steady-state assumption. Focusing on the deep basin, the finite difference model covers the bottom 40 m of the 70 m deep basin, and has a layer thickness of 0.5 m. The model is set up by discretizing Eq. 3.1, and consists of 80 discrete points along a straight line, which extends out from the sediment surface (z = 0). Each point represents the centre of a layer, and the activity or concentration in each layer progresses through time using the simple Euler forward approximation. Initially, the bottom 30 m of the water column is assumed to be fully mixed and set to an initial activity or concentration (e.g. 6 dpm 100 L^{-1} for ^{224}Ra) to represent the properties at the time of the deep water intrusion event. For the ^{224}Ra run, Ra is set to a constant value (A_0 = 22.5 dpm 100 L^{-1}) at the bottom (assuming a constant source of Ra from the sediments) and is mixed upwards by turbulent diffusion, at a rate defined by K_Z. The model is run until the water column activity distribution becomes relatively constant (i.e. the system reaches steady-state).

By removing the decay term, and modifying the finite source term, the model is also run for DIC and O_2. A benthic source for DIC, and sink for O_2, are imposed as well as an additional term for water column respiration, to assess the relative importance of these

processes in the deep basin. For both DIC and O_2, the model is run first with a single constant flux (mmol m^{-2} d^{-1}) at the sediment surface. The fluxes used are 56 mmol DIC m^{-2} d^{-1} and -55 mmol O_2 m^{-2} d^{-1}, which are based on the results of this study. A second run then includes a constant, and vertically homogeneous, respiration term ($\pm$ 0.3 mmol m^3 d^{-1}) which adds an incremental amount of DIC to (or removes O_2 from) each layer per time step. By assuming the intrusion event occurred just before the sampling period, the DIC and O_2 distributions predicted by the model after a given number of days can be directly compared to the observations.

3.4 Results

3.4.1 Radium Distribution

The vertical ^{224}Ra distributions during the six-week sampling period (Figure 3.5) show relatively small activities in shallow and intermediate waters, with relatively large enrichments near the sediment surface. The ^{224}Ra signal in the upper 10 m of the water column can be attributed to the Sackville river, which discharges Ra-rich freshwater a few kilometres northeast of the sampling site. Variability in river discharge and the flushing effect of the daily tidal cycle may explain the minor variability between surface and shallow (10 meter) samples (Figure 3.5a).

Focusing on deeper samples (Figure 3.5b), significant ^{224}Ra enrichment is observed near the sediment surface in all 5 profiles, indicating a source of ^{224}Ra from the seafloor, similar to water-column observations in the deep Southern Ocean (*Charette et al.*, 2007) and pore water results in many coastal environments (*Hancock et al.*, 2006; *Colbert and Hammond*, 2008; *Moore et al.*, 2011). Due to the ^{224}Ra isotopes short half-life ($t_{1/2}$ = 3.66 d) and the quiescent nature of Bedford Basin's deep water, a decrease in radium activity is observed over a relatively short distance away from the sediments. The application of the 1-D diffusive model, illustrated in Figure 3.5b, yields K_Z values ranging from 1.0-3.3 cm^2 s^{-1}, with uncertainties ranging from 25-30 %, with the exception of the October 26th profile, which yields a value of 25.7 cm^2 s^{-1} with uncertainties near 100 % (Table 3.1). The single outlier on October 26th was attributed to additional advective forces from a lateral intrusion event, violating the negligible advection assumption of the 1-D diffusive model. Therefore, the data were not used in further analysis (see discussion). In general, however, the observed diffusivity remains relatively stable throughout the remainder of the

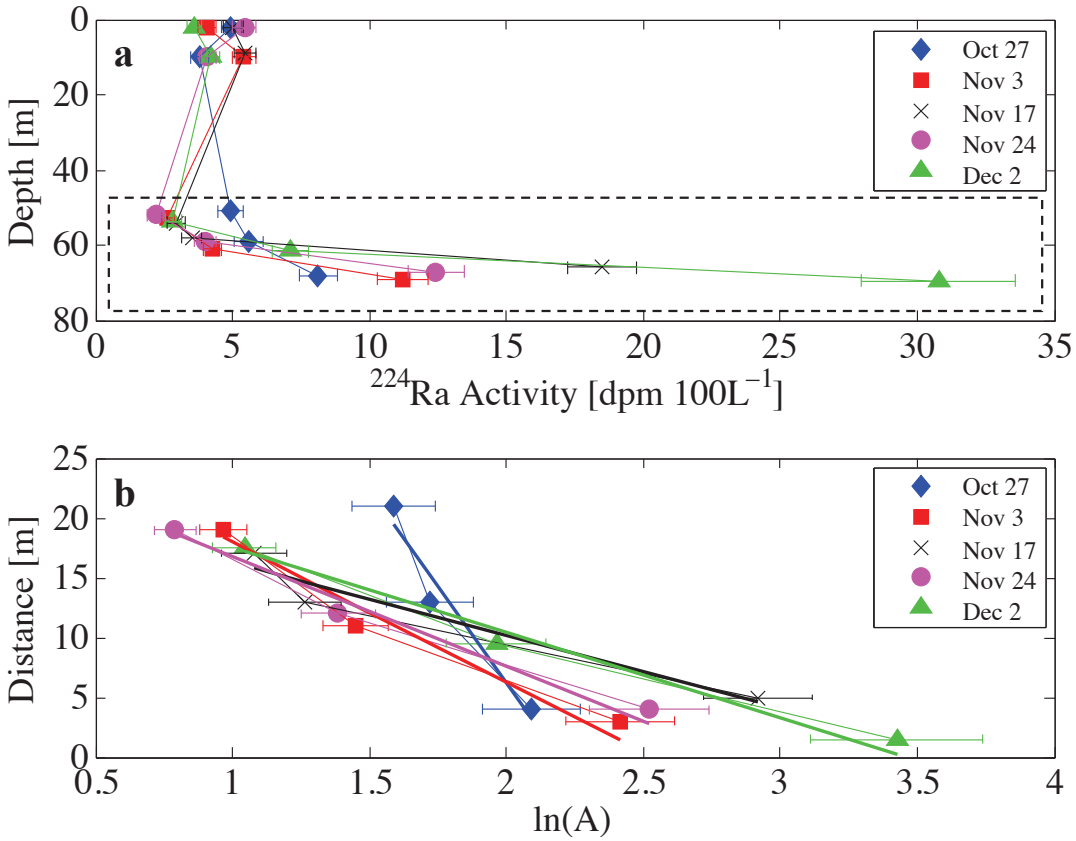

Figure 3.5: **(a)** Vertical profiles of ^{224}Ra. Black dashed box indicates deep-water samples used in 1-D diffusive model. **(b)** Natural logarithm (ln) transformations of ^{224}Ra activity plotted as a function of distance from the sediment surface (dotted line). Each daily set of points is fit with a least-squares regression used to estimate mixing rates (K_Z) and interface activities (A_0). The different characteristics of the 27-Oct plot relative to all other days represents the different mixing regime during this period. Figure redrawn from Burt et al. (2013a) with permission from Copernicus Publications.

Table 3.1: Results from ^{224}Ra, carbon and oxygen analyses. Daily results of eddy diffusion coefficients (K_Z), ^{224}Ra activities at the sediment water column interface (A_0), as well as benthic fluxes of ^{224}Ra (Q_{Ra}) and DIC (Q_{DIC}) out of the sediments (indicated by positive values) and fluxes of oxygen (Q_{O2}) into the sediments (indicated by negative values), are shown. Table redrawn from Burt et al. (2013a) with permission from Copernicus Publications.

Sampling Date	K_Z cm^2 s^{-1}	A_0 dpm 100 L^{-1}	Q_{Ra} atoms m^{-2} s^{-1}	Q_{DIC} mmol m^{-2} d^{-1}	Q_{O2} mmol m^{-2} d^{-1}
26-Oct *	25.7 $\pm$ 24.3	8.8 $\pm$ 1.8	-	-	-
03-Nov	3.3 $\pm$ 1.0	11.9 $\pm$ 2.2	24.4 $\pm$ 17.0	19.9 $\pm$ 11.6	-36.5 $\pm$ 18.8
17-Nov	1.0 $\pm$ 0.3	31.6 $\pm$ 8.7	35.5 $\pm$ 18.0	-	-
24-Nov	1.9 $\pm$ 0.5	16.3 $\pm$ 3.7	25.5 $\pm$ 7.3	41.5 $\pm$ 11.0	-48.8 $\pm$ 12.6
02-Dec	1.2 $\pm$ 0.3	30.3 $\pm$ 8.1	36.9 $\pm$ 15.2	58.7 $\pm$ 15.5	-44.1 $\pm$ 11.6
Mean	1.8 $\pm$ 0.6	22.5 $\pm$ 5.4	30.6 $\pm$ 14.6	-	-

*Values not included in flux analysis or mean calculations

sampling period.

3.4.2 ^{224}Ra, DIC, O_2 and Nutrient Fluxes

The interpolated Ra activities at the sediment surface (A_0) (see Eq. 3.3) range from 11.9-31.6 dpm 100 L^{-1} with uncertainties ranging from 19-27 % (Figure 3.5b). Utilizing these estimates of daily A_0 along with the K_Z values, daily radium fluxes (Q_{Ra}) are obtained that range from 24.4-36.9 atoms Ra m^{-2} s^{-1}. Uncertainties on this term varied significantly and in some cases were high (17-70 %) due to the cubic relationship of the slope term in the error propagation formula. These results are summarized in Table 3.1.

The overall trends seen in the vertical distributions of DIC and O_2 in Bedford Basin (Figure 3.6b, c) mimic those seen in the Ra observations, with clear vertical gradients near the sediment surface. No visible gradients, however, are seen in the deep-water AT data (Figure 3.6a). The DIC gradient also becomes increasingly negative throughout the study period (i.e. concentration decreases with distance from the sediments, see Figure 3.6), while the opposing O_2 gradient generally becomes increasingly positive. The vertical gradients in both DIC (Figure 3.6d) and O_2 (Figure 3.6e) were quantified for each sampling day using a weighted least-squares regression of all data over the same depth ranges. The interpolation of the DIC linear regressions to the sediment surface yields a range of interface concentrations (2199-2336 mmol m^{-3}, 2146-2280 μmol kg^{-1}), which tend to increase considerably throughout the sampling period.

While estimates of K_Z were made weekly throughout the sampling period, and weekly

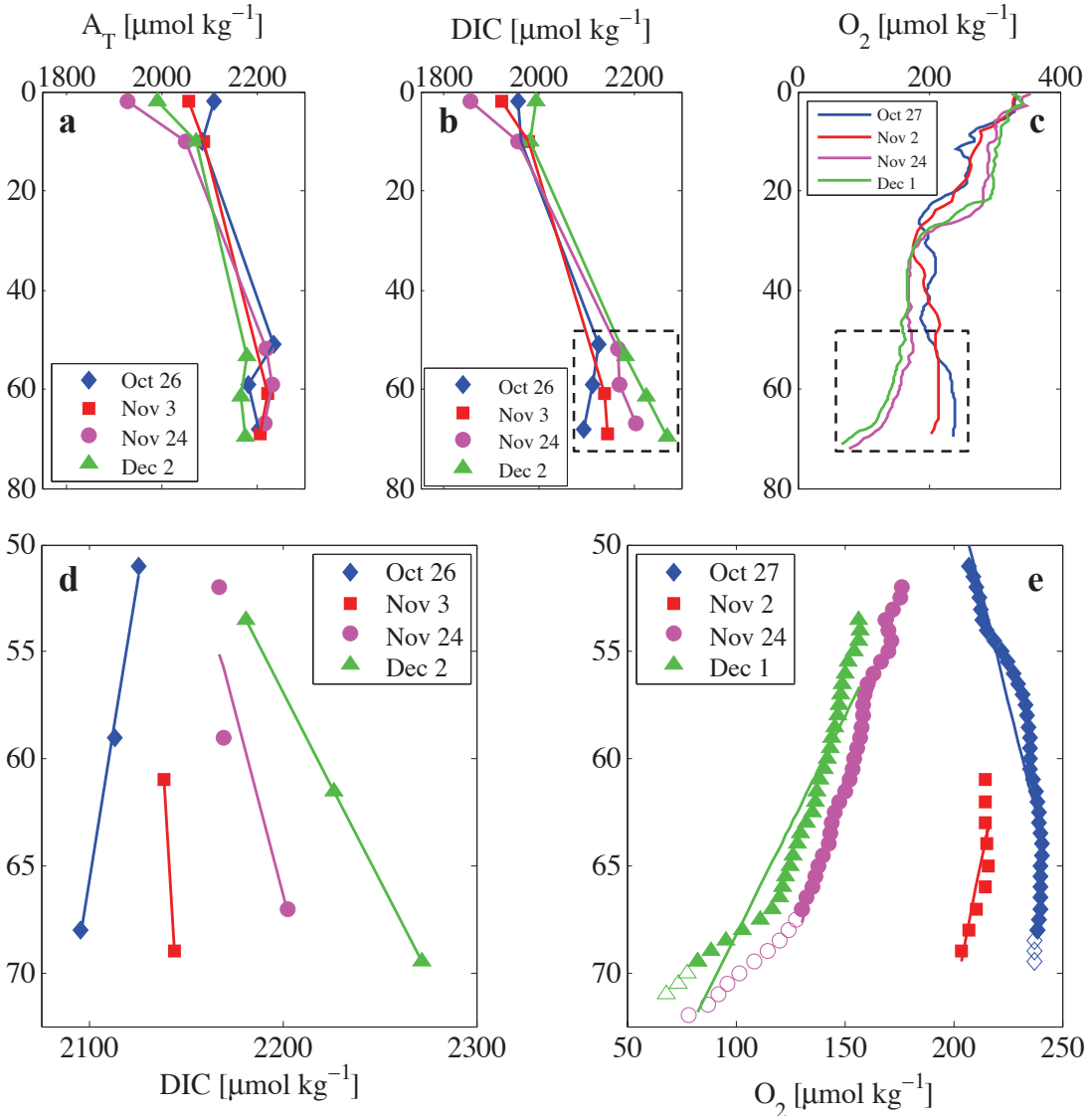

Figure 3.6: Top: Vertical profiles of AT **(a)** , DIC **(b)**, and O_2 **(c)** in Bedford Basin. Black dashed boxes indicate deep-water samples shown in bottom panels. Bottom: Vertical profiles of DIC **(d)** and O_2 **(e)** in deep waters with least-square regression lines indicating gradients. For deep water O_2 profiles (panel e), linear regressions are done over the same depth ranges as used for DIC (panel d) in order to be consistent with the depth ranges used to deduce the slopes. Open markers indicate deeper samples not used in the regressions. It is clear that the CTD based O_2 sensor provides a better resolution of the near sediment gradients, which cannot be resolved with the 30 L niskin bottle used for sampling DIC and ^{224}Ra. Figure redrawn from Burt et al. (2013a) with permission from Copernicus Publications.

Table 3.2: Comparison of calculated DIC fluxes out of sediments (i.e. positive fluxes), O_2 fluxes into sediment (i.e. negative values), and resulting O_2:DIC flux ratios. Table redrawn from Burt et al. (2013a) with permission from Copernicus Publications.

	Radium Method (Figure 3.6)	Inventory Method (see Section 3.4.2)	O_2 Slope Method (Figure 3.7b)
Q_{DIC} (mmol C m^{-2} d^{-1})	35.8	56.2	N/A
Q_{O2} (mmol O_2 m^{-2} d^{-1})	-43.7	-55.5	N/A
O_2:DIC	-1.22	-0.99	-0.90

O_2 profiles are consistently available from the Bedford Basin Monitoring Program, the DIC and O_2 fluxes were calculated only for days where both DIC and ^{224}Ra observations were made. As seen in Table 3.1, both DIC and O_2 fluxes strengthen, with opposing signs, throughout the majority of the sampling period. Assuming the changes in these fluxes occur linearly between sampling days, a linear interpolation between the flux values for the duration of the sample period (30 days) yields average fluxes of DIC and O_2 of 35.8 $\pm$ 11.9 mmol DIC m^{-2} d^{-1} and -43.7 $\pm$ 15.1 mmol O_2 m^{-2} d^{-1} respectively. Further independent DIC and O_2 flux estimates were made by assessing the deep-water DIC and O_2 inventory changes seen in Figure 3.6. This inventory method yields average increases of 56.2 mmol DIC m^{-2} d^{-1} and -55.5 mmol O_2 m^{-2} d^{-1}.

A third DIC flux estimate of 48.6 $\pm$ 23.6 mmol DIC m^{-2} d^{-1} can be made using the product of the Ra-based O_2 flux and the O_2:DIC ratio defined using the slope in Figure 3.7b. These latter approaches yield similar DIC flux values compared to the above Ra method (35.8 mmol DIC m^{-2} d^{-1}), providing support for the flux estimates reported in this study. A comparison of the independently calculated DIC and O_2 fluxes, and their corresponding DIC:O_2 ratios, are shown in Table 3.2. It is important to note that the Ra-based estimates represent DIC and O_2 fluxes obtained from individual profiles, while the inventory and ratio-based estimates require time-series measurements. For the further context of this paper, DIC fluxes refer to the Ra-based flux estimates.

The time series measurements of nitrate, phosphate and O_2 taken at the Compass Buoy Site during the sampling period (Figures 3.4 and 3.7a) show a decrease (i.e. consumption) in O_2 at 60 m depth with increases (i.e. production) in both nitrate and phosphate. The plots of O_2 vs. nitrate, phosphate and DIC, respectively (Figure 3.7b), show similar trends, with increases in NO_3^-, PO_4^{3-} and DIC with decreasing oxygen. These slopes are then used to calculate O_2:NO_3^- and O_2:PO_4^{3-} ratios, which, using Eq. 3.7 and Eq. 3.8, yield

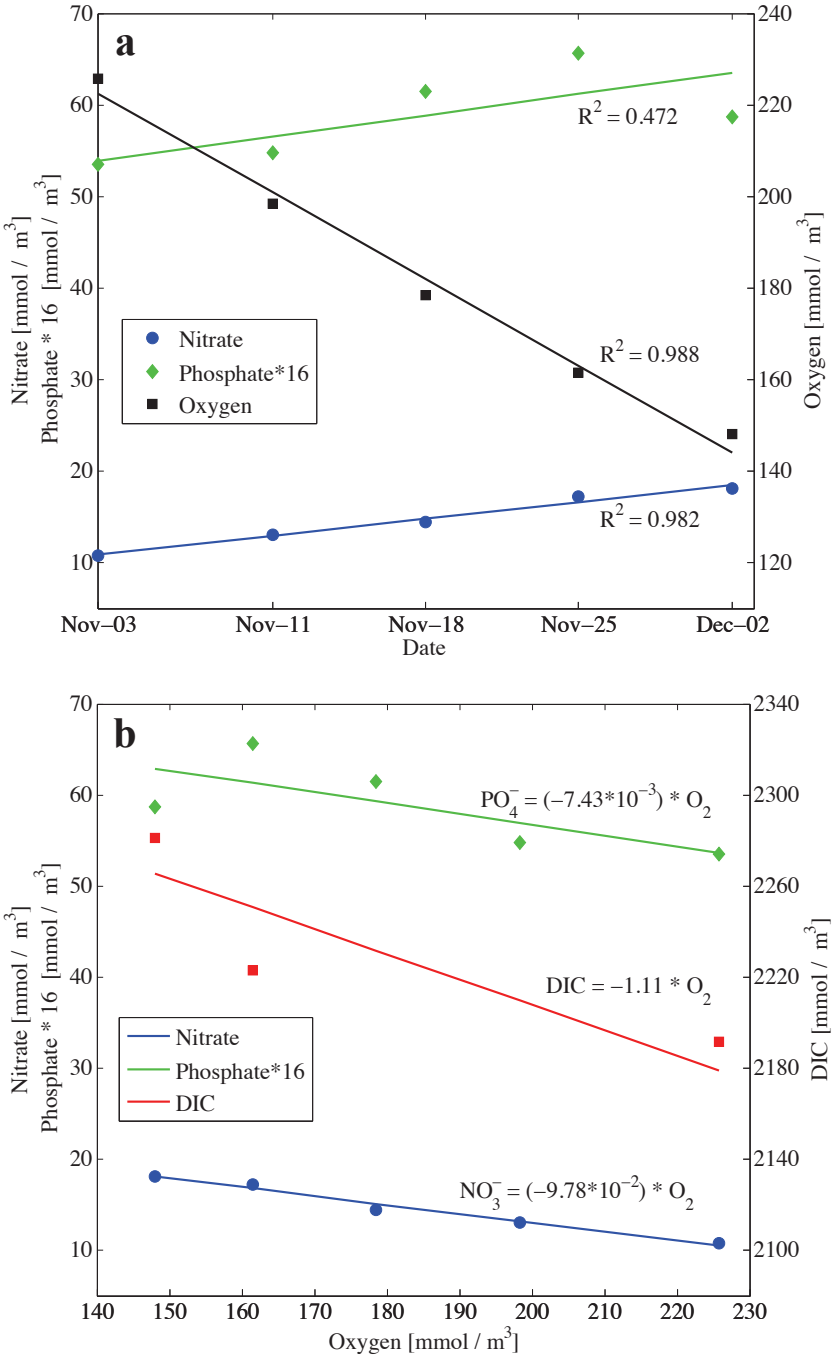

Figure 3.7: **(a)** Time-series measurements at 60 m in Bedford Basin during the sampling period (as shown in Figure 3.4). The R^2 values represent the quality of the fit, which largely affects the uncertainties in the final flux estimates. **(b)** Deep-water (60 m) O_2 vs. NO_3^-, PO_4^{3-} and DIC. Flux ratios (listed in Table 3.3) are shown as the slopes of the linear regression curves. Note that phosphate regression coefficients are from the original data rather than 'Phosphate*16', which is shown to better illustrate the parallel nature of the nitrate and phosphate slopes. Figure redrawn from Burt et al. (2013a) with permission from Copernicus Publications.

Table 3.3: Chemical fluxes in Bedford Basin. Table redrawn from Burt et al. (2013a) with permission from Copernicus Publications.

(a) Fluxes of DIC, O_2 and nutrients, with respective flux ratios			
Fluxes from Sediment*		Ratios**	
DIC (Q_{DIC}, Radium Method)[a]	35.8 $\pm$ 11.9 mmol C m^{-2} d^{-1}	O_2:DIC	-0.9 $\pm$ 0.3
Oxygen (Q_{O2}, Radium Method)[a]	-43.7 $\pm$ 15.1 mmol O_2 m^{-2} d^{-1}	DIC:NO_3^-	11.4 $\pm$ 4.0
Nitrate (NO_3^-) (Q_{NO3})[b]	4.27 $\pm$ 1.50 mmol N m^{-2} d^{-1}	O_2:PO_4^{3-}	150 $\pm$ 80.5
Phosphate (PO_4^{3-}) (Q_{PO4})[c]	0.32 $\pm$ 0.17 mmol P m^{-2} d^{-1}	O_2:PO_4^{3-}	-10.2 $\pm$ 0.7
		O_2:PO_4^{3-}	135 $\pm$ 55.7
		NO_3^-:PO_4^{3-}	13.1 $\pm$ 5.5
(b) Carbon Fluxes in the Surface Layer	mmol C m^{-2} d^{-1}		
DIC Uptake by Primary Production[d]	-50.1		
DIC from Sackville River[e]	14.5		
OrgC from Sackville River[f]	0.38		
OrgC from Sewage Outfall[g]	0.22		

*During the 30 day sampling period (Nov3rd-Dec2nd, 2010). Positive values indicate fluxes out of sediments while negative values indicate fluxes into sediments.
**Calculated using slopes of O_2 vs. NO_3^-/PO_4^{3-}/DIC (see Figure 3.7b)
[a] Average of linearly interpolated Q_DIC/O_2 values (Table 3.1)
[b] Product of Q_{O2} and O_2:NO_3^- ratio
[c] Product of Q_{O2} and O_2:PO_4^{3-} ratio
[d] Daily average from Platt (1975)
[e] Using riverine DIC endmember (601 μmol kg^{-1}, (*Shadwick et al.*, 2011), average river discharge (1.5 x 10^8 m^3 yr^{-1}, (*Kepkay et al.*, 1997), and 17 km^2 for surface area of basin
[f] From *Hargrave and Taguchi* (1978)
[g] Converted from CBOD data provided by Mill Cove Wastewater Treatment Plant (WWTP).

nitrate ($Q_{NO_3^-}$) and phosphate ($Q_{PO_4^{3-}}$) fluxes from the sediment into the water column of 4.27 ± 1.50 mmol NO_3^- m^{-2} d^{-1} and 0.32 ± 0.17 mmol PO_4^{3-} m^{-2} d^{-1} respectively. The relative uncertainties in these values differ due to the differing R_2 values of the linear fits. These nutrient fluxes and flux ratios are summarized in Table 3.3, and combined with the carbon and oxygen estimates, now present a more complete and quantitative understanding of the transfer of important chemical constituents through the sediment-water interface in Bedford Basin.

3.5 Discussion

3.5.1 K_Z measurements

This study demonstrates the utility of water column ^{224}Ra measurements in assessing vertical eddy diffusive coefficients using the simple 1-D diffusion model. The K_Z values calculated in this study (1.0-3.3 cm^2 s^{-1}) fall within the lower end of the range of values (1-100 cm^2 s^{-1}) obtained during an extensive dye tracing experiment in coastal and estuarine waters around the UK (*Riddle and Lewis*, 2000). This is not surprising given the relatively quiescent nature of the deep waters of Bedford Basin. Although no prior estimates are available for Bedford Basin, similar models in other regions have produced similar K_Z values. *Charette et al.* (2007) used the longer lived ^{228}Ra isotope in a similar diffusion model to calculate a K_Z of 1.5 cm^2 s^{-1} in the intermediate waters (300-1000 m) of the Southern Ocean. *Berelson et al.* (1982) used ^{222}Rn in the 500 m deep Santa Barbara basin to calculate a vertical diffusivity of 3.4 cm^2 s^{-1}, but also reported that near-bottom mixing caused difficulties in fitting the 1-dimensional model. *Sarmiento et al.* (1976) measured vertical profiles of both ^{228}Ra and ^{222}Rn during two GEOSECS expeditions and used a 1-D diffusion model to calculate values of K_Z between 5-440 cm^2 s^{-1} in the deep Atlantic and Pacific Oceans. As is mentioned by *Sarmiento et al.* (1976), estimates of K_Z can vary by orders of magnitude when comparing different regions or approaches. Therefore, caution must be taken when directly comparing the observed results here to those found in other regions, or calculated using different methods, due to variations in numerous important factors, including sediment characteristics. Estimates of these coefficients in Bedford Basin will facilitate a number of useful applications in the future. For example, the mixing schemes of physical models in general, are often tuned using a wide range of acceptable mixing coefficients from other published literature. Therefore, observational estimates of

coefficients like eddy diffusion on a small scale, like the ones reported here, can be very useful in areas where physical models are in place. In this case, the observed diffusivities are useful to validate and improve the vertical mixing scheme of the coastal circulation model for Halifax Harbour (*Shan et al.*, 2011). Furthermore, these estimates can be directly used to fine-tune the vertical eddy diffusivity coefficient used as an input parameter for the random walk process in the recently implemented particle tracking model for Halifax Harbour (*Shan and Sheng*, 2012).

3.5.2 Deep-water Intrusion

The results here reveal distinct benthic releases of ^{224}Ra, DIC, and nutrients from the sediment, with a corresponding consumption of O_2. For this study, the substantial deep-water intrusion, which, in effect, reset the chemical gradients in the deep basin, provided a rare opportunity to monitor the reestablishment of the near-bottom biogeochemical gradients throughout the sampling period. The intrusion event appears to have taken place just prior to the initial sampling day (26 October), affecting the entire deep water column (Figures 3.2 and 3.4). At this time, very little gradient in ^{224}Ra is observed and the inferred vertical diffusivity of 25.7 cm^2 s^{-1} is an order of magnitude higher than those calculated for all subsequent profiles in this study (Table 3.1, Figure 3.5). This observation suggests the presence of enhanced vertical mixing due to the intrusion event. In a recent study by *Li and Cai* (2011), the same 1-D diffusion model as is used here is shown to be very sensitive to advection, with the maximum sensitivity occurring when values of K_Z are small, and when using the shorter-lived isotope (i.e. ^{224}Ra). The large relative uncertainty calculated in this instance for K_Z (95 %) likely reflects the sensitivity to small K_Z values and advective signals. The immediate effects of the lateral intrusion are also visible in the biogeochemical data collected on 27 October, namely the abrupt increases in deep water O_2 and particulate organic carbon (POC) levels and corresponding decreases in nutrients (Figure 3.4), which indicate the intrusion originated from near the surface. The temperature and salinity properties (Figure 3.2) of the deep basin during this time reveal a shift to warmer, more saline water immediately following the event, suggesting a shallow, offshore intrusion source, which is consistent with the mechanism described for these intrusion events (*Platt*, 1975). As a whole, the data in late October indicate a relatively well-mixed deep water column as a result of a lateral intrusion of a water-mass rich in oxygen and POC, and depleted in DIC and nutrients.

The observations throughout the remainder of the sampling period illustrate a re-stabilization of the water column after the intrusion event. The increasing magnitude of the vertical radium gradient after 27 October (Figure 3.5) results in an initial decrease and eventual stability of calculated K_Z values over time. However, while decreases in the diffusive coefficients will tend to dampen the flux terms (Eq. 3.5 and 3.6), the intensification of the vertical DIC and O_2 gradients cause the magnitude of the DIC and O_2 fluxes to increase considerably throughout November 2010. These trends can be attributed to the processes that occur after the lateral intrusion event, namely the settling of intruded sedimentary material and the biogeochemical reactions that take place within the sediments after deposition. For example, a sharp increase in POC levels at 60 m water depth on 27 October (Figure 3.4), followed by its decline one week later, indicate enhanced delivery and settling of POC on the seafloor, eventually fueling chemical reactions within the sediments.

The substantial intrusion of warm, salty, and therefore relatively dense water (Figure 3.2) into the deep basin almost every fall season (Figure 3.3) is an event which, to date, has not received extensive scientific attention. The event in 2010 marks the annual temperature and salinity maximum for the deep basin waters, with cooling, freshening and oxygen depletion occurring throughout the following fall and winter.

3.5.3 Remineralization of Organic Material

While the calculated fluxes (Table 3.3) indicate clear sources and sinks of various chemical constituents, the ratios of these fluxes can provide further insight into the origin of the organic material and allow us to speculate about the dominant pathways for remineralization. The observations seen here (Figure 3.7b, Table 3.3) are consistent with the general notion of benthic respiration as a source of the various chemical constituents released from sediments. An assumption of negligible water column respiration in the deep basin is made based on the short residence time of sinking organic particles in the deep basin waters. Organic particles tend the sink through the water column at velocities ranging from a few meters, to hundreds of meters per day (*Armstrong et al.*, 2009), and within Bedford Basin, particle sinking rates observed at 70 m depth ranged from $\sim$5-170 meters per day (*Syvitski et al.*, 1995). Even when considering the lower end of these ranges, organic particles spend little time in the deep water column before reaching the sediments. Conceptually, the overall net reaction of benthic respiration describes the degradation of

organic matter by bacteria within the sediments resulting in both the consumption of O_2, or other electron acceptors, and the formation of DIC (*Burdige*, 2011). Subsequently, DIC, along with Ra, diffuse into the water column, while oxygen diffuses into the sediment. The result is a water column flux of DIC away from sediments and an opposing flux of O_2 into the sediment. The effect of these opposing fluxes can be observed in the vertical DIC and O_2 distributions of Bedford Basin (Figure 3.6).

According to the concepts first described by *Redfield et al.* (1963), marine organic matter contains carbon, nitrogen and phosphorus in the average composition of C:N:P = 106:16:1. Therefore, the net oxidation of this material to DIC, NO_3^- and PO_4^{3-} by bacteria within sediments should produce similar ratios in the pore water, with an O_2:DIC flux across the sediment water interface nearing -1.3:1 (*Jahnke and Jahnke*, 2000). The Bedford Basin observations (Figure 3.7b) suggest an O_2:DIC ratio of -0.9 $\pm$ 0.3:1 for benthic fluxes, while DIC:NO_3^-:PO_4^{3-} ratios are approximately 150:13:1 (Table 3.3). These ratios are a strong indication that bacterial respiration of marine organic matter within the sediments fuels the benthic fluxes into the overlying water column. However, remineralization of organic matter can occur via a number of pathways, involving reactions that result in deviations from the Redfield values, most importantly, denitrification.

The reactions governing the respiration of POM in sediments will depend on the availability of various electron acceptors, with O_2 being most favourable in terms of energy gained (*Burdige*, 2011). The surface sediment at the Compass Buoy Site is considered to be a poorly oxygenated, fine-grained mud, with very high organic carbon content (OCC = 5-6 %) (*Fader and Miller*, 2008; *Buckley and Hargrave*, 1989). Therefore, aerobic oxidation will tend to dominate within the thin oxygenated layer of sediment directly beneath the sediment-water interface. Beneath this layer, in the absence of O_2, the system can be assumed to favour the reduction of NO_3^- (denitrification), resulting in a conversion of NO_3^- to elemental N_2, and the production of AT (*Chen and Wang*, 1999). Similarly, in the absence of available NO_3^-, the reduction of manganese, iron and sulphate will produce Mn^{2+}, Fe^{2+} and H_2S, respectively, also increasing AT by varying amounts (*Chen and Wang*, 1999). However, ignoring the potential burial of S^{2-} as pyrite, upward diffusion of these reduced products into the oxygenated sediment layer will result in their reoxidation, with the corresponding AT consumed. In this case, without any direct measurements of the sediment biogeochemistry, the extent of most anaerobic reactions is not fully traceable. For

denitrification, however, the reaction produces DIC and AT while creating an irreversible loss of NO_3^- from the system in the form of N_2, which should, in effect, increase the DIC:NO_3^-, and O_2:NO_3^- ratios of the observed fluxes. The observed DIC:NO_3^- ratio of 11.4:1 is considerably higher than Redfield values (6.6:1), and those previously reported for both deposited and suspended particulate matter in sediment traps in Bedford Basin by *Hargrave and Taguchi* (1978). Overall, observed DIC:NO_3^- and NO_3^-:PO_4^{3-} flux ratios indicate a deficit of NO_3^- (e.g. NO_3^-:$PO_4^{3-} < 16$) suggesting that denitrification plays a role in the respiration of POM within the sediments. However, no increase in AT is observed in the water column (Figure 3.6a), despite the fact that denitrification produces 0.99 mol AT per 1 mol N denitrified (*Chen and Wang*, 1999). This AT signal may be masked by the aerobic processes occurring in the oxygenated sediment layers. Also, considering the much larger water column background of AT ($\sim$2200 mmol m^{-3}) compared to NO_3^- ($\sim$10 mmol m^{-3}), a weak AT signal produced by denitrification may not be discernible in the observations.

The observed oxygen fluxes represent considerable rates of sediment oxygen uptake given the generally low temperature of the water column. Given the high organic carbon content and anoxic characteristics of the Bedford Basin sediment, the substantial intrusion of oxygenated waters could facilitate increased oxygen uptake during the sampling period. *Hargrave* (1978) used incubations of undisturbed sediment cores collected in the deep basin to calculate annual mean oxygen uptake values of 17 mmol O_2 m^{-2} d^{-1}. While deep water temperatures in the basin are similar in both studies, no deep-water oxygen intrusion is reported in the *Hargrave* (1978) study, possibly explaining the factor of 2.5 difference between their results, and those reported here. In fact, the results are quite comparable given the vast differences in analytical techniques and general methodologies between these two studies. *Hargrave* (1978) also reported a 1-2 month delay in peak sediment oxygen uptake after deposition of fresh organic matter by the spring bloom, similar to the observations seen here in the fall. This delayed response in benthic ecosystems has also been observed in laboratory studies (*Ståhl et al.*, 2004) and in other coastal environments (*Rudnick and Oviatt*, 1986). Finally, very little benthic biomass has been reported in the deep basin (7 ± 12 g m^{-2}) indicating that bioturbation and bio-irrigation are likely not key contributors to the oxygen uptake observations made here (*Hargrave et al.*, 1989).

3.5.4 Numerical Model Results

In order to better understand the validity of the steady-state assumption, a time-dependent finite-difference diffusion model is used in an attempt to reproduce the ^{224}Ra, DIC and O_2 observations. The model is initialized with a constant intrusion activity of 6 dpm 100 L^{-1} over the bottom 30 m of the water-column, and 1 dpm 100 L^{-1} in the upper water column. The model is run with the mean observed mixing rate (K_Z = 1.84 cm^2 s^{-1}) and the mean observed interface activities (A_0 = 22.5 dpm 100 L^{-1}), listed in Table 3.1. Overall, the large majority of the ^{224}Ra observations fall within the error margins of the K_Z and A_0 terms (see Figure 3.8a and b), indicating that the assumptions used in the 1-D diffusion model are consistent with the observations from Bedford Basin. According to the time-dependent model, a steady-state Ra distribution is reached within approximately 7 days of the intrusion event, which is reasonable given the short half-life of ^{224}Ra. Therefore, a steady-state, which is assumed for the 1-D diffusion model, is likely present throughout a large majority of the sampling period. Furthermore, the fit of the numerical model to the observations is encouraging given the exclusion of any horizontal mixing or secondary Ra sources from the model runs.

Assuming the same diffusive mixing rate as described above, the model results for DIC and O_2 are shown in Figure 3.8 (c to f). The initial concentrations in the model were based on the October 27th observations, with intrusion concentrations for the bottom 30 m of 2165 mmol DIC m^{-3} and 240 mmol O_2 m^{-3}, and concentrations in the upper water column of 2190 mmol DIC m^{-3} and 180 mmol O_2 m^{-2} d^{-1}. The models were run with constant fluxes of 56 mmol DIC m^{-2} d^{-1} and -55 mmol O_2 m^{-2} d^{-1}, which are based on the inventory method results listed in Table 3.2. When run with only a constant benthic flux, the finite-difference numerical model provides a relatively good fit to the observations (see Figure 3.8c and d), with the only significant deviations from the observations occurring near the sediments. The model consistently predicts too little DIC, and too much O_2 in the later stages of the sampling period.

In order to test whether these deviations of the model results from the observations were due to the omission of water column respiration, a constant water column respiration rate is added to the model, which in turn would cause a gradual build-up of water column DIC, with a corresponding loss of O_2, over time. Assuming a DIC:O_2 ratio of 1:1, this term added 0.3 mmol DIC m^{-3} d^{-1} to each layer, or removed O_2 at a rate of

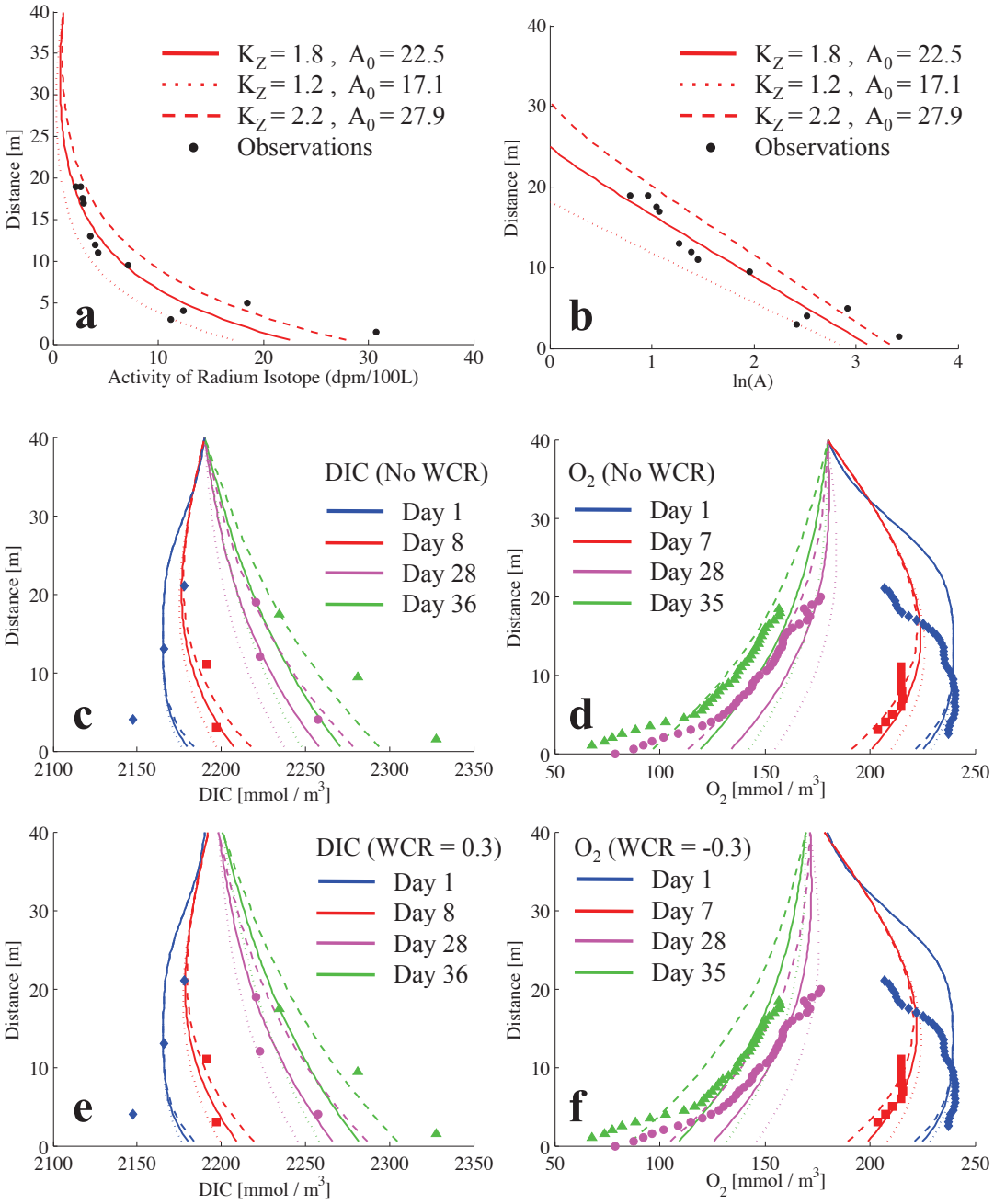

Figure 3.8: Finite difference model results. **(a)** Vertical ^{224}Ra distribution at steady-state. **(b)** Natural log of activity with distance from sediment at steady-state. Results after 30 day runs are shown (steady-state reached within 7 days). Dashed and dotted lines show error margins given the uncertainties in K_Z and A_0 (see Table 3.1). **(c)** DIC and **(d)** O_2 distributions for different days following an intrusion event (with no water column respiration (WCR) term). **(e)** DIC and **(f)** O_2 distributions with WCF term added. Assuming a 25 % uncertainty on the benthic flux values, the lower (dotted line) and upper (dashed line) uncertainty ranges are shown. Observations are overlaid as discrete points, with model run days matching the sampling days given an intrusion event beginning on Oct. 26th (see Figure 3.6). Figure redrawn from Burt et al. (2013a) with permission from Copernicus Publications.

-0.3 mmol O_2 m^{-3} d^{-1}. This chosen respiration rate is small compared to prior estimates on the nearby Scotian Shelf (*Thomas et al.*, 2012), and lies in the low end of the range (0.02-75 mmol O_2 m^{-3} d^{-1}) listed in a global compilation study of water column respiration rates (*Robinson and Williams*, 2005). Assuming homogenous respiration over the bottom 40 m, this water column respiration term (12 mmol DIC m^{-2} d^{-1}) represents approximately 20 % of the benthic flux term (56 mmol m^{-2} d^{-1}). The addition of the water column respiration term provides a slightly better fit to some of the observations (see Figure 3.8e and f), but the required magnitude of this term to obtain an improved fit is small, suggesting its contribution to the system is minor, if not negligible. Any further investigation into the relative effects of water column respiration goes beyond the scope of this paper and the capacity of the current dataset.

In this study, the model is applied in order to assess the non-steady state behaviour of the carbon and oxygen systems during the sampling period, and test the assumptions regarding the neglect of water column respiration in the 1-D diffusion model. Overall, this time-dependent 1-D model, which illustrates the diffusion of a benthic signal into the water-column, is able to reproduce the general trends in both the DIC and O_2 observations, indicating that the benthic release of DIC and uptake of O_2 are the dominant processes shaping their distributions in the deep basin.

3.5.5 Carbon Budgets

Considering the short period over which these fluxes are measured (30 days), they constitute substantial additions to the carbon inventory of the basin (Table 3.3). For example, the Sackville River, on average, delivers only 14.5 mmol DIC m^{-2} d^{-1} to the surface waters of Bedford Basin (Table 3.3), which corresponds to less than half of the daily benthic DIC release into the deep water column. Furthermore, when integrating over the 30-day sampling period, the benthic DIC return flux corresponds to approximately 6 % of the annual DIC uptake by primary production in the surface waters (*Platt*, 1975). While similarly large benthic DIC contributions have been reported previously (*Chen and Wang*, 1999; *Jahnke et al.*, 2005), they are more common in warmer, shallower shelf environments. In such environments, the euphotic zone is in close proximity to sediments allowing large amounts of organic carbon formed in the surface to reach the sediments, where the organic carbon is respired rapidly. A sediment trap study in the basin by *Hargrave and Taguchi* (1978) provided annual mean organic carbon sedimentation rates at 60 m depth of

17 mmol C m^{-2} d^{-1}, approximately half of the DIC return flux calculated here during the sampling period. Therefore, even when assuming no long-term burial of sedimented material, the results represent enhanced benthic carbon fluxes compared to those reported by *Hargrave and Taguchi* (1978). Allochthonous inputs of organic material from rivers and sewage appear to play a very modest role in organic carbon supply to Bedford Basin (*Hargrave et al.* (1976), Table 3.3), and allow the episodic ventilation events to sustain oxic conditions in the deep basin (Figure 3.3). This is in line with the observed flux ratios calculated here, which resemble Redfield values, and thus point to the respiration of marine organic matter, rather than other organic materials.

POC concentrations increased in the deep waters following the intrusion event in late October (Figure 3.4). As argued by Hargrave and Taguchi (1978), an inflow of dense surface water, rich in labile POM and re-suspended sediments, could import the additional organic material necessary to fuel the benthic fluxes observed here. Furthermore, the occurrence of the autumn bloom in mid-October (Figure 3.4) may have led to organic carbon delivery both vertically via increased particle export from the surface layer (Figure 3.4) and laterally via the deep-water intrusion. Regardless of the delivery mechanism, the observations indicate that an enhanced supply of organic matter becomes available for rapid respiration, which is reflected by observations of high return fluxes. It is important to note that these fluxes may occur over a short time period and do not necessarily reflect the annual mean fluxes. While the notion of enhanced delivery of POM to the deep basin via lateral intrusion appears reasonable, direct observations of these rare events are needed to completely understand their impact on the chemical budgets, as well as the physical structure, of Bedford Basin.

3.6 Conclusions

Corresponding trends between various hydrochemical measurements point to enhanced benthic respiration and subsequent pore water fluxes of DIC, O_2, and nutrients into the deep water column of Bedford Basin, paralleled by a release of ^{224}Ra. The application of the 1-D diffusion model to near-bottom distributions of ^{224}Ra was useful in understanding the evolving mixing regime of the deep basin following a considerable water-exchange event and yielded vertical eddy diffusivities and fluxes. Fluxes of DIC, nutrients and O_2, consistent in magnitude with Redfield ratios, point to benthic respiration of marine organic

matter. Only minor discrepancy of results from field observations, and those obtained using numerical simulations, indicate that the assumptions of the 1-D diffusion model are consistent with the ^{224}Ra observations in Bedford Basin. Interpolation throughout the 30-day sampling period yields a benthic DIC return flux which constitutes as much as 6 % of the annual primary production in surface waters. This presumed short-term substantial flux is believed to result from enhanced delivery of particulate organic carbon (POC) to deep waters associated with the co-occurrence of the autumn bloom and a deep-water intrusion event.

High seasonal variability in sedimentation rate and relatively high carbon sedimentation rates during fall months have been reported by *Hargrave and Taguchi* (1978). Long-term Ra and carbon would be needed in order to gain better understanding of the mixing regimes and benthic fluxes at an annual scale.

3.7 Acknowledgements

Thank you to John Smith, Jeff Spry, Kevin Pauley, the crew of the CCGS Sigma T, as well as Bill Li and the DFO Bedford Basin Plankton Monitoring Program. This work contributes to IGBP/IHDP LOICZ. Also, many thanks the 2 anonymous referees, whose comments have substantially improved the manuscript.

CHAPTER 4

RADIUM ISOTOPE DISTRIBUTIONS AND CROSS-SHELF TRANSPORT ON THE SCOTIAN SHELF

4.1 Abstract

Radium (Ra) isotopes have become an established tool for investigating mixing rates on continental shelves, and more recently have been used to quantify the release of dissolved compounds enriched in pore waters into the water column. Results from Ra sampling of the Scotian Shelf region of the Canadian northwestern Atlantic Ocean are presented, which reveal cross-shelf Ra distributions that are unique compared to other coastal regions. The observations of lower ^{224}Ra activities near the coast, relatively high activities at large distances offshore ($>$ 100 km), and gradients in both offshore and onshore directions are explained by referring to regional geomorphology, as well as shelf bathymetry and circulation patterns. Vertical mixing above shallow offshore banks allows for Ra enrichments in offshore surface waters, while horizontal dispersion of this bottom-generated signal can transport Ra off the shelf break in surface waters, and towards the shore beneath the surface mixed layer. On the Scotian Shelf, estimating horizontal diffusivity (K_X) using a 1-D Ra diffusion model is limited by the presence of two distinct Ra sources (land and sediment), by three dimensional shelf topography, as well as by complex hydrodynamic conditions. Here, a numerical 2-D diffusion model reproduces Ra distributions on the shelf using both coastal and benthic sources. Horizontal and vertical mixing coefficients are then calculated by minimizing deviations between model output and observations. Onshore gradients in CO_2 and nutrient species combined

with model-derived K_X values can yield onshore carbon and nutrient fluxes in subsurface waters, which in turn supply the CO_2 outgassing from the Scotian Shelf. These results provide constraints for cross-shelf transports of carbon and nutrients on the Scotian Shelf in order to guide mass balance or model based budget approaches in future studies.[1]

4.2 Introduction

The use of radium (Ra) isotopes as a tracer of coastal mixing is a growing method in chemical oceanographic studies. Many such studies have focused on quantifying rates of horizontal turbulent diffusion using offshore measurements of short-lived Ra, ^{224}Ra and ^{223}Ra, on the continental shelf. The method, first described by *Moore* (2000), utilizes assumptions regarding the dominant mixing regime, the Ra sources, and steady-state. Subsequent studies have built on this model by adding terms for additional sources (*Hancock et al.*, 2006), a sloping shelf bottom (*Stachelhaus et al.*, 2012), by applying the model in the vertical direction (see chapter 3, or *Charette et al.* (2007)), or by comparing results to outputs from physical models (*Colbert and Hammond*, 2007). More recently, the limitations of the model for use on the continental shelf were discussed by examining its sensitivity to advective forces (*Li and Cai*, 2011).

The sediments are a well studied source of short-lived Ra to the water column. High activities have been observed above surface sediments in various environments including beaches (*Colbert and Hammond*, 2008), coastal lagoons (*Hancock et al.*, 2006), coastal inlets (chapter 3), tidal mudflats (*Moore et al.*, 2011), and along the continental shelf (*Moore*, 2007; *Stachelhaus et al.*, 2012). However, these enrichments are often restricted to nearshore and near-bottom environments. On the open shelf, ^{224}Ra isotopes are typically only observed in surface waters within 50 km of the shoreline, due to their rapid decay after mixing away from their continental source.

The continental shelf system of southeastern Canada (Scotian Shelf, Figure 4.1) is a physically complex and unique shelf system. This region is home to the largest seasonal sea surface temperature variations in the North Atlantic ($\sim$20 K, *Umoh and Thompson* (1994)) and is affected by some of the largest tidal forces on the planet. The Scotian Shelf

[1] Aside from minor alterations to the wording, this chapter consists of a manuscript by W. J. Burt, H. Thomas, and J. P. Auclair entitled *Short-lived Radium Isotopes on the Scotian Shelf: Unique Distribution and Tracers of Cross-shelf CO_2 and Nutrient Transport* published by Elsevier Science in Marine Chemistry in 2013.

also experiences large storm events throughout the winter, occasional tropical storms in late summer, and high-wind episodes throughout the year which fuel coastal upwelling (*Shan et al.*, 2011). Furthermore, before reaching the steep shelf break, the broad, gently downward sloping shelf, typical for most passive continental margins, is interrupted by a series of shallow banks located at various distances offshore, which introduce small scale circulation patterns (*Loder et al.*, 1988; *Urrego-Blanco and Sheng*, 2012). As a result, considerable uncertainty exists regarding the seasonal circulation patterns on the Scotian Shelf, and their effects on transporting chemical tracers between the adjacent open ocean and sedimentary systems.

Uncertainties also exist regarding the CO_2 system of the Scotian Shelf. While coastal seas are, in general, thought to transfer atmospheric CO_2 from the atmosphere into the deeper ocean (*Tsunogai et al.*, 1999; *Thomas et al.*, 2004; *Chen and Borges*, 2009), recent studies on the Scotian Shelf reveal the area as a net source of CO_2 to the atmosphere (*Shadwick et al.*, 2010, 2011). The Mid and South Atlantic Bights, two open continental shelf systems located just downstream (southwest), are considered to act as net sinks of CO_2 (*Boehme et al.*, 1998; *DeGrandpre et al.*, 2002; *Signorini et al.*, 2013). Outgassing into the atmosphere requires supersaturated levels of CO_2 in surface waters, and in the case of the Scotian Shelf, the respective CO_2 source has not yet been fully understood (e.g. *Shadwick and Thomas* (2011)).

Ra isotopes are often considered ideal tracers for coastal mixing studies (*Charette et al.*, 2007), and they appear to be particularly useful for studies on the offshore Scotian Shelf banks. First, once released into the water column, the distributions of ^{224}Ra and ^{223}Ra are affected only by mixing and decay, while other chemical tracers, such as CO_2 and nutrients, are also affected by biological metabolism. Furthermore, short-lived Ra isotopes can be used to examine mixing processes which occur over a timescale of days to weeks, while the longer-lived Ra isotopes (^{226}Ra and ^{228}Ra) can be treated as more conservative tracers with essentially no decay over a period of months. Finally, once 100 km offshore, the background ^{224}Ra signal is often very low, making benthic additions more easily detectable. The potential pore water release of other dissolved species, such as CO_2 or nutrients, are not easily delineated from the large background already present in shelf waters at $\sim$100 m depth. However, mixing coefficients obtained using Ra isotope methods can be combined with gradients of carbon and nutrients to calculate sediment-water column fluxes of these

important biogeochemical species (e.g. see chapter 3).

The current study focuses on some of the unique patterns exhibited in the short-lived Ra isotopes from the Scotian Shelf, and represents the first published Ra dataset from the region. Observed features include relatively small coastal signals, considerable activities far offshore atop shallow banks, and activities consistently above the detection limit in both surface waters and beneath the mixed layer throughout the entire shelf, as well as in open ocean waters. The effects of a benthic Ra signal and offshore advection on estimates of horizontal mixing using a 1-D diffusive model are discussed, as is the usefulness and limitations associated with applying this model in shelf environments. To better represent conditions observed on the Scotian Shelf, the steady state solution to the 2-D diffusion of Ra over the shelf is obtained numerically. Optimal values of mixing coefficients and Ra source terms are found by minimizing deviations from observations. Finally, future applications of Ra studies on the Scotian Shelf are explored, including estimates of onshore carbon and nutrient fluxes.

4.3 Oceanographic Setting

The Scotian shelf is a broad ($\sim$200 km) continental margin off Eastern Canada (Figure 4.1), uniquely located at the boundary between the subpolar and subtropical gyres (*Loder et al.*, 1997). To the north, the Gulf of St. Lawrence provides the major freshwater input to the system, via the Cabot Strait. Water exiting the Cabot Strait feeds the Nova Scotia current (NSC), which flows southwest along the coastline. The outflow also joins a branch of the Labrador Current (LC), which flows parallel along the shelfbreak (*Hannah et al.*, 2001). These currents show strong seasonal fluctuations in strength, with the inner shelf NSC ranging in peak speeds from 10 cm s^{-1} in spring/summer to 25 cm s^{-1} in winter (*Han and Loder*, 2003).

The outer shelf contains a series of offshore banks and channels (Figure 4.1), which greatly influence the regional circulation (*Hannah et al.*, 2001). Specifically, these topographic features cause interruption of the LC, creating small scale anticylonic (clockwise) surface gyres, with cyclonic (counter clockwise) gyres forming above the channels in between, and both of which effectively transport water in a cross-shelf direction (*Han and Loder*, 2003). Recent numerical model simulations clearly show these small-scale circulation patterns (*Urrego-Blanco and Sheng*, 2014). Results from current profilers

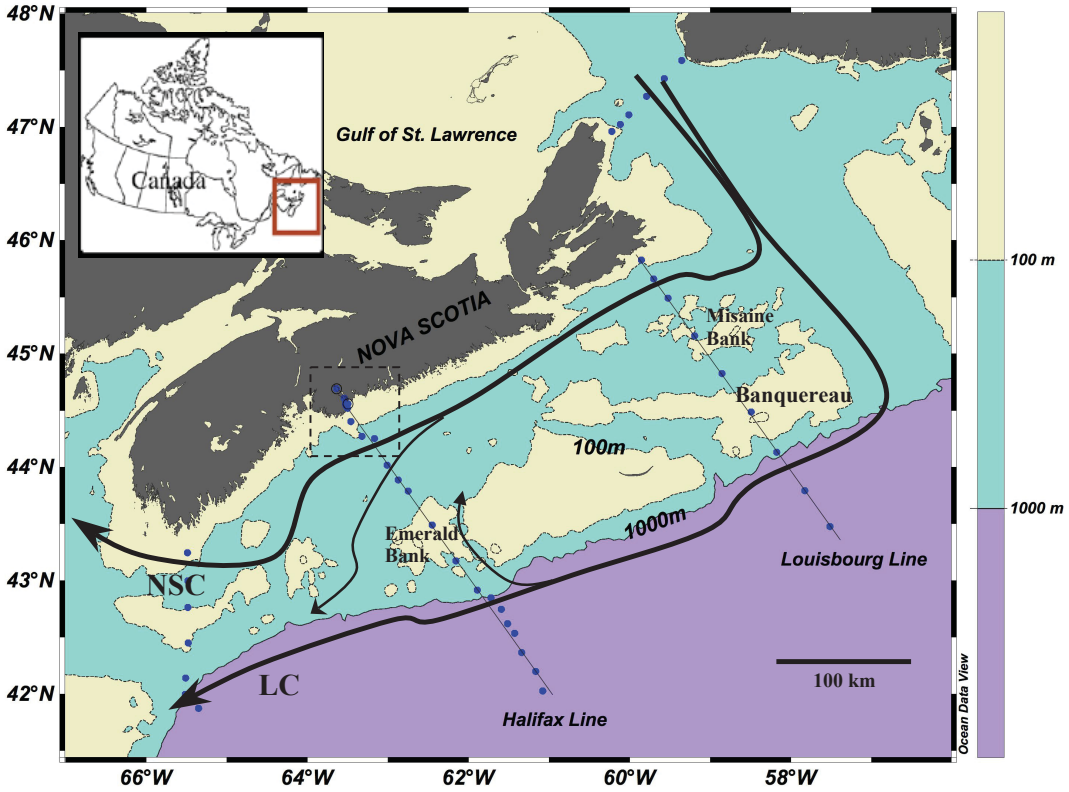

Figure 4.1: Map showing sampling transects on the Scotian Shelf. Contours are shown to indicate locations of offshore banks. Black arrows illustrate the general circulation across the shelf including the Nova Scotia current (NSC) and Labrador current (LC). The black dashed box indicates the location of the Outer Harbour and nearshore stations seen in Figure 4.2. Figure redrawn from Burt et al. (2013b) with permission from Elsevier Science.

indicate enhanced vertical mixing above the plateaus of banks (*Loder et al.*, 1988). These areas are also of particular interest because they have been characterized as important spawning areas for numerous commercial fish species, as well as areas of hydrocarbon production and sand transport across the shelf (*Hannah et al.*, 2001).

4.4 Methods

4.4.1 Sample Collection and Analysis

Most data were collected aboard the CCGS Henry Hudson during the Atlantic Zone Monitoring Program (AZMP) cruise in April, 2010. Additional samples at a particular station (HL2) were taken during the following year, in April 2011. The AZMP program involves 2 annual expeditions covering the Scotian Shelf region (Figure 4.1), during which various hydrographic, chemical, and biological data are collected, culminating in numerous studies intended to better understand the biogeochemical cycling and chemical budgets of the region (e.g. *Greenan et al.* (2008); *Shadwick et al.* (2011)). Additional Ra samples were collected aboard the CCGS Sigma T during a number of daytrips between October 2010 and January 2011 in the nearshore regions of the Halifax Line transect, and in areas of Halifax Harbour (Figure 4.2a).

During the 2010 AZMP cruise (Figure 4.1), water samples for ^{224}Ra analysis were taken at two distinct depths (2 m and 80 m) along the majority of the Halifax and Louisbourg lines, which extend from the Nova Scotia coast to the deep North Atlantic over 300 km offshore (Figure 4.1). Surface samples were collected using the ships continuously flowing seawater intake, while deep samples used multiple 10-L Niskin bottles attached to a rosette. Using the same rosette system in April, 2011, two deep-water profiles were taken at station HL2 between 140-160 m, in an attempt to better observe the strong sedimentary signal seen the previous year. Each profile consisted of 4 samples equally spaced between 2-18 meters off the bottom, with precise depths obtained using an altimeter attached to the rosette system. On the smaller Sigma T, all samples were collected from the surface using a small bilge pump hand-lowered to 2 m depth, with the exception of a single daytrip to station HL2 in October, 2010, where one deep sample was collected $\sim$3 m off the bottom sediments using multiple casts of a single 30 L Niksin bottle. Sample volumes ranged from $\sim$100 L for near-bottom sampling, to $\sim$200 L for surface and intermediate water column sampling. Please also refer to chapter 3 for sampling details.

After collection, particulate material was removed by pre-filtering the entire volume through 10 and 1 micron cartridges. Filtered samples were stored in large plastic drums, then pumped slowly ($<$1 L min^{-1}) through plastic cartridges containing Mn-impregnated acrylic fiber, which extracts dissolved Ra. A consistent extraction efficiency of 92 $\pm$ 3 % (n = 8) was observed in this study by pumping some samples through two cartridges placed in series. All samples were then dried with compressed air before insertion onto the RaDeCC system for counting. For more details on the counting procedure, refer to *Moore and Arnold* (1996). All samples were initially counted within 2 days of collection. Samples were recounted onboard after 11-16 days to correct for the supported parent thorium-228 (^{228}Th) isotope. This correction uses the initial count results to account for the 4-12 % of ^{224}Ra still remaining on the fiber during the second count. Uncertainties are calculated based on the methods described by *Garcia-Solsona et al.* (2008). The initial uncertainty, based on the one sigma counting statistics (see section 2.5.1), is propagated through calculations for counter efficiency, sample volume, and supported Ra, all of which have individual errors. The detection limit of the delayed coincidence counter for ^{224}Ra is considered to be approximately 0.1 dpm for a 100 L sample (*Moore*, 2008). The uncertainty for ^{224}Ra ranged from 13-110 %, with very high values ($>$50 %) corresponding to samples with very low count rates, and correspondingly low activities ($<$ 0.25 dpm 100 L^{-1}).

Aboard the Hudson, Ra samples taken using the rosette (i.e. deep samples) were paralleled by measurements of temperature, salinity, pressure and oxygen for each Niskin bottle, with the single surface Niskin data used for surface Ra samples. Full depth profiles of dissolved inorganic carbon (DIC), alkalinity (AT), and nutrients (NO_3^-, PO_4^{3-} and SiO_4) were also analyzed onboard for the majority of stations as part of the AZMP cruise program (see *Johnson et al.* (1993) for a full description of DIC and AT instrumental methods, and *Shadwick et al.* (2011) for a detailed description of chemical sampling and analysis during the AZMP expeditions).

4.4.2 Determining Diffusive Mixing Coefficients using Ra isotopes

If the assumption is made that Ra is transported away from its source by dominantly diffusive processes, a one-dimensional system can be described using the diffusion equation with an additional decay term:

$$\frac{\partial A}{\partial t} = K_X \frac{\partial^2 A}{\partial x^2} - \lambda A, \tag{4.1}$$

where A is ^{224}Ra activity, x represents the distance from the Ra source, K_X is the horizontal eddy diffusion coefficient, and λ is the isotope's known half-life. Assuming a single, constant source of Ra (A_0), as well as steady-state, Eq. 4.1 can be solved by:

$$A(x) = A_0 e^{-x\sqrt{\lambda/K_X}}, \tag{4.2}$$

where A_X is the Ra activity at a given distance (x). A least-squares regression of Ra activities over a distance from source thus provides the diffusive mixing coefficient (K_X). Uncertainties in the mixing coefficients are determined using the least-squares regression routine in MATLAB, which uses the uncertainties of individual observations to calculate uncertainties in the slope and intercept coefficients of the linear fit, and propagates those errors into uncertainties in K_X.

4.4.3 2-D Numerical Radium Simulations

In order to arrive at Eq. 4.2, the above 1-D model requires assumptions regarding a single source and steady-state. By generalizing Eq. 4.1 to two dimensions, a benthic Ra source can be considered. A numerical model is then created to integrate the time-dependent equation until a steady state solution is reached. The model uses a 1 km horizontal resolution extending 300 km offshore along the Halifax Line, which covers the entire shelf and into the open ocean. Vertically, the model has a layer thickness of 6.5 m, and extends from the base of a constant 10 m mixed layer, chosen based on the approximated mixed layer depth along the Halifax Line during the 2010 AZMP sampling, down to 260 m. Shelf topography is obtained by interpolation of an ETOPO 1 x 1 bathymetry dataset. Assuming the activity is equal throughout the mixed layer, the activity at the upper model boundary therefore represents the activity in the surface waters, which allows for comparison with observations taken at 2 m depth. At the shoreward open boundary, a vertical profile of activity satisfying Eq. 4.1, is specified, with the exception of an elevated value in the uppermost cell to represent surface transport from the coast. The offshore boundary is considered to be open and every open water grid cell is initialized at zero. The bottom boundary (i.e. the sediments) is set to a constant activity of 4 dpm 100 L^{-1} which falls within the range of observed near-bottom Ra activities on the shelf (Figure 4.2c). At each time step, the model progresses using a Euler forward approximation, with ^{224}Ra carried away from the source cells at a rate calculated from K_X, K_Z and activity gradients. The model continues until the change in activity summed over all model cells is less than

0.01 dpm 100 L^{-1}, thus providing a steady-state solution. Optimal values of K_X, K_Z, and bottom activity are found using an Inverse Monte Carlo technique. Observations are compared to the steady-state solution of the model output at the appropriate grid points. The mean relative deviation (γ, the average percent difference) between observations (y_i) and model output ($\hat{y}_i$) is calculated using the equation:

$$\gamma = \frac{1}{n} \sum_i \frac{y_i - \hat{y}_i}{y_i}. \tag{4.3}$$

This error value is calculated for a wide range of parameters, providing a 2-dimensional grid of error values and optimal parameter values are obtained from the combination yielding the lowest γ for all runs.

4.5 Results

4.5.1 Ra Distribution

All transects aboard the Sigma T exhibited relatively high ^{224}Ra activities at the mouth of the Halifax Outer Harbour (McNabs Isle, Figure 2a), averaging 4.8 dpm 100 L^{-1} (Figure 4.2b). Similar activities were consistently observed further inshore within Bedford Basin, located at the head of Halifax Harbour (chapter 3). Moving offshore from McNabs Isle, activities dropped off abruptly and remain below 1.5 dpm 100 L^{-1} once on the Scotian shelf. A single daytrip to station HL2, located approximately 30 km offshore, in mid-October, 2010, yielded a surface activity of 0.6 dpm 100 L^{-1} (Figure 4.2b), and a near-bottom activity of 4.0 dpm 100 L^{-1} (Figures 4.2c and 4.4b). The activity near the sediments at HL2, as well as the surface activities measured during this daytrip, agree well with the observations from corresponding stations sampled during the 2010 and 2011 AZMP cruises (Figure 4.2b and c).

During the 2010 AZMP cruise, the distributions of ^{224}Ra across the Scotian Shelf revealed low Ra activities in the surface waters (Figure 4.3). For both transects, relatively elevated activities (1-2 dpm 100 L^{-1}) were seen near the coast in both surface and deep samples, with similar activities off the Halifax (Figure 4.3a and b) and Louisbourg coasts (Figure 4.3d and e). In both transects, surface water activities dropped below 1 dpm 100 L^{-1} within 20 km from shore. In almost every sample, however, activities remained above $\sim$0.3 dpm 100 L^{-1}, and considerable surface water activities

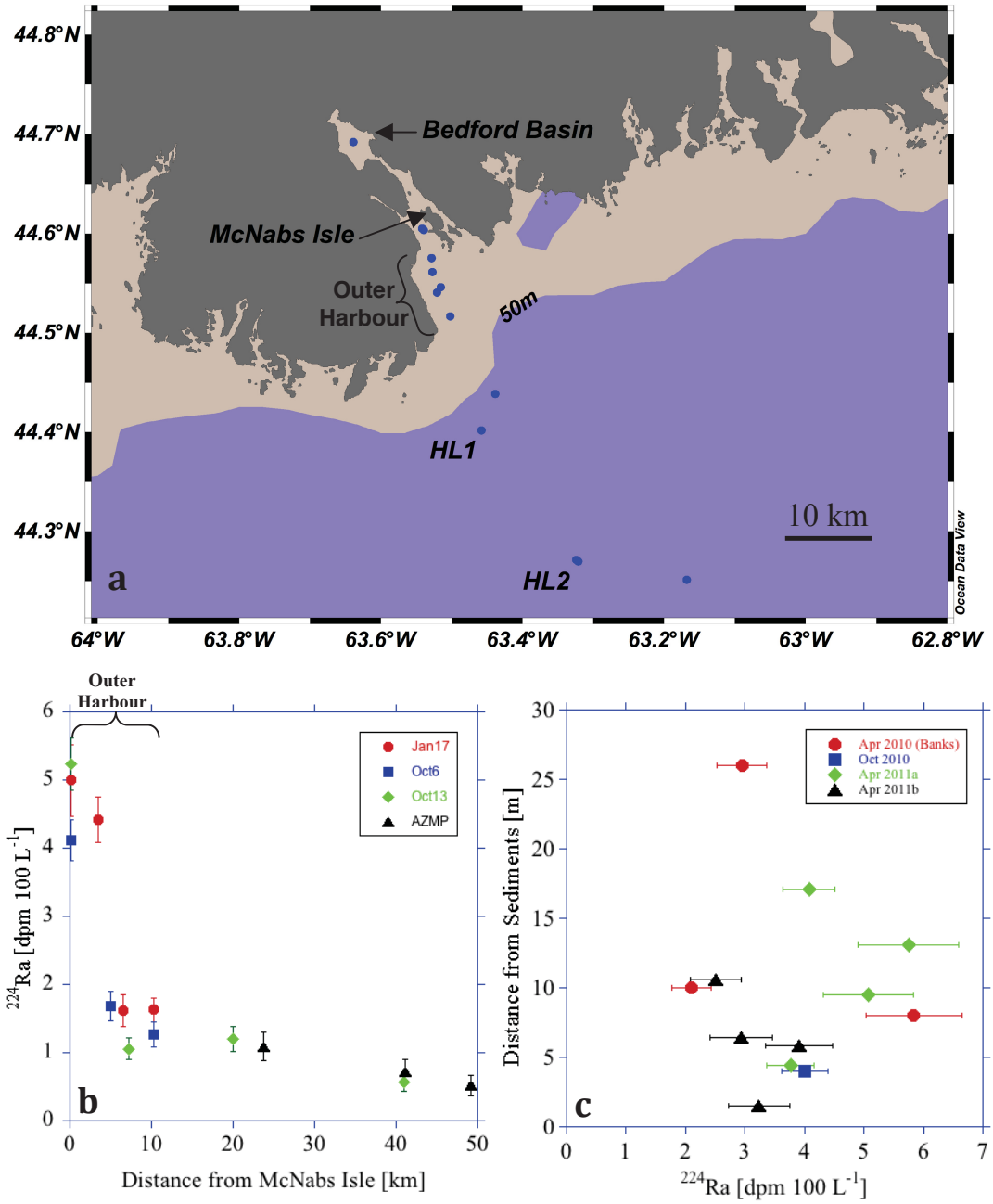

Figure 4.2: **(a)** Map of nearshore stations. **(b)** Offshore ^{224}Ra vs. distance plots showing three daytrip transects (Oct. 2010-Jan. 2011) compared to nearshore stations sampled during the 2010 AZMP cruise. The first ∼10km of the transect are within the Outer Harbour. **(c)** Vertical distribution of ^{224}Ra near the sediments in various regions of the Scotian Shelf. Figure redrawn from Burt et al. (2013b) with permission from Elsevier Science.

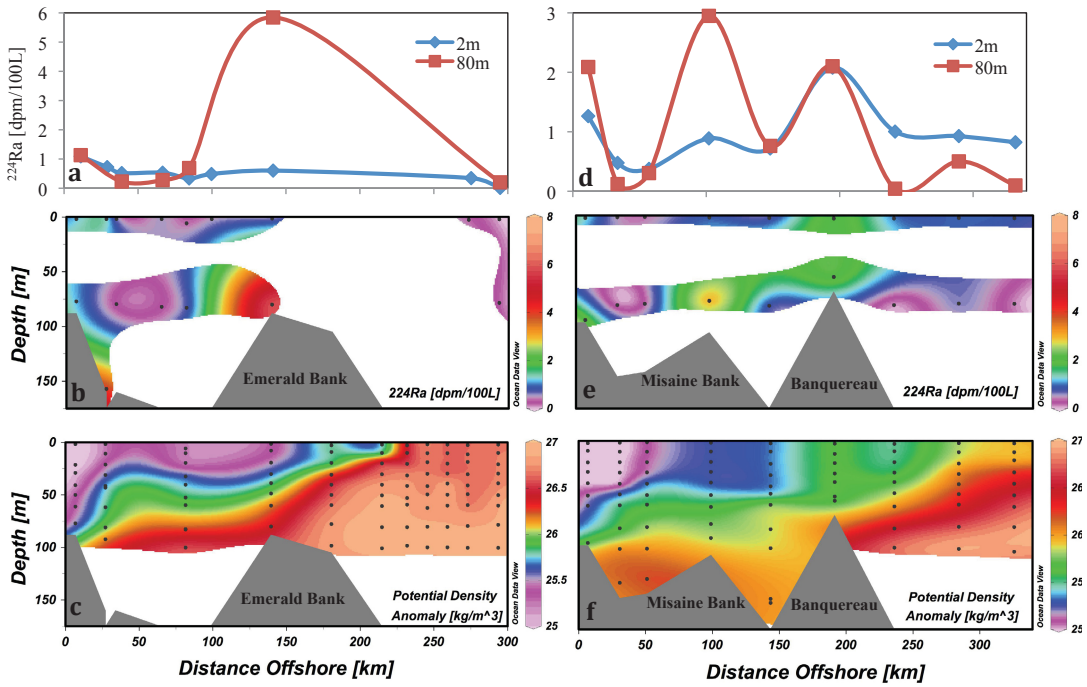

Figure 4.3: Surface and deep (80 m) transects of offshore ^{224}Ra for the Halifax Line **(a,b)** and Louisbourg Line **(d,e)**. Top plots **(a,d)** show ^{224}Ra activity vs. distance, middle plots **(b,e)** illustrate the affect of bottom topography, and bottom plots **(c,f)** indicate variations in mixed layer depths (MLD) across the shelf using potential density. In general, the MLD is deeper and more variable along the Louisbourg Line (panel **e**). The visual gaps are an attempt to restrict the graphical interpolation **(b,e)** to a sensible level given the spacing of station locations (black dots). Figure redrawn from Burt et al. (2013b) with permission from Elsevier Science.

(0.7-1.0 dpm 100 L^{-1}) were found beyond the shelf break on the Louisbourg Line (Figure 4.3d and e).

Unique features of the Ra distribution on the Scotian Shelf were observed further offshore. Along the Halifax Line (Figure 4.3a), surface ^{224}Ra is slightly higher above the Emerald Bank, approximately 140 km offshore. Similar surface enrichments along the Louisbourg Line (Figure 4.3d) occurred approximately 100 km offshore above the Misaine Bank and $\sim$200 km offshore above Banquereau. Samples at 80 m depth revealed similar trends to those at the surface. Activities were typically below 1 dpm 100 L^{-1}, except for those samples taken near the sediment surface, where the highest activities on the shelf were consistently observed.

Further radium sampling was conducted during the April 2011 AZMP cruise in an attempt to re-sample the elevated near-bottom Ra activities, and observe vertical gradients in both Ra and carbonate species near the sediments. Results showed elevated Ra activities in all samples, averaging 3.9 dpm 100 L^{-1} (Figure 4.2c, Apr 2011a and b), which agrees well with the single bottom sample taken aboard the Sigma T in October, 2010 (Figure 4.2c, October 2010). However, activities showed significant variability, ranging from 2.5-5.7 dpm 100 L^{-1}, and unlike in the Bedford Basin, clear vertical gradients away from the sediments were not observed.

4.6 Discussion

4.6.1 Evaluation of Background Ra Signals

The offshore ^{224}Ra distribution on the Scotian Shelf differs significantly from those measured in most continental shelf regions. Specifically, high activities are present above the shallow offshore banks, and detectable activities are measured at all locations across the shelf. Elevated ^{224}Ra at areas far offshore must result from either enhanced offshore transport (i.e. advection), the presence of another source to these locations (i.e. the bottom), or a background signal produced by analytical errors or shipboard contamination.

The potential for contamination of samples from ^{228}Th build-up on the ships intake system, inside Niskin bottles, and on the walls of sample storage tanks has been discussed in various studies (*Charette et al.*, 2007; *Moore*, 2007, 2008; *Stachelhaus et al.*, 2012), and was confirmed in a recent Ra intercalibration study (*Charette et al.*, 2012). The ships intake system flowed continuously throughout the cruise, so little ^{228}Th accumulation is

expected. Accumulation of ^{228}Th on shipboard equipment could lead to an increase in ^{228}Th activities during the cruise as more samples are collected (*Moore*, 2007). Average ^{228}Th activities of 0.6 and 0.7 dpm 100 L^{-1} were measured on the Louisbourg and Halifax lines respectively, which are in line with values reported from nearby studies off New Jersey (^{228}Th = 0.4-0.8 dpm 100 L^{-1}, *Kaufman et al.* (1981); *Stachelhaus et al.* (2012)), and no trends of increasing activity during the cruise is observed, suggesting no substantial addition from shipboard systems. Furthermore, detectable ^{224}Ra activities and similar ^{228}Th activities were observed for samples collected using both the ships intake and with Niskin bottles, and no consistent patterns could be seen that would indicate the contamination of either system relative to the other. While no samples were collected by both systems, identical ^{224}Ra activities were observed using both systems in the fully mixed waters above Banquereau bank (Figure 4.3). Finally, stations re-sampled the subsequent fall using the bilge pump system aboard the Sigma T showed activities within 0.2 dpm 100L^{-1} of those collected aboard the Hudson. While it cannot be ruled it out entirely, it is believed that the non-zero values seen here are not produced by shipboard contamination. Instead, a combination of mechanisms, such as strong surface layer mixing, high vertical turbulent mixing beneath the mixed layer, rapid along-shelf currents, as well as a component of onshore and offshore flow from both topographic features (*Loder et al.*, 1988; *Urrego-Blanco and Sheng*, 2014) and an estuarine-type circulation (*Shadwick et al.*, 2010) could bring waters recently in contact with sediments into regions where sampling took place.

4.6.2 Vertical Radium Distributions: Seafloor Ra Additions

Data from the Scotian Shelf clearly indicate that, at various distances offshore, the release of Ra from the sediments atop shallow banks (Figure 4.3a and d), and at the greater depths of station HL2 (Figure 4.2c), adds considerable ^{224}Ra to the water column. This benthic addition is most clear above offshore banks, where the background ^{224}Ra signal in both surface and deep waters is usually very low. Samples taken above the 3 banks all show high activities near the sediments, which translate into elevated surface Ra activities (Figure 4.3). For all three banks, the varying magnitude of the observed surface enrichments correspond well to variations in mixed layer depth (Figure 4.3), which implies that the vertical diffusive mixing rate and near-bottom activities are similar above each bank.

Vertical mixing coefficients have previously been calculated by applying the 1-D diffusive model to vertical profiles of Ra isotopes (see chapter 3, or *Charette et al.* (2007)).

Observations from station HL2 (Figure 4.2c), at approximately 150 m depth, suggest that substantial vertical mixing is observed far below the mixed layer. This is inferred in the two vertical profiles, which have no clear gradients in ^{224}Ra activity with increasing distance off the bottom, suggesting that waters with high activity can be transported well into the intermediate water column before substantial decay occurs. Previous studies using current measurements from moored instruments have reported vertical eddy diffusivities (K_Z) ranging from 6-600 cm^2 s^{-1} above shallow banks in the Scotian Shelf region due in large part to the small-scale circulation patterns commonly found above these topographic features (*Loder et al.*, 1988). In this study, with only two data points above each bank, and a lack of any discernable gradients in deeper vertical profiles, quantifying vertical turbulent diffusivities from the Ra observations alone is difficult. As a result, these observational results are used quantitatively in the Inverse Monte Carlo simulation, and also provide interesting qualitative results that may lead to future studies in the region.

4.6.3 Horizontal Dispersion of the Outer-Shelf Ra Signal

The Ra signal produced by offshore banks may also affect the horizontal distribution of Ra on the outer shelf and off the shelf break. For example, Ra activities observed in deep ocean stations of the Louisbourg Line are considerably above the detection limit (Figure 4.3). *Kadko and Muench* (2005) reported ^{224}Ra activities as far as 200 km from the shelf in the western Arctic. These authors describe shelf-break currents and other mesoscale processes that may contribute to this relatively rapid offshore transport. On the Scotian Shelf, anticyclonic gyres are persistent features above both Banquereau and Emerald Bank, creating along shore transport at the inshore and offshore bank edges, as well as cross shelf transport along the side of banks (*Hannah et al.*, 2001). Offshore advection has been previously observed on the eastern side of Banquereau (*Han and Loder*, 2003), which could carry high Ra surface waters above Banquereau into adjacent shelf break waters. At the shelf break, the intersection with the Labrador Current (LC) and the associated shelf/slope front (*Han and Loder*, 2003) may inhibit cross-shelf mixing, as was seen in the Mid-Shelf Front of the MAB (*Stachelhaus et al.*, 2012). However, a slight offshore component of the LC, which reaches alongshore current speeds of 55 cm s^{-1} in spring, would provide the transport necessary to observe ^{224}Ra at the outer limits of the Louisbourg transect, as observed here. Similar to statements made by *Kadko and Muench* (2005), it is suggested here that further Ra studies in the shelf-slope region may be useful

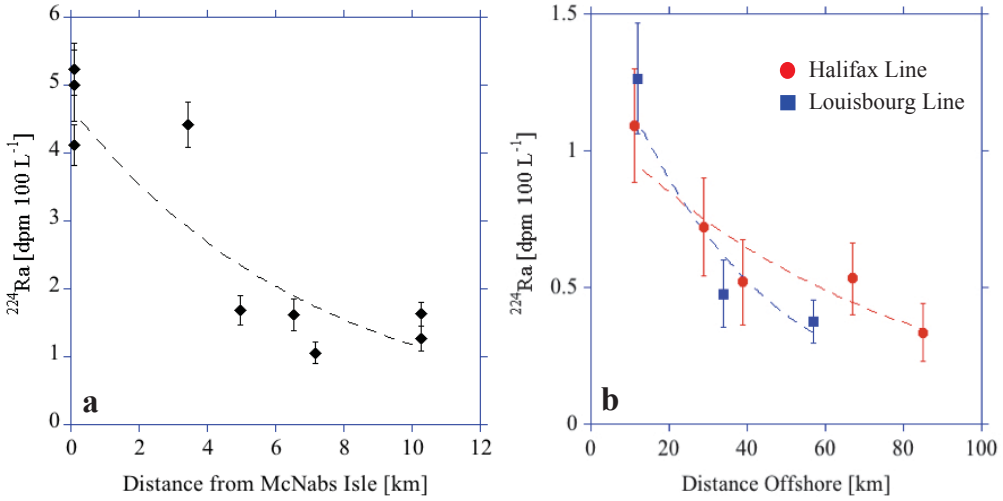

Figure 4.4: Offshore transects from within the Outer Harbour **(a)**, and on the Scotian Shelf **(b)**, showing the best fit curves for the 1-D analytical model (dashed lines). Note, the Louisbourg Line fit is shown for comparative purposes only. Figure redrawn from Burt et al. (2013b) with permission from Elsevier Science.

in quantifying offshore mass-transport of water into the open ocean, a key transport term in coastal carbon and nutrient budgets.

4.6.4 Horizontal Mixing Coefficients: 1-D Diffusion Model

In general, the ^{224}Ra activities observed near the Nova Scotia coast are considerably lower than those found in other coastal regions, including the MAB (*Moore*, 2000; *Stachelhaus et al.*, 2012) located downstream of the Scotian Shelf, as well as the Gulf of Mexico (*Moore*, 2003), and Great Barrier Reef (*Hancock et al.*, 2006). The geomorphology of Nova Scotias Atlantic coast is dominantly granitoid bedrock with localized thin layers of glacial till and, in general, very little sediment cover (*Fader and Miller*, 2008). As a result, these areas tend to produce very little groundwater percolation compared to other regions. The coast is also characterized by relatively little river input, which may also contribute to the small coastal signal. Inshore of the formal Halifax Line stations, within the semi-enclosed Outer Harbour, short ^{224}Ra transects off McNabs Isle show relatively sharp decreases in activity away from shore (Figure 4.4a). Fitting this pattern to an exponential decrease with the 1-D horizontal diffusion model yields a horizontal diffusivity (K_X) of 102 ± 47 m^2 s^{-1}, which is comparable to values obtained from other coastal studies using this model (*Moore*, 2000, 2003; *Colbert and Hammond*, 2007; *Stachelhaus et al.*, 2012). This particular result could be used in future studies to quantify the fluxes of carbon, nutrients, or pollutants (i.e.

sewage, metals, etc.) from the densely populated Halifax area through the harbour and into the open Scotian Shelf.

With clear bottom-generated signals present above offshore banks, horizontal mixing coefficients were only calculated along inner regions of the Halifax and Louisbourg transects (<100 km from shore). Applying the model to surface data from the Halifax Line produces a mixing coefficient of 10149 $\pm$ 7124 m^2 s^{-1} (Figure 4.4b). This value is orders of magnitude higher than previous studies, with the exception of those calculated in the Drake Passage of the Southern Ocean (*Dulaiova et al.*, 2009). Although the steeper offshore gradient along the Louisbourg Line suggests a smaller mixing coefficient, it is not reported due to a lack of available data points, as shown in Figure 4.4b. Compared to the Scotian Shelf, the Outer Harbour is a considerably more sheltered body of water, largely unaffected by the strong alongshore currents, upwelling systems, and the formation of eddies, which are common on the inner shelf, and may explain the large difference in calculated coefficients between these two adjacent regions. Thus, a single value of K_X should not be used across the Outer Harbour and inner shelf, due to different mixing regimes between the regions. The extremely large K_X and uncertainty for the open shelf are likely due to a number of complex processes, including additions from bottom sediments and offshore advection, both of which are assumed negligible for the model. In an effort to better constrain mixing coefficients on the shelf, a numerical model is employed, which takes into account two distinct Ra sources, as well as mixing in two dimensions.

4.6.5 Optimized Coefficients using a 2-D Diffusion Model

In order to better represent the effects of benthic Ra additions and the mixing conditions on the Halifax Line, Ra distributions are reproduced using a 2-D diffusion model. Due to large offshore variations in mixed layer depths during the Louisbourg Line sampling (Figure 4.3f), the model, which represents a constant mixed layer, is only applied over the Halifax Line. The results of the model are shown in Figure 4.5. The Inverse Monte Carlo technique provided optimized K_X and K_Z values of 700 m^2 s^{-1} and 26 cm^2 s^{-1}, respectively, resulting in a Halifax Line cross-section (Figure 4.5a) that recreates many features of the observed data (Figure 4.3b). The K_X value is slightly higher than those calculated using the 1-D diffusion model in other coastal regions (*Moore*, 2000; *Hancock et al.*, 2006), likely due to additional cross-shelf advective forces caused by topographic steering of the strong along-shelf currents. The K_Z value falls within the range of published

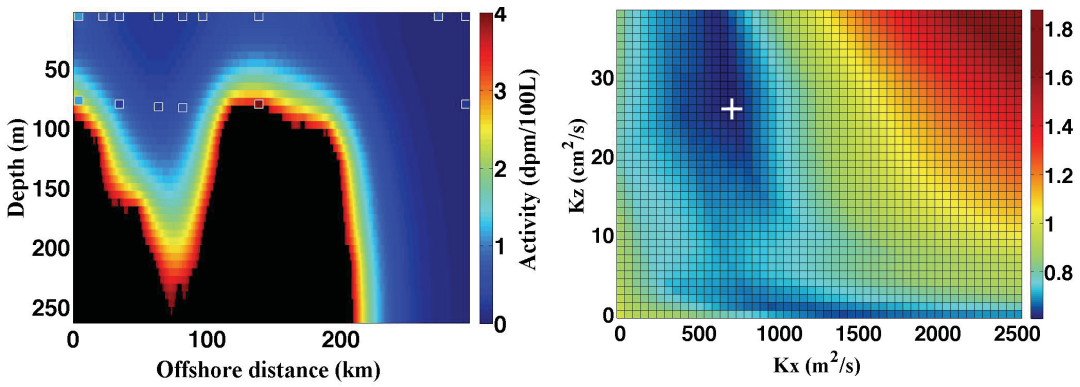

Figure 4.5: **Left:** Steady-state solution of the 2-D diffusion model along the Halifax Line. Black areas represent the ocean floor. Observations (small boxes) are placed over the image. The continuous addition of Ra from the seafloor is shown to affect water column activities from more than one direction (most clearly visible in areas of changing topography). **Right:** Visual representation of the Inverse Monte Carlo technique. Each cell in the diagram represents a model run with a distinct set of mixing parameters. This image shows all results for a bottom activity of 4 dpm 100 L^{-1}, with the minimum γ (z-axis, mean relative deviation, 1 = 100 % deviation) located at K_X = 700 m^2 s^{-1} and K_Z = 26 cm^2 s^{-1} (white cross). Figure redrawn from Burt et al. (2013b) with permission from Elsevier Science.

coefficients from the Scotian Shelf (*Loder et al.*, 1988) and the coastal UK (*Riddle and Lewis*, 2000), and compares well to estimates made by applying a vertical 1-D model to observations above each offshore bank (with knowledge of the mixed layer depth). Overall, this method combines observational and modeling approaches to provide estimates of horizontal and vertical mixing coefficients which include Ra additions from both the coast and the seafloor, and reassures the assumption regarding a steady-state system. Assuming that these coefficients are also applicable to intermediate waters of the Louisbourg line, they can then be used to yield fluxes of carbon and nutrients on the shelf.

4.6.6 Estimates of Carbon and Nutrient Transport

A recent study of the Scotian Shelf carbon system concluded that unlike the vast majority of coastal shelf systems, the Scotian Shelf is a net outgasser of CO_2 to the atmosphere (*Shadwick et al.*, 2010), which conflicts with the conceptual understanding of oceanic CO_2 uptake and storage in coastal seas (*Chen and Borges*, 2009), and the general trends of global climatology models (*Takahashi et al.*, 2009). The Scotian Shelf observations were explained by describing the cross-shelf dynamics of the shelf as an estuarine-type system, where, at depth, high offshore concentrations of CO_2 and nutrients are transported

onshore, where they are upwelled to the surface, increasing the partial pressure of CO_2 (pCO_2) in surface water and causing CO_2 outgassing (*Shadwick et al.*, 2010). This study lends support to this concept by identifying and quantifying the diffusive component of onshore DIC, AT, and nutrient transport using clear onshore gradients of these properties in intermediate waters of the mid-shelf basins across both Scotian Shelf transects (Figure 4.6).

If this type of transport is dominant (i.e. onshore cross-shelf transport at 80 m, Figure 4.6), the primary source of Ra to mid-shelf basin waters will be lateral transport off the offshore banks. This can be observed when examining the Ra data at depth along both transects (Figure 4.6b and f). For the Halifax Line, the 1-D analytical model would produce a K_X of 1549 ± 630 m^2 s^{-1}, considerably higher than the model-derived value (700 m^2 s^{-1}). This nicely exemplifies the importance of considering bottom topography and 2-D mixing, and thus the utility of the 2-D model. When including a second vertical source, as well as the physical extension of the bank itself (Figure 4.5a), less lateral mixing would be required to transport the signal onshore. Similarly, in the 2-D model, the vertical diffusion of a benthic source lowers the required horizontal mixing in the offshore surface transects by as much as an order of magnitude.

Applying the model-derived K_X value to the horizontal onshore gradients of DIC, AT and NO_3^- yields fluxes of each constituent (see Table 4.1). These values (mol m^{-2} y^{-1}) describe onshore horizontal fluxes which are considered to be constant throughout the intermediate water column, or between the plateau of Emerald and Misaine banks and the average mixed layer depth. Taking the ratio of the onshore DIC and AT gradients for the Halifax and Louisbourg transects yielded values of 1.26 and 1.59 respectively (Table 4.1). On the Scotian shelf, DIC:AT ratios are typically $\sim$0.9-1.0 (*Shadwick et al.*, 2011), meaning that these fluxes bring waters with excess DIC relative to AT, onshore. If these waters are brought to the surface via coastal upwelling or deep vertical mixing, this excess DIC will be outgassed to the atmosphere, fuelling the CO_2 release previously observed on the Scotian Shelf. Similarly, once brought to the surface, primary producers will take up DIC and NO_3^- in ratios similar to the Redfield Ratio (C:N = 106/16 or 6.6). The observed DIC:NO_3^- gradient ratios for the two transects were 21.4 and 7.8 respectively, indicating that uptake of DIC and NO_3^- by photosynthesizing organisms in Redfieldian stoichiometry would result in surplus DIC in the surface layer. These ratios both suggest that excess DIC

is brought onto the shelf from the deep ocean, fuelling the surface DIC supersaturation, and release into the atmosphere. Despite the fact that these ratio and flux terms are subject to considerable uncertainty, they still provide a quantitative estimate of cross-shelf carbon and nutrient transports as required to understand and balance the mechanisms controlling the CO_2 system on the Scotian Shelf.

In an attempt to further understand the role of the onshore transport of DIC in governing the CO_2 release from the Scotian Shelf and its surface water pH conditions, the onshore transport of excess DIC (DIC_{ex}) and excess protons (H^+_{ex}), relative to equilibrated surface water conditions, is computed. A surface water pCO_2 of 400 μatm is used as an equilibrium value with the atmosphere, and the DIC_{ex} and H^+_{ex} is computed for the deep water samples (Figure 4.6a) as the difference between the observed DIC and H^+ values and those occurring under the same alkalinity, T and S conditions, but with pCO_2 values of 400 μatm:

$$DIC_{ex} = DIC_{obs} - DIC_{pCO2=400} \tag{4.4}$$

$$H^+_{ex} = H^+_{obs} - H^+_{pCO2=400} \tag{4.5}$$

The corresponding gradients and fluxes of DIC_{ex} and H^+_{ex} are listed in Table 4.1. Both quantities affect the surface water conditions such that surface water pCO_2 and pH conditions, prevailing in equilibrium conditions with the atmosphere (i.e., presently at pCO_2 = 400 μatm), would be perturbed by upwelled waters from the deeper layers of the shelf. At present times any upwelled quantity of these waters would lower the pH and raise the pCO_2, depending on the amount of water brought into the surface. In dependence of the ventilation history (i.e., age) of such upwelled waters, two scenarios would be possible under future higher atmospheric CO_2 conditions. 1: Assuming a fairly short ventilation history, and thus a young age of the waters, the DIC_{ex} and H^+_{ex} conditions appear primarily controlled by respiratory processes, and the build-up of DIC_{ex} and H^+_{ex} would be more or less an addition to the equilibrated DIC and pH conditions. Upwelling would continue to supply DIC for outgassing and to lower the pH. 2: If, on the other hand the upwelled waters revealed a longer ventilation history, thus were ventilated under lower atmospheric CO_2 conditions, it would also be possible that the surface equilibrium conditions would set higher DIC and H^+ conditions than the upwelled waters would reveal, which eventually

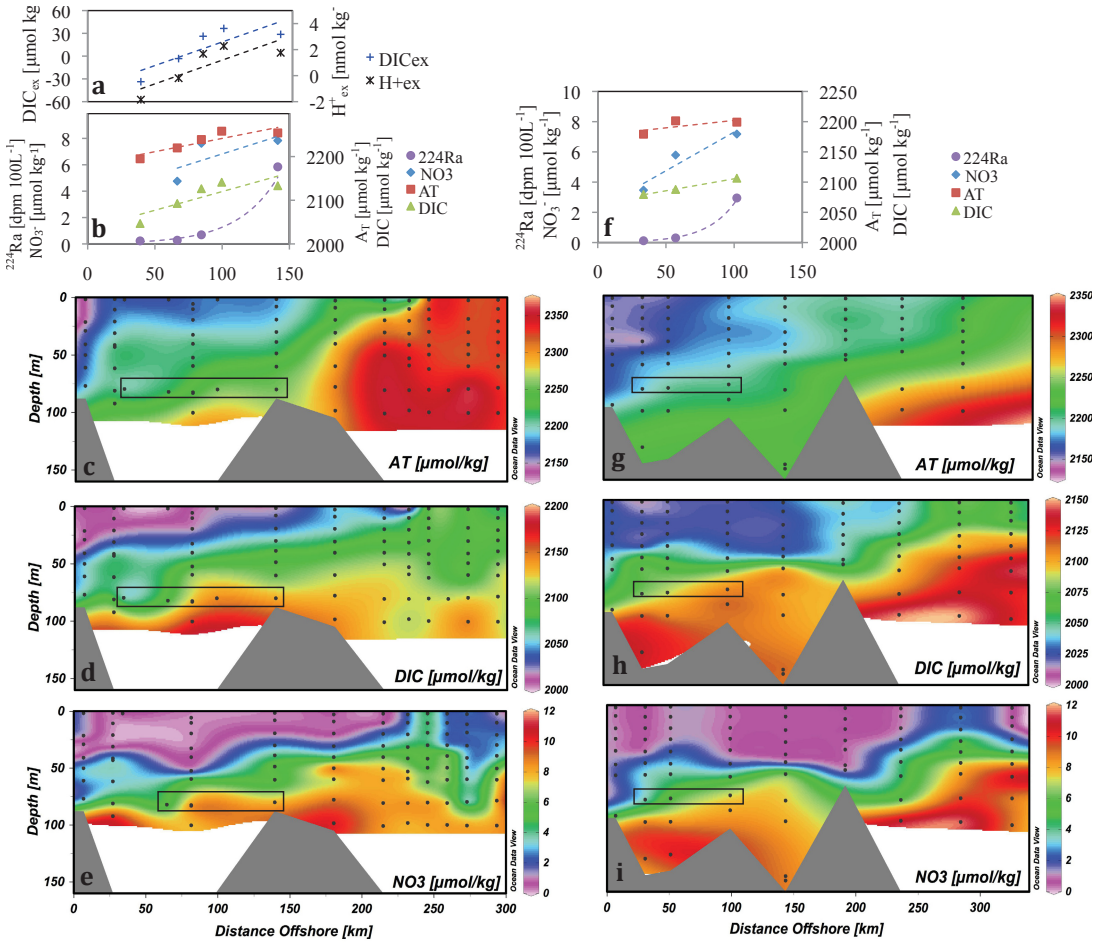

Figure 4.6: Chemical gradients (from least-squares regressions) at 80 m depth horizon across the Halifax **(a,b)** and Louisbourg **(f)** lines (see Table 4.1). Distributions of AT, DIC and NO_3^- for the Halifax Line are shown in the left panels **(c,d,e)**, with Louisbourg Line distributions in right panels **(g,h,i)**. Black dots represent sampling sites. Black boxes represent the samples used for onshore flux calculations. Figure redrawn from Burt et al. (2013b) with permission from Elsevier Science.

Table 4.1: Onshore chemical fluxes in intermediate waters along Halifax Line (a) and Louisbourg Line (b). Table redrawn from Burt et al. (2013b) with permission from Elsevier Science.

	Gradient (d/dx) μmol m^{-3} per m	K_X m^2 s^{-1}	Flux (Q) μmol m^{-2} s^{-1}	Flux (Q) x 10^4 mol m^{-2} y^{-1}
(a) Halifax Line				
AT	0.539	700	377	1.19
DIC	0.681	700	477	1.50
NO_3^-	0.033	700	23.1	0.07
DIC_{ex}	0.647	700	453	1.43
H_{ex}^+	0.380 x 10^{-4}	700	0.027	0.85 x 10^{-4}
Gradient Ratio DIC/AT	1.26			
Gradient Ratio DIC/NO_3^-	21.4			
(b) Louisbourg Line				
AT	0.262	700	183	0.577
DIC	0.415	700	291	0.918
NO_3^-	0.053	700	37.1	0.117
Gradient Ratio DIC/AT	1.59			
Gradient Ratio DIC/NO_3^-	7.8			

would cause the upwelled waters to lower the pCO_2 and to raise the pH. Based on one year of observations it is currently not possible to establish which of these two scenarios applies to the Scotian Shelf. Continued time series observations will help resolve this question.

Results shown here provide approximations of fluxes which have not been previously reported on the Scotian Shelf. The estimates of cross-shelf fluxes can advise models about the magnitude of cross shelf transport, an area of uncertainty in current shelf carbon and nitrogen studies (*Shadwick et al.*, 2011; *Fennel*, 2010; *Shadwick and Thomas*, 2014). Enhanced spatial coverage in future studies along these deep transects could help further constrain these onshore fluxes for further modeling and budget applications. Similarly, by differentiating the various sources supplying the surface layer with Ra, fluxes directed offshore at the surface could be evaluated. Finally, sampling across the shelf-slope front may provide information about fluxes into the deep ocean. These types of fluxes could become important in balancing carbon and nitrogen shelf budgets and, in general, help unravel the uncertainties surrounding the carbon and nutrient cycling on the Scotian Shelf.

4.7 Conclusions

To date, the use of Ra isotopes to study coastal mixing processes in Canadian waters is very limited, with this study representing the first published Ra dataset from the Scotian Shelf region. The Ra distribution on the Scotian Shelf exhibits features which have not been observed in other shelf regions. Offshore banks, which add Ra to the outer shelf waters, affect the horizontal and vertical mixing regimes across the shelf. The shallow banks cover a considerable area across the shelf (Figure 4.1), with Banquereau alone covering an area over 10000 km^2. Assuming sedimentary Ra release is homogenous across these regions, the benthic Ra signals constitute very large additions of Ra to the intermediate and surface waters of the Scotian Shelf. Previous studies have linked benthic Ra signals to fluxes of AT, DIC, nutrients and metals into the overlying water column (see chapter 3, or *Moore et al.* (2011)). In this case, any discernible fluxes of carbon, nutrients or metals from the bank sediments would represent significant additions to their chemical budgets on the shelf, providing motivation towards future Ra studies of the bank areas. Specifically, in order to make further quantitative analyses, higher resolution water column sampling teamed with additional pore water sampling from sediment cores are necessary. This more complete sampling strategy would provide information regarding sediment end-member activities, the mechanism of benthic Ra release, as well as vertical mixing rates.

While limitations exist when computing mixing coefficients using the analytical 1-D model in the uneven shelf environment, a numerical 2-D approach can yield coefficients with multiple Ra sources and provide a steady-state solution. Mixing coefficients obtained using Ra observations can be applied to onshore gradients of CO_2, nutrients or other dissolved substances, to obtain cross-shelf flux estimates, which could help gain understanding about important biogeochemical processes on the Scotian Shelf. Finally, computation of excess DIC and H^+ in intermediate waters provide insight into how these onshore fluxes may affect the surface water pCO_2 and pH both at present and under future climate scenarios. Turbulent diffusion may vary regionally, nevertheless, the approach developed here can guide investigations in other regions.

4.8 Acknowledgements

Many thanks to M. Fraser, R. Moore, CA. Black, E. Horne., J. Spry and K. Pauley for their help collecting all of the 200 L samples, the captain and crew of the CCGS Husdon as well as Rick and Chuck aboard the CCGS Sigma T for their cooperation with field work, and the organizers of the Atlantic Zone Monitoring Program (AZMP) for providing ship time on the shelf. Also, many thanks to S. Colbert, M. Rutgers Van-der Loeff, M. Charette, P. Van-Beek, M. Souhaut and WS. Moore for their assistance with Ra processing techniques. Helmuth Thomas holds a Canada Research Chair.

CHAPTER 5

SEDIMENT-WATER COLUMN EXCHANGE IN THE NORTH SEA

5.1 Abstract

Sediment-water column exchange plays an important role in coastal biogeochemistry. Here, sediment-water column exchange of short-lived radium isotopes (^{224}Ra and ^{223}Ra) is quantified using a variety of methods, and results are used to understand the dominant physical processes and sediment characteristics which govern this exchange. The comprehensive survey, conducted in September 2011, represents the first of its kind conducted in the North Sea. Two main sources are found to regulate surface Ra distributions: minor coastal input from rivers and shallow mudflats, and North Sea sediments as the dominant source. Pore waters show 100-fold larger activities than the water column. North Sea sediment characteristics such as porosity and mean grain size, as well as turbulence at the sediment-water interface, are the dominant factors contributing to variability of Ra efflux. Ra inventory and mass-balance approaches consistently yield high benthic Ra effluxes in the southern North Sea, driven by strong tidal and wind mixing, which in turn cause high sediment irrigation rates. These results exceed incubation-based Ra flux estimates, and the majority of previously reported Ra flux estimates for other regions. Ra-based estimates of benthic alkalinity fluxes compare well to observed values and the high rates of Ra efflux imply a potentially significant exchange of other products of sedimentary reactions, including carbon and nutrient species. Passive tracer simulations lend strong support to the Ra source attribution and imply seasonal variation in the surface water Ra

distribution depending on stratification conditions.[1]

5.2 Introduction

The cycling of material between the water column and the underlying sediments can play an important role in biogeochemical cycles. This is especially true in coastal and shelf sea regions like the North Sea, where high sedimentation rates generate intense chemical cycling within the sediments. As seawater enters and flows through permeable sediments, it becomes chemically enriched in the products of numerous diagenetic reactions. The sediment pore waters, rich in carbon, nutrients and metals, are then transported through the sediment-water interface by a variety of transport mechanisms.

Diffusion and bioturbation are important processes in fine-grained cohesive sediments. However, exchange in more permeable sandy sediment, which is the predominant sediment type both in the North Sea, and globally in shelf seas, is often dominated by advective flows (*Aller*, 1980; *Janssen et al.*, 2005a). Advective transport, termed here as sediment irrigation, is driven mainly by pressure gradients as boundary currents or gravity waves flow over sediment topography (*Precht and Huettel*, 2003). In subtidal regions, sediment irrigation can also occur via tidal flooding or groundwater pumping (*Rusch and Huettel*, 2000).

Strong tidal and wind induced mixing of relatively shallow waters can bring sediments into contact with surface waters, allowing direct and rapid exchanges between the sedimentary, marine and atmospheric reservoirs. An important consequence of this is that sediment-water exchange of recycled nutrients also plays a significant role in nutrient and carbon cycling of the North Sea (*Luff and Moll*, 2004). In general, burial of organic material is considered negligible throughout the majority of the North Sea (*de Haas et al.*, 2002; *Pätsch and Kühn*, 2008) meaning that the estimated 17-45 % of North Sea primary production that is degraded within sediments (*Van Duyl and Kop*, 1994) is almost entirely released back into the water column. In this type of coupled system, sedimentary reactions such as denitrification and sulphate reduction can lead to the release of excess alkalinity from sediments, which has an effect on the buffering capacity of coastal surface waters

[1] Aside from minor alterations to the wording, this chapter consists of a manuscript by W. J. Burt, H. Thomas, J. Pätsch, A. M. Omar, C. Schrum, U. Daewel, H. Brenner, and H. J. W. de Baar entitled *Radium Isotopes as a Tracer of Sediment-Water Column Exchange in the North Sea* published in Global Biogeochemical Cycles in 2014.

(*Thomas et al.*, 2009). This leads to an alteration in the ability of surface waters to take up atmospheric CO_2.

Marine sediments are also enriched in thorium (Th), which is strongly adsorbed to particle surfaces and is thus scavenged rapidly from the water column and builds up in sediments. Alpha decay of Th continuously generates radium (Ra) isotopes that, due to their lower affinity to particles, build-up in the pore waters. Once transported through the sediment-water interface, Ra is dispersed away from its source and its activity decreases due to decay. In coastal systems, dissolved Ra enters both laterally across the land-ocean boundary (i.e. from the subterranean estuary or from rivers), and vertically across the sediment-water column boundary. Knowledge of the distinct source regions along with relatively simple behavior, make Ra isotopes powerful tracers for quantifying rates of sediment-water column exchange. Another benefit of the Ra suite of tracers is their largely varying half-lives (3.7 days to 1600 years), which allow for interpretation of processes that occur over multiple spatial and temporal scales. For example, at regions far offshore ($>$100 km), the coastal signal of the shorter-lived Ra species, ^{224}Ra ($t_{1/2}$ = 3.7 d) and ^{223}Ra ($t_{1/2}$ = 11.4 d), is likely negligible, meaning any detectable activities must come from relatively recent interaction with bottom sediments (e.g. see chapter 4).

Although the North Sea is one of the world's most heavily studied coastal regions, many uncertainties still exist regarding the effects of different boundary exchanges on the biogeochemistry of the system. For example, recent studies have shown that the combination of sediment-water column exchange within the shallow mudflats of the adjacent Wadden Sea, and subsequent lateral (i.e. land-ocean) exchange through tidal channels are an important source of dissolved nutrients, trace metals and alkalinity to the North Sea (*Thomas et al.*, 2009; *Moore et al.*, 2011; *Winde et al.*, 2014), and directly influence atmospheric CO_2 fluxes (*Omar et al.*, 2010). Numerous studies have closely examined aspects of sediment-water column exchange in the Wadden Sea (e.g. *Beck et al.* (2008); *Moore et al.* (2011)), yet direct observations of this exchange in the open North Sea are lacking. Prior studies are limited to estimates of diffusive nutrient fluxes in different regions of the southern North Sea using pore water profiles and sediment incubations (*Rutgers Van Der Loeff*, 1980; *Raaphorst et al.*, 1990; *Van Raaphorst et al.*, 1992). Current numerical modeling studies in the North Sea have concluded that better representation of these exchanges are needed to improve the modeled biogeochemical cycling in the coastal

regions (*Daewel and Schrum*, 2013), and adding complexity to sediment modules remains critical to better representing the North Sea biogeochemistry as a whole.

To date, Ra studies in the North Sea region have been very limited. *Shaw* (2003) first discussed the potential utility of Ra isotopes in quantifying the transport of chemically enriched waters from the Wadden Sea into the North Sea. *Schmidt et al.* (2011) provided the first published Ra measurements in the German Bight of the North Sea, as well as insight and motivation towards future Ra studies. Finally, an extensive study by *Moore et al.* (2011) created a Ra mass balance to successfully quantify the discharge of chemically enriched pore waters into the Wadden Sea as well as the release of Ra and other dissolved substances into the North Sea.

In this paper, rates of sediment-water column exchange in the North Sea are examined. We employ results from a basin-wide Ra isotope survey of the North Sea, conducted in the summer of 2011. Water column distributions are used to identify key Ra sources to the North Sea, and benthic Ra fluxes are quantified using a variety of independent approaches, including laboratory sediment incubations. The important mechanisms of sediment-water column exchange in the North Sea are identified, as are the dominant controls on the observed Ra fluxes. Estimates of pore water Ra activity facilitate the quantification of the volume of water exchanged through the sediment-water interface, which can then be used to estimate benthic alkalinity fluxes. Finally, the use of a 3D hydrodynamic model allows us to simulate the distributions of Ra as a passive tracer, which provides insight into Ra source attribution and seasonal variations of Ra distributions in the North Sea. Overall, the results presented highlight the utility of Ra isotopes for use as a tracer of sediment-water column exchange in coastal systems.

5.3 Study Area

The North Sea (Figure 5.1), located on the NW European shelf, can be separated into two distinct regions: The shallower (<50 m depth) southern North Sea (SNS) is strongly influenced by tidal and wind-induced mixing with part of it well-mixed throughout the year. The deeper northern North Sea (NNS) is seasonally stratified (*Lee*, 1980). For this study, the border between these two regions can be drawn almost flawlessly using the 50 m depth contour (Figure 5.1, black dashed line).

Exchange with the North Atlantic Ocean at the open northern boundary dominates the

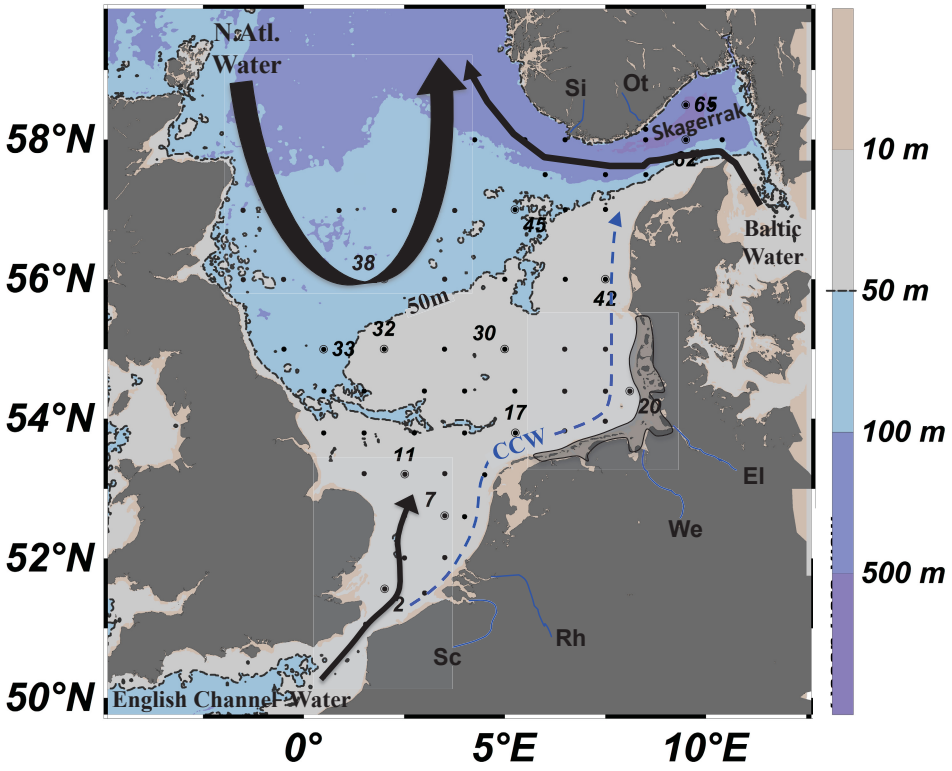

Figure 5.1: Map of North Sea with stations sampled for Ra during the 2011 cruise (black dots). Stations with any additional Ra sampling (deep profile, incubation or pore water) are labeled with the station number. The 50 m contour (dashed line) roughly traces the border between well-mixed stations to the south, and stratified stations to the north during the time of observations. The Wadden Sea is outlined in the black shaded box and the general circulation paths of the major water masses and continental coastal waters (CCW) are shown. Relevant rivers are also labeled: Sc = Scheldt, Rh = Rhine, We = Weser, El = Elbe, Ot = Otra, Si = Sira. Figure redrawn from Burt et al. (2014) with permission from John Wiley and Sons.

volume transport. The general circulation pattern is a cyclonic flow with inflow through the Shetland Channel and Faire Island Channel on the western side of the open boundary, and outflow through the Norwegian trench along the eastern side (*Lee*, 1980). The large majority of this North Atlantic input is steered along the topographic boundary separating the northern and southern regions, and therefore only a small fraction reaches the shallow southern North Sea. A smaller input of North Atlantic water enters the southern regions via the English Channel.

The main freshwater sources are the major rivers of the European continent, that discharge along the southern and southeastern coast of the North Sea and join the relatively fresh continental coastal watermass (CCW) (*Lee*, 1980). The CCW flows northeasterly along the coast and is also fed by an outflow from the Wadden Sea, which extends for over 500 km along the Dutch, German and Danish coasts (Figure 5.1). The Wadden Sea, spanning approximately 5000 km^2, consists of sandy and muddy tidal flats, most of which are exposed at low tide. Small rivers, controlled freshwater release from sluices (siels or small lockable waterways), as well as fresh and brackish submarine groundwater discharge (SGD) all enter the Wadden Sea before being flushed through a series of tidal channels into the southeastern bight (SEB) region of the North Sea (Figure 5.2). The flushing time for these waters is estimated at about 4 days (*Moore et al.*, 2011). Over a tidal cycle, organic material from the North Sea is imported into the Wadden Sea as the tide rises, with subsequent export of remineralized inorganic substances back into the North Sea during the falling tide. Whereas the contribution of freshwater from the Wadden Sea is relatively minor, this tidal exchange of dissolved and particulate materials is an important process in the biogeochemistry of the North Sea (*Thomas et al.*, 2009; *Moore et al.*, 2011). Low salinity Baltic Sea water also enters the North Sea from the east via the Skagerrak (Figure 5.1).

The majority of North Sea sediments are permeable sands, with finer-grained and muddy sediments limited to small patches and to deeper regions of the Skagerrak and Norwegian trench (*Wiesner et al.*, 1990; *Slomp et al.*, 1997). In most regions, resuspension and remineralization during fall and winter months results in negligible annual sediment accumulation. Accumulation can occur near river mouths in the German Bight in the postglacial Elbe river valley and in the Norwegian trench area. These regions are also characterized by higher organic carbon content compared to the rest of the North Sea

(*Wiesner et al.*, 1990; *Slomp et al.*, 1997).

5.4 Methods

5.4.1 Sample Collection and Analysis

All data were obtained during a 3-week cruise in September, 2011, aboard the R/V Pelagia. The cruise followed an approximate 1° x 1° sampling grid of the entire North Sea covering 88 total stations (Figure 5.1, for further details of typical North Sea sampling procedure, see *Bozec et al.* (2006)). Conductivity, temperature and pressure (CTD) profiles with accompanying rosette water sampling were done at every station. At 19 of these stations additional samples were collected using multiple deployments of zooplankton nets and a boxcorer.

Ra isotope samples were collected from surface waters (at 5 m depth) at 61 stations. At 13 of these stations, 2-3 additional samples were taken near the sediment surface in 3-5 meter vertical intervals in an attempt to capture chemical gradients near the sediment surface. In total, 99 water column samples were collected with sample volumes ranging from 80-212 L. Pore waters were sampled from boxcores at 7 stations using a type of pushpoint sampler (small metal tube with thin slits near the bottom) connected to a glass cyclinder and extracted using a small vacuum pump. The pushpoint sampler was inserted approximately 30 cm into the core, thus the measured values are considered average activities over approximately this depth. Sample volumes for pore water ranged from 0.7-1.1 L.

Further Ra sampling was done at 11 stations in conjunction with the sediment incubation team onboard. Between 10-15 cm of undisturbed sediment collected using the box-corer was sub-sampled and transferred into a benthic flux chamber and a further 10-15 cm of bottom water collected from the rosette was placed atop the sediment. To test the effect of water column turbulence on benthic fluxes, the overlying water was stirred at two different rates (40 and 80 revolutions per minute, RPM) using spinning plates suspended 10-15 cm above the sediment surface. Previous studies have shown the importance of the chamber geometry on the benthic boundary layer thickness and therefore on solute fluxes through the sediment-water interface (*Santschi et al.*, 1991; *Tengberg et al.*, 2005). Due to the short time on-station and the unknown sediment composition, it was not possible to adapt the chamber design or stirring rates to in-situ conditions. Thus, two stirring rates were chosen

to mimic a range of interfacial pressure gradients and solute exchange conditions (*Huettel and Gust*, 1992; *Janssen et al.*, 2005b). Following the incubations, which ranged from 12-24 hours, the overlying water was removed for Ra analysis. Incubation sample volumes ranged from 3-8 L. A table of all samples collected is provided in appendix A.

Water column samples were prefiltered through 10 μm and 1 μm filter cartridges placed in sequence and smaller volume incubation samples were passed through the 1 μm filter only. After prefiltering, all samples were pumped slowly ($<$1 L min^{-1}) through a MnO_2-coated acrylic fiber to extract Ra. Pore water samples were prefiltered by gravity before Ra-extraction to conserve the smaller volumes. All samples were counted onboard using the RaDeCC delayed coincidence system (*Moore and Arnold*, 1996). For all samples, initial counts were made within 2 days of collection. A second count was made while onboard, 7-13 days after initial collection, to determine the amount of supported ^{224}Ra present from the parent ^{228}Th isotope. At this time, between 9 and 38 % of the initial ^{224}Ra remains on the fiber, which is corrected for using the activities obtained from both counts. A subset of 21 samples was counted a third time after about 5 months to determine an approximate value of the actinium parent of ^{223}Ra. The values of ^{224}Ra and ^{223}Ra listed here are therefore excess Ra activities.

Uncertainties for measurements of short-lived Ra isotopes are calculated using propagation of errors in various terms, including counting efficiency, volume estimates, as well as background and spurious counts. The initial source of error is defined by the standard 1σ counting statistics, where the fractional uncertainty for a particular Ra sample is proportional to the square root of the number of counts registered (i.e. if samples are counted for similar times, 'hotter' samples will produce lower relative uncertainties). ^{224}Ra consistently exhibited count rates approximately 10x higher than those of ^{223}Ra, resulting in an average ^{224}Ra uncertainty (13 %) approximately 3x lower than that of ^{223}Ra (36 %).

Porosity data were obtained using an extensive data compilation done at the Helmholtz Zentrum Geesthacht. Data were compiled from a number of studies to create a fine scale map of porosities throughout the entire North Sea (W. Puls, pers. comm, 2013). A coarser-scale grid (0.25° x 0.25°) was then made by binning data from the fine scale map. Using the precise coordinates of the relevant stations (see appendix A), porosities were then assigned directly from this grid. Thus, each value represents an average of between 16-36 porosity measurements made within that grid cell. Mean grain size distribution was

determined during the cruise using a Malvern Mastersizer 2000 particle analyzer. Mixed layer depths were determined using profiles of potential density anomalies (σ_θ) and are defined as the depth where the change in σ_θ from the surface bottle exceeds 0.1 kg m^{-3}. Potential density anomalies are calculated based on temperature, salinity and pressure of a given water sample, and using a reference surface pressure of 0 dbar.

5.4.2 Flux Calculations from Incubations

Benthic fluxes of Ra are calculated according to methods proposed by *Hancock et al.* (2000) for fluxes in benthic chambers. Assuming the flux out of sediments F (dpm m^{-2} d^{-1}) is constant, the change in Ra activity (dpm: atoms decaying per minute) in the overlying water A_{olw} (dpm m^{-3}) during the incubation time t (days) can be described as:

$$\frac{dA_{olw}}{dt} = \frac{F}{H} - \lambda A_{olw}, \tag{5.1}$$

where λ is the decay constant for the respective Ra isotope, and H is the height of the overlying water column assuming a well mixed water column. Assuming the activity at the beginning of the incubation ($A_{t=0}$) is equal to the near-bottom water column activity, which was measured (see above), the above equation can be solved and re-arranged as:

$$F = \frac{H\lambda}{1 - e^{-\lambda t}}[A_{olw} - A_{t=0}e^{-\lambda t}]. \tag{5.2}$$

Uncertainties in the benthic flux are calculated by applying the uncertainty propagation for uncorrelated variables formula to Eq. 5.2.

5.4.3 Radium Inventories

Ra inventories are calculated based on the assumption that a single surface measurement represents the activity throughout the mixed water column. This assumption is reasonable given that 7 out of 8 vertical profiles measured in the SNS show constant activities with depth (station 11 shows slight enrichment near the bottom). The Ra inventory, then, is the surface Ra activity (in dpm m^{-3}) multiplied by water depth. In the stratified NNS, surface inventories are calculated using the depth of the surface mixed layer. Uncertainty for a given Ra inventory is calculated using the uncertainty in the corresponding Ra activity.

At steady state, the Ra inventory of a m^2 water column with a lone benthic Ra source and no exchange with surrounding waters is a function of the benthic flux and the decay

constant. Thus, if an assumption is made that no other Ra sources or sinks exist at a particular location, the inventory can be used to back calculate a water column based estimate of the average benthic Ra flux.

5.4.4 Ra Mass Balance

Building a Ra mass balance and solving for the sedimentary input provides a third independent approach to estimate the benthic flux. The distribution of Ra represents a balance of Ra sources and sinks from a variety of locations throughout the North Sea. Considering the SEB region of the North Sea, and assuming that the sources of Ra to the SEB are balanced by the sinks (i.e. steady-state), a surface water Ra mass-balance, rearranged to solve for sedimentary input, can be written as:

$$Q_{Sed} = Q_{Decay} + Q_{Mix} + Q_{WS} + Q_{Riv} + Q_{SPM} \tag{5.3a}$$

$$F_{Sed} = \frac{Q_{Sed}}{A_{SEB}}, \tag{5.3b}$$

where inputs are the efflux from SEB sediments (Q_{Sed},), the addition from the Wadden Sea (Q_{WS}), the river flux (Q_{Riv}), and a potential source from suspended particulate matter (SPM) in the SEB (Q_{SPM}). To balance these inputs, Ra is lost by decay (Q_{Decay}), and via exchange with lower activity waters outside the SEB (Q_{Mix}). A simple schematic describing the mass-balance set-up is shown in Figure 5.2. Units for sources and sinks are dpm d^{-1}, thus dividing Q_{Sed} by the surface area of the SEB (A_{SEB}), provides a flux term (F_{Sed}) in the appropriate units.

The input of Ra from the Wadden Sea is calculated using a similar approach as *Moore et al.* (2011), who computed Ra loss from the Wadden Sea to the open North Sea using an equation of the form:

$$Q_{WS} = \frac{V_{WS}(Ra_{WS} - Ra_{SEB})}{\tau_{WS}}. \tag{5.4}$$

Ra_{WS} and Ra_{SEB} are the average Ra activities of the Wadden Sea and SEB respectively, τ_{WS} is the approximate timescale of mixing between Wadden Sea tidal flats and the SEB, and V_{WS} is the estimated volume of the Wadden Sea. Eq. 5.4 is also used to estimate the loss of Ra from the SEB via mixing with the rest of the North Sea (Q_{Mix}), using corresponding mixing timescales τ_{SEB} and average Ra activities for all North Sea samples taken outside the SEB (Ra_{NS}). Q_{Decay} is the product of the SEB volume (V_{SEB}), Ra_{SEB},

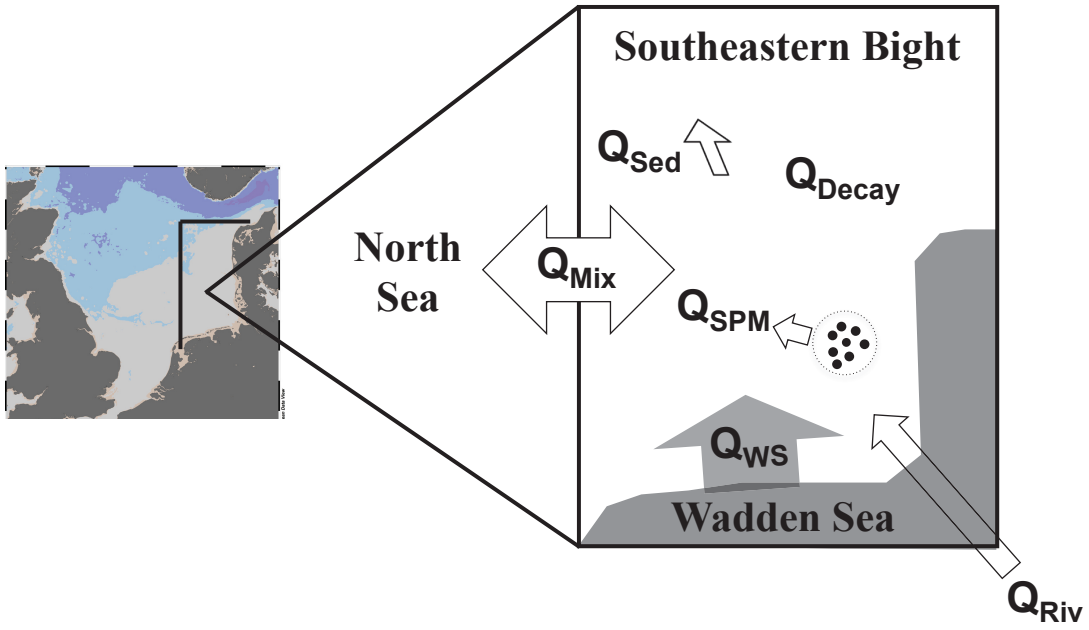

Figure 5.2: Schematic showing the location of the Southeastern Bight (SEB) and the mass-balance setup. Q_{Riv} is the sum of 4 river inputs. Q_{SPM} is the Ra given off from suspended particles in the water column, shown as small black circles. Q_{Seds} is shown as an arrow coming out of the seafloor. Figure redrawn from Burt et al. (2014) with permission from John Wiley and Sons.

and the decay constant (λ). Q_{Riv} is approximated using the total freshwater discharge into the SEB multiplied by the riverine Ra activity (Ra_{Riv}). Finally, Q_{SPM} is the product of the previously reported sediment desorption rate of Ra, an approximation for SPM in the SEB, V_{SEB}, and λ. All terms used in the mass balance, as well as the source for these values, are listed in Table 5.1.

5.4.5 Passive Tracer Modeling

Surface Ra distributions in the North Sea are reproduced using Ra as a decaying passive tracer in the 3 dimensional hydrodynamic module of the coupled physical-biological ECOSMO model, which has earlier been extensively validated (*Daewel and Schrum*, 2013). The model uses a 20-minute time step, with 6' x 10' horizontal resolution, a vertical grid of 5 m in the upper 40 m, and a decreasing vertical grid resolution below that depth. The current model has been equipped by a less diffusive and more accurate total variation diminishing scheme (TVDS) (see *Barthel et al.* (2012)). In the North Sea, the TVDS is rigorously validated against high-resolution observations from volunteer observing ships (here: 'FerryBox' observations), and has been shown to better preserve frontal structures and narrow coastal currents compared to prior methods (*Barthel et al.*, 2012; *Daewel and Schrum*, 2013). In separate runs, Ra was added from 3 distinct sources: the sediments, using the average of the inventory and mass-balance fluxes (see section 5.5 and Table 5.3 below), the Wadden Sea, using the rate calculated in the mass-balance (Q_{WS}), and from rivers, using an estimate for riverine Ra (Table 5.1) and the average monthly discharges already present in the model. Both sedimentary and Wadden Sea inputs are held constant throughout the model runs, the implications of which are discussed in section 5.5.5.

For each model run, the quality of the fit between the simulated activities and the observations can be quantified and illustrated using a method described by *Taylor* (2001). For a given simulation, the numerical difference between modeled activities and observed activities is quantified as the centered root mean square (RMS) error. The centered RMS error defines the discrepancy in pattern variation rather than the absolute differences between observations and model output because the means are subtracted before performing the RMS. A complementary measurement of pattern similarity between the observational and model data is given by the correlation coefficient (CC). Finally, the standard deviation (SD) in the modeled dataset is compared to that of the observations. All three parameters (RMS, CC, SD) are plotted on a single Taylor diagram, which summarizes the relative

Table 5.1: Values used in mass-balance model. Table redrawn from Burt et al. (2014) with permission from John Wiley and Sons.

Variable	**Value**		**Source**
SEB Surface Area (m^2)[(1)]	1.4 x 10^{11}		*Thomas et al.* (2009)
SEB Volume (m^3)	4.5 x 10^{12}		*Thomas et al.* (2009)
WS Surface Area (m^2)	5.0 x 10^9		*Thomas et al.* (2009)
WS Average Depth (m)	5		this work
Flushing of SEB, τ_{SEB} (d)	42		*Thomas et al.* (2009)
Flushing of WS, τ_{WS} (d)	4		*Moore et al.* (2011)
SPM (mg L^{-1}) [(2)]	2		Holt and James, 1999
SEB River Discharge (m^3 d^{-1}) [(3)]	1.5 x 10^8		Patsch and Lenhart, 2011
	^{224}**Ra**	^{223}**Ra**	
RaWS (dpm 100 L^{-1})	46.0	2.4	*Moore et al.* (2011)
RaSEB (dpm 100 L^{-1})	5.7 ± 0.5	0.8 ± 0.2	this work
RaNS (dpm 100 L^{-1})	3.9 ± 0.4	0.5 ± 0.1	this work
RaRiv (dpm 100 L^{-1}) [(4)]	20.0	1.1	(*Moore et al.*, 2011) and others
Lambda, λ (d^{-1})	0.19	0.06	
Desorption Rate (dpm g^{-1}) [(5)]	2	0.1	(*Moore et al.*, 2011)
Q_{decay} (dpm d^{-1})	4.9 x 10^{13}		
Q_{Mix} (dpm d^{-1})	1.9 x 10^{12}		
Q_{WS} (dpm d^{-1})	2.5 x 10^{12}		
Q_{Riv} (dpm d^{-1})	2.8 x 10^{10}		
Q_{SPM} (dpm d^{-1})	3.4 x 10^{12}		
Q_{Sed} (dpm d^{-1})	4.5 x 10^{13}		

[(1)]Lowered slightly from *Thomas et al.* (2009) to account for the fact that sediments within the small, stratified area of the SEB will not contribute to Q_{Seds}.
[(2)]Average of September observations from a SNS cruise
[(3)]Combined annual average discharges of Elbe, Weser and Ems rivers, as well as Lake Ijessel
[(4)]Maximum activity measured by *Moore et al.* (2011) in a small channel emptying into the Wadden Sea. Similar activities have been measured elsewhere (*Moore et al.*, 2006; *Kelly and Moran*, 2002)
[(5)]Equal to activity of parent isotope, assuming 100 % desorption. ^{227}Ac on sediments estimated to be 5 % of ^{228}Th

skill with which each model run simulates the observations.

5.5 Results and Discussion

5.5.1 North Sea Ra Distributions and Sources

The surface distributions of the two short-lived Ra isotopes show similar patterns (Figure 5.3a and b). The highest Ra activities, ranging from 7.6-14.6 dpm 100 L^{-1} for ^{224}Ra, and 0.7-2.2 dpm 100 L^{-1} for ^{223}Ra, are consistently observed at the lower salinity stations near to the Belgian, Dutch, German and Danish coastlines, in the continental coastal waters (CCW). Although activities decrease further offshore, they remain high throughout the entire SNS, from 2.2-7.5 dpm 100 L^{-1} for ^{224}Ra, and 0.3-0.9 dpm 100 L^{-1} for ^{223}Ra. In the NNS, almost all ^{224}Ra activities drop to less than 1.0 dpm 100 L^{-1}, while ^{223}Ra is near to or, in many cases, below the detection limit. Though difficult to distinguish on the large-scale map, stations 66 and 67, at the mouths of the Norwegian Otra and Sira rivers, respectively, have slightly elevated Ra (1.9 and 1.1 dpm 100 L^{-1} for ^{224}Ra, 0.4 and 0.1 dpm 100 L^{-1} for ^{223}Ra) compared to other NNS stations.

Vertical distributions of Ra mimic the patterns in potential density anomalies (Figure 5.4). In the SNS (Figure 5.4, stations 2 and 17), the constant density profiles confirm a well-mixed water column, and Ra activities are constant within the error margins. For stations in the NNS (Figure 5.4, stations 33 and 45), activities near the bottom are consistently higher than at the surface, where they drop towards the detection limit. These near-bottom enrichments, however, are relatively small compared to the high activities observed throughout the entire water column in all SNS stations. The water column distributions of Ra, salinity and the stratification factor (Figures 5.3 and 5.4) clearly indicate two Ra sources for the North Sea. First, the combination of runoff from European continental rivers, and discharge from the Wadden Sea make up a coastal source, which is likely to support the highest Ra activities observed in the CCW. This is reasonable given that rivers are a well-known source of Ra, and significant Ra release from the Wadden Sea tidal channels has been observed in previous studies (*Schmidt et al.*, 2011; *Moore et al.*, 2011). Second, consistently high Ra activities throughout the SNS point to a sedimentary Ra source. Sediments are a well-documented source of short-lived Ra (*Hancock et al.*, 2006; *Moore*, 2007; *Colbert and Hammond*, 2008) (also see chapter 3) and strong vertical mixing in shallow regions of continental shelves has been shown to cause localized surface

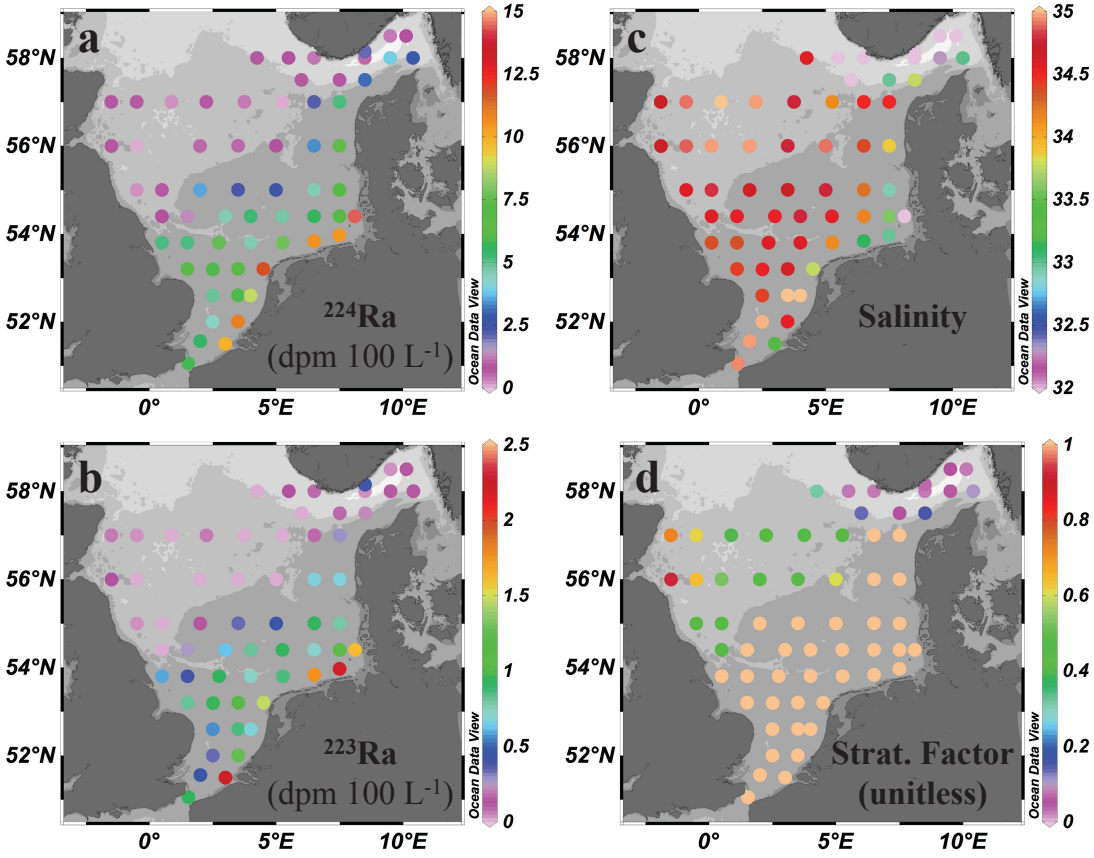

Figure 5.3: Surface distributions of ^{224}Ra **(a)**, ^{223}Ra **(b)**, salinity **(c)** and stratification factor **(d)** in the North Sea. Stratification factor (SF) is the mixed layer depth divided by water column depth, so a SF of 1 indicates a fully mixed water column. Note the different color scales between the two Ra distributions. The depth contours shown are the same as in Figure 5.1. Figure redrawn from Burt et al. (2014) with permission from John Wiley and Sons.

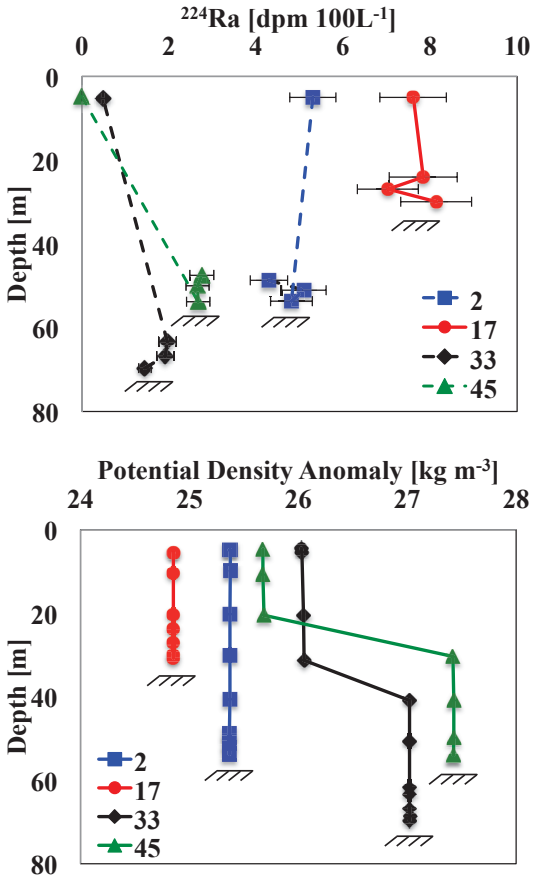

Figure 5.4: Vertical profiles of ^{224}Ra **(top)** and density **(bottom)**. Dashed lines are used in profiles where larger sampling gaps exist in the intermediate water column. Feathers beneath profiles indicate the depth of the sediment surface. Figure redrawn from Burt et al. (2014) with permission from John Wiley and Sons.

enrichments in ^{224}Ra too far offshore to be caused by lateral transports from the coast (chapter 4). Whereas previous Ra studies in the region report undetectable short-lived Ra beyond 60 km offshore of the Wadden Sea (*Schmidt et al.*, 2011; *Moore et al.*, 2011), the substantially greater sample volumes collected here (1.5-3x larger than previous work) allow for a better detection limit of low Ra signals.

In contrast to the CCW, no significant short-lived Ra source is observed from the British or Norwegian coastlines. Slightly higher activities are observed along the northern British coast, but this may be related to the large increase in mixed layer depth (Figure 5.3d) bringing surface waters closer to the sediment source. Minor Ra enrichments near the Norwegian coast are likely due to localized river sources. The lack of a substantial Ra source from either Norwegian and British coasts is likely due to a combination of smaller river discharges in general, and to differences in surficial and bedrock geology in these regions compared to the European continental coast.

Baltic Sea waters entering via the Skagerrak do not appear to be a discernible source of short-lived Ra to the North Sea despite its coastal origin and correspondingly low salinities. Whereas activities may indeed be higher in the Baltic Sea, the short half-lives of these isotopes likely prevent significant transport into the Skagerrak. Furthermore, Baltic Sea water entering the Skagerrak flows over a steep drop in topography, isolating surface waters from benthic Ra inputs. It remains unclear from the limited number of data points whether North Atlantic waters entering via the English Channel supply a small additional input of short-lived Ra to the SNS.

Water depths in the North Sea increase with distance away from the continental coast. Therefore, in the fully mixed SNS, surface activities will be diluted as the depth of the water column increases if sedimentary sources dominate. This suggests the use of vertical Ra inventories (dpm m^{-2}) to further investigate the sources of short-lived Ra to the North Sea. Mixed-layer Ra inventories of both short-lived isotopes are plotted with distance from the continental coast (Figure 5.5). Similar to the activity distributions, Ra inventories are highest in the CCW, with the largest Ra inventories found at stations near the mouths of the Rhine, Weser, Elbe and Scheldt rivers. In contrast, low Ra inventories within the CCW are found at stations bordering the Danish coastline (see Figure 5.5). This indicates a lack of a coastal Ra source at this region of coastline that is not as apparent using activity distributions alone.

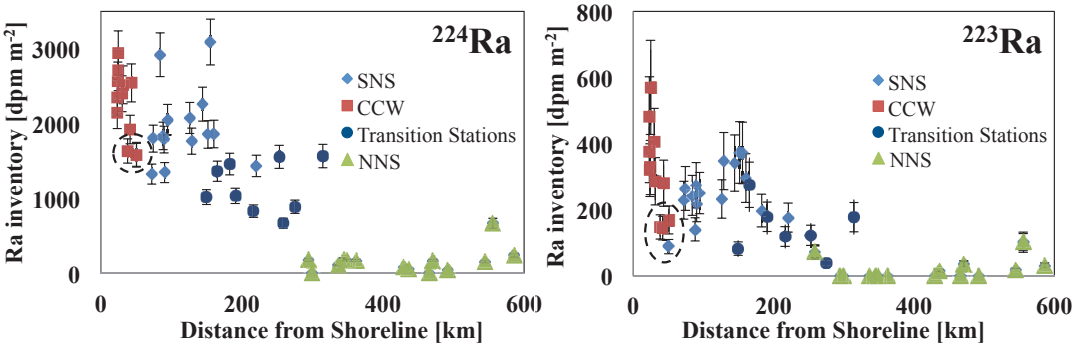

Figure 5.5: Ra inventories (^{224}Ra on **left**, ^{223}Ra on **right**) plotted in transect away from the European continental coast. SNS stations (blue diamonds) are averaged to obtain the estimate of sedimentary Ra flux. Transition stations (blue circles) refer to stations bordering the NNS and SNS, and indicate mixing between these two regions. Black dashed circles show low values along the Danish coast. Figure redrawn from Burt et al. (2014) with permission from John Wiley and Sons.

Stations in the SNS, characterized by a fully mixed water column (stratification factor = 1, Figure 5.3d) show consistently high Ra activities and inventories. In fact, beyond the CCW, at regions from 70-160 km offshore, Ra inventories remain constant or even increase with distance away from shore. These findings indicate that the high activities are maintained by benthic input. Therefore, it is clear that bottom sediments, rather than the continental coastline, are the dominant source of Ra to the North Sea.

Once released from sediments, Ra will be immediately mixed into surface waters of the SNS, whereas in the deeper stratified stations of the NNS the benthic source is not in direct contact with surface waters. The lack of any local source results in near-background activities in NNS surface waters, as well as very low mixed layer inventories ($<$400 dpm m^{-2} for ^{224}Ra and $<$100 dpm m^{-2} for ^{223}Ra). Below the mixed-layer, near-bottom activities are slightly higher because of the benthic source (Figure 5.4). Intermediate mixed-layer inventories (500-1100 dpm m^{-2}) at stations between 200-330 km offshore (i.e. bordering the SNS and NNS) imply mixing of stratified NNS waters with the shallow, sediment-supported SNS waters.

5.5.2 Independent Estimates of Benthic Ra Flux

The bottom sediments have been identified as the dominant source of short-lived Ra to the North Sea. Therefore, the following section details the quantification of this benthic source

using three independent approaches: sediment incubations, mixed-layer inventories, and mass-balance.

5.5.2.1 Incubation-based Ra Fluxes

Pore water activities were in excess of a hundred times higher than the majority of water column samples, ranging from 6.5-10.9 dpm L^{-1} for ^{224}Ra and 0.4-1.1 dpm L^{-1} for ^{223}Ra (Table 5.2). A benthic Ra flux is generated by the strong activity gradient across the sediment-water interface, and the flushing of high activity pore waters into the overlaying water column by advective processes. We have carried out incubation experiments in order to directly quantify sediment-water column exchange of Ra. Significant Ra enrichments were observed in the overlying water column following all sediment incubations, with calculated benthic fluxes ranging from 35-282 dpm m^{-2} d^{-1} for ^{224}Ra and 0.7-11.1 dpm m^{-2} d^{-1} for ^{223}Ra. For stations where incubations were conducted at both stir rates (i.e. turbulence regimes), observed ^{224}Ra fluxes at 80 RPM were higher than those at 40 RPM, with the exception of station 30, where the 2 values fall well within each others error margins (Table 5.2).

Uncertainties in pore water ^{224}Ra activities range from 8-12 %. Benthic flux uncertainties ranged from 7-25 % for ^{224}Ra and scale with the relative uncertainties of the ^{224}Ra activities before and after incubations (see Table 5.2). Due to the low volumes sampled, the total number of ^{223}Ra counts registered for incubation and pore water samples ranged from 6-37 and 22-60 counts, respectively. Such low count rates result in $>$50 % uncertainties for the majority of individual samples, creating uncertainties in the fluxes that range from 21-205 %. Results from ^{223}Ra incubations are not reported in Table 5.2, but the overall average fluxes are shown later in Table 5.3 for comparative purposes.

5.5.2.2 Inventory-based Benthic Flux

In order to calculate benthic Ra fluxes from inventories, stations with an assumed sole benthic source must be isolated. This requires the removal of numerous stations, including those in the CCW, which are affected by coastal inputs, transition stations, which lose Ra to the adjacent NNS, as well as NNS stations themselves, where surface waters are isolated by stratification (see Figure 5.5). Using the remaining stations, average ^{224}Ra and ^{223}Ra inventories of 1889 $\pm$ 185 dpm m^{-2} and 252 $\pm$ 54 dpm m^{-2}, respectively, are obtained. These inventories correspond to benthic Ra fluxes of 358 $\pm$ 35 dpm m^{-2} d^{-1} for

Table 5.2: Results from ^{224}Ra sediment incubations and pore water sampling, including comparison to literature values. Table redrawn from Burt et al. (2014) with permission from John Wiley and Sons.

Station	Sediment Description[(1)]	Ra Flux 40 RPM (dpm m^2 d^{-1})	Ra Flux 80 RPM (dpm m^2 d^{-1})	Pore water (dpm L^{-1})	Water Flux[(2)] (L m^{-2} d^{-1})[(2)]
7	medium sand	48.0 ± 9.1	220.5 ± 27.3	-	5.7 ± 1.2*
2	medium sand	70.6 ± 9.5	153.5 ± 18.0	-	8.4 ± 1.4*
11	medium sand	35.4 ± 8.9	58.4 ± 8.7	6.4 ± 0.7	5.5 ± 1.5
17	fine sand	108.2 ± 17.1	-	8.7 ± 1.0	12.4 ± 2.4
20	fine sand	139.7 ± 82.4	-		16.7 ± 3.1*
32	fine sand	88.4 ± 11.2	256.3 ± 29.7	7.3 ± 0.9	12.1 ± 2.1
30	fine sand	242.8 ± 32.7	218.6 ± 37.1	9.4 ± 1.1	25.7 ± 4.5
38	fine sand	164.4 ± 19.5	195.0 ± 22.3	10.9 ± 0.8	15.1 ± 2.1
45	medium sand	50.6 ± 7.8	122.3 ± 13.4	10.5 ± 0.7	4.8 ± 0.8
62	coarse silt	282.0 ± 18.8	-	-	33.7 ± 4.1*
65	coarse silt	60.3 ± 7.5	-	-	7.2 ± 1.2*
42	fine sand	-	-	5.4 ± 0.4	-
Average**		117.3 ± 82.4	174.9 ± 68.1	8.4 ± 2.1	13.4 ± 9.1

Study	Sediment Description	Reported Ra Flux (dpm m^2 d^{-1})	Pore water (dpm L^{-1})	Water Flux (L m^{-2} d^{-1})
Moore et al. (2011)	Wadden Sea Muds	97	9.8 ± 2.3	17.0
Colbert and Hammond (2008)	Beach Sands	368	8.2 ± 4.2	27.0
Moore et al. (2006)	Salt Marsh	175	5.0	33-36
Hancock et al. (2006)	Great Barrier Reef	202	-	-
Hancock et al. (2000)	Silts-Clays	228	12-36	-

*Calculated using average pore water activity

**Standard deviation of all samples (i.e. measure of the spatial variability)

[(1)]Wentworth scale definitions based on measurements of mean grain size

[(2)]Ra flux at 40 RPM divided by pore water activity

^{224}Ra, and 15.8 $\pm$ 3.3 dpm m^{-2} d^{-1} for ^{223}Ra. These fluxes, which are based on in-situ water column observations, are consistently higher than those calculated using laboratory core incubations (2.5x for both isotopes, see Table 5.3). Further comparisons between the calculated fluxes are discussed in detail in section 5.5.3.2.

Inventories in the SNS show substantial variability. This variability is likely due to changes in water depth over small spatial scales, high tidal currents, and horizontal advection of waters over regions of variable topography. For example, station 15 ($\sim$160 km offshore), with the largest observed inventory for both isotopes, is located in a narrow canyon feature with shallower water depths to the immediate north and south. As discussed later, spatial variations in sediment characteristics affect the Ra flux, which will create some variability in the average inventory calculation.

5.5.2.3 Ra Mass-balance

For the ^{224}Ra isotope, entering all calculated values from Table 5.1 into Eq. 5.3 and considering the uncertainties in the observed Ra activities both inside the SEB (Ra$_{SEB}$), and outside (Ra$_{NS}$) yields:

$$F_{Sed} = \frac{4.90\times10^{13}+1.94\times10^{12}-2.52\times10^{12}-2.79\times10^{10}-3.42\times10^{12}}{1.35\times10^{11}} = 333 \pm 40\,\text{dpm}\,\text{m}^{-2}\,\text{d}^{-1}.$$

Evident from this calculation are the relative contributions of each source and sink to the overall mass-balance. For example, according to this result, Ra distribution in the SEB is essentially a balance between sediment flux, which accounts for 88 % of the total inputs, and decay, which accounts for 96 % of the losses. This is likely due to the combined effects of a large spatial scale, and the short half-life of ^{224}Ra. Coastal sources are almost negligible because the signal does extend far enough offshore, and mixing becomes unimportant because it occurs over timescales (6 weeks, Table 5.1) that are much longer than the timescales of ^{224}Ra decay ($\sim$10 days). This finding is supported by the passive tracer model results (see section 5.5.5). The effect of spatial scale is tested by considering only the 7 southernmost data points in the SEB and thereby reducing the SEB surface area by approximately 85 %. After adjusting the Ra$_{SEB}$ and Ra$_{NS}$ appropriately, and reducing τ_{SEB} by half, the sediments and decay still provide 70 % and 88 % of the respective inputs and outputs and a comparable F$_{Seds}$ of 360 dpm m^{-2} d^{-1} is calculated. It is important to note that according to the mass-balance, suspended sediments are a stronger short-lived Ra source to the SEB than the Wadden Sea and major rivers combined.

Future studies in turbid coastal waters like the SNS should be aware of this potentially important Ra source, especially in nearshore regions like the Belgian Coastal Zone where prior studies have reported very high SPM concentrations (>200 mg/L, *Fettweis et al.* (2007)).

The reported uncertainty is equivalent to the maximum sensitivity of the calculation to uncertainties in the Ra_{SEB} and Ra_{NS} terms shown in Table 5.1. Nevertheless, the uncertainty reported here should be considered a minimum estimate, as further unknowns exist in other input variables. Input from rivers, SPM and the Wadden Sea may be slightly overestimated as the higher end of available variables were chosen. Furthermore, terms such as Ra_{Riv} are uncertain, as these observations are not available for the region. The input terms Q_{Riv}, Q_{SPM} and Q_{WS} are 1-2 orders of magnitude smaller than other terms in the mass-balance (Table 5.1), so overestimations and uncertainties in these terms will have a negligible effect of the results.

5.5.3 Sediment-water Ra exchange: important mechanisms and dominant controls

As is shown in the previous sections, the short-lived Ra tracer can be utilized in a number of ways to quantify sediment-water column exchange in coastal systems. By further investigating sources of variability within the incubation-based values, conclusions are drawn regarding the dominant processes controlling benthic Ra fluxes, and in turn, the observed North Sea Ra distributions. Then, comparing flux results first between the three independent methods presented here, and then between the reported results and prior studies reaffirms the importance of these processes.

5.5.3.1 Variability in Flux Incubations

Incubation-based fluxes vary substantially in the North Sea (see Table 5.2): some of this spatial variability can be explained by differences in sediment characteristics. Higher Ra fluxes are measured in cores with a smaller mean grain size (Figure 5.6a). Smaller grain sizes with a greater surface area to volume ratio generally contain more adsorbed Th, and therefore, release more Ra per unit volume (*Cai et al.*, 2014). The relationship between sediment porosity and ^{224}Ra efflux (Figure 5.6b) implies that, given constant near-bottom stresses above sandy sediments, more Ra is released at higher porosities (i.e. smaller grain size).

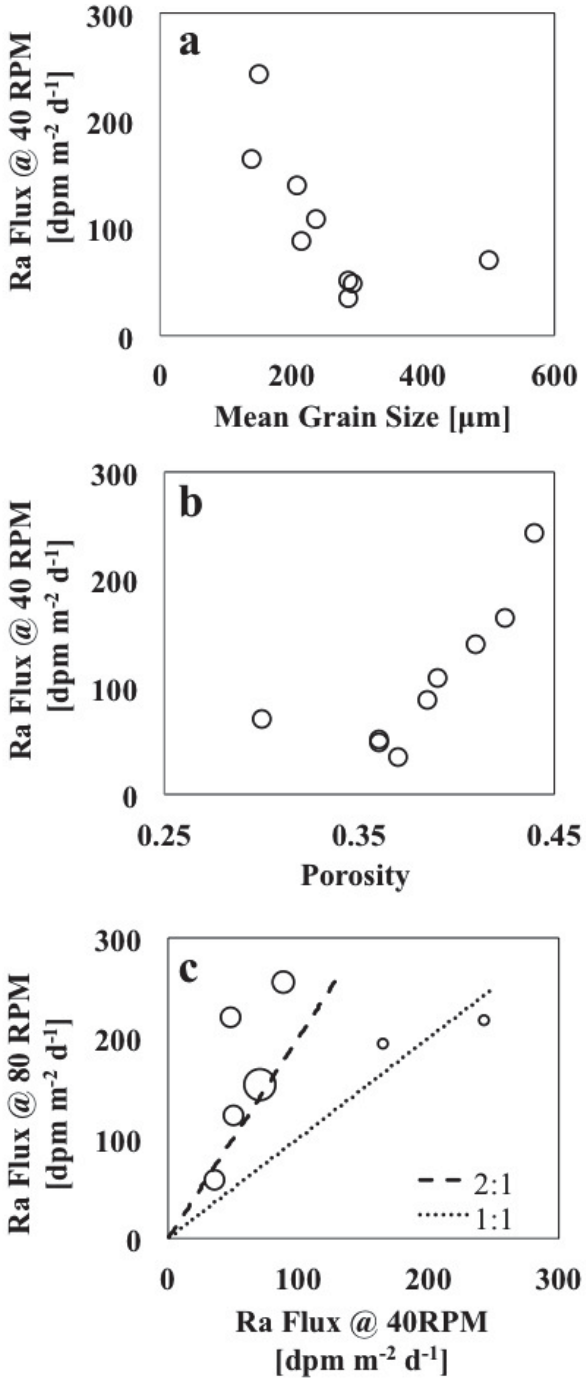

Figure 5.6: **(a)** Relationship between ^{224}Ra efflux and mean grain size. **(b)** Relationship between ^{224}Ra efflux and sediment porosity. **(c)** Effect of stirring rate on ^{224}Ra efflux. Size of symbols is directly proportional to the mean grain size in the sediment core (i.e. large circles represent coarser-grained sands). Figure redrawn from Burt et al. (2014) with permission from John Wiley and Sons.

The turbulence regime in the overlying water column also plays an important and concurrent role in determining the Ra flux. In permeable sandy sediments, which cover the majority of the North Sea, advection via sediment irrigation is often considered the dominant physical process governing pore water transport (*Jahnke et al.*, 2005). The North Sea is also characterized by intense mixing and strong near bottom currents which, when accompanied by topographic gradients such as sand ripples, will induce large pressure gradients on the sandy sediments. Maximum tidal currents are significantly stronger in the SNS than in the NNS, thus increased sediment-water column exchange via sediment irrigation is expected in the SNS. In sediment incubations, where water column turbulence regimes can be held constant (i.e. at 40 RPM) no patterns between SNS and NNS stations are evident. Likewise, no regional pattern in sediment characteristics exists between these two regions.

For incubations, different sediments respond differently to an increase in stirring rates. In coarser sands, doubling the stirring rate results in a near doubling of the benthic Ra flux, while in finer grained, more cohesive sediments, fluxes for both stirring rates fall close to a 1:1 line (Figure 5.6c). Sediment irrigation, which is the dominant transport mechanism in coarse (i.e. permeable) sands, will be increased at higher turbulence regimes, while water column turbulence has a lesser or negligible effect in finer grained (i.e. less permeable or impermeable) sediments. Therefore, while maximum Ra fluxes are found at stations with smaller grain size with larger pore water volume (i.e. higher porosity), Ra efflux is eventually limited by decreases in permeability at very fine grain sizes.

Sediment characteristics do not appear to play a role in the deep waters of the Skagerrak, where two stations, 62 (308 m depth) and 65 (534 m depth) of very similar sediment types (high porosity, small mean grain size), have vastly different incubation ^{224}Ra fluxes (282 dpm m^{-2} d^{-1} and 60 dpm m^{-2} d^{-1}, respectively). In-situ observations confirm this difference in ^{224}Ra efflux, with near-bottom ^{224}Ra activities ranging from 3.7-5.3 dpm 100 L^{-1} and 0.6-1.7 dpm 100 L^{-1} for the two respective stations. Different near-bottom turbulence regimes may exist on the shallower slope (Stn. 62) compared to the bottom of the Norwegian Trench (Stn. 65), but the exact causes for this substantial difference in benthic Ra flux is not clear from the observations presented here. Focused sampling across the steep Norwegian Trench could be of interest for future study.

In summary, the results show that both the turbulence regime and the sediment characteristics exert the major controls on the observed Ra fluxes across the North Sea. Whereas the shallower SNS experiences much more turbulent conditions than the deeper NNS, sediment characteristics in turn do not reveal clear spatial patterns across the North Sea. As a consequence, there does not appear to be a clear relationship between the magnitude of the Ra fluxes and the geographical location of the station (i.e. between Ra fluxes and stratification conditions only).

5.5.3.2 Comparing Flux Results

The importance of the turbulence regime in the overlying water column is evident when comparing sedimentary ^{224}Ra and ^{223}Ra fluxes computed using all 3 approaches (Table 5.3). For both isotopes, considerably larger fluxes are calculated using methods based on in-situ observations (inventory and mass balance) compared to those obtained using incubations. This suggests that the prescribed mixing conditions of the onboard laboratory incubations significantly under-represent the conditions present in this region, resulting in underestimated rates of sediment-water column exchange. This is unsurprising given that the incubation experiments aim to recreate pore water exchange through irrigation without inducing sediment resuspension (*Janssen et al.*, 2005b). Given the high turbidity observed in the water column of the SNS, sediment resuspension was undoubtedly occurring in this region during the cruise. Furthermore, sediment cores used for incubations may lack the significant topographic gradients that generate pressure gradients in cross-flow regimes. The inability to reconstruct physical conditions near the sediment-water interface is a well-documented limitation of incubation chambers in general (*Lohse et al.*, 1996; *Jahnke et al.*, 2000; *Cai et al.*, 2012). In the North Sea, prior discrepancies in pore water profiles between laboratory and field studies have been attributed to intense wave action and tidal currents (*Lohse et al.*, 1996). Despite this, incubation results show clear geographical and hydrodynamical variation in the fluxes, and thus provide valuable information regarding the dominant controls on benthic Ra fluxes in the North Sea.

Fluxes based on inventories and mass-balance are high when compared to a variety of studies that calculated Ra fluxes in different coastal systems (Table 5.2). *Moore* (2007) compiled Ra flux estimates for fine-grained sediments, yielding rather consistent values around 225 dpm m^{-2} d^{-1}. The majority of these studies took place in estuarine settings (lagoons, marshes), where permeability is likely lower and physical conditions

Table 5.3: Comparison of Ra benthic flux estimates. Table redrawn from Burt et al. (2014) with permission from John Wiley and Sons.

Method	Spatial Scale Considered	^{224}Ra (dpm m^2 d^{-1})	^{223}Ra (dpm m^2 d^{-1})
Incubations*	Entire sample area	146 ± 18	6.4 ± 3.4
Inventories	Subset of SNS	358 ± 35	15.8 ± 3.3
Mass-balance	SEB (see Figure 5.2)	333 ± 40	17.7 ± 5.8

*Average (mean) and standard deviation of the 40 RPM and 80 RPM results from Table 5.2.

near the sediment surface are likely less turbulent than the conditions found in the SNS. Like results shown here, *Colbert and Hammond* (2008) calculated higher Ra fluxes (368.2 dpm m^{-2} d^{-1} for ^{224}Ra and 21.9 dpm m^{-2} d^{-1} for ^{223}Ra) at the sandy shoreline of San Pedro Bay (USA), where breaking waves were thought to induce considerable sediment-water column exchange. *Cai et al.* (2014) observed very high ^{224}Ra fluxes in the Yangtze Estuary, ranging from 170-1780 dpm m^{-2} d^{-1}, and concluded that sediment irrigation is responsible for 70 % of the total benthic flux. Direct comparison between their Ra/Th disequilibrium method and separate incubation results revealed that in the shallow, turbulent estuarine region, incubation results greatly underestimated the flux, in agreement with the findings reported above, while in deeper outer shelf sediments, both methods yielded similar values (Cai, P., pers. comm.).

The activity of Ra in the pore waters of North Sea sediments appears comparable to the majority of previous studies (Table 5.2), thus the higher Ra fluxes calculated by both inventory and mass-balance methods likely reflect higher rates of sediment irrigation induced by the strong mixing conditions of the SNS. Further to these rather physical considerations, bioturbation also enhances sediment-water column exchange, and thus higher Ra fluxes, especially in the SNS where densities of benthic macrofauna are generally quite high (*Dauwe et al.*, 1998). *Braeckman et al.* (2014) showed that macrobenthic abundances in SNS sediment cores are highly dependent on sediment type, with order of magnitude higher densities in fine sandy sediment compared to cores with more permeable sands or muddy sediments. This suggests that variability in Ra flux from incubations could be related to differences in macrobenthic abundances, along with differences in porosity and grain size. Furthermore, high macrobenthic densities in fine sandy sediments could account for some of the discrepancies between fluxes measured via incubations and in-situ methods.

It is clear from these results that sediments release a considerable amount of Ra enriched pore water into the water column. These same pore waters are likely enriched in other chemical species, such as nutrients, metals, and carbon species, suggesting that sediment-water column interaction plays an important role in other North Sea chemical budgets.

5.5.4 Pore water fluxes and implications for carbon biogeochemistry

Pore water Ra measurements taken from North Sea box cores compare well to values published in previous studies (Table 5.2). Compared to samples taken in the Wadden Sea by *Moore et al.* (2011), the values fall within the error margins of each other. Dividing the Ra efflux (dpm m^{-2} d^{-1}) by the pore water activity (dpm L^{-1}) yields estimates of the volume flux through sediments. For incubation samples, volume fluxes vary from 5.5-25.5 L m^{-2} d^{-1} for ^{224}Ra, and 1.1-10.0 L m^{-2} d^{-1} for ^{223}Ra (Table 5.2). If the inventory and mass-balance approaches are considered to better represent in-situ sediment-water column exchange in the North Sea, then using the corresponding ^{224}Ra fluxes in Table 5.3 and the average pore water ^{224}Ra activity, volume fluxes of 40-42 L m^{-2} d^{-1} are obtained for the North Sea. These values represent the extent of sediment-water column exchange by all potential mechanisms, and compare well to previous estimates of volume fluxes, which are based on a variety of methods including a numerical model of non-local exchange (*Colbert and Hammond*, 2008), and laboratory experiments of wave-driven advection (*Precht and Huettel*, 2003). The volume fluxes should be considered as upper-limits, as they are based on Ra effluxes that include diffusive transport across the sediment-water interface, which does not involve volume exchange. Volume fluxes can be combined with estimates of pore water concentrations of nutrient or carbon species to estimate fluxes of those substances into the North Sea. Sediment-water column exchange plays a key role in both carbon and nutrient cycling in coastal regions. This is especially true in the shallow SNS, where large quantities of organic matter are transported to, and regenerated within sediments relatively rapidly. More specifically, alkalinity fluxes from sediments have been shown to contribute significantly to the carbon budget (*Thomas et al.*, 2009) and to variations in air-sea exchange of CO_2 in the North Sea (*Omar et al.*, 2010). Here, the Ra-based measurements of volume flux during incubations can be used to make a first-order estimate of incubation alkalinity fluxes. Since literature estimates of pore water alkalinity (AT) are not available in the open North Sea, deep profiles of AT in Wadden Sea

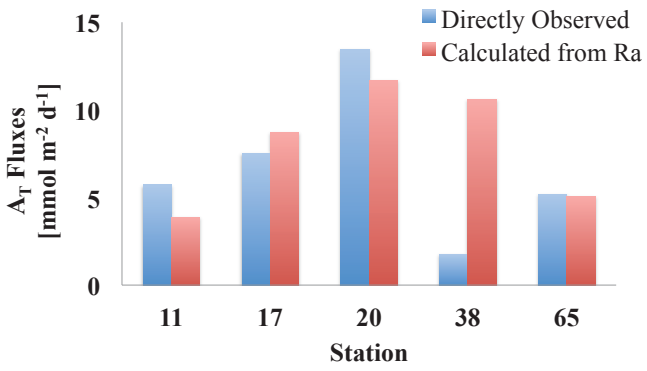

Figure 5.7: Comparison of Ra-based alkalinity fluxes to those calculated directly in sediment incubations. Incubation data from Heiko Brenner (pers. comm., 2013). Figure redrawn from Burt et al. (2014) with permission from John Wiley and Sons.

sediments during a multi-year time-series are considered an appropriate substitute. Values of pore water AT at both 0.05 and 1 m depths were around 3 mmol L^{-1}, and showed very little variability during the time series (*Moore et al.*, 2011). Similar pore water AT ($\sim$2.6 mmol L^{-1}) was measured in a Wadden Sea tidal channel by *Hoppema* (1990).

Taking the average water column AT observed in the SNS during the cruise (2.3 mmol L^{-1}), excess AT in pore waters is approximately 0.7 mmol L^{-1}, which multiplied by the estimates of water fluxes during incubations (Table 5.2), yields AT fluxes from incubations ranging from 3.4-23.6 mmol m^{-2} d^{-1}. These values compare well to directly observed AT fluxes from the onboard incubations (Figure 5.7). The discrepancy at the lone NNS station (station 38) may result from applying a single pore water AT value to all stations in the Ra-based method. Whereas both Ra pore water activities and fluxes in the SNS and NNS stations are similar (Table 5.2), observed AT fluxes are consistently much lower in the NNS (Brenner, H., pers. comm.), suggesting that pore water AT in these sediments is also lower.

Using an independent closing term approach, *Thomas et al.* (2009) estimated benthic AT fluxes of a similar order of magnitude (9.6 mmol m^{-2} d^{-1}) throughout the southeastern bight and Wadden Sea during autumn. Like the Ra fluxes, the incubation-based AT fluxes are likely lower than the in-situ fluxes, especially in the SNS. Nevertheless, more representative fluxes could be obtained using the volume fluxes estimated above from the water column based methods, which account for in-situ turbulence conditions.

In the absence of other data, pore water AT in North Sea sediments can be approximated using data from the adjacent Wadden Sea. Also it is assumed that no re-oxidation occurs between 5 cm depth, where the pore water was sampled (*Moore et al.*, 2011), and the sediment-water interface. It is important to note that these AT calculations represent an order of magnitude first-estimate, and the comparisons are made simply to recognize the potential application of Ra-based volume fluxes.

5.5.5 Passive Tracer Study

In order to further corroborate the observation-based Ra fluxes, i.e. the Ra sources to the North Sea, the distributions of ^{224}Ra are simulated as a passive tracer using the hydrodynamic module of the ECOSMO model (*Daewel and Schrum*, 2013). The ^{224}Ra sources (Table 5.3) are held constant throughout the run, except for the minor ^{224}Ra input related to time varying runoff. This means that any differences in surface Ra distributions over time can be attributed entirely to changes in hydrographic conditions. Balancing the relatively short half life of ^{224}Ra (3.7 days) with the time scales of turbulent mixing and molecular diffusion, the vertical structure of the water column – stratified vs. vertically mixed – plays a crucial role in how the predominantly sedimentary ^{224}Ra inputs are reflected in the surface waters. The expectation is that in stratified waters transport of ^{224}Ra to surface waters is diffusion-controlled. Thus, surface activities drop to undetectable levels because the timescale of diffusive transport is beyond the half-life of ^{224}Ra. In contrast, in a fully mixed water column, ^{224}Ra released from sediments is homogenously distributed, and thus is detectable in the surface layers (see chapter 4). Accordingly, model results are displayed as a mean ^{224}Ra distribution for the summer months of 2007 (June-August, Figure 5.8a) where seasonal stratification extends far south into the SNS, with the boundary between mixed and stratified water approximating the 30 m water depth isopleth. Furthermore, Figure 5.8b shows the mean ^{224}Ra distribution for the autumn months of 2007 (Oct-Dec, Figure 5.8b), when the fully-mixed region of the SNS expands further north, with the boundary between mixed and stratified water approximately mirroring the 50 m water depth isopleth. The cruise, in September 2011, coincided with numerous autumn storms, resulting in a substantially mixed SNS (see stratification factor, Figure 5.3d), and thus the observed surface ^{224}Ra distributions can be expected to be best represented by the autumn simulation (Figure 5.8b).

Little or no Ra is predicted in the NNS due to long persisting seasonal and beyond

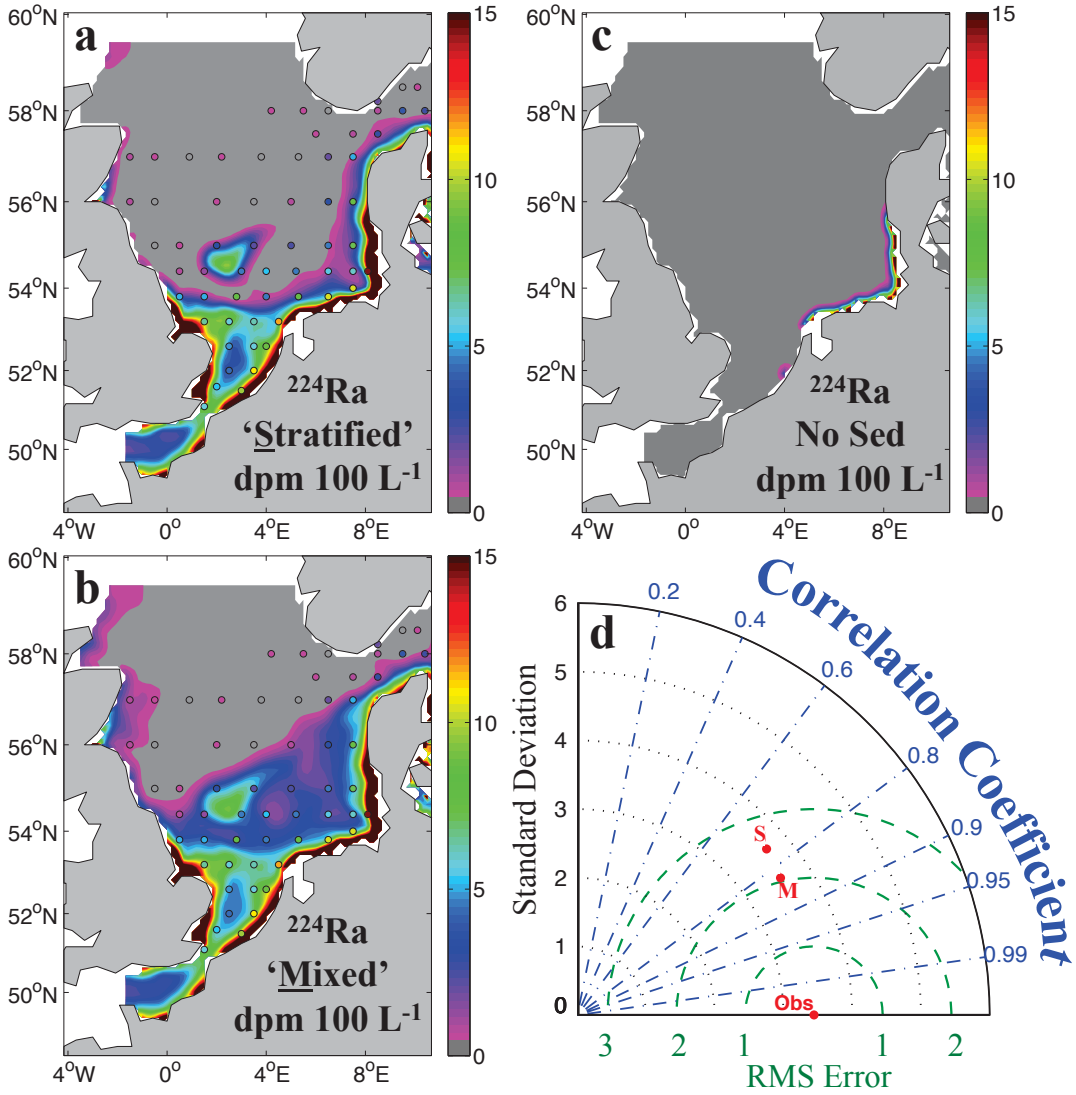

Figure 5.8: ECOSMO model output of mean ^{224}Ra distributions for **(a)** June to August 2007 (i.e. during seasonal stratification in the SNS) and **(b)** October to December 2007 (i.e. strong mixing in the SNS). Observations are overlain (small circles, same color scale) for comparative purposes. **(c)** ^{224}Ra distributions with sediment source removed. Here, the annual average is shown because seasonality of this distribution is indistinguishable. **(d)** Taylor diagram for all ^{224}Ra observations and the simulation S (stratified water column, shown in (a)) and M (mixed water column, shown in (b)). Green curved lines are 1 dpm 100 L^{-1} contours of centered RMS error between observations and model output, blue straight lines show correlation between observations and model output, and black dots represent the factor of standard deviation for each simulation compared to the standard deviation of the observations. Figure redrawn from Burt et al. (2014) with permission from John Wiley and Sons.

seasonal stratification, higher water depths and inflow of Atlantic water which is here considered to contain no Ra. Furthermore, model runs without a sediment source (Figure 5.8c) show the extent of the coastal signal into the North Sea. This result is consistent with the small relative contribution of coastal sources observed in the Ra mass balance and indicates that calculated values for Wadden Sea and riverine input are too small to explain the high activities and inventories observed in the CCW.

As is illustrated in the Taylor diagram (Figure 5.8d), the 'mixed' simulation generally agrees best with observations (Figure 5.8d). The autumn simulation shows a lower root mean square error, and a stronger correlation between the simulation and observations compared to the summer 'stratified' simulation. The quality of the fit indicates that the calculated benthic flux terms obtained in this study are reasonable.

Given that seasonal variations in benthic Ra fluxes have not been reported previously, the assumption that the ^{224}Ra flux is constant over time is a reasonable one. Enhanced wind-mixing in wintertime may induce more sediment-water column exchange via irrigation, but the magnitude of this increase is unclear. Unlike benthic oxygen, carbon and nutrients fluxes, which show significant seasonal variations in the North Sea (*Luff and Moll*, 2004), Ra efflux is not affected by seasonally varying deposition of organic material and therefore is not expected to exhibit substantial seasonal cycles.

We also assumed that the ^{224}Ra flux is invariant in space. Possibly an improved agreement between observed and simulated ^{224}Ra distributions can be achieved by resolving the spatial variability of the ^{224}Ra fluxes into the water column. As argued above, currently there does not appear to be a clear direct spatial/regional dependency of the ^{224}Ra fluxes, rather this dependency is mediated by the sediment typology (see Figure 5.6). Future studies dedicated to improved sediment sampling resolution could address this.

5.6 Conclusions

Throughout the North Sea, short-lived Ra is enriched in the water column due to interactions with the underlying sediments. Results from sediment incubations show considerable variation in benthic Ra efflux throughout the North Sea, attributable to differences in sediment characteristics such as porosity and grain size. Two independent water column based approaches, Ra inventory and mass-balance, yield benthic fluxes that are consistent and larger than both the incubation estimates reported here, and flux estimates reported for

most other regions. These relatively large fluxes are attributed to the turbulent conditions at the interface of permeable sandy sediments in the SNS, which lead to substantial irrigation and large amounts of sediment-water column exchange. Using Ra flux estimates and pore water measurements, volume fluxes across the sediment-water interface are calculated, which are related to benthic AT exchanges. Finally, results from the ECOSMO model runs further validate the estimated benthic fluxes while providing insight into seasonal variability of Ra distribution in the North Sea.

Sediment-water column exchange plays an important role in coastal biogeochemistry, and this study, along with previous ones, indicates that short-lived Ra is a useful tracer for quantifying rates of this exchange. This study represents the first large scale study of short-lived radium in the North Sea, and details a unique sampling strategy, including three dimensional water column coverage as well as sediment sampling. This work should also provide motivation towards future use of Ra in both benthic-pelagic coupling studies, and studies related to impacts of coastal inputs, specifically from the Wadden Sea. Future North Sea sampling regimes would further this understanding of spatial and temporal variation in North Sea fluxes, which could lead to refined Ra modeling techniques. From a methodological standpoint, utilization of the recently developed Th/Ra disequilibrium method (*Cai et al.*, 2014) in North Sea boxcore samples could lead to more precise estimates of benthic nutrient, oxygen and carbon fluxes, as well as to a more in depth understanding of the links between Ra and other important dissolved materials, such as alkalinity and carbon dioxide.

5.7 Acknowledgements

Many thanks to U. Braeckman, M. Hagens, L. Salt, and E. Jones along with the captain and crew of the R/V Pelagia for helping with sample collection and general cooperation with fieldwork. Additional thanks to M. Rutgers Van-der Loeff for assistance with the data analysis. Finally, thank you to both reviewers, whose detailed comments undoubtedly led to improvements in the manuscript. Financial support was provided by the POME exchange program (SIU, Norwegian Center for international Cooperation in Education), the Dutch Science Foundation (NWO, National Programme Sea and Coastal Research ZKO grant number 839.10.500), and Killam Trusts. Data used is contained in appendix A.

CHAPTER 6

EVALUATING NORTH SEA CARBON SOURCES USING RADIOGENIC AND STABLE CARBON ISOTOPE TRACERS

6.1 Abstract

A multi-tracer approach is applied to assess the role of boundary fluxes (e.g. benthic input from sediments or lateral inputs from the coastline) in the overall biogeochemistry of the North Sea. Analyses of basin-wide observations in the North Sea reveal that surface distributions of the δ^{13}C signature of dissolved inorganic carbon (DIC) are predominantly controlled by a balance between biological production and respiration, as well as a freshwater input near the European continental coast. Consequently, differences in surface water $\delta^{13}C_{DIC}$ signatures are attributed to varying amounts of metabolic DIC production. Variability in metabolic DIC throughout stations in the well-mixed southern North Sea indicates the presence of an external carbon source, which is traced to the European continental coastline using naturally-occurring radium isotopes (^{224}Ra and ^{228}Ra) with well-identified sources from the seafloor and coastal boundaries. Furthermore, ^{228}Ra is shown to be a highly effective tracer of North Sea total alkalinity (AT) compared to the more conventional use of salinity. Coastal alkalinity inputs are calculated using relationships with ^{228}Ra, and the DIC:AT ratio of these coastal inputs suggest denitrification as the main metabolic pathway for their formation. Finally, the AT input paralleling the metabolic DIC release prevents a significant decline in pH as compared to aerobic (i.e. unbuffered) release of metabolic DIC. This highlights the importance of coastal AT production in regulating pH

in the southern North Sea.[1]

6.2 Introduction

The ever-increasing threat of ocean acidification has been shown to be more severe in shallow continental shelf systems compared to the adjacent open ocean (*Orr et al.*, 2005; *Thomas et al.*, 2007; *Wootton et al.*, 2008). This is due, in part, to the fact that many shelf regions represent a strong sink for atmospheric carbon dioxide (CO_2). The North Sea has been identified as a strong continental shelf pump system, where CO_2 invades into surface waters, and is exported below the thermocline into the deep ocean (*Thomas et al.*, 2004). Coastal seas in densely populated regions also experience large fluxes of organic and inorganic nutrients from riverine, groundwater, and atmospheric sources, further accelerating acidification (*Doney et al.*, 2009; *Borges and Gypens*, 2010; *Duarte et al.*, 2013). This susceptibility has led to numerous studies focused on describing the North Sea carbonate system (*Bozec et al.*, 2005, 2006; *Thomas et al.*, 2009), and its change over time (*Salt et al.*, 2013).

By excluding the inputs of carbon from the North Atlantic Ocean (via the Faire Island, Shetland, and English Channels), *Thomas et al.* (2005) developed a net carbon budget of the North Sea that was dominated by 3 major inputs: European continental rivers, the atmosphere, and import from the Baltic Sea. Before reaching the open North Sea, many of these rivers empty onto the shallow mudflats of the Wadden Sea, a region known to play an important role in the biogeochemical cycling of the North Sea (*Brasse et al.*, 1999; *Thomas et al.*, 2009; *Omar et al.*, 2010). *Schwichtenberg et al.* (2012) concluded that annual changes in total alkalinity for the southeastern North Sea (the German Bight) are controlled predominantly by inputs from the Wadden Sea. *Salt et al.* (2013) revealed that the relative abundance of three major water masses (Baltic Sea, German Bight, and North Atlantic waters) directly influence the pH and partial pressure of CO_2 (pCO_2) in North Sea surface waters. Intense primary productivity, along with water column and benthic remineralization of organic matter, also alter the North Sea carbonate system throughout the year. Whereas it is clear that various important carbon fluxes exist in the North Sea, it remains difficult to resolve how each source or process contributes to the carbon content

[1]This chapter consists of a manuscript by W. J. Burt, H. Thomas, M. Hagens, J. Pätsch, L. Salt and N. Clargo in preparation for submission under the same title to Limnology and Oceanography.

of the North Sea at any given location (*Pätsch and Kühn*, 2008; *Kühn et al.*, 2010).

The stable carbon isotope composition of dissolved inorganic carbon ($\delta^{13}C_{DIC}$) is commonly used to follow transformations of carbon in the water column, and identify various sources and sinks (*Quay and Stutsman*, 2003). In the open ocean, spatial variability of $\delta^{13}C_{DIC}$ is typically quite small, and is considered to reflect a balance between biological and thermodynamic processes (*Gruber et al.*, 1999). Air-sea exchange, and its temperature dependence, can also play an important role in large ocean basins, where residence times of surface waters far exceed those required for isotopic equilibrium between the atmosphere and surface ocean ($\sim$10 years). Indeed, the continual input of isotopically light anthropogenic CO_2 into the world's oceans (known as the oceanic Suess effect), has been used to estimate accumulation rates of anthropogenic carbon in surface waters (*Quay et al.*, 2007), as well as to elaborate on paleoclimate scenarios (*Olsen and Ninnemann*, 2010). Overall, the dominant controls on $\delta^{13}C_{DIC}$ signals are well described for open ocean systems (*Gruber et al.*, 1999; *Racapé et al.*, 2013). In coastal systems, spatial variability of $\delta^{13}C_{DIC}$ is often much higher and freshwater sources tend to confound the signal. As a result, much less is known regarding the dominant controls governing the $\delta^{13}C_{DIC}$ distributions in a given coastal region. In the Wadden Sea, *Winde et al.* (2014) used co-variations in $\delta^{13}C_{DIC}$ and DIC to identify key inputs from freshwater sources (groundwater, rivers and inlets) and North Sea waters, and demonstrated that mixing between these two water masses greatly affects the $\delta^{13}C_{DIC}$, DIC and pCO_2 in the shallow water column of the Wadden Sea.

The Wadden Sea is also a source of two naturally-occurring radium isotopes, ^{224}Ra and ^{228}Ra, to the North Sea (*Moore et al.*, 2011). Both ^{224}Ra and ^{228}Ra have thorium (Th) parent isotopes that are strongly adsorbed to particle surfaces, thus both will enter the water column at two major sediment-water column boundaries, the seafloor and the coastline. Because of their vastly differing half lives ($t_{1/2}$), these isotopes are indicators of very different processes. On basin-wide scales, short-lived ^{224}Ra ($t_{1/2}$ = 3.7 d) has a negligible coastal signal as it cannot disperse far offshore before decaying, but it has a strong benthic signal because it can rapidly regenerate in sediment pore waters. As a result, ^{224}Ra is considered to be a direct tracer of sediment-water column interaction in the shallow well-mixed waters of the southern North Sea (see chapter 5). In contrast, longer-lived ^{228}Ra ($t_{1/2}$ = 5.8 y) can be transported vast distances away from its source

regions, but regenerates very slowly in sediments (*Moore*, 2007). Therefore, ^{228}Ra can be utilized to trace the dispersion of dissolved materials away from a coastal source, such as the Wadden Sea.

In this study, a novel multi-tracer approach is utilized to quantify key fluxes and transformations of carbon in the North Sea. First, the dominant controls on the $\delta^{13}C_{DIC}$ distributions of surface waters are discussed, and the biological carbon fractionation factor is quantified. Relationships between DIC, $\delta^{13}C_{DIC}$ and Ra are then used to quantify a coastal carbon source in the North Sea. A strong relationship is found between AT and ^{228}Ra, which supports the use of ^{228}Ra as a AT tracer. Coastal inputs of AT are then derived and ratios of coastal DIC and AT inputs are used to infer the dominant processes responsible for their formation. Finally, the extent to which coastal AT inputs can affect the buffering capacity of the southern North Sea is assessed.

6.3 Oceanographic Setting

The major water masses of the North Sea, as well as a generalized circulation pattern, are shown in Figure 6.1. The largest input is from the North Atlantic, which enters primarily through the Shetland and Faire Island Channels at the northern boundary and circulates counter-clockwise before exiting through the deep Norwegian trench. Much of this circulation is limited to the north and central North Sea, with a smaller fraction flowing through the southern region (*Turrell et al.*, 1992).

A small fraction of North Atlantic water also enters via the English Channel, and flows into the southern North Sea. European continental runoff enters the North Sea via various rivers and groundwater sources along the European continental coast, and predominantly flows northeast along the coast as continental coastal water. A large fraction of this runoff is transported to the North Sea via the Wadden Sea, which extends across much of the continental coastline (see Figure 6.1). English Channel water and European continental runoff are the main components of the Southern or German Bight watermass. Baltic Sea water enters the North Sea via the Skaggerak and exits via the Norwegian Trench.

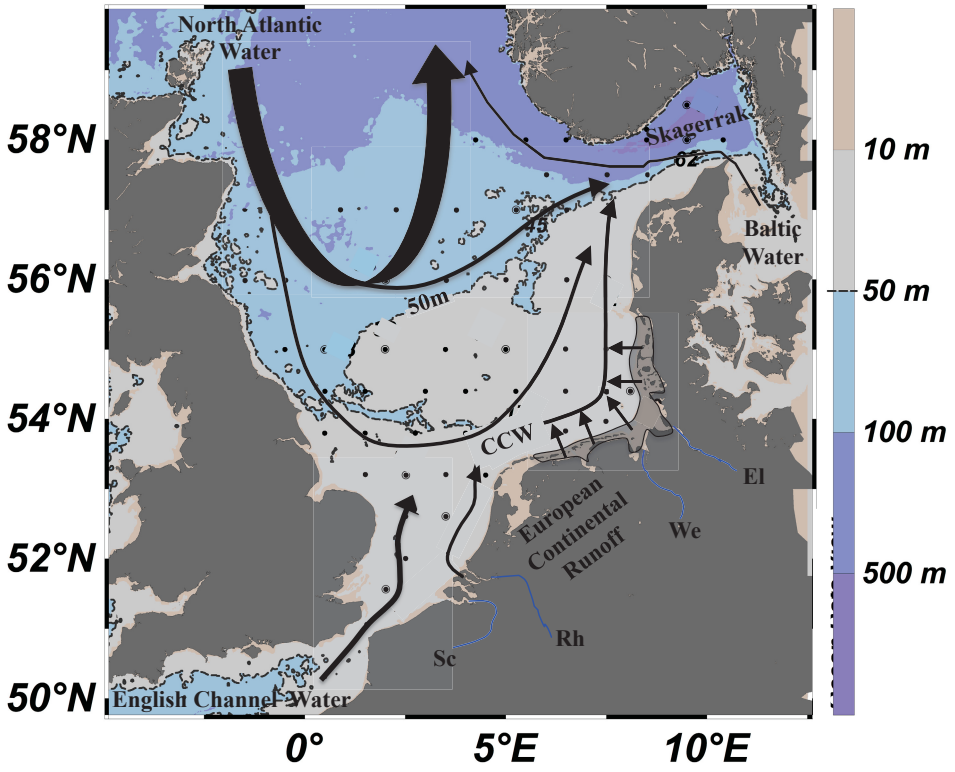

Figure 6.1: Map of North Sea with stations sampled during 2011 cruise (black dots). The 50 m contour (dashed line) roughly traces the border between well-mixed stations to the south, and stratified stations to the north. The Wadden Sea is outlined in the black shaded box. Black arrows show the general circulation pattern and the inputs of primary water masses (from *Turrell et al.* (1992)). Widths of the arrows roughly illustrate the magnitude of volume transport. CCW = Continental coastal waters, and major rivers are labeled: Sc = Scheldt, Rh = Rhine, We = Weser, El = Elbe. Map altered from Figure 5.1.

6.4 Methods

6.4.1 Sample Collection and Analysis

All samples were collected during a basin-wide North Sea survey conducted in September, 2011 aboard the *R/V Pelagia* (as part of the NWO, Dutch Science Foundation National Programme Sea and Coastal Research ZKO grant number 839.10.500). Conductivity, temperature and pressure, along with rosette bottle sampling for DIC, AT and $\delta^{13}C_{DIC}$ were conducted in vertical profiles at 88 stations. DIC and AT were analyzed onboard using a dual VINDTA 3C system provided by the Royal Netherlands Institute for Sea Research (NIOZ). Details of the respective coulometric and potentiometric determinations for DIC and AT are provided in chapter 2. $\delta^{13}C_{DIC}$ samples were collected in 30 mL glass serum bottles and injected with 60 μL of a $HgCl_2$ solution to halt biological activity. $\delta^{13}C_{DIC}$ analysis was done using continuous-flow isotope-ratio-monitoring mass spectrometry (CF-IRMMS) on a Thermo Finnigan MAT 253 gas mass spectrometer coupled to a Thermo Electron Gas Bench II via a Thermo Electron Conflo IV split interface. Standard solutions of 2 mM Na_2CO_3 and Li_2CO_3 (LSVEC) were used. Isotope ratios are expressed in per mil (‰) notation relative to the international Vienna Pee Dee Belemnite (VPDB) standard:

$$\delta^{13}C_{DIC} = \frac{(^{13}C/^{12}C)_{sample} - (^{13}C/^{12}C)_{VPDB}}{(^{13}C/^{12}C)_{VPDB}} * 1000‰. \quad (6.1)$$

This method has a reproducibility of 0.1 ‰ VPDB, which is used as the uncertainty for all $\delta^{13}C_{DIC}$ values reported here.

Ra isotopes were collected onto MnO_2-coated acrylic fibers from surface waters (5 m) at 61 stations, with near-bottom vertical profiles conducted at 13 stations. ^{224}Ra activities were determined using the Radium Delayed Continuous Counting (RaDeCC) system. All samples were counted within 2 days of sample collection to avoid significant ^{224}Ra decay. Samples were then recounted between 7-13 days after collection to determine activities of supported ^{228}Th, that were subtracted to obtain excess ^{224}Ra activities. More detailed descriptions of the methods for Ra isotope collection and analysis of ^{224}Ra are found in chapter 5. ^{224}Ra uncertainties range from 7-23 %. Following ^{224}Ra analysis, fibers were aged for $>$ 36 months before recounting on the RaDeCC. After this aging time, a significant amount of the original ^{228}Ra will have decayed to ^{228}Th, and the ^{228}Ra -^{228}Th and ^{228}Th-^{220}Rn isotope pairs have reached secular equilibrium. Therefore, recounting

fibers on the RaDeCC yields the extent of ^{228}Th ingrowth, which, using the various decay constants, can be used to back calculate the activity of ^{228}Ra at the time of sampling. Uncertainties for both ^{224}Ra and ^{228}Ra activities are calculated using the propagation of error technique described in chapter 2. Uncertainties for individual ^{228}Ra counts range from 5-8 %. For samples counted multiple times (n = 27), the resulting activities and uncertainties are averaged. Samples counted multiple times show good agreement between their individual measurements, with a mean relative standard deviation of 6 % for the twenty-seven samples.

6.4.2 Formulation of the 1-D Diffusion Model

A time-dependent 1-D finite difference diffusion model is used to assess the relative importance of the coastal source in contributing to the observed distributions of ^{224}Ra and ^{228}Ra. The model is constructed using a similar approach to that described in chapter 3 (section 3.3.5), namely by discretizing a general diffusion equation (which includes a decay term, see equation 3.1) and progressing the activity in a horizontal arrangement of points through time using the simple Eular forward approximation. The model itself consists of 200 discrete points, each with a width of 5 km, that extend out from a single origin (located at x = 0). Here, the origin represents the European continental coastline of the North Sea. A single constant coastal source is represented by setting the first cell with a constant activity throughout the model run, and this signal diffuses away from the coastline at a constant rate defined by the turbulent diffusivity (in units of km^2 d^{-1}). Ra activities at the coastline are chosen based on average activities measured in Wadden Sea tidal channels by *Moore et al.* (2011) (46 dpm 100 L^{-1} for ^{224}Ra and 36 dpm 100 L^{-1} for ^{228}Ra). A turbulent diffusivity of 10 km^2 d^{-1} was chosen for both isotopes, which provides the best fit to observed activities. The model is initialized with zero activity at all points except at the origin, and the model is run until the activities in all cells no longer change (i.e. steady state is reached). For the shorter-lived ^{224}Ra runs, steady-state is reached within 30 days, whereas $\sim$ 25 years is required for the ^{228}Ra distribution to reach steady-state.

6.4.3 Determination of the Biological Component of DIC (DIC$_{bio}$)

The surface water DIC concentration of a given water mass is altered by air-sea gas exchange, and the biological production/consumption of organic matter and calcium

carbonate ($CaCO_3$). Therefore, to isolate the biological component, a surface DIC concentration at atmospheric equilibrium is computed and subsequently from the observed DIC (DIC_{obs}):

$$DIC_{bio} = DIC_{obs} - DIC_{pCO2=383.26}. \tag{6.2}$$

At each station, $DIC_{pCO2=383.26}$ is computed using the same temperature, salinity and alkalinity as the corresponding DIC_{obs}. The atmospheric equilibrium value of 383.26 μatm is the average atmospheric pCO_2 in September 2011, as measured at the Mace Head atmospheric station in Ireland. This method assumes that any excess or deficit from the atmosphere-equilibrated DIC value ($DIC_{pCO2=383.26}$) is due solely to biological processes. However, compared to oxygen, atmospheric equilibration of CO_2 is relatively slow, and thus deviations in $DIC_{pCO2=383.26}$ could be related to other processes which occur on relatively short time scales (i.e. a few weeks). Air-sea exchange of CO_2 over short (e.g. weekly) timescales has a negligible effect on DIC concentrations. Physical processes, notably a change in water temperature, could alter the pCO_2 of surface waters relatively rapidly (i.e. before CO_2 air-sea equilibration occurs), and thus, alter the $DIC_{pCO2=383.26}$ term. Therefore, this method also assumes that surface water temperature does not vary, or varies only incrementally in the weeks preceding the observations. Sea surface temperatures throughout the North Sea are relatively stable during the summer plateau, with slight declines beginning in September (*Prowe et al.*, 2009). Hence, the effect of temporal variability in temperature is considered to be minor. If slight cooling does occur, $DIC_{pCO2=383.26}$ will be slightly overestimated, resulting in an underestimation of the respiratory (i.e. positive component) of DIC_{bio}. For example, a $1°C$ drop in temperature results in a $\sim$7-8 μmol kg^{-1} decrease in DIC_{bio}, which is small compared to the range of values observed in this study. Furthermore, since short term temperature changes will be comparable throughout the North Sea, their impact on the spatial variability of DIC_{bio} can be deemed minor. Finally, it is assumed that the combined effect of pelagic $CaCO_3$ formation or dissolution on DIC concentrations is negligible in the North Sea relative to the effect of organic matter production. Formation and dissolution of $CaCO_3$ are considered to be in steady-state in the well-mixed southern North Sea (F. Gazeau, pers. comm.), and recent estimates show approximately 4-8 times larger rates of organic matter production compared to production of $CaCO_3$ (F. Gazeau and H. Brenner, pers. comm.).

Given these assumptions, an increase in DIC_{bio} represents the production of DIC via the respiration of organic matter, whereas a decrease represents the uptake of DIC by primary producers during photosynthesis. As this statement implies, DIC_{bio} is used as a relative property, meaning that only relative changes in its magnitude are considered, rather than the magnitude of any particular value itself.

6.4.4 Calculating Biological Fractionation using DIC_{bio} and $\delta^{13}C_{DIC}$

The extent to which organisms preferentially take up light carbon (^{12}C) duing photosynthesis is quantified as the biological fractionation factor (ϵ). When considering only biological processes (i.e. assuming no air-sea fractionation in the open ocean), *Broecker and Maier-Reimer* (1992) surmised that $\delta^{13}C_{DIC}$ should be tightly correlated to dissolved phosphate concentrations, and that a plot of these two variables should produce a slope (x) according to the equation:

$$x = \frac{\epsilon}{DIC_{avg}} * \left[\frac{C}{P}\right]_{OM} \tag{6.3}$$

where DIC_{avg} is the average DIC concentration in a given basin, and the final term is the carbon to phosphate (C/P) ratio of organic matter. Phosphate is used because it is considered to only vary due to biological uptake or release, and the C/P ratio is used so that biological changes relate to changes in phosphate, rather than to changes in DIC. Therefore, it is assumed here that dividing x by the C/P ratio yields a new slope (m) which corresponds to a plot of $\delta^{13}C_{DIC}$ against a term for biologically-mediated DIC, which, in this study, is defined as DIC_{bio}. Assuming further that carbon and phosphate are transformed in a near-Redfield ratio (C/P ratio = 106), and using the observed average DIC in North Sea surface waters during the September 2011 cruise (2083.8 μmol/kg), Eq. 6.3 can be rearranged to solve for ϵ:

$$\epsilon = DIC_{avg} * m. \tag{6.4}$$

Uncertainty in ϵ is calculated by applying the standard error propagation formula for uncorrelated variables to Eq. 6.4. The uncertainties reported for all of the derived variables are determined using this approach.

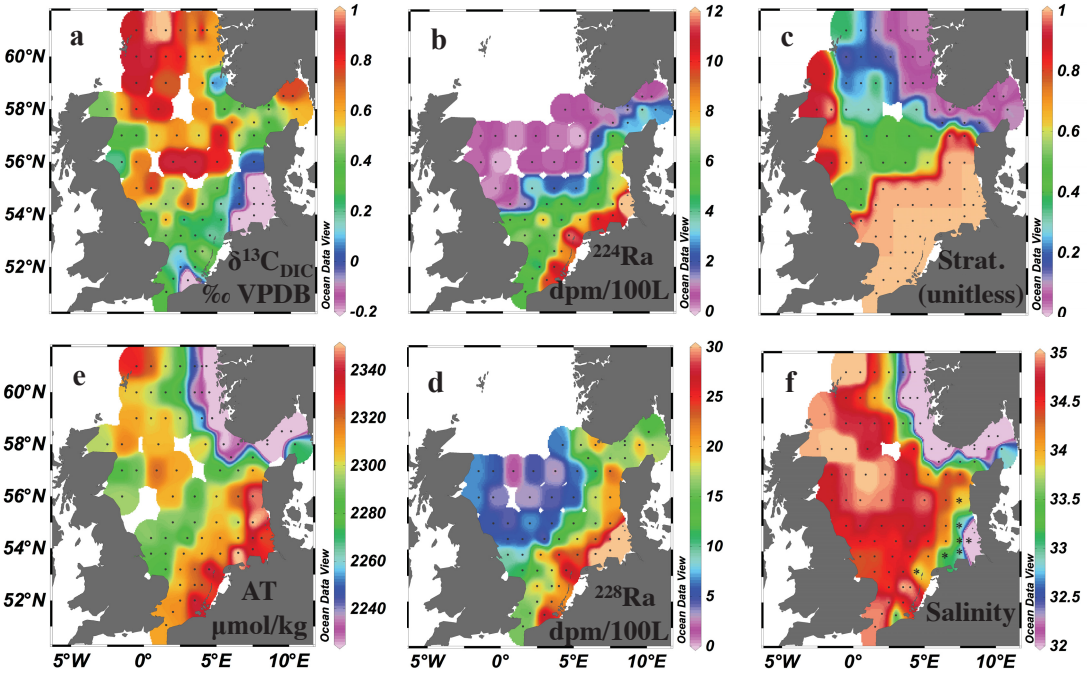

Figure 6.2: Surface maps of various species. Strat. refers to stratification factor (bottom depth/mixed layer depth), where 1 represents a fully mixed water column. Stations labeled as low salinity (S $<$ 34) throughout the manuscript are marked by asterisks (*, in panel f). Both AT and DIC were not available at the low-salinity station near the Scheldt/Rhine rivers (51.5°N, 3.0°E), thus are not included in further analyses, and the station is not labeled with an asterisk. Note that the strong minimum values of $\delta^{13}C_{DIC}$ and salinity ($\delta^{13}C_{DIC}$ = -1.92 ‰, S = 29.3), as well as the maximum Ra activities (^{224}Ra = 14.4 dpm/100L, ^{228}Ra = 47.4 dpm/100L) in the Elbe Estuary are not well represented by the scales.

6.5 Results and Discussion

6.5.1 North Sea Surface Distributions

The surface distributions of $\delta^{13}C_{DIC}$, Ra isotopes, AT and salinity show clear patterns (Figure 6.2). First, in the three top panels of Figure 6.2, an abrupt change in $\delta^{13}C_{DIC}$ (a) and ^{224}Ra (b) distributions occurs at the border between stratified waters to the north, and fully mixed waters to the south (stratification conditions shown in panel c). The effect of stratification on the vertical structure of $\delta^{13}C_{DIC}$ in the water column is shown in Figure 6.3. In the deeper northern North Sea, much of the organic matter formed in surface waters will sink and be respired below the pycnocline. This creates a separation of production

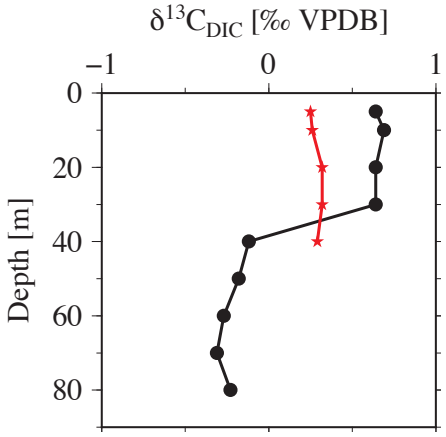

Figure 6.3: $\delta^{13}C_{DIC}$ vertical profiles in the southern mixed region (red stars, station 16, 53.8°N, 4.0°E) and in the northern stratified region (black circles, station 47, 57.0°N, 2.2°E)

and respiration, with surface waters exhibiting the enriched $\delta^{13}C_{DIC}$ signal indicative of net production, and $\delta^{13}C_{DIC}$ depletion in deeper waters due to net respiration (Figure 6.3).

In stratified waters, the majority of the ^{224}Ra generated by seafloor sediments will decay within the deeper layer, leaving surface waters highly depleted. In contrast, sediments are in direct contact with surface waters in the fully-mixed southern North Sea, which explains the high ^{224}Ra activities exhibited throughout the region. Additionally, organic matter produced within these fully-mixed waters cannot escape the surface layer, and is respired in the water column, or via recycling through the underlying sediments. The result is a net balance between production and respiration in the southern North Sea, exemplified by a vertically consistent isotopic signature which is relatively depleted compared to surface waters further north, and relatively enriched compared to deeper waters further north (Figures 6.2 and 6.3).

Surface distributions (Figure 6.2) display a distinct source of AT, Ra and freshwater from the European continental coastline. The highest AT values are located near the northern Wadden Sea, along the Danish (Jutland) coastline, in agreement with results from *Schwichtenberg* (2013), who found that this region of the Wadden Sea produces more AT than the southeastern (Frisian) side. Surface salinity (Figure 6.2, panel f) reveals the major freshwater inputs to the North Sea, most notably the Baltic Sea (via the Skagerrak), and the major European rivers. Aside from the Scheldt and Rhine Rivers, which empty near

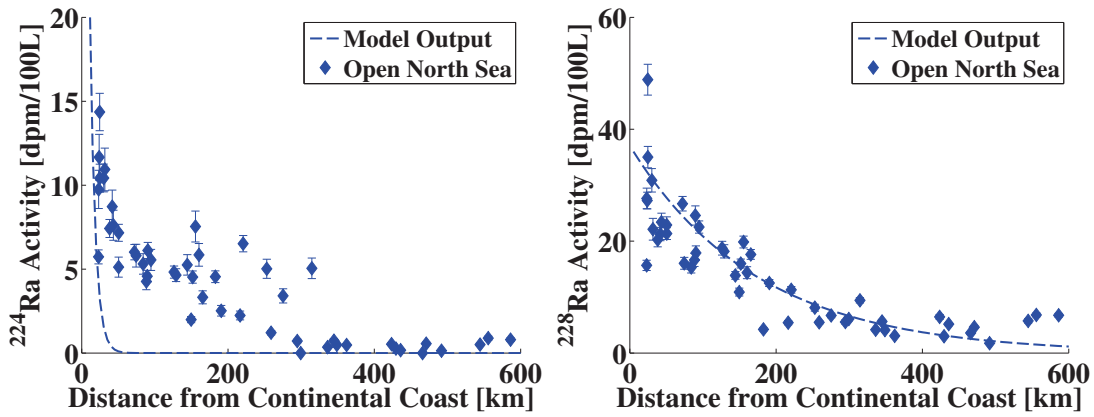

Figure 6.4: Offshore transects of ^{224}Ra (**left**) and ^{228}Ra (**right**) computed using the 1-D diffusion model. Ra activities at the coastline (distance = 0 km) are based on Wadden Sea data from *Moore et al.* (2011) (^{224}Ra = 46 dpm 100 L^{-1}, ^{228}Ra = 36 dpm 100 L^{-1}). Observations, with their associated uncertainties, are overlain as blue diamonds. The slight ^{228}Ra enrichment observed at distances $>$ 500 km is likely due to the proximity of these stations to the British coastline, where slightly lower salinities are also observed relative to surrounding stations.

the southernmost station (51.5°N, 3.0°E), these rivers empty first into the Wadden Sea and then into the German Bight. Outside of the Skagerrak, the salinity minimum is located in the southeastern corner of the sampling grid (54.4°N, 8.1°E), at the mouth of the Elbe river estuary. Here, a minimum $\delta^{13}C_{DIC}$ value and maximum Ra activities are also observed.

Overall, Figure 6.2 shows the importance of the stratification pattern in governing the $\delta^{13}C_{DIC}$ and ^{224}Ra distributions, as well as the role of the continental coastline in contributing Ra, AT and isotopically light carbon to the North Sea. In the nearshore, patterns in salinity closely mimic those of $\delta^{13}C_{DIC}$, but high Ra and AT are also found in coastal regions with higher salinity. This indicates that additions in Ra and AT may be more strongly associated with processes like brackish groundwater discharge or sediment-water column interaction, whereas freshwater may be more important in altering coastal $\delta^{13}C_{DIC}$ signals.

Offshore distributions in both ^{224}Ra and ^{228}Ra are shown in Figure 6.4. The ^{224}Ra observations show a step-wise pattern, with high nearshore activities attributed to the coastal source, consistent activities in the southern North Sea related to the benthic source, and an abrupt drop to near-background activities further offshore in the stratified region. In contrast, ^{228}Ra activities steadily decrease with distance from the shoreline and show little dependence on stratification conditions. Figure 6.4 includes output from a 1-D

diffusion model, wherein a single coastal Ra source is mixed offshore (see section 6.4.2 for model details). The model output highlights the relative importance of the benthic and coastal sources for each isotope. The step-wise pattern for ^{224}Ra distributions cannot be reproduced with a single coastal source (Figure 6.4, left panel), regardless of the mixing rates and source activities that were input into the model. This result lends further support to the North Sea ^{224}Ra source attributions, namely the dominant benthic source, made in chapter 5. On the other hand, modeled ^{228}Ra reproduces the observed patterns quite well (Figure 6.4, right panel) despite the lack of a benthic source. In fact, the model slightly overestimates the activity at some stations, likely because the model ignores potential variability in the coastal ^{228}Ra source value across the southern coastline, and instead, takes one value based on data from the Wadden Sea. Most importantly, even a small benthic ^{228}Ra source would result in a sizable overestimation throughout the entire region, thus it is assumed that this source is negligible.

6.5.2 Biological Fractionation and Freshwater $\delta^{13}C_{DIC}$ Signals

Surface water $\delta^{13}C_{DIC}$ distributions show substantial variability within the North Sea, ranging from -1.92 to 1.04 ‰VPDB. The magnitude of this variability is due in large part to the addition of freshwater at the European coastline, as seen in Figure 6.2 (panels a and f). Rivers and fresh groundwater are often depleted in $\delta^{13}C_{DIC}$, due to dissolution of biogenic carbon ($\delta^{13}C_{DIC} \cong$ -25‰) in soils (*Spiker*, 1980). Anoxic pore waters can also carry a heavily depleted $\delta^{13}C_{DIC}$ signal because of the potential formation and oxidation of methane ($\delta^{13}C_{DIC} \cong$ -50 to -100 ‰, *Himmler* (2011)).

The various processes that cause covariations between the isotopic composition and concentration of DIC are: photosynthesis and oxic respiration (termed together as biological processes), invasion and degassing of CO_2 (termed together as air-sea exchange), $CaCO_3$ dissolution and formation, addition of freshwater, and addition of anoxic pore water. These processes and their effects in coastal systems are illustrated in a DIC vs. $\delta^{13}C_{DIC}$ plot presented by *Winde et al.* (2014). These authors later describe the processes that may be important in the Wadden Sea. Here, a similar approach is taken by isolating the key processes in the North Sea, and in doing so, quantifying the role of biological transformations in governing $\delta^{13}C_{DIC}$.

A plot of DIC against $\delta^{13}C_{DIC}$ in surface waters (Figure 6.5a) reveals a trend similar to that reported by *Winde et al.* (2014). However, considerable scatter is present, which could

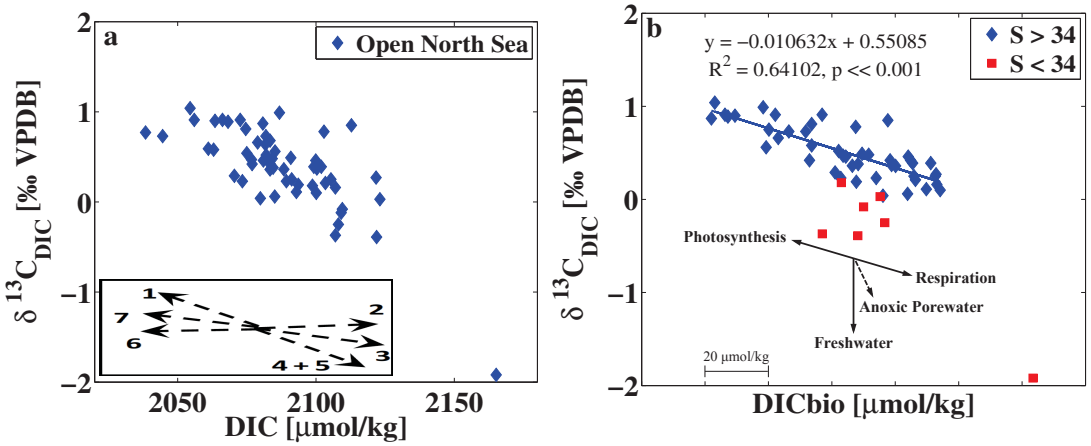

Figure 6.5: **a**: Covariations of DIC and $\delta^{13}C_{DIC}$. Schematic in bottom left shows processes that can affect the covariation: 1 & 4 Photosynthesis/Respiration, 2 & 6 $CaCO_3$ dissolution and formation, 3 & 7 CO_2 uptake and degassing, 5 additions of freshwater and/or anoxic pore water. Schematic altered from *Winde et al.* (2014). **b**: Covariations of DIC_{bio} and $\delta^{13}C_{DIC}$. Note that processes 4 and 5 (respiration and mixing with freshwater/anoxic pore water) are no longer combined, as freshwater does not affect DIC_{bio}. Also, the dashed line for anoxic pore water indicates that the exact influence, and thus the precise slope of this line, is unknown. DIC_{bio} is a relative variable, thus no values are shown along the x-axis, but each tick mark represents a DIC_{bio} change of 20 μmol/kg. Finally, note that lower salinity stations (red squares) fall below the general trend in the data. Stations within the Skagerrak region are not shown.

be due, in part, to air-sea exchange. As illustrated by the shallow-slope of arrows 3 and 7 in Figure 6.5a, the effects of air-sea exchange are much smaller for $\delta^{13}C_{DIC}$ compared to DIC. This is because chemical equilibrium of CO_2 between the ocean and atmosphere occurs approximately ten times more rapidly than isotopic equilibrium (*Gruber et al.*, 1999). In coastal systems like the North Sea, where the residence time of waters is relatively short compared to the open ocean, changes in $\delta^{13}C_{DIC}$ due to isotopic equilibration will be even smaller, and thus, are not considered to be important here. Focusing then on DIC, a water parcel's atmosphere-equilibrated DIC will vary considerably depending on its salinity and temperature. To remove this hydrographic variability, DIC_{bio} is used, which assumes all waters, independent of salinity and temperature conditions, are equilibrated with the atmosphere, and subtracts this equilibrated DIC from the observed value. Once the equilibrated DIC is eliminated, it is assumed that changes in both DIC_{bio} and $\delta^{13}C_{DIC}$ are related solely to biological transformations because air-sea interaction is too slow to affect DIC and $\delta^{13}C_{DIC}$ on short (i.e. subseasonal) timescales.

As mentioned previously, it is assumed that carbonate formation and dissolution do not play a role in the North Sea. In this case, variability between DIC_{bio} and $\delta^{13}C_{DIC}$ (Figure 6.5b) can only be controlled by the balance between biological production and respiration, along with mixing with freshwater and/or anoxic pore water. As described above, DIC_{bio} is not affected by freshwater inputs, making the impact of freshwater on $\delta^{13}C_{DIC}$ clearer (Figure 6.5b). A best-fit line drawn through the lower salinity data (Figure 6.6), all of which border the Wadden Sea, yields a zero-salinity endmember of -15.0 $\pm$ 0.8 ‰, which is consistent with typical riverine endmembers ($\sim$ -15 ‰, *Ahad et al.* (2008)). Indeed, *Winde et al.* (2014) reported freshwater inputs to a small bay within the Wadden Sea for October 2010, with an average $\delta^{13}C_{DIC}$ of -15.7 ‰. Slightly more enriched $\delta^{13}C_{DIC}$ values ($\sim$ -12 ‰) were consistently measured during a time-series at the mouth of the Elbe River, the major freshwater source to the German Bight (*Amann et al.*, 2014). The freshwater endmember shown here is derived using a relatively high and narrow salinity range, so it may be more appropriate to consider this value a freshwater endmember altered by processes in the Wadden Sea. Such processes may include input of anoxic pore waters, that would cause a slight $\delta^{13}C_{DIC}$ depletion.

When excluding stations with discernible freshwater input (salinities < 34), a strong correlation exists between DIC_{bio} and $\delta^{13}C_{DIC}$ (Figure 6.5b) that is assumed to be related exclusively to biological processes. The computed slope of the linear least-squares regression now quantifies the relationship between $\delta^{13}C_{DIC}$ and the biological uptake/production of DIC. That is, an isotopic signature change of -0.0106 ‰ relates to a release of 1 μmol/kg DIC. This slope can be used to convert $\delta^{13}C_{DIC}$ values into biological changes in DIC concentrations. This 'metabolic DIC' (DIC_{meta}), is derived from DIC_{bio}, and thus is also considered a relative variable, meaning only relative changes in DIC_{meta} will be considered here. Using the method described in section 6.4.4, the calculated slope of -0.106 (Fig. 6.5b) yields a fractionation factor (ϵ) of -22.2 $\pm$ 2.5. This factor falls at the lower end of values thought to characterize the marine environment (-22 and -32, *Zeebe and Wolf-Gladrow* (2001)). However, the extent to which $\delta^{13}C_{DIC}$ will change due to organic matter respiration in both the water column and sediments will depend primarily on the isotopic signature of the organic matter that is respired. The isotopic signature of total carbon ($\delta^{13}C_{TC}$) measured using sediment cores at eight stations during the cruise have values ranging from -20 to -28 ‰ with an average of -25 ‰ (M. Hagens,

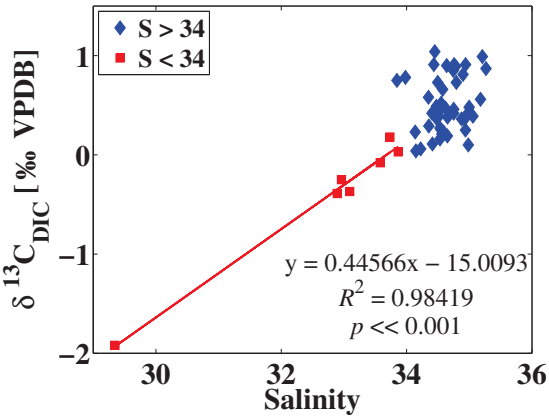

Figure 6.6: Salinity relationship with $\delta^{13}C_{DIC}$. Regression is placed through lower salinity stations only.

pers. comm.). Assuming that calcifiers make up a negligible amount of the TC, this is a reasonable estimate for the isotopic signature of total organic carbon ($\delta^{13}C_{TOC}$). The isotopic signature of organic carbon in the majority of the global oceans varies from -21 to -25 ‰ (*Williams and Gordon*, 1970), and the $\delta^{13}C_{TOC}$ within Wadden Sea sediments range from -20 to -26 ‰ (*Böttcher et al.*, 1998). Overall, the good agreement between the ϵ calculated here and those reported in other studies helps to validate the use of DIC_{bio} and provides confidence in the observed DIC_{bio} vs. $\delta^{13}C_{DIC}$ slope. It is also important to note that biological fractionation is species specific, thus the calculated factor here should be considered an average for the North Sea during the study.

6.5.3 Coastal Carbon Fluxes

As determined in the previous sections, the $\delta^{13}C_{DIC}$ signature throughout the majority of North Sea surface waters is governed by the relative balance between production and respiration. In stratified water columns, a separation is caused by vertical transport (sinking) of organic material out of surface waters. The extent of this separation, and thus the $\delta^{13}C_{DIC}$ signatures in the surface waters of the stratified northern region, could vary spatially due to differences in productivity or mixed layer depth. Yet, considerable variability in $\delta^{13}C_{DIC}$ is observed throughout the entire North Sea, including within the fully-mixed southern region, where pelagic production and respiration should be relatively well-balanced. In fact, a south to north gradient is visible in the surface distributions of $\delta^{13}C_{DIC}$ (Figure 6.2), with surface waters becoming isotopically heavier with increased

distance from the continental coastline. Given the well-mixed nature of $\delta^{13}C_{DIC}$ profiles in the southern North Sea (Figure 6.3), variability in surface waters suggests the presence of a non-pelagic carbon source with a different isotopic signature.

One such source could be the underlying sediment. Respiration of organic matter creates a buildup of isotopically depleted DIC within sediment pore waters, which is eventually released during sediment-water column interaction. If, for example, production and respiration in the fully-mixed water column are decoupled by prolonged deposition of organic matter on the seafloor, the sediments could represent a spatially varying carbon source with a net respiratory $\delta^{13}C_{DIC}$ signal. In the southern North Sea, a spring to summer transition between CO_2 undersaturation and supersaturation has been linked to the decoupling of production during the spring bloom, and respiration of that organic material later in the summer (*Thomas et al.*, 2004). Delayed remineralization of the organic matter formed during the spring bloom was also observed by the North Sea coupled sediment-water model ECOHAM (*Luff and Moll*, 2004).

A further, allochthonous source of carbon to southern North Sea stations is the lateral advection of waters originating at the European coastline, where high DIC and AT, as well as low $\delta^{13}C_{DIC}$ are clearly visible (Figure 6.2). *Winde et al.* (2014) observed an export of DIC from the Wadden Sea into the North Sea with a $\delta^{13}C_{DIC}$ of $\sim$-2.2 ‰, whereas *Schwichtenberg* (2013) concluded that export from the Wadden Sea and Rhine Estuary (which comprise most of the European continental coastline) have significant impacts on DIC and AT concentrations throughout the North Sea. Lateral input of isotopically light carbon would create a net respiratory signal in surface water $\delta^{13}C_{DIC}$, and the dispersion of this signal throughout the southern North Sea would set up a south to north gradient in $\delta^{13}C_{DIC}$ similar to the one shown in Figure 6.2a.

In contrast to $\delta^{13}C_{DIC}$, biological activity has no effect on the observed Ra activities. Ra builds up alongside DIC in sediment pore waters by radioactive decay of particle-bound Th, and is simultaneously released by sediment-water column exchange. Similarly, the tidally-induced exchange between the Wadden Sea and North Sea has been shown to concurrently export DIC, AT and Ra (*Moore et al.*, 2011). Figure 6.7 (panels a and c) shows the relationships between $\delta^{13}C_{DIC}$ and both ^{224}Ra and ^{228}Ra isotopes. In general, both isotopes show a correlation with $\delta^{13}C_{DIC}$, with a slightly stronger correlation for ^{228}Ra. This figure illustrates that a higher Ra activity corresponds to a more depleted $\delta^{13}C_{DIC}$

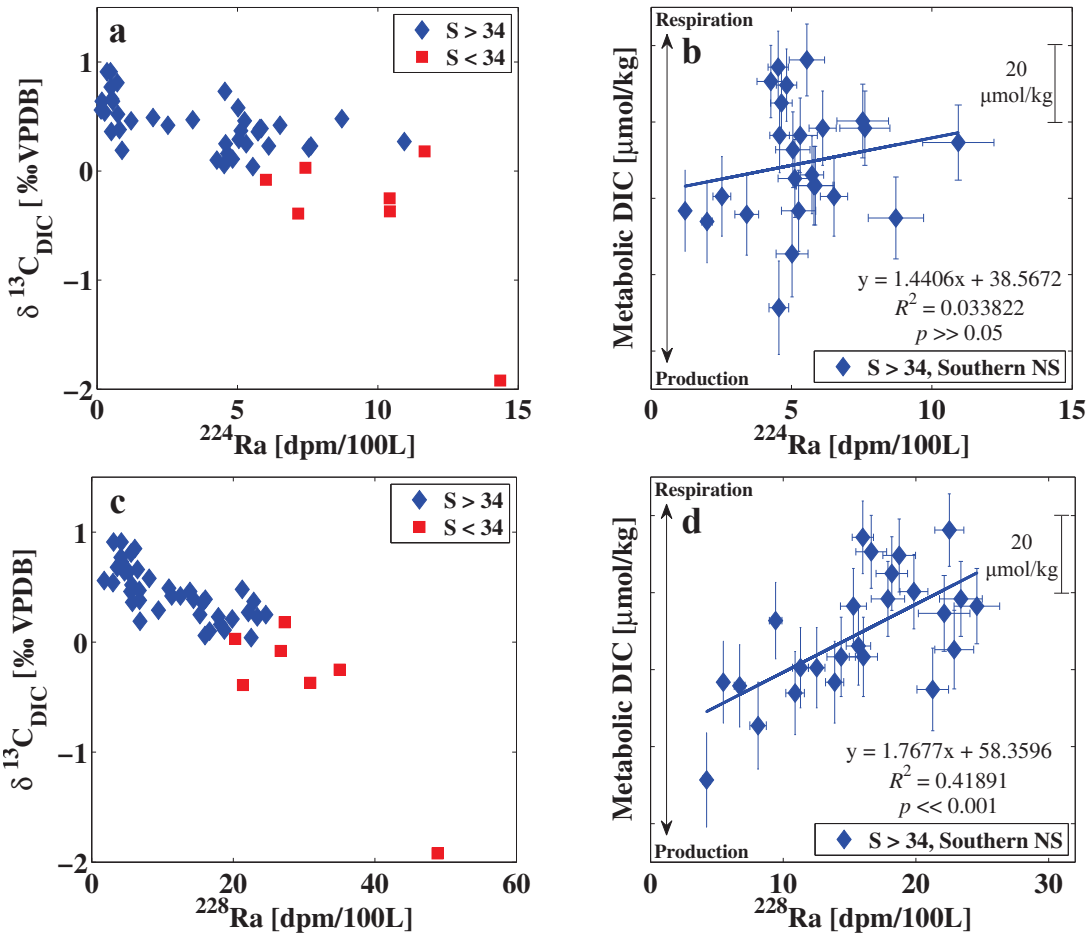

Figure 6.7: Left: Correlations between $\delta^{13}C_{DIC}$ and Ra isotopes (**a**: ^{224}Ra, **c**: ^{228}Ra). Right: Correlations between Metabolic DIC and Ra isotopes (**b**: ^{224}Ra, **d**: ^{228}Ra) in well-mixed stations at salinities above 34. The y-axes contain no values because metabolic DIC is a relative variable, but each tick mark represents a 20 μmol/kg change. Higher metabolic DIC is indicative of more organic matter respiration whereas lower values point to more production. Equations show the quality of the least-squares regressions, with the significance of the fit given by the p-values.

signature, and thus an increase in the net respiratory signal. At low salinity stations, this relationship is likely related to characteristically high-Ra, low-$\delta^{13}C_{DIC}$ freshwater inputs rather than biological processes. Similarly, stations with very depleted Ra and enriched $\delta^{13}C_{DIC}$ correspond to surface waters at stations in the stratified northern region. At fully-mixed stations with no discernable freshwater input, variability in $\delta^{13}C_{DIC}$ which is captured by differences in Ra activities can be attributed specifically to a benthic or coastal source of respiratory carbon.

To further quantify the relationships shown in the Figure 6.7 (panels a and c), $\delta^{13}C_{DIC}$ values are converted into metabolic DIC concentrations and plotted against ^{224}Ra and ^{228}Ra at all fully-mixed, southern North Sea stations without a discernible freshwater input (i.e. $S > 34$) (Figure 6.7b and d). In these panels, absolute values are not assigned to the y-axis, but each tick mark represents a change in metabolic DIC of 20 μmol/kg. A least-squares regression yields a slope which infers and quantifies the amount of metabolic DIC added for every measured unit of Ra. No correlation is found between ^{224}Ra and metabolic DIC, indicating that a respiratory DIC source from sediments, if present, cannot be detected during the 1-2 week lifetime of the ^{224}Ra isotope. In contrast, a significant correlation exists between ^{228}Ra and metabolic DIC. Assuming ^{228}Ra is predominantly sourced from the coastline, the strong correlation and the slope shown in Figure 6.7d allows a coastally-sourced metabolic DIC concentration to be inferred directly using ^{228}Ra activity.

As these stations are all fully-mixed, surface ^{228}Ra activities can be presented as water column inventories by integrating over the water depth. Similarly, the metabolic DIC concentration, which corresponds to a given ^{228}Ra using the slope ($m_{Ra-MetaDIC}$) in Figure 6.7d, can be converted into an inventory metabolic DIC input (DIC_{Meta_I}) per unit area of water column using the depth (z) and density (ρ) at a given station:

$$DIC_{Meta\_I}\,[\mu\text{mol C/m}^2] = (^{228}Ra * m_{Ra-MetaDIC})\,[\mu\text{mol/kg}] * \rho\,[\text{kg/m}^3] * z\,[\text{m}]. \quad (6.5)$$

Metabolic DIC inventories throughout the southern North Sea range from 0.25 ± 0.06 to 1.74 ± 0.44 mol C m^{-2}, and their spatial distribution throughout the southern North Sea is shown in Figure 6.8. From this map it is evident that the primary source of metabolic DIC is the coastline, and more specifically, the Wadden Sea. Larger inventories are also observed near the English Channel or the southern UK coast. These water-column inputs

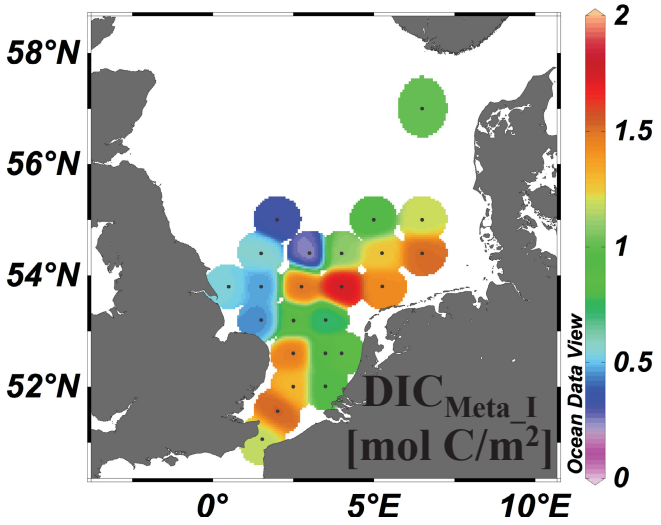

Figure 6.8: Metabolic DIC inventory [mol C/m^2] throughout the mixed stations of the southern North Sea . Note that low-salinity stations near the continental coastline are not included, as the relationship between $\delta^{13}C_{DIC}$ and DIC_{bio} does not apply to these stations (see Figure 6.5).

correspond to alterations in surface water DIC concentrations of 7-43 μmol/kg. For comparison, mean surface DIC concentrations in the German Bight exhibit seasonal variations of $\sim$ 40-70 μmol/kg (*Bozec et al.*, 2006; *Schwichtenberg*, 2013). In a recent modeling study, the effect of Wadden Sea DIC and AT export was discussed by comparing simulated German Bight DIC and AT concentrations with and without Wadden Sea export (*Schwichtenberg*, 2013). The results of the modeling study show that the average September DIC concentration in the German Bight increases by 30-40 μmol/kg when Wadden Sea exports are included, which agrees well with the results shown here.

6.5.4 ^{228}Ra as a Tracer of AT

The cycling of AT through the North Sea has been the subject of numerous studies (*Kempe and Pegler*, 1991; *Thomas et al.*, 2009). The common convention to identify important water masses influencing the carbonate system is to plot DIC or AT against salinity. In the North Sea, this consistently leads to the identification of three main water masses: the central North Sea (or North Atlantic input), the Skagerrak (or Baltic Sea input), and the Southern (or German) Bight (*Kempe and Pegler*, 1991; *Bozec et al.*, 2005). The relative abundances of these three water masses has been shown to significantly alter the pCO_2 and pH dynamics of the North Sea (*Salt et al.*, 2013). Here, salinity plotted against AT (Figure

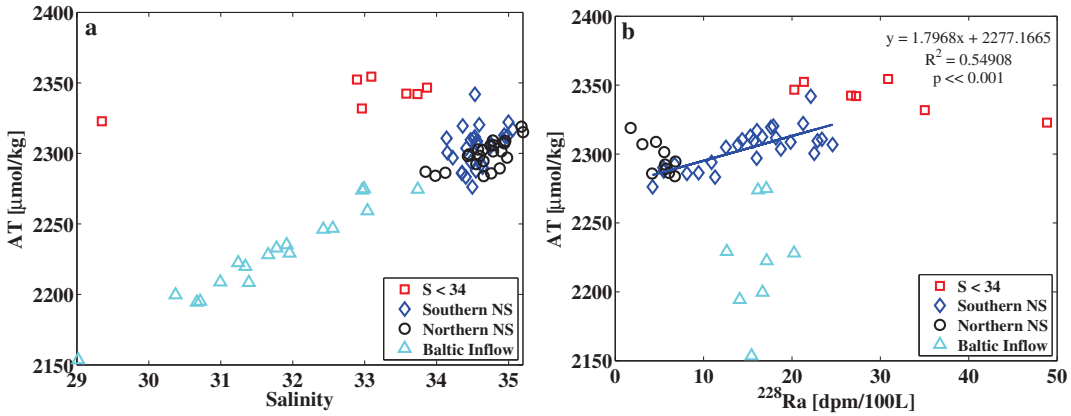

Figure 6.9: Comparison of water mass distinctions using **a**: Salinity against AT and **b**: ^{228}Ra against AT.

6.9a) shows the same distinctions as in these prior studies, with lower salinity waters from the Baltic (via the Skaggerak) and the European coastline (i.e. German Bight) influencing AT in the remaining stations of the North Sea. However, the North Atlantic endmember is not distinguishable from North Sea waters because salinity differences between the North Atlantic and central North Sea are too small. In contrast, typical ^{228}Ra activities in the open North Atlantic are between 1-3 dpm/100 L (*Kaufman et al.*, 1973), which is distinctly lower than the vast majority of the observed North Sea samples. As a result, plotting ^{228}Ra against AT (Figure 6.9b) provides three distinct endmembers, all of which converge in the central North Sea.

Figure 6.9 illustrates features of the general circulation in the North Sea, and shows that characteristics of the surface AT map (Figure 6.2) can be more readily explained using ^{228}Ra compared to the conventional salinity relationship. The low-^{228}Ra, high-AT stations are located in the northwest corner of the ^{228}Ra map, and are indicative of offshore waters flowing in through the Shetland or Faire Island Channels. The high-^{228}Ra, high-AT stations are all bordering the European coastline, clearly indicating this region as a source. Finally, Baltic water outflow, characterized by low-AT and intermediate ^{228}Ra, intrudes across the central North Sea creating the band of lower-AT waters between 53 and 56 degrees North (see Figure 6.2). Future sampling of ^{228}Ra in the more northern regions of the North Sea, or in the Baltic Sea, could better resolve the respective North Atlantic and Baltic endmembers and mixing lines.

Looking again at stations within the fully-mixed southern North Sea, a relationship

between ^{228}Ra and AT is found which is similar to that observed between ^{228}Ra and metabolic DIC (Figure 6.7b). That is, increased AT is associated with increased ^{228}Ra, and the European coastline is a clear AT source. Another least-squares regression through these points yields a slope of 1.80 μmol/kg AT per unit of ^{228}Ra. Assuming that the majority of ^{228}Ra is sourced from the coastline, water column inventories of ^{228}Ra equate to coastal water column integrated AT additions of 0.25 $\pm$ 0.05 to 1.77 $\pm$ 0.34 mol m^{-2}. These inventory inputs correspond to surface AT concentrations between 8 and 44 μmol/kg, which are similar in magnitude to seasonal variations in the North Sea ($\sim$17-33 μmol/kg, *Schwichtenberg* (2013)). Including Wadden Sea exports in the German Bight simulations, *Schwichtenberg* (2013) found increases of $\sim$18-30 μmol/kg in the mean September AT concentrations. These values are almost identical to the coastal AT inputs, which are assumed to come mostly from the Wadden Sea.

The AT inputs calculated here are almost identical to the metabolic DIC inventories, meaning this coastal input provides nearly equal amounts of biologically produced DIC and AT. If metabolic DIC was predominantly produced by aerobic respiration, it is expected that this input would exhibit net AT consumption, with an approximate DIC/AT ratio of -6.6. Here, the calculated DIC/AT ratio of +1.02 is indicative of anaerobic processes, and more specifically, denitrification, which produces near-equal amounts of DIC and AT (ratio = 1.25). Benthic respiration in open North Sea sediments is likely dominated by aerobic processes, due to the consistent ventilation of the predominantly sandy sediments by overlying waters. In the shallow mudflats of the Wadden Sea, however, anaerobic processes are dominant (*Böttcher et al.*, 2000). These results consistently point to the Wadden Sea as an important source of metabolic DIC and AT, both of which are well traced by concurrent inputs of ^{228}Ra.

This calculated export of AT from the European continental coastline affects the acid-base buffering capacity of the southern North Sea. To further investigate this, the potential change in pH induced by removing the coastally sourced AT from the observed values, is quantified. First, pH is calculated at all stations using observations of DIC and AT. Then, the AT concentrations associated with the coastal inventory input are subtracted, pH is recalculated, and the difference is considered the induced pH change. This pH change (ΔpH) is more appropriately quantified by taking the difference in proton concentration ($\Delta[H^+]$) (Figure 6.10). If the coastal AT input is removed, the surface pH at southern

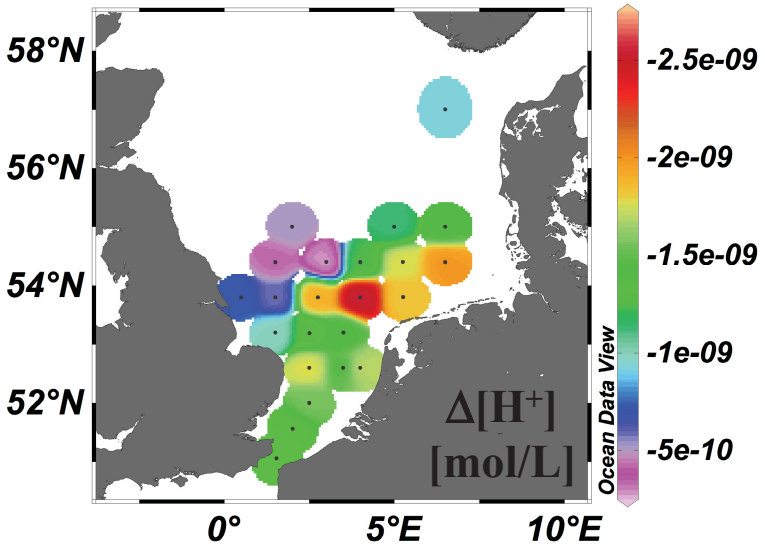

Figure 6.10: Changes in proton concentration ($\Delta[H^+]$) induced by removing the coastal AT input from the observed values. For reference, the largest value, located at station 16 (53.8°N, 4.8°E, red color), is equivalent to a drop in pH from 7.99 to 7.89 at that station, while the difference at the furthest offshore station (55.0°N, 2.0°E, purple color) corresponds to a drop in pH from 8.07 to 8.06.

North Sea stations decreases between 0.01 and 0.10 units. According to *Provoost et al.* (2010), the past 2 decades have seen annual pH declines of a similar magnitude in the southern North Sea (-0.02 to -0.03 units per year). This represents an order of magnitude faster rate of ocean acidification compared with the open North Atlantic (-0.0017 units per year, *Santana-Casiano et al.* (2007)).

It is thought that declines in primary productivity over recent decades, attributed to decreases in coastal nutrient loading, are largely responsible for observed pH declines in the southern North Sea (*Borges and Gypens*, 2010; *Provoost et al.*, 2010). These studies propose that reduced primary productivity has caused an ecosystem shift from one of net productivity (autotrophic) to one of net respiration (heterotrophic), which has the effect of increasing the standing stock of DIC and the pCO_2 in the mixed water column, while decreasing the pH. Irrespective over multi-year or decadal timescales, DIC will re-equilibrate with atmospheric CO_2 in the well-ventilated waters of the southern North Sea, thus changes in the standing stock of DIC and pCO_2 will have very little effect on pH.

Here, an complementary mechanism for the observed pH decline is suggested which is more related to changes in alkalinity, rather than to primary productivity and DIC. The

North Sea is subject to coastal eutrophication, during which AT is often produced via denitrification of allochthonous (i.e. land-derived) nitrate. This process creates an net increase in the standing stock of alkalinity, which buffers against pH change. In addition to decreases in primary productivity, the coastal regions of the southern North Sea have also seen a decline in coastal eutrophication (*Borges and Gypens*, 2010). With less AT production, equilibration with atmospheric CO_2 will result in stronger declines in pH. The DIC:AT ratios calculated here suggest that denitrification is the dominant process forming the coastal AT inputs. Therefore, it is possible that the coastal AT inputs observed here are substantially smaller than in previous years and decades, which is reflected in observations of rapid pH decline since $\sim$1990 (*Provoost et al.*, 2010). This highlights the importance of these coastal alkalinity inputs in maintaining the pH balance of the North Sea, as well as the need to monitor changes in biogeochemical cycling within coastal systems. Finally, given its effectiveness as a tracer of AT, these findings suggest that ^{228}Ra sampling should be considered during future North Sea observational campaigns.

6.6 Summary and Conclusions

A more complete understanding of the carbonate system in the North Sea is obtained using a suite of radiogenic and stable isotope tracers. Surface distributions of ^{224}Ra, ^{228}Ra and $\delta^{13}C_{DIC}$ indicate the importance of seafloor sediments and the European coastline as a source of these tracers, and show patterns relating to the presence, or absence, of stratification in the North Sea. Variability in $\delta^{13}C_{DIC}$ distributions is mostly related to the balance between primary production and oxic respiration, as well as a localized freshwater input near the coastline. The relationship between $\delta^{13}C_{DIC}$ and the biological component of DIC (DIC_{bio}) allow differences in $\delta^{13}C_{DIC}$ throughout the well-mixed southern North Sea to be attributed to different sources of biologically mediated (i.e. metabolic) DIC production. Metabolic DIC inputs are traced to the European continental coastline because of their strong correlation with coastally-sourced ^{228}Ra .

This study identifies ^{228}Ra as a strong tracer of alkalinity in the North Sea, and suggests further ^{228}Ra sampling in specific locations to better constrain endmember activities and mixing regimes. Furthermore, the relationship between AT and ^{228}Ra in the southern North Sea was used to quantify coastal AT inventory inputs which are of the same magnitude as seasonal AT cycles in the German Bight and which match recently calculated Wadden Sea

AT export rates (*Schwichtenberg*, 2013). Export from the Wadden Sea is further indicated as the source of these coastal inputs, as their DIC:AT ratios point toward anaerobic denitrification as the dominant process responsible for their formation. Finally, coastal AT inputs are shown to play an important role in buffering against acidification of surface waters in the North Sea.

6.7 Acknowledgements

Thank you to E. Jones along with the captain and crew of the R/V Pelagia for helping with sample collection and general cooperation with fieldwork. Thanks also to Arnold van Djik (Utrecht University) for conducting the $\delta^{13}C_{DIC}$ measurements. Also, many thanks to Lesley Salt and Nikki Clargo for providing the DIC and AT data, and Mathilde Hagens and Johannes Pätsch for providing valuable advice and suggestions for the manuscript.

CHAPTER 7

CONCLUSIONS

The purpose of this thesis research is to establish novel flux estimates at the boundaries of various coastal systems, and to assess the importance of these exchanges in the biogeochemical cycling of each system. This research also aims to establish robust methodologies for Ra sampling and analysis in the laboratory, to highlight the utility of Ra as a coastal tracer, and to reveal new applications to guide future Ra-based research. Throughout this research, short-lived Ra is consistently found to be an effective tracer of sediment-water column exchange across the broad spectrum of physical regimes and sediment characteristics encountered at our study sites. In chapter 4, ^{224}Ra is also used as an effective tracer of cross-shelf mixing on the Scotian Shelf, whereas in chapter 6, cross-shelf inputs are calculated using the longer-lived ^{228}Ra isotope.

7.1 Methodological Improvements and Novel Approaches

One significant achievement of this work is the establishment of detailed methodologies for radium sampling and analysis at Dalhousie. This includes building a suitable and efficient apparatus for collecting, filtering, and extracting radium from large volume ($>$ 100 L) seawater samples on a variety of vessels. In chapter 2, the steps required to process RaDeCC data into high quality radium activity data with well defined uncertainties are outlined in detail. This is a significant contribution to the community because it provides future users with the background necessary to not only calculate accurate activities of three isotopes (^{224}Ra , ^{223}Ra, and ^{228}Ra) and their associated uncertainties, but to also conceptually understand the steps taken to do so. Furthermore, this more complete

methodology, which considers both statistical counting uncertainties and propagation of errors, is useful given that the radium scientific community does not currently have a unanimous method for estimating the activities and errors of RaDeCC measurements. This study also includes a rigorous assessment of signal contamination and radium background, which is of value for future studies in regions where low radium activities are common, such as continental shelves. The use of voltage curves to improve instrument efficiency, intercalibration analyses to further quality control the RaDeCC, along with examples of replicate sampling strategies, will help guide future sampling efforts. As a whole, this thesis work will help ensure that future radium collection and analyses both at Dalhousie, and elsewhere, are efficient and reliable.

This study also includes novel radium-based approaches, and is among the first to use radium as a tracer of carbonate system parameters. The water column-based approach highlighted in chapter 3 could be expanded to calculate the fluxes of other important chemical species from the sediments and could be applied in other deep basins, such as Saanich Inlet on the Canadian west coast. On the Scotian Shelf, the 1-D radium-based analytical model introduced by *Moore* (2000) is expanded into two dimensions using a numerical simulation and the Inverse Monte Carlo technique. This approach, which accounts for both coastal and benthic radium sources, can be readily applied to a wide variety of continental shelf systems. The use of radium as a passive tracer in 3 dimensional hydrodynamic models (e.g. the ECOSMO model, chapter 5) presents a powerful tool which can expand the current understanding of radium inputs and, in general, boundary exchanges, over various temporal and spatial scales (for an example of this, see *Kwon et al.* (2014)). Finally, the multi-tracer approach and radium-alkalinity relationships outlined in chapter 6 highlight the importance of sampling radium in parallel to other chemical tracers in future.

7.2 Major Findings

This study addresses a number of gaps in our current understanding of carbon and nutrient cycling in coastal regions. The major findings of the work correspond to the primary objectives listed in chapter 1, and are as follows:

- Benthic fluxes of carbon, oxygen and nutrients were calculated during a Bedford Basin time-series study in the Fall of 2011. DIC effluxes represent rates of carbon

regeneration to the water column and thus provide a more complete understanding of the Bedford Basin carbon cycle. The total carbon efflux during the 30-day time-series is found to be substantial, amounting to $\sim 6\%$ of the annual primary production in the surface layer. We present an hypothesis wherein enhanced delivery of organic material to sediments via a deep-water intrusion event and the autumn bloom fuel these high benthic fluxes. In addition to the DIC flux, effluxes of nitrate and phosphate, as well as sediment oxygen uptake, are observed. Fluxes of these species are consistent with Redfield ratios, indicating that the respired organic material has a marine origin. Finally, the absence of a detectable AT flux points to either predominantly aerobic respiration, the reoxidation of anaerobic products within the sediment, or an AT flux too small to detect above the background.

- On the Scotian Shelf, onshore fluxes of carbon and nutrients in subsurface waters are calculated from transect measurements of ^{224}Ra , DIC and nitrate. Subsurface waters are shown to have excess DIC relative to both their nutrient content and their alkalinity, lending further support to the proposed mechanism of surface CO_2 outgassing via onshore DIC transport. Offshore mixing rates in surface waters of the outer Halifax Harbour are also quantified, which can provide rates of land-ocean interaction for the Scotian Shelf. Finally, this study provides a combined observational-numerical approach to obtaining Ra-based mixing coefficients in more complex regions, such as the Scotian Shelf. This work utilizes and builds upon the 1-D model used in chapter 3 and described by *Moore* (2000).

- The Scotian Shelf exhibits unique Ra distributions when compared with other coastal regions. This is mainly due to the significant ^{224}Ra source observed above offshore banks. Detection of ^{224}Ra in surface waters indicates that products of sediment-water column interaction are rapidly transported into surface waters above the shallow banks.

- Three-dimensional water column sampling, porewater collection, and core incubation experiments led to a North Sea Ra dataset with unprecedented spatial coverage for a single basin. This reflects the methodological improvements made during the study. Substantial ^{224}Ra activities observed throughout the southern North Sea are attributed to extensive sediment-water column exchange, which is then quantified

using a variety of methods. Spatial variability in Ra fluxes correlates with differences in sediment porosity and grain size. Turbulence in the overriding water column is shown to play an important role in regulating fluxes from sandy sediments. Observed ^{224}Ra distributions are well reproduced using observation-based fluxes placed into a 3-D circulation model, providing support for the accuracy of the flux terms. The model output also shows significant seasonal variability in Ra activities that are related to changes in stratification.

- Unraveling of the $\delta^{13}C_{DIC}$ signature of North Sea surface waters show that the high variability is controlled predominantly by the metabolic uptake and release of DIC (i.e. photosynthesis and respiration), with a localized freshwater signal near the coastline. $\delta^{13}C_{DIC}$ is thus presented as a tracer of metabolic DIC production in the North Sea.

- In the well-mixed southern North Sea, where biological production and respiration are expected to be in balance, metabolic DIC is found to be spatially variable and well correlated with the coastally-sourced ^{228}Ra isotope. As a result, the European continental coastline is shown to be an important source of ^{228}Ra, AT, and metabolically produced DIC to the North Sea. Furthermore, ^{228}Ra is revealed as a more useful conservative tracer of North Sea AT than salinity, and coastal AT inputs are shown to play an important role in buffering against acidification of the southern North Sea.

7.3 Outlook and Perspectives

Throughout this study, benthic flux estimates are based predominantly on water column sampling. In the future, one could validate these water-column based approaches by calculating benthic fluxes using the sediment-based Ra:Th disequilibrium method, described recently by *Cai et al.* (2012). This method, which involves measuring depth distributions of ^{224}Ra and ^{228}Th throughout a sediment core, provides a robust and precise measurement of the Ra flux to the overlying water column in the form of a depth integrated ^{224}Ra deficit. A comparative study between this method, the water-column profile approach used in Bedford Basin (chapter 3), as well as the incubation and inventory approaches from the North Sea (chapter 5), would provide important information regarding the caveats of each

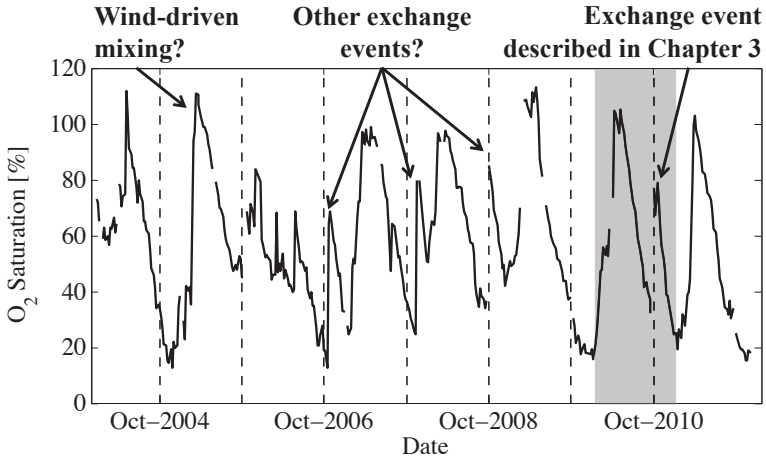

Figure 7.1: In Bedford Basin, large increases in deep water oxygen saturation are observed every year, with many events occurring in the month of October (vertical dashed lines drawn through Oct.1st). More abrupt increases at times of strong surface stratification (i.e. early October) are indicative of deep-water exchange events (*Platt et al.*, 1972), whereas larger, more prolonged increases later in fall or during winter are more likely due to deep wind-driven mixing. In 2010 (shaded box), a very large increase is observed in January, likely due to wind driven mixing, whereas the event in late-September is confirmed to be from deep-water exchange (see chapter 3).

individual method. Furthermore, the Ra:Th disequilibrium method is based on sample counting on the RaDeCC, and thus could be implemented into future work with relative ease.

The Ra isotope datasets presented in this study are the first of their kind in each individual study region. These datasets have led to some key findings in each region, many of which also provide motivation for future Ra studies. In Bedford Basin, for example, the sediments are highly metal-contaminated, and in some areas, they are described as 'methane-charged' (*Buckley and Winters*, 1992). Large-scale resuspension of these sediments, which could be triggered by the type of deep-water exchange event described in chapter 3, could lead to substantial release of harmful contaminants into Halifax Harbour and onto the Scotian Shelf. In chapter 4, rates of offshore mixing out of Halifax Harbour are observed, which combined with transect data of contaminants (e.g. lead concentrations), would yield offshore flux terms across the land-ocean boundary onto the Scotian Shelf. Furthermore, despite the fact that substantial and abrupt deep-water ventilation events within Nova Scotia harbours and basins have been documented along the entire coastline since as

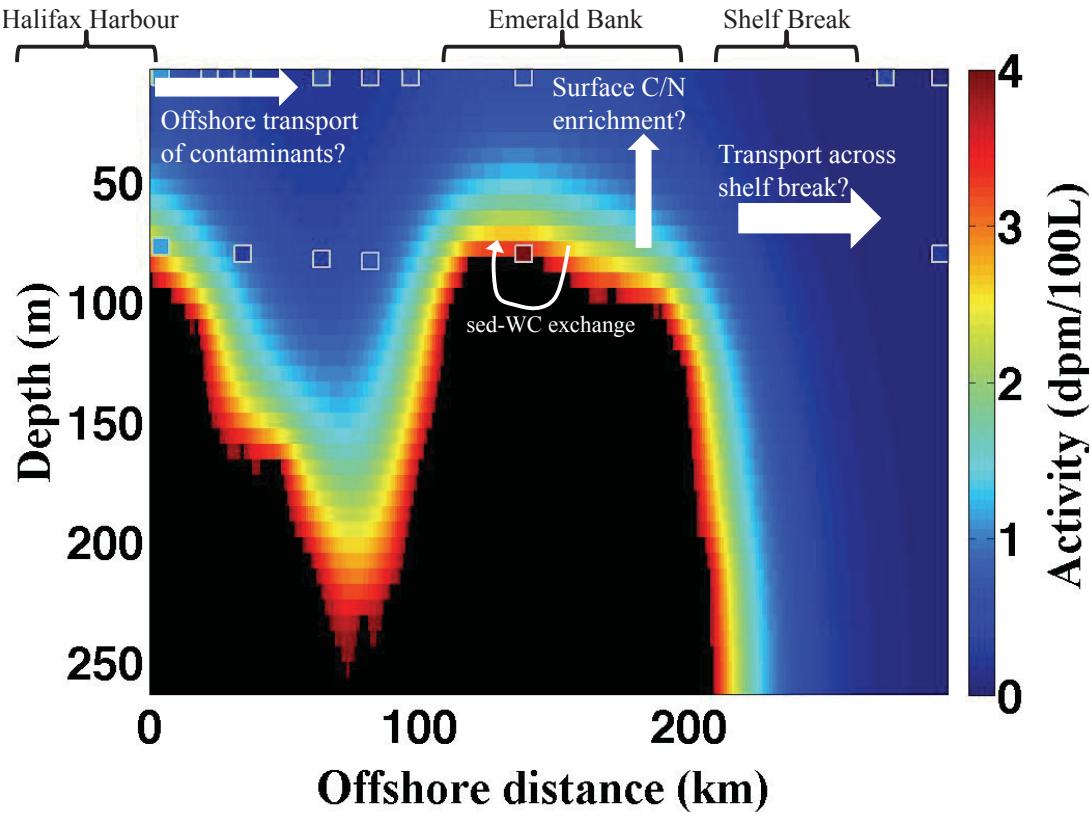

Figure 7.2: Potential future Ra-related studies on the Scotian Shelf. Image of Ra activities along the offshore transect are model results taken from chapter 3, Figure 3.8.

early as 1924 (*Platt et al.*, 1972), this study represents one of the first to assess their biogeochemical impact rather than their basic physical mechanism. Findings presented here should motivate further time-series studies focused on capturing deep-water exchange events in Bedford Basin, especially given that these events are relatively consistent annual October occurrences (Figure 7.1), and are reasonably predictable using wind data.

The presence of short-lived Ra above shallow offshore banks (see chapter 4), which are wide-spread across the Scotian Shelf, provide motivation for future studies in a number of fields (see Figure 7.2). First, detailed sampling offshore of the banks could provide estimates of offshore transport across the shelf-break, a process that has been a major area of uncertainty over decades of coastal carbon cycle studies (e.g. *Rowe et al.* (1986); *Walsh* (1991)). *Stachelhaus et al.* (2012) used offshore Ra transects to quantify transport across mid-shelf fronts on the Mid-Atlantic Bight, but the Scotian Shelf provides a unique

opportunity for shelf-break studies given the nearby short-lived Ra source from offshore banks. Alternatively, further analysis of the sediments atop these banks could provide information about whether the sediment-water column exchange observed in this study plays a role in contributing to other chemical cycles on the Scotian Shelf. Finally, a Scotian Shelf ^{228}Ra budget, potentially established by measuring over the regular Scotian Shelf cruise transects, could provide insight about numerous larger-scale processes, including those illustrated in Figure 7.2.

A fundamental concept of this research is the exploitation and examination of a perturbation to an equilibrium state and the subsequent relaxation of the system back to equilibrium. Excess radium in the water column, the measurement of which forms the backbone of this work, is created by a perturbation to the secular equilibrium whereby particle-reactive radium parents are rapidly scavenged from the water column, and build up in seafloor sediments (see chapter 1). Similarly, the rapid disruption and return to secular equilibrium between various isotope pairs forms the basis for accurate radium counting by the RaDeCC system (chapter 2). Throughout the remainder of the study, radium is used as a tool to trace processes that occur following various disruptions from chemical or thermodynamic equilibrium: in Bedford Basin (chapter 3) substantial organic matter delivery by a ventilation event represents a large perturbation, and the relaxation of the system towards equilibrium occurs in the form of high benthic fluxes. Key derived variables, such as DIC$_{ex}$ (chapter 4), and DIC$_{bio}$ (chapter 6) describe the extent of metabolic disequilibrium that results from rapid transformation of carbon and nutrients by biological activities. Finally, anthropogenic CO_2 release represents a global climate perturbation. One response to this perturbation is the increased uptake of CO_2 by the surface oceans, the result of which is ocean acidification. Using techniques building upon decades of prior research in the fields of radiochemistry and biogeochemistry, this study represents a contribution towards a greater understanding of how coastal systems have responded, and will continue to respond to such perturbations on both local and global scales.

APPENDIX A

NORTH SEA RA DATA TABLE

Surface (5m) Ra activities and a sampling summary for all 61 stations used in chapter 5 are provided in Table A1.

Table A.1: Summary of samples. Additional sampling at each station is indicated by an 'x'. NBP = Near Bottom Profile, Incube = Incubation Samples, PW = Pore Water Samples.

Station	Latitude °N	Longitude °E	^{224}Ra*	^{223}Ra*	NBP	Incube	PW
1	51.1	1.5	5.7	0.9			
2	51.6	2	5.3	0.4	x	x	
3	51.5	3	9.7	2.2			
4	52	3.5	10.9	1.2			
5	52	2.5	4.3	0.3			
6	52.6	2.5	4.8	0.5			
7	52.6	3.5	5.8	0.9	x	x	
8	52.6	4	8.7	0.7			
9	53.2	4.5	11.7	1.5			
10	53.2	3.5	6.1	1			
11	53.2	2.5	5.8	0.9	x	x	x
12	53.2	1.5	6.5	0.8			
13	53.8	0.5	5	0.6			
14	53.8	1.5	5	0.4			
15	53.8	2.8	7.5	0.9			
16	53.8	4	4.6	0.7			

Continued on next page

Table A.1 – *Continued from previous page*

Station	Latitude °N	Longitude °E	^{224}Ra*	^{223}Ra*	NBP	Incube	PW
17	53.8	5.3	7.6	0.8	x	x	x
18	53.8	6.5	10.4	1.8			
19	54	7.5	10.4	2.2			
20	54.4	8.1	14.4	1.6	x	x	
21	54.4	7.5	6	1			
22	54.4	6.5	5.5	0.7			
23	54.4	5.2	4.6	0.9			
24	54.4	4	5.3	0.8			
25	54.4	3	4.5	0.6			
26	54.4	1.5	1.2	0.2			
27	54.4	0.5	0.7	0			
28	55	7.5	7.2	0.8			
29	55	6.5	4.5	0.9			
30	55	5	2.5	0.4	x	x	x
31	55	3.5	2.2	0.3			
32	55	2	3.4	0.1	x	x	x
33	55	0.5	0.5	0	x		
34	55	-0.5	0.2	0			
35	56	-1.5	0.9	0.1			
36	56	-0.5	0	0			
38	56	2	0.5	0	x	x	x
39	56	3.5	0.4	0			
40	56	5	0.7	0			
41	56	6.5	3.3	0.7			
42	56	7.5	7.4	0.7	x	x	
43	57	7.5	5.1	0.3			
44	57	6.5	2	0.2			
45	57	5.3	0	0	x	x	
46	57	3.8	0.3	0			
47	57	2.2	0.6	0			

Continued on next page

Table A.1 – *Continued from previous page*

Station	Latitude °N	Longitude °E	^{224}Ra*	^{223}Ra*	NBP	Incube	PW
48	57	0.9	0.1	0			
49	57	-0.5	0.5	0			
50	57	-1.5	0.8	0			
51	57.5	6	0.5	0			
52	57.5	7.5	0.8	0.1			
53	57.5	8.5	3	0.2			
59	58	4.2	0.5	0			
60	58	5.5	0.7	0.1			
61	58	8.5	0.9	0			
62	58	9.5	3.8	0.1	x	x	
63	58	10.4	2.8	0.1			
64	58.5	10.1	0.6	0.1			
65	58.5	9.5	0.3	0	x	x	
66	58.2	8.5	1.9	0.4			
67	58	6.5	1.1	0.1			

*Units of Ra activities are dpm 100 L $^{-1}$

APPENDIX B

COPYRIGHT PERMISSION

JOHN WILEY AND SONS LICENSE TERMS AND CONDITIONS

Apr 06, 2015

This Agreement between William Burt ("You") and John Wiley and Sons ("John Wiley and Sons") consists of your license details and the terms and conditions provided by John Wiley and Sons and Copyright Clearance Center.

License Number	3583211310756
License date	Mar 06, 2015
Licensed Content Publisher	John Wiley and Sons
Licensed Content Publication	Global Biogeochemical Cycles
Licensed Content Title	Radium isotopes as a tracer of sediment-water column exchange in the North Sea
Licensed Content Author	W. J. Burt,H. Thomas,J. Pätsch,A. M. Omar,C. Schrum,U. Daewel,H. Brenner,H. J. W. Baar
Licensed Content Date	Aug 12, 2014
Pages	19
Type of use	Dissertation/Thesis
Requestor type	Author of this Wiley article
Format	Electronic
Portion	Full article
Will you be translating?	No
Title of your thesis / dissertation	THE USE OF RADIUM ISOTOPES TO INVESTIGATE BOUNDARY EXCHANGES IN COASTAL OCEAN SYSTEMS
Expected completion date	Apr 2015
Expected size (number of pages)	150
Requestor Location	William Burt Department of Oceanography 1355 Oxford St. Halifax, NS B3H4J1 Canada Attn: William Burt
Billing Type	Invoice
Billing Address	William Burt Department of Oceanography 1355 Oxford St. Halifax, NS B3H4J1 Canada Attn: William Burt
Total	0.00 USD
Terms and Conditions	

BIBLIOGRAPHY

Ahad, J. M., J. A. Barth, R. S. Ganeshram, R. G. Spencer, and G. Uher, Controls on carbon cycling in two contrasting temperate zone estuaries: The Tyne and Tweed, UK, *Estuarine, Coastal and Shelf Science*, *78*, 685 – 693, 2008.

Aller, R. C., Diagenetic processes near the sediment-water interface of Long Island Sound, *Adv. Geophys*, *22*, 237–350, 1980.

Amann, T., A. Weiss, and J. Hartmann, Inorganic carbon fluxes in the inner Elbe estuary, Germany, *Estuaries and Coasts*, pp. 1–19, 2014.

Armstrong, R. A., M. L. Peterson, C. Lee, and S. G. Wakeham, Settling velocity spectra and the ballast ratio hypothesis, *Deep Sea Research Part II: Topical Studies in Oceanography*, *56*, 1470–1478, 2009.

Azetsu-Scott, K., and B. D. Johnson, Time series of the vertical distribution of particles during and after a spring phytoplankton bloom in a coastal basin, *Continental Shelf Research*, *14*, 687–705, 1994.

Barthel, K., U. Daewel, D. Pushpadas, C. Schrum, M. Årthun, and H. Wehde, Resolving frontal structures: on the payoff using a less diffusive but computationally more expensive advection scheme, *Ocean Dynamics*, *62*, 1457–1470, 2012.

Beck, M., O. Dellwig, G. Liebezeit, B. Schnetger, and H.-J. Brumsack, Spatial and seasonal variations of sulphate, dissolved organic carbon, and nutrients in deep pore waters of intertidal flat sediments, *Estuarine, Coastal and Shelf Science*, *79*, 307–316, 2008.

Berelson, W., D. Hammond, and C. Fuller, Radon-222 as a tracer for mixing in the water column and benthic exchange in the southern California borderland, *Earth and Planetary Science Letters*, *61*, 41–54, 1982.

Berelson, W., D. Hammond, and K. Johnson, Benthic fluxes and the cycling of biogenic silica and carbon in two southern California borderland basins, *Geochimica et Cosmochimica Acta*, *51*, 1345–1363, 1987.

Biscaye, P. E., C. N. Flagg, and P. G. Falkowski, The shelf edge exchange processes experiment, SEEP-II: an introduction to hypotheses, results and conclusions, *Deep Sea Research Part II: Topical Studies in Oceanography*, *41*, 231 – 252, 1994.

Boehme, S. E., C. L. Sabine, and C. E. Reimers, CO_2 fluxes from a coastal transect: a time-series approach, *Marine Chemistry*, *63*, 49–67, 1998.

Borges, A., and N. Gypens, Carbonate chemistry in the coastal zone responds more strongly to eutrophication than to ocean acidification, *Limnology & Oceanography*, *55*, 2010.

Böttcher, M. E., B. Oelschläger, T. Höpner, H.-J. Brumsack, and J. Rullkötter, Sulfate reduction related to the early diagenetic degradation of organic matter and "black spot" formation in tidal sandflats of the German Wadden Sea (southern North Sea): stable isotope (^{13}C,^{34}S,^{18}O) and other geochemical results, *Organic Geochemistry*, *29*, 1517–1530, 1998.

Böttcher, M. E., B. Hespenheide, E. Llobet-Brossa, C. Beardsley, O. Larsen, A. Schramm, A. Wieland, G. Böttcher, U.-G. Berninger, and R. Amann, The biogeochemistry, stable isotope geochemistry, and microbial community structure of a temperate intertidal mudflat: an integrated study, *Continental Shelf Research*, *20*, 1749–1769, 2000.

Boudreau, B. P., A. Mucci, B. Sundby, G. W. Luther, and N. Silverberg, Comparative diagenesis at three sites on the Canadian continental margin, *Journal of Marine Research*, *56*, 1259–1284, 1998.

Bozec, Y., H. Thomas, K. Elkalay, and H. J. de Baar, The continental shelf pump for CO_2 in the North Sea–evidence from summer observation, *Marine Chemistry*, *93*, 131–147, 2005.

Bozec, Y., H. Thomas, L.-S. Schiettecatte, A. V. Borges, K. Elkalay, and H. J. de Baar, Assessment of the processes controlling seasonal variations of dissolved inorganic carbon in the North Sea, *Limnology and Oceanography*, *51*, 2746–2762, 2006.

Braeckman, U., M. Y. Foshtomi, D. Van Gansbeke, F. Meysman, K. Soetaert, M. Vincx, and J. Vanaverbeke, Variable importance of macrofaunal functional biodiversity for biogeochemical cycling in temperate coastal sediments, *Ecosystems*, *17*, 720–737, 2014.

Brander, K., and P. C. Hurley, Distribution of early-stage Atlantic cod (gadus morhua), haddock (melanogrammus aeglefinus), and witch flounder (glyptocephalus cynoglossus) eggs on the Scotian Shelf: a reappraisal of evidence on the coupling of cod spawning and plankton production, *Canadian Journal of Fisheries and Aquatic Sciences*, *49*, 238–251, 1992.

Brasse, S., A. Reimer, R. Seifert, and W. Michaelis, The influence of intertidal mudflats on the dissolved inorganic carbon and total alkalinity distribution in the German Bight, southeastern North Sea, *Journal of Sea Research*, *42*, 93–103, 1999.

Broecker, W. S., and E. Maier-Reimer, The influence of air and sea exchange on the carbon isotope distribution in the sea, *Global Biogeochemical Cycles*, *6*, 315–320, 1992.

Buckley, D., and B. Hargrave, Geochemical characteristics of surface sediments, in *Investigations of Marine Environmental Quality in Halifax Harbour*, edited by H. Nicholls, pp. 9–36, Can. Tech. Rep. Fish Aqua. Sci., 1989.

Buckley, D. E., Deposition and diagenetic alteration of sediment in emerald basin, the Scotian Shelf, *Continental Shelf Research*, *11*, 1099 – 1122, 1991.

Buckley, D. E., and G. V. Winters, Geochemical characteristics of contaminated surficial sediments in Halifax Harbour: impact of waste discharge, *Canadian Journal of Earth Sciences*, *29*, 2617–2639, 1992.

Buckley, D. E., J. N. Smith, and G. V. Winters, Accumulation of contaminant metals in marine sediments of Halifax Harbour, Nova Scotia: environmental factors and historical trends, *Applied Geochemistry*, *10*, 175–195, 1995.

Burdige, D., Estuarine and coastal sediments – coupled biogeochemical cycling, in *Treatise on Estuarine and Coastal Science, Vol. 5*, edited by E. Wolanski and D. McLusky, Academic Press, Waltham, 2011.

Burnett, W. C., H. Bokuniewicz, M. Huettel, W. S. Moore, and M. Taniguchi, Groundwater and pore water inputs to the coastal zone, *Biogeochemistry*, *66*, 3–33, 2003.

Burt, W. J., H. Thomas, K. Fennel, and E. Horne, Sediment-water column fluxes of carbon, oxygen and nutrients in Bedford Basin, Nova Scotia, inferred from Ra-224 measurements, *Biogeosciences*, *10*, 53–66, 2013.

Cai, P., X. Shi, W. Moore, and M. Dai, Measurement of 224Ra:228Th disequilibrium in coastal sediments using a delayed coincidence counter, *Marine Chemistry*, *138139*, 1 – 6, 2012.

Cai, P., X. Shi, W. Moore, S. Peng, G. Wang, and M. Dai, 224Ra:228Th disequilbrium in coastal sediments: Implications for solute transfer across the sediment-water interface, *Geochim. Cosmochim. Acta.*, *125*, 68–84, 2014.

Charette, M. A., and J. C. Scholten, Marine chemistry special issue: the renaissance of radium isotopic tracers in marine processes studies, *Marine Chemistry*, *109*, 185–187, 2008.

Charette, M. A., M. E. Gonneea, P. J. Morris, P. Statham, G. Fones, H. Planquette, I. Salter, and A. N. Garabato, Radium isotopes as tracers of iron sources fueling a Southern ocean phytoplankton bloom, *Deep Sea Research Part II: Topical Studies in Oceanography*, *54*, 1989–1998, 2007.

Charette, M. A., H. Dulaiova, M. E. Gonneea, P. B. Henderson, W. S. Moore, J. C. Scholten, and M. Pham, Geotraces radium isotopes interlaboratory comparison experiment, *Limnol. Oceanogr.: Methods*, *10*, 451–463, 2012.

Chen, C.-T. A., and A. V. Borges, Reconciling opposing views on carbon cycling in the coastal ocean: Continental shelves as sinks and near-shore ecosystems as sources of atmospheric CO_2, *Deep Sea Research Part II: Topical Studies in Oceanography*, *56*, 578–590, 2009.

Chen, C.-T. A., and S.-L. Wang, Carbon, alkalinity and nutrient budgets on the East China Sea continental shelf, *Journal of Geophysical Research: Oceans (1978–2012)*, *104*, 20675–20686, 1999.

Coachman, L., and J. Walsh, A diffusion-model of cross-shelf exchange of nutrients in the southeastern Bering Sea, *Deep Sea Research Part I: Oceanographic Research Papers*, *28*, 819–846, 1981.

Colbert, S. L., and D. E. Hammond, Temporal and spatial variability of radium in the coastal ocean and its impact on computation of nearshore cross-shelf mixing rates, *Continental Shelf Research*, *27*, 1477–1500, 2007.

Colbert, S. L., and D. E. Hammond, Shoreline and seafloor fluxes of water and short-lived ra isotopes to surface water of san pedro bay, ca, *Marine Chemistry*, *108*, 1–17, 2008.

Daewel, U., and C. Schrum, Simulating long-term dynamics of the coupled North Sea and Baltic sea ecosystem with ECOSMO II: model description and validation, *Journal of Marine Systems*, *119*, 30–49, 2013.

Dauwe, B., P. M. Herman, and C. Heip, Community structure and bioturbation potential of macrofauna at four North Sea stations with contrasting food supply, *Marine Ecology Progress Series*, *173*, 1998.

de Haas, H., T. C. van Weering, and H. de Stigter, Organic carbon in shelf seas: sinks or sources, processes and products, *Continental Shelf Research*, *22*, 691–717, 2002.

DeGrandpre, M., G. Olbu, C. Beatty, and T. Hammar, Air-sea CO_2 fluxes on the US Middle Atlantic Bight, *Deep Sea Research Part II: Topical Studies in Oceanography*, *49*, 4355–4367, 2002.

Dickson, A., An exact definition of total alkalinity and a procedure for the estimation of alkalinity and total inorganic carbon from titration data, *Deep Sea Research Part A. Oceanographic Research Papers*, *28*, 609–623, 1981.

Dickson, A. G., C. L. Sabine, and J. R. Christian, *Guide to best practices for ocean CO_2 measurements*, North Pacific Marine Science Organization, 2007.

Doney, S. C., V. J. Fabry, R. A. Feely, and J. A. Kleypas, Ocean acidification: the other CO_2 problem, *Marine Science*, *1*, 169–192, 2009.

Duarte, C. M., I. E. Hendriks, T. S. Moore, Y. S. Olsen, A. Steckbauer, L. Ramajo, J. Carstensen, J. A. Trotter, and M. McCulloch, Is ocean acidification an open-ocean syndrome? Understanding anthropogenic impacts on seawater pH, *Estuaries and Coasts*, *36*, 221–236, 2013.

Dulaiova, H., and W. C. Burnett, Evaluation of the flushing rates of apalachicola bay, florida via natural geochemical tracers, *Marine Chemistry*, *109*, 395–408, 2008.

Dulaiova, H., M. Ardelan, P. B. Henderson, and M. A. Charette, Shelf-derived iron inputs drive biological productivity in the southern Drake Passage, *Global Biogeochemical Cycles*, *23*, 2009.

Emeis, K.-C., J. van Beusekom, U. Callies, R. Ebinghaus, A. Kannen, G. Kraus, I. Kröncke, H. Lenhart, I. Lorkowski, V. Matthias, et al., The North Sea–A shelf sea in the Anthropocene, *Journal of Marine Systems*, *141*, 18–33, 2015.

Emerson, S., R. Jahnke, and D. Heggie, Sediment-water exchange in shallow water estuarine sediments, *Journal of Marine Research*, *42*, 709–730, 1984.

Fader, G. B., and R. Miller, *Surficial geology, halifax harbour, nova scotia*, Geological Survey of Canada, 2008.

Fennel, K., The role of continental shelves in nitrogen and carbon cycling: Northwestern North Atlantic case study, *Ocean Science*, *6*, 539–548, 2010.

Fennel, K., J. Wilkin, J. Levin, J. Moisan, J. O'Reilly, and D. Haidvogel, Nitrogen cycling in the Middle Atlantic Bight: Results from a three-dimensional model and implications for the North Atlantic nitrogen budget, *Global Biogeochemical Cycles*, *20*, 2006.

Fennel, K., D. Brady, D. DiToro, R. W. Fulweiler, W. S. Gardner, A. Giblin, M. J. McCarthy, A. Rao, S. Seitzinger, M. Thouvenot-Korppoo, et al., Modeling denitrification in aquatic sediments, *Biogeochemistry*, *93*, 159–178, 2009.

Fettweis, M., B. Nechad, and D. Van den Eynde, An estimate of the suspended particulate matter (SPM) transport in the southern North Sea using SeaWiFS images, in situ measurements and numerical model results, *Continental Shelf Research*, *27*, 1568–1583, 2007.

Frankignoulle, M., and A. V. Borges, European continental shelf as a significant sink for atmospheric carbon dioxide, *Global biogeochemical cycles*, *15*, 569–576, 2001.

Garcia-Solsona, E., J. Garcia-Orellana, P. Masqu, and H. Dulaiova, Uncertainties associated with 223ra and 224ra measurements in water via a delayed coincidence counter (radecc), *Marine Chemistry*, *109*, 198–219, 2008.

Gattuso, J.-P., M. Frankignoulle, and R. Wollast, Carbon and carbonate metabolism in coastal aquatic ecosystems, *Annual Review of Ecology and Systematics*, pp. 405–434, 1998.

Giffin, C., A. Kaufman, and W. Broecker, Delayed coincidence counter for the assay of actinon and thoron, *Journal of Geophysical Research*, *68*, 1749–1757, 1963.

Grant, J., C. Emerson, B. Hargrave, and J. Shortle, Benthic Oxygen-Consumption on Continental Shelves off Eastern Canada, *Continental Shelf Research*, *11*, 1083–1097, 1991.

Greenan, B., B. Petrie, W. Harrison, and P. Strain, The onset and evolution of a spring bloom on the Scotian Shelf, *Limnology and Oceanography*, *53*, 1759, 2008.

Gruber, N., C. D. Keeling, R. B. Bacastow, P. R. Guenther, T. J. Lueker, M. Wahlen, H. A. J. Meijer, W. G. Mook, and T. F. Stocker, Spatiotemporal patterns of carbon-13 in the global surface oceans and the oceanic suess effect, *Global Biogeochemical Cycles*, *13*, 307–335, 1999.

Han, G., and J. W. Loder, Three-dimensional seasonal-mean circulation and hydrography on the eastern Scotian Shelf, *Journal of Geophysical Research: Oceans (1978–2012)*, *108*, 2003.

Hancock, G., I. Webster, P. Ford, and W. Moore, Using Ra isotopes to examine transport processes controlling benthic fluxes into a shallow estuarine lagoon, *Geochimica et Cosmochimica Acta*, *64*, 3685–3699, 2000.

Hancock, G. J., I. Webster, T. C. Stieglitz, et al., Horizontal mixing of Great Barrier Reef waters: Offshore diffusivity determined from radium isotope distribution, *Journal of Geophysical Research: Oceans (1978–2012)*, *111*, 2006.

Hannah, C. G., J. A. Shore, J. W. Loder, and C. E. Naimie, Seasonal circulation on the western and central Scotian Shelf, *Journal of Physical Oceanography*, *31*, 591–615, 2001.

Hargrave, B., Seasonal changes in oxygen uptake by settled particulate matter and sediments in a marine bay, *Journal of the Fisheries Board of Canada*, *35*, 1621–1628, 1978.

Hargrave, B., and S. Taguchi, Origin of deposited material sedimented in a marine bay, *Journal of the Fisheries Board of Canada*, *35*, 1604–1613, 1978.

Hargrave, B., G. A. Phillips, and S. Taguchi, *Sedimentation measurements in Bedford Basin, 1973-1974*, Research and Development Directorate, Marine Ecology Laboratory, Bedford Institute of Oceanography, 1976.

Hargrave, B., D. Peer, and H. Wiele, Benthic biological observations, in *Investigations of Marine Environmental Quality in Halifax Harbour*, edited by H. Nicholls, pp. 37–45, Can. Tech. Rep. Fish Aqua. Sci., 1989.

Himmler, T., Signitures of geochemical changes at methane-seeps as recorded by seep carbonates, Ph.D. thesis, University of Bremen, 2011.

Hoppema, J., The distribution and seasonal variation of alkalinity in the southern bight of the North Sea and in the western Wadden Sea, *Netherlands journal of sea research*, *26*, 11–23, 1990.

Houghton, R. W., P. C. Smith, and R. O. Fournier, A simple model for cross-shelf mixing on the Scotian Shelf, *Journal of the Fisheries Research Board of Canada*, *35*, 414–421, 1978.

Huettel, M., and G. Gust, Solute release mechanisms from confined sediment cores in stirred benthic chambers and flume flows., *Marine ecology progress series. Oldendorf*, *82*, 187–197, 1992.

Huettel, M., and I. Webster, Porewater flow in permeable sediment, in *The benthic boundary layer: Transport processes and biogeochemistry*, edited by B. Boudreau and B. Jørgensen, pp. 144–179, Oxford University Press, New York, 2001.

Huthnance, J. M., Circulation, exchange and water masses at the ocean margin: the role of physical processes at the shelf edge, *Progress in Oceanography*, *35*, 353–431, 1995.

IPCC, Contribution of working groups i, ii and iii to the fourth assessment report of the intergovernmental panel on climate change, in *Climate Change 2007: Synthesis report*, edited by R. Pachauri and A. Reisinger, IPCC, Geneva, Switzerland, 2007.

Jahnke, R., M. Richards, J. Nelson, C. Robertson, A. Rao, and D. Jahnke, Organic matter remineralization and porewater exchange rates in permeable South Atlantic Bight continental shelf sediments, *Continental Shelf Research*, *25*, 1433–1452, 2005.

Jahnke, R. A., and D. B. Jahnke, Rates of c, n, p and si recycling and denitrification at the US Mid-Atlantic continental slope depocenter, *Deep Sea Research Part I: Oceanographic Research Papers*, *47*, 1405–1428, 2000.

Jahnke, R. A., J. R. Nelson, R. L. Marinelli, and J. E. Eckman, Benthic flux of biogenic elements on the southeastern US continental shelf: influence of pore water advective transport and benthic microalgae, *Continental Shelf Research*, *20*, 109–127, 2000.

Janssen, F., P. Faerber, M. Huettel, V. Meyer, and U. Witte, Pore-water advection and solute fluxes in permeable marine sediments (I): Calibration and performance of the novel benthic chamber system sandy, *Limnology and Oceanography*, *50*, 768–778, 2005a.

Janssen, F., M. Huettel, and U. Witte, Pore-water advection and solute fluxes in permeable marine sediments (II): Benthic respiration at three sandy sites with different permeabilities (German Bight, North Sea), *Limnology and Oceanography*, *50*, 779–792, 2005b.

Johnson, K., K. Wills, D. Butler, W. Johnson, and C. Wong, Coulometric total carbon dioxide analysis for marine studies: maximizing the performance of an automated gas extraction system and coulometric detector, *Marine Chemistry*, *44*, 167–187, 1993.

Kadko, D., and R. Muench, Evaluation of shelf-basin interaction in the western arctic by use of short-lived radium isotopes: The importance of mesoscale processes, *Deep Sea Research Part II: Topical Studies in Oceanography*, *52*, 3227–3244, 2005.

Kaufman, A., R. Trier, W. Broecker, and H. Feely, Distribution of 228Ra in the world ocean, *Journal of Geophysical Research*, *78*, 8827–8848, 1973.

Kaufman, A., Y.-H. Li, and K. K. Turekian, The removal rates of ^{234}Th and ^{228}Th from waters of the New York Bight, *Earth and Planetary Science Letters*, *54*, 385–392, 1981.

Kelly, R., and S. Moran, Seasonal changes in groundwater input to a well-mixed estuary estimated using radium isotopes and implications for coastal nutrient budgets, *Limnology and Oceanography*, *47*, 1796–1807, 2002.

Kempe, S., and K. Pegler, Sinks and sources of CO_2 in coastal seas: the North Sea, *Tellus B*, *43*, 224–235, 1991.

Kepkay, P., S. Niven, and J. Jellett, Colloidal organic carbon and phytoplankton speciation during a coastal bloom, *Journal of plankton research*, *19*, 369–389, 1997.

Ketchum, H., and D. J. Keen, The accumulation of river water over the continental shelf between Cape Cod and Chesapeake Bay, *Journal in Marine Biology and Oceanography*, *3*, 346–357, 1955.

Kühn, W., J. Pätsch, H. Thomas, A. V. Borges, L.-S. Schiettecatte, Y. Bozec, and A. Prowe, Nitrogen and carbon cycling in the North Sea and exchange with the North Atlantic–A model study, Part II: Carbon budget and fluxes, *Continental Shelf Research*, *30*, 1701–1716, 2010.

Kwon, E. Y., G. Kim, F. Primeau, W. S. Moore, H.-M. Cho, T. DeVries, J. L. Sarmiento, M. A. Charette, and Y.-K. Cho, Global estimate of submarine groundwater discharge based on an observationally constrained radium isotope model, *Geophysical Research Letters*, 2014.

Lee, A., North Sea: Physical oceanography, in *Physical and Chemical Oceanography, vol. 24B*, edited by F. Banner, M. Collins, and K. Massie, Elsevier, Amsterdam, 1980.

Lettmann, K. A., N. Riedinger, R. Ramlau, N. Knab, M. E. Böttcher, A. Khalili, J.-O. Wolff, and B. B. Jørgensen, Estimation of biogeochemical rates from concentration profiles: A novel inverse method, *Estuarine, Coastal and Shelf Science*, *100*, 26–37, 2012.

Lewis, E., and D. Wallace, CO_2SYS–program developed for the CO_2 system calculations. carbon dioxide information analysis center, *Tech. rep.*, Report ORNL/CDIAC-105, Oak Ridge, Tenn., USA, 1998.

Li, C., and W.-J. Cai, On the calculation of eddy diffusivity in the shelf water from radium isotopes: High sensitivity to advection, *Journal of Marine Systems*, *86*, 28–33, 2011.

Li, W., and P. Dickie, Monitoring phytoplankton, bacterioplankton, and virioplankton in a coastal inlet (Bedford Basin) by flow cytometry, *Cytometry*, *44*, 236–246, 2001.

Li, W. K., and W. G. Harrison, Propagation of an atmospheric climate signal to phytoplankton in a small marine basin, *Limnol. Oceanogr*, *53*, 1734–1745, 2008.

Loder, J. W., C. K. Ross, and P. C. Smith, A space-and time-scale characterization of circulation and mixing over submarine banks, with application to the northwestern Atlantic continental shelf, *Canadian Journal of Fisheries and Aquatic Sciences*, *45*, 1860–1885, 1988.

Loder, J. W., G. Han, C. G. Hannah, D. A. Greenberg, and P. C. Smith, Hydrography and baroclinic circulation in the Scotian Shelf region: winter versus summer, *Canadian Journal of Fisheries and Aquatic Sciences*, *54*, 40–56, 1997.

Lohse, L., E. Epping, W. Helder, and W. Van Raaphorst, Oxygen pore water profiles in continental shelf sediments of the North Sea: turbulent versus molecular diffusion, *Marine Ecology Progress Series*, *145*, 63–75, 1996.

Luff, R., and A. Moll, Seasonal dynamics of the North Sea sediments using a three-dimensional coupled sediment–water model system, *Continental Shelf Research*, *24*, 1099–1127, 2004.

Men, W., F. Wang, and G. Liu, 224Ra and its implications in the East China Sea, *Journal of Radioanalytical and Nuclear Chemistry*, *288*, 189–195, 2011.

Meybeck, M., H. Dürr, S. Roussennac, and W. Ludwig, Regional seas and their interception of riverine fluxes to oceans, *Marine Chemistry*, *106*, 301–325, 2007.

Moore, W., M. Beck, T. Riedel, M. R. van der Loeff, O. Dellwig, T. Shaw, B. Schnetger, and H.-J. Brumsack, Radium-based pore water fluxes of silica, alkalinity, manganese, doc, and uranium: A decade of studies in the German Wadden Sea, *Geochimica et Cosmochimica Acta*, *75*, 6535 – 6555, 2011.

Moore, W. S., Sampling 228Ra in the deep ocean, *Deep Sea Research and Oceanographic Abstracts*, *23*, 647–651, 1976.

Moore, W. S., Radium 228 in the South Atlantic Bight, *Journal of Geophysical Research: Oceans (1978–2012)*, *92*, 5177–5190, 1987.

Moore, W. S., Determining coastal mixing rates using radium isotopes, *Continental Shelf Research*, *20*, 1993–2007, 2000.

Moore, W. S., Sources and fluxes of submarine groundwater discharge delineated by radium isotopes, *Biogeochemistry*, *66*, 75–93, 2003.

Moore, W. S., Seasonal distribution and flux of radium isotopes on the southeastern US continental shelf, *Journal of Geophysical Research: Oceans (1978–2012)*, *112*, 2007.

Moore, W. S., Fifteen years experience in measuring 224Ra and 223Ra by delayed-coincidence counting, *Marine Chemistry*, *109*, 188–197, 2008.

Moore, W. S., and R. Arnold, Measurement of 223Ra and 224Ra in coastal waters using a delayed coincidence counter, *Journal of Geophysical Research: Oceans*, *101*, 1321–1329, 1996.

Moore, W. S., and P. Cai, Calibration of radecc systems for ^{223}Ra measurements, *Marine Chemistry*, *156*, 130–137, 2013.

Moore, W. S., and J. de Oliveira, Determination of residence time and mixing processes of the Ubatuba, Brazil, inner shelf waters using natural Ra isotopes, *Estuarine, Coastal and Shelf Science*, *76*, 512–521, 2008.

Moore, W. S., and D. F. Reid, Extraction of radium from natural waters using manganese-impregnated acrylic fibers, *Journal of Geophysical Research*, *78*, 8880–8886, 1973.

Moore, W. S., J. O. Blanton, and S. B. Joye, Estimates of flushing times, submarine groundwater discharge, and nutrient fluxes to Okatee Estuary, SouthCarolina, *Journal of Geophysical Research: Oceans (1978–2012)*, *111*, 2006.

Mucci, A., B. Sundby, M. Gehlen, T. Arakaki, S. Zhong, and N. Silverberg, The fate of carbon in continental shelf sediments of eastern canada: a case study, *Deep Sea Research Part II: Topical Studies in Oceanography*, *47*, 733–760, 2000.

Olsen, A., and U. Ninnemann, Large δ13C gradients in the preindustrial North Atlantic revealed, *Science*, *330*, 658–659, 2010.

Omar, A., A. Olsen, T. Johannessen, M. Hoppema, H. Thomas, and A. Borges, Spatiotemporal variations of fCO_2 in the North Sea, *Ocean Science*, *6*, 2010.

Orr, J. C., V. J. Fabry, O. Aumont, L. Bopp, S. C. Doney, R. A. Feely, A. Gnanadesikan, N. Gruber, A. Ishida, F. Joos, et al., Anthropogenic ocean acidification over the twenty-first century and its impact on calcifying organisms, *Nature*, *437*, 681–686, 2005.

Pan, Y., and D. Rao, Impacts of domestic sewage effluent on phytoplankton from Bedford Basin, eastern Canada, *Marine pollution bulletin*, *34*, 1001–1005, 1997.

Pätsch, J., and W. Kühn, Nitrogen and carbon cycling in the North Sea and exchange with the North Atlantica model study. part i. nitrogen budget and fluxes, *Continental Shelf Research*, *28*, 767–787, 2008.

Petrie, B., and P. Yeats, Simple models of the circulation, dissolved metals, suspended solids and nutrients in Halifax Harbour, *Water Poll. Res. J. Canada*, *25*, 325–349, 1990.

Platt, T., Analysis of the importance of spatial and temporal heterogeneity in the estimation of annual production by phytoplankton in a small, enriched, marine basin, *Journal of Experimental Marine Biology and Ecology*, *18*, 99–109, 1975.

Platt, T., and R. Conover, Variability and its effect on the 24h chlorophyll budget of a small marine basin, *Marine Biology*, *10*, 52–65, 1971.

Platt, T., A. Prakash, and B. Irwin, Phytoplankton nutrients and flushing of inlets on the coast of Nova Scotia, *Natur Can*, 1972.

Precht, E., and M. Huettel, Advective pore-water exchange driven by surface gravity waves and its ecological implications, *Limnology and Oceanography*, *48*, 1674–1684, 2003.

Provoost, P., S. van Heuven, K. Soetaert, R. Laane, and J. Middelburg, Seasonal and long-term changes in pH in the Dutch coastal zone, *Biogeosciences*, *7*, 3869–3878, 2010.

Prowe, A. F., H. Thomas, J. Pätsch, W. Kühn, Y. Bozec, L.-S. Schiettecatte, A. V. Borges, and H. J. de Baar, Mechanisms controlling the air–sea CO2 flux in the North Sea, *Continental Shelf Research*, *29*, 1801–1808, 2009.

Punshon, S., and R. M. Moore, Nitrous oxide production and consumption in a eutrophic coastal embayment, *Marine chemistry*, *91*, 37–51, 2004.

Quay, P., and J. Stutsman, Surface layer carbon budget for the subtropical N. Pacific: δ13C constraints at Station ALOHA, *Deep Sea Research Part I: Oceanographic Research Papers*, *50*, 1045–1061, 2003.

Quay, P., R. Sonnerup, J. Stutsman, J. Maurer, A. Körtzinger, X. Padin, and C. Robinson, Anthropogenic co_2 accumulation rates in the North Atlantic Ocean from changes in the $^{13}C/^{12}C$ of dissolved inorganic carbon, *Global biogeochemical cycles*, *21*, 2007.

Raaphorst, W. V., H. T. Kloosterhuis, A. Cramer, and K. J. Bakker, Nutrient early diagenesis in the sandy sediments of the Dogger Bank area, North Sea: Pore water results, *Netherlands Journal of Sea Research*, *26*, 25–52, 1990.

Racapé, V., C. Pierre, N. Metzl, C. Lo Monaco, G. Reverdin, A. Olsen, P. Morin, M. Vázquez-Rodríguez, A. F. Ríos, and F. F. Pérez, Anthropogenic carbon changes in the Irminger Basin (1981–2006): Coupling $\delta^{13}C_{DIC}$ and DIC observations, *Journal of Marine Systems*, *126*, 24–32, 2013.

Redfield, A., B. Ketchum, and F. Richards, The influence of organisms on the composition of sea water, in *Comparative and Descriptive Oceanography*, edited by M. Hill, Wiley, New York, 1963.

Riddle, A., and R. Lewis, Dispersion experiments in UK coastal waters, *Estuarine, Coastal and Shelf Science*, *51*, 243–254, 2000.

Riley, G., Mathematical model of nutrient conditions in coastal waters, *Bulletin of the bingham oceanographic collection*, *19*, 72–&, 1967.

Robinson, C., and P. l. B. Williams, Respiration and its measurement in surface marine waters, *Respiration in aquatic ecosystems*, pp. 148–181, 2005.

Rowe, G., S. Smith, P. Falkowski, T. Whitledge, R. Theroux, W. Phoel, and H. Ducklow, Do continental shelves export organic matter?, *Nature*, *324*, 559–561, 1986.

Rudnick, D. T., and C. A. Oviatt, Seasonal lags between organic carbon deposition and mineralization in marine sediments, *Journal of Marine Research*, *44*, 815–837, 1986.

Rusch, A., and M. Huettel, Advective particle transport into permeable sediments- evidence from experiments in an intertidal sandflat, *Limnology and Oceanography*, *45*, 525–533, 2000.

Rutgers Van Der Loeff, M., Nutrients in the interstitial waters of the southern bight of the North Sea, *Netherlands Journal of Sea Research*, *14*, 144–171, 1980.

Sabine, C. L., R. A. Feely, N. Gruber, R. M. Key, K. Lee, J. L. Bullister, R. Wanninkhof, C. Wong, D. W. Wallace, B. Tilbrook, et al., The oceanic sink for anthropogenic CO_2, *Science*, *305*, 367–371, 2004.

Salt, L. A., H. Thomas, A. Prowe, A. V. Borges, Y. Bozec, and H. J. Baar, Variability of North Sea pH and CO_2 in response to North Atlantic oscillation forcing, *Journal of Geophysical Research: Biogeosciences*, *118*, 1584–1592, 2013.

Santana-Casiano, J. M., M. González-Dávila, M.-J. Rueda, O. Llinás, and E.-F. González-Dávila, The interannual variability of oceanic CO_2 parameters in the northeast Atlantic subtropical gyre at the estoc site, *Global Biogeochemical Cycles*, *21*, 2007.

Santschi, P. H., R. F. Anderson, M. Q. Fleisher, and W. Bowles, Measurements of diffusive sublayer thicknesses in the ocean by alabaster dissolution, and their implications for the measurements of benthic fluxes, *Journal of Geophysical Research: Oceans (1978–2012)*, *96*, 10641–10657, 1991.

Sarmiento, J., H. Feely, W. Moore, A. Bainbridge, and W. Broecker, The relationship between vertical eddy diffusion and buoyancy gradient in the deep sea, *Earth and Planetary Science Letters*, *32*, 357–370, 1976.

Schmidt, C., C. Hanfland, P. Regnier, P. Van Cappellen, M. Schlüter, U. Knauthe, I. Stimac, and W. Geibert, 228Ra, 226Ra, 224Ra and 223Ra in potential sources and sinks of land-derived material in the German Bight of the North Sea: implications for the use of radium as a tracer, *Geo-Marine Letters*, *31*, 259–269, 2011.

Schwichtenberg, F., Drivers of the carbonate system variability in the southern North Sea: River input, anaerobic alkalinity generation in the Wadden Sea and internal processes, Ph.D. thesis, University of Hamburg, 2013.

Schwichtenberg, F., J. Pätsch, I. Lorkowski, T. Amann, V. Winde, M. Schartau, H. Thomas, O. Dellwig, J. van Beusekom, J. Hartmann, et al., Impact of internal and external alkalinity fluxes on the carbonate system of the larger German Bight, in *EGU General Assembly Conference Abstracts*, vol. 14, p. 11029, 2012.

Shadwick, E., and H. Thomas, Carbon dioxide in the coastal ocean: a case study in the Scotian Shelf region, *Ocean Year Book*, *25*, 171–204, 2011.

Shadwick, E., and H. Thomas, Seasonal and spatial variability in the CO_2 system on the Scotian Shelf (Northwest Atlantic), *Marine Chemistry*, *160*, 42–55, 2014.

Shadwick, E. H., H. Thomas, A. Comeau, S. E. Craig, C. W. Hunt, and J. E. Salisbury, Air-sea CO_2 fluxes on the Scotian Shelf: seasonal to multi-annual variability, *Biogeosciences*, *7*, 3851–3867, 2010.

Shadwick, E. H., H. Thomas, K. Azetsu-Scott, B. J. Greenan, E. Head, and E. Horne, Seasonal variability of dissolved inorganic carbon and surface water pCO_2 in the Scotian Shelf region of the Northwestern Atlantic, *Marine Chemistry*, *124*, 23–37, 2011.

Shan, S., and J. Sheng, Examination of circulation, flushing time and dispersion in Halifax Harbour of Nova Scotia, *Water Quality Research Journal of Canada*, *47*, 353–374, 2012.

Shan, S., J. Sheng, K. R. Thompson, and D. A. Greenberg, Simulating the three-dimensional circulation and hydrography of Halifax Harbour using a multi-nested coastal ocean circulation model, *Ocean Dynamics*, *61*, 951–976, 2011.

Shaw, T. J., Methods and models for estimating advective pore water exchange in tidal flats, *Berichte des Forschunszentrums Terramare*, *12*, 2003.

Signorini, S. R., A. Mannino, R. G. Najjar, M. A. Friedrichs, W.-J. Cai, J. Salisbury, Z. A. Wang, H. Thomas, and E. Shadwick, Surface ocean pCO_2 seasonality and sea-air CO_2 flux estimates for the North american east coast, *Journal of Geophysical Research: Oceans*, *118*, 5439–5460, 2013.

Simmons, G., Importance of submarine groundwater discharge (SGWD) and seawater cycling to material flux across sediment/water interfaces in marine environments, *Marine Ecology Progress Series*, *84*, 1992.

Slomp, C., J. Malschaert, L. Lohse, and W. Van Raaphorst, Iron and manganese cycling in different sedimentary environments on the North Sea continental margin, *Continental Shelf Research*, *17*, 1083–1117, 1997.

Smith, P. C., Low-frequency fluxes of momentum, heat, salt, and nutrients at the edge of the Scotian Shelf, *Journal of Geophysical Research: Oceans*, *83*, 4079–4096, 1978.

Spiker, E., The behavior of C-14 and C-13 in estuarine water; effects of in situ CO_2 production and atmospheric change, *Radiocarbon*, *22*, 647–654, 1980.

Stachelhaus, S. L., S. B. Moran, D. S. Ullman, and R. P. Kelly, Cross-shelf mixing and mid-shelf front dynamics in the Mid-Atlantic Bight evaluated using the radium quartet, *Journal of Marine Research*, *70*, 141–172, 2012.

Ståhl, H., A. Tengberg, J. Brunnegård, E. Bjørnbom, T. Forbes, A. Josefson, H. Kaberi, I. Hassellöv, F. Olsgard, P. Roos, et al., Factors influencing organic carbon recycling and burial in skagerrak sediments, *Journal of Marine Research*, *62*, 867–907, 2004.

Sun, Y., and T. Torgersen, The effects of water content and mn-fiber surface conditions on 224ra measurement by 220rn emanation, *Marine Chemistry*, *62*, 299 – 306, 1998a.

Sun, Y., and T. Torgersen, Rapid and precise measurement method for adsorbed 224ra on sediments, *Marine chemistry*, *61*, 163–171, 1998b.

Syvitski, J. P., K. Asprey, and K. Leblanc, In-situ characteristics of particles settling within a deep-water estuary, *Deep-sea research. Part 2. Topical studies in oceanography*, *42*, 223–256, 1995.

Taguchi, S., and B. Hargrave, Loss rates of suspended material sedimented in a marine bay, *Journal of the Fisheries Board of Canada*, *35*, 1614–1620, 1978.

Takahashi, T., S. C. Sutherland, R. Wanninkhof, C. Sweeney, R. A. Feely, D. W. Chipman, B. Hales, G. Friederich, F. Chavez, C. Sabine, et al., Climatological mean and decadal change in surface ocean pCO_2, and net sea-air co_2 flux over the global oceans, *Deep Sea Research Part II: Topical Studies in Oceanography*, *56*, 554–577, 2009.

Tay, K.-L., K. G. Doe, S. J. Wade, D. A. Vaughan, R. E. Berrigan, and M. J. Moore, Sediment bioassessment in halifax harbour, *Environmental toxicology and chemistry*, *11*, 1567–1581, 1992.

Taylor, K. E., Summarizing multiple aspects of model performance in a single diagram, *Journal of Geophysical Research: Atmospheres (1984–2012)*, *106*, 7183–7192, 2001.

Tengberg, A., P. Hall, U. Andersson, B. Lindén, O. Styrenius, G. Boland, F. De Bovee, B. Carlsson, S. Ceradini, A. Devol, et al., Intercalibration of benthic flux chambers: Ii. hydrodynamic characterization and flux comparisons of 14 different designs, *Marine Chemistry*, *94*, 147–173, 2005.

Thomas, H., Y. Bozec, K. Elkalay, and H. J. De Baar, Enhanced open ocean storage of CO_2 from shelf sea pumping, *Science*, *304*, 1005–1008, 2004.

Thomas, H., Y. Bozec, H. J. De Baar, K. Elkalay, M. Frankignoulle, L.-S. Schiettecatte, G. Kattner, A. Borges, et al., The carbon budget of the North Sea, *Biogeosciences*, *2*, 87–96, 2005.

Thomas, H., L.-S. Schiettecatte, K. Suykens, Y. Koné, E. Shadwick, F. Prowe, Y. Bozec, H. J. de Baar, and A. Borges, Enhanced ocean carbon storage from anaerobic alkalinity generation in coastal sediments, *Biogeosciences*, *6*, 267–274, 2009.

Thomas, H., S. Craig, B. Greenan, W. Burt, G. Herndl, S. Higginson, L. Salt, E. Shadwick, and J. Urrego-Blanco, Direct observations of diel biological CO_2 fixation on the Scotian Shelf, northwestern Atlantic ocean, *Biogeosciences*, *9*, 2301–2309, 2012.

Thomas, H., A. Friederike Prowe, S. van Heuven, Y. Bozec, H. J. de Baar, L.-S. Schiettecatte, K. Suykens, M. Kone, A. V. Borges, I. D. Lima, et al., Rapid decline of the CO_2 buffering capacity in the North Sea and implications for the North Atlantic ocean, *Global Biogeochemical Cycles*, *21*, 2007.

Tsunogai, S., S. Watanabe, and T. Sato, Is there a continental shelf pump for the absorption of atmospheric CO_2?, *Tellus B*, *51*, 701–712, 1999.

Turrell, W., E. Henderson, G. Slesser, R. Payne, and R. Adams, Seasonal changes in the circulation of the northern North Sea, *Continental Shelf Research*, *12*, 257–286, 1992.

Umoh, J. U., and K. R. Thompson, Surface heat flux, horizontal advection, and the seasonal evolution of water temperature on the Scotian Shelf, *Journal of Geophysical Research: Oceans (1978–2012)*, *99*, 20403–20416, 1994.

Urrego-Blanco, J., and J. Sheng, Interannual variability of the circulation over the eastern canadian shelf, *Atmosphere-Ocean*, *50*, 277–300, 2012.

Urrego-Blanco, J., and J. Sheng, Study on subtidal circulation and variability in the gulf of st. lawrence, Scotian Shelf, and gulf of maine using a nested-grid shelf circulation model, *Ocean Dynamics*, *64*, 385–412, 2014.

Van Duyl, F., and A. Kop, Bacterial production in North Sea sediments: clues to seasonal and spatial variations, *Marine Biology*, *120*, 323–337, 1994.

Van Raaphorst, W., H. T. Kloosterhuis, E. M. Berghuis, A. J. Gieles, J. F. Malschaert, and G. J. Van Noort, Nitrogen cycling in two types of sediments of the southern North Sea (Frisian Front, Broad Fourteens): field data and mesocosm results, *Netherlands Journal of Sea Research*, *28*, 293–316, 1992.

Walsh, J., Importance of continental margins in the marine biogeochemical cycling of carbon and nitrogen, *Nature*, *350*, 53–55, 1991.

Wiesner, M. G., B. Haake, and H. Wirth, Organic facies of surface sediments in the North Sea, *Organic Geochemistry*, *15*, 419–432, 1990.

Williams, P., and L. Gordon, Carbon-13: carbon-12 ratios in dissolved and particulate organic matter in the sea, *Deep Sea Research and Oceanographic Abstracts*, *17*, 19 – 27, 1970.

Winde, V., M. Böttcher, P. Escher, P. Böning, M. Beck, G. Liebezeit, and B. Schneider, Tidal and spatial variations of $DI^{13}C$ and aquatic chemistry in a temperate tidal basin during winter time, *Journal of Marine Systems*, *129*, 396–404, 2014.

Wollast, R., and L. Chou, The carbon cycle at the ocean margin in the northern gulf of biscay, *Deep Sea Research Part II: Topical Studies in Oceanography*, *48*, 3265–3293, 2001.

Wootton, J. T., C. A. Pfister, and J. D. Forester, Dynamic patterns and ecological impacts of declining ocean pH in a high-resolution multi-year dataset, *Proceedings of the National Academy of Sciences*, *105*, 18848–18853, 2008.

Zeebe, R. E., and D. Wolf-Gladrow, *CO_2 in Seawater: Equilibrium, Kinetics, Isotopes*, Elsevier, 2001.